



The
University
Of
Sheffield.

***An investigation into the mechanisms of liquid contact
spreading in tumbling drums***

**A thesis submitted to the
University of Sheffield for admission to the degree of**

Doctor of Philosophy

By

Mr Joshua Green

Masters of Engineering (Chemical) Honours I

Loughborough University

The University of Sheffield

Faculty of Engineering

Department of Chemical and Biological Engineering

March 2019

Declaration

The work presented in this thesis is, to the best of my knowledge, original, except as acknowledged in the text, and has not been submitted in whole or in part, for a degree at this or any other institution.

Joshua Green

Acknowledgements

I would firstly like to thank my supervisor, Dr. Rachel Smith, for giving me the opportunity to study this PhD and for her help through its entirety. Also, to Professor Karen Hapgood, for putting me onto the PhD track and suggesting I find Dr Smith in England. I would also like to extend my thanks to everyone at Procter & Gamble (Newcastle, UK) for their help with my project and the many fruitful hours spent on teleconferences.

To everyone in the particle technology group at the University of Sheffield (both present, recently departed and soon to be departed), I am extremely grateful for all the group lunches, help in the lab and useful discussions. To Norzaida Yusof in particular, for sharing in the pain of washing particles and being an excellent lab partner. To my friends also struggling through their PhDs in the department (and outside it, Kit), I am extremely grateful for the Friday evenings of entertainment and lunchtime laughs. And to the source of most of that fun, The Red Deer - other pubs are now just a constant source of disappointment. To the failed medic who dropped out of University and allowed me to move into a house with a bunch of chaps who would become fantastic mates, I hope you found your calling (although I am admittedly glad you didn't do so in Sheffield). A special thank you to Gloria Padmaperuma and the Henderson Reays for letting me stay in their homes over the last few months of my PhD, and for being good friends long before that. To Kate Pitt, the best postdoc I could have wished for, without who I, and no doubt countless others, would never have finished their theses on time. Although maybe it could have been quicker, if not infinitely duller, had we not spent so much time in the pub... I will be eternally grateful for all the time you spent helping me. To Jon Tew, thanks for helping me submit (and being a very dependable part of the pub crew)!

To my friends outside of Sheffield, I am super grateful that you occasionally dragged me out of the PhD bubble. Old school friends, Loughborough friends, and everyone else in-between. Special shout to Tori G for being there throughout.

Finally, to my family. You are a big bunch, but I am grateful to you all. To my grandparents, I would like to thank you for your constant support, and unwavering ability to always provide extremely delicious baked goods (specifically Grandma Shirley). To my aunties, uncles and cousins, thank you for always making family bashes highly amusing. To Sam and Matthew, I will thank you for being top brothers and always being a good source of entertainment. To my mum and dad, I cannot express how grateful I am for everything you have done for me and for all the support (both financial and otherwise) you have given me through my many-many-many years of education. I know you thought it would never end but I appreciate it all enormously.

List of Publications and Presentations

Date	Title
March 2019	A novel method for the analysis of particle coating behaviour via contact spreading in a tumbling drum: Effect of coating liquid viscosity
Draft	Analysing particle coating behaviour via contact spreading in a tumbling drum: Effect of tumbling regime
Sept 2018	Sheffield 30-month confirmation
April 2018	World Congress on particle technology
Feb 2018	Leeds chemical engineering day 2018
June 2016	International fine particle research institute

Abstract

Coating is a very important industrial process. It is well documented that several parameters, both those relating to the materials and the processing equipment, can easily influence the final coating quality. Conceptually, the coating process can be divided into two mechanisms. The first, involving the spray and initial deposition of droplets on the powder bed, is well researched. The second, investigated here, is termed contact spreading. This involves the spreading of liquid from particle to particle, via the creation and rupture of liquid bridges, and is less well defined. The coefficient of variation (CoV), a term commonly used to describe the coating variability in a system, is often employed as a product quality critical attribute; failure to meet these standards can result in batch rejection and heavy financial losses.

In this study, the first experimental work on contact only spreading is introduced, utilising a novel image analysis set-up developed at the University of Sheffield to quantify the CoV. Two types of alumina ceramic particles (termed the model system) and sodium percarbonate particles were used to investigate the effect of material density, particle size, and particle size distribution. Four different molecular weight polyethylene glycol solutions were used to allow the investigation of solution viscosity. Drum sizes and speeds were varied to also study the impact of these variables. When using the lighter density material, the time taken for the systems to homogenise were much longer; this was amplified when using high viscosity coating solutions. Lower viscosity solutions resulted in lower coating times regardless of the particle type used. The effect of particle size showed interesting results; a distribution which contained a large percentage of fines agglomerated heavily, whereas a system using a narrow distribution of small sized particles showed much greater contact spreading than a narrow distribution of large particles. Liquid ingress was also studied; porous materials absorb more liquid, reducing the volume of liquid available on the surface for liquid contact spreading. Particle surface roughness was investigated alongside liquid ingress. The more porous materials had a higher degree of irregularity on the surface, trapping liquid and preventing the formation of liquid bridges. Drum size showed two separate effects; for dense particles, larger drums promoted faster coating, whereas lighter materials showed quicker coating in smaller drums. Alongside this, it was hypothesised that particle mixing, in both the radial and axial directions, also effected contact spreading. Finally, a regime map is proposed which relates a coating number (Co) to a mixing function. Although this mixing function is not fully defined, parameters which are considered to have a large effect on the mixing have been discussed. The work has developed the mechanistic understanding of contact spreading during liquid-particle coating.

Table of contents

Declaration	i
Acknowledgements	iii
List of Publications	v
Abstract	vii
Table of Contents	ix
List of Figures	xiii
List of Tables	xxiii
List of Symbols	xxv
1. Introduction	
1.1 Project background.....	2
1.2 Introduction to industrial coating.....	2
1.3 Aims and objectives.....	4
1.4 Thesis outline.....	5
2. Literature Review	
2.1 Introduction.....	8
2.2 Coating methods.....	9
2.2.1 Dry coating.....	9
2.2.2 Melt coating.....	9
2.2.3 Liquid encapsulation.....	10
2.2.4 Wet coating.....	10
2.3 Coating equipment.....	11
2.3.1 Fluidised bed coaters.....	12
2.3.2 Spouted bed coaters.....	12
2.3.3 Wurster coaters.....	14
2.3.4 Tumbling drums.....	15
2.4 Liquid bridges.....	21
2.4.1 Introduction.....	21
2.4.2 Young-Laplace equation.....	23
2.4.3 Static liquid bridge strength.....	24
2.4.4 Dynamic liquid bridge strength.....	25
2.4.5 Bridge profile approximations.....	28
2.4.6 Experimental methods for measuring bridge strength.....	30
2.4.7 Liquid bridges between three particles.....	31
2.4.8 Rupture distance.....	33
2.4.9 Liquid distribution upon bridge rupture.....	34
2.4.10 Success of particle collisions.....	36
2.5 Wetting and spreading.....	37
2.6 Coating behaviour: Coefficient of Variation.....	39
2.6.1 Experimentally characterising coating uniformity.....	40
2.6.2 Intra-particle coating variability.....	43
2.6.3 Inter-particle coating variability.....	45
2.6.4 Particle tracking: velocity profiles.....	49
2.7 Previous work on contact spreading.....	51
2.6 Conclusions.....	54

3. Materials and Methods	58
3.1 Introduction.....	58
3.2 Material systems.....	58
3.3 Material characterisation.....	59
3.3.1 Particle size.....	60
3.3.2 Density.....	65
3.3.3 Porosity.....	67
3.3.4 Flowability	68
3.3.5 Scanning Electron Microscopy (SEM).....	70
3.3.6 Solution densities.....	70
3.3.7 Surface tension measurements.....	71
3.3.8 Solution viscosity measurements.....	73
3.3.9 Solution contact angle measurements.....	74
3.4 Methods.....	79
3.4.1 Tumbling drum.....	79
3.4.2 Colourimetric image analysis.....	83
3.5 Summary.....	85
4. Mechanistic understanding of contact spreading: Study of material properties	88
4.1 Introduction.....	88
4.2 Methods.....	89
4.3 Data processing: Typical data set.....	91
4.3.1 Frequency distribution data.....	91
4.3.2 Coefficient of Variation	92
4.3.3 Coating rate constant.....	95
4.3.4 Exponential function optimisation.....	96
4.3.5 Time to reach asymptote.....	97
4.4 Results.....	97
4.4.1 Coating behaviour: Effect of material density and coating liquid viscosity.....	97
4.4.2 Analysis of fractured particles.....	105
4.5 Discussion.....	108
4.5.1 Exponential model and analysis evaluation.....	109
4.5.2 Understanding mechanisms effecting contact spreading.....	113
4.6 Conclusions.....	121
5. Mechanistic understanding of contact spreading: Study of drum parameters	124
5.1 Introduction.....	124
5.2 Methods.....	125
5.3 Results and discussion.....	127
5.3.1 Alumina 1: Effect of drum size on coating variation.....	127
5.3.2 Alumina 2: Effect of drum size on coating variation	137
5.3.3 Agglomeration in coating processes.....	145
5.3.3.1 Alumina 1.....	146

5.3.3.2 Alumina 2: Effect of viscosity on agglomeration.....	150
5.3.3.3 Alumina 1: Effect of drum size on agglomeration.....	152
5.3.4 Collision number.....	153
5.4 Conclusions.....	157
6. Mechanistic understanding of contact spreading: Study of material characteristics and drum parameters.....	
6.1 Introduction.....	160
6.2 Methods.....	161
6.2.1 Tumbling drum experiments.....	163
6.2.2 Liquid bridge growth experiments.....	164
6.3 Results and discussion.....	166
6.3.1 Effect of particle size distribution.....	166
6.3.2 Effect of particle size.....	173
6.3.3 Effect of viscosity.....	176
6.3.4 Liquid ingress and surface properties.....	178
6.3.5 Effect of drum speed.....	181
6.3.5 Effect of drum size.....	184
6.3.6 Liquid bridge strength: effect of collision velocity and droplet size.....	185
6.3.7 Collision number.....	190
6.4 Conclusions.....	192
7. Regime map development: a discussion on mixing, segregation and a collision number.....	
7.1 Introduction.....	196
7.2 Need for a regime map.....	196
7.3 Collision number (Co).....	198
7.4 Mixing and segregation.....	200
7.5 Thoughts on a mixing function.....	203
7.6 Conclusions.....	205
8. Conclusions.....	
8.1 Conclusions.....	208
8.2 Future Work.....	210
9. References.....	

List of Figures

Chapter 1

- Figure 1-1** The two conceptualised mechanisms for liquid coating, a) initial drop deposition and spreading, b) distribution of liquid through contact spreading. Blue drops represent liquid and cream represents powder particles.
-

Chapter 2

- Figure 2-1** Different configurations of the fluidised bed coating equipment a) top spray, b) bottom spray, c) Wurster coater. Adapted from Toschkoff & Khinast (2013).
- Figure 2-2** Schematic of tumbling drum spray coater. Adapted from Freireich et al., 2015.
- Figure 2-3** Mode of granular motion in a rotating drum (Pirard et al. 2009). Reprinted from Chemical Engineering Journal, 146, S.L. Pirard., G. Lumay., N. Vandewalle., J.P. Pirard., Motion of carbon nanotubes in a rotating drum: The dynamic angle of repose and a bed behaviour diagram, pp.143-147, (2009), with permission from Elsevier.
- Figure 2-4** Example of a bed behaviour diagram (Shariati et al., 2015).
- Figure 2-5** Fish-bone diagram of the tumbling drum coating process. Reprinted from Journal of Pharmaceutical Sciences, 104, A.M. Agrawal., P. Pandey., Scale up of pan coating process using quality by design principles, pp. 3589-3611, (2015), with permission from Elsevier.
- Figure 2-6** The four types of structure seen in liquid particle interactions. Reprinted from Powder Technology, 117, S.M. Iveson., J.D. Litster., K. Hapgood., B.J Ennis., Nucleation, growth and breakage phenomena in agitated wet granulation processes: a review, pp. 3-39, (2001), with permission from Elsevier.
- Figure 2-7** Phenomena occurring during wet coating. Reprinted from Handbook of Powder Technology, K. Saleh., P. Guigon., Coating and Encapsulation Processes in Powder Technology, pp. 323-375, (2007), with permission from Elsevier.
- Figure 2-8** Schematic of a pendular bridge between two equi-sized spheres. Adapted from Iveson et al., 2001. Reprinted from Powder Technology, 117, S.M. Iveson., J.D. Litster., K. Hapgood., B.J Ennis., Nucleation, growth and breakage phenomena in agitated wet granulation processes: a review, pp. 3-39, (2001), with permission from Elsevier.
- Figure 2-9** Schematic of the toroidal approximation of a liquid bridge for a concave profile. Red dotted line shows the arc of the circle used to approximate the bridge profile. Reprinted from Handbook of Powder Technology, S. Simons., Liquid Bridges in Granules, pp. 1257-1316, (2007), with permission from Elsevier.
- Figure 2-10** Schematic of the toroidal approximation of a liquid bridge for a convex profile. Red dotted line shows the arc of the circle used to approximate the bridge profile. Reprinted from Handbook of Powder Technology, S. Simons.,

Liquid Bridges in Granules, pp. 1257-1316, (2007), with permission from Elsevier.

- Figure 2-11** Schematic of the parabolic approximation of a liquid bridge. Reprinted from Handbook of Powder Technology, S. Simons., Liquid Bridges in Granules, pp. 1257-1316, (2007), with permission from Elsevier.
- Figure 2-12** Experimental tensile strength profiles at a) 0.2 mm/s stretching speed and b) 2.0 mm/s stretching speed. Reprinted with permission from Springer: Nature, Granular Matter, Experimental and numerical studies on liquid bridge formed among three spheres, K. Murase., T. Mochida., H. Sugama., (2004).
- Figure 2-13** Schematic of a static liquid bridge between three particles with grid generation for simulation purposes in spherical co-ordinates (Murase et al. 2008). Reprinted from Advanced Powder Technology, 19, K. Murase., T. Mochida., Y. Sagawa., H. Sugama., Estimation on the Strength of a liquid bridge adhered to three spheres, pp. 349 – 367, (2008), with permission from Elsevier.
- Figure 2-14** Liquid transfer fraction as a function of capillary number for two different contact angles. Adapted from Salcudean et al., 2010.
- Figure 2-15** Evolution of a liquid bridge for liquid transfer between two surfaces (. Reprinted with permission from Langmuir, H. Chen., T., Tang, A. Amirfazli., Fast liquid transfer between surfaces, Breakup of stretched liquid birdges. Copyright (2015) American Chemical Society.
- Figure 2-16** Contact angles for droplets on a surface showing a) non-wetting, b) partial wetting, and c) complete wetting.
- Figure 2-17** DEM predictions of intra-tablet coefficient of variation plotted as a function of number of coats for six tablet shapes. Reprinted from Chemical Engineering Science, 66, B. Freireich., W.R. Ketterhagen., C. Wassgre., Intra-tablet coating variability for several pharmaceutical tablet shapes, pp. 2535 – 2544, (2011), with permission from Elsevier.
- Figure 2-18** Simulated flow of particles in an un-baffled horizontal rotating drum. The black arrows represent the particles general circulating loop, the solid black line represents the spray zone, and the passive bed zone is indicated by the red region. Reprinted from Chemical Engineering Science, 125, R. Kumar., B. Freireich., C. Wassgren., DEM-compartment-population balance model for particle coating in a horizontal rotating drum, pp. 144-157, (2015), with permission from Elsevier.
- Figure 2-19** Schematic of liquid birdge spherical caps used to determine the liquid bridge volume. Reprinted from Powder Technology, 184, D. Shi., J.J. McCarthy., Numerical simulation of liquid transfer between particles, pp. 64-75, (2008), with permission from Elsevier.
- Figure 2-20** Post-rupture liquid distribution model. Reprinted by permission from Springer: Nature, Granular Matter, Liquid migration in sheared unsaturated granular media, R. Mani., D. Kadau., H.J. Herrmann., (2012).
- Figure 2-21** Graphs showing the coefficient of variation as a function of time as predicted by three models; left) liquid viscosity = 0.001 Pa.s, and right) liquid viscosity = 0.1 Pa.s. Reprinted from Chemical Engineering Research and Design, 110, K. Washino., K. Miyazaki., T. Tsuji., T. Tanaka., A new contact liquid disperison

mode for discrete particle simulation, pp. 123-130, (2016), with permission from Elsevier.

Figure 2-22 Example of discretisation method used by Schmelzle et al with 1001 discretised potential liquid storage points. Reprinted from Powder Technology, 338, S. Schmelzle, E. Asylbekov., B. Radel., H. Nirschl., Modelling of partially wet particles in DEM simulations of a solid mixing process, pp, 354-364 (2018), with permission from Elsevier.

Chapter 3

- Figure 3-1** Flowchart showing an overview of the experimental procedure.
- Figure 3-2** Images of the particles employed in this research.
- Figure 3-3** Particle size distribution of sodium percarbonate obtained via sieve analysis.
- Figure 3-4** Cumulative particle size distribution of sodium percarbonate obtained via sieve analysis.
- Figure 3-5** Particle size and cumulative particle size distribution of Alumina 1 obtained via sieve analysis.
- Figure 3-6** Particle size and cumulative particle size distribution of Alumina 2 (Batch 1) obtained via sieve analysis.
- Figure 3-7** Particle size and cumulative particle size distribution of Alumina 2 (Batch 2) obtained via sieve analysis.
- Figure 3-8** Schematic diagram of experimental work for angle of repose a) top view showing the x and y dimensions of the particle pile, and b) side view showing the height (h) of the particle pile.
- Figure 3-9** Angle of repose and angle of wall friction for all materials used in this research and other materials used for reference.
- Figure 3-10** Snapshot of pendant droplet (810 mPa.s viscosity PEG solution) used to measure interfacial tension.
- Figure 3-11** Viscosity as a function of shear rate for all solutions. Circles represent the PEG/water solutions used with alumina particles. Diamonds represent the PEG/water/ethanol solutions used with sodium percarbonate particles.
- Figure 3-12** Example of the initial contact angles formed on sodium percarbonate tablets using a) 179, b) 810, c) 4,080, and d) 20,200 mPa.s PEG solutions.
- Figure 3-13** Contact angle as a function of time for four different viscosity coating solutions on a powdered bed of Alumina 1 material.
- Figure 3-14** Contact angle as a function of time for four different viscosity coating solutions on a powdered bed of Alumina 2 material.
- Figure 3-15** Contact angle as a function of time for four different viscosity coating solutions on a powdered bed of sodium percarbonate particles.
- Figure 3-16** Contact angle as a function of time for four different viscosity coating solutions on sodium percarbonate tablets.

Figure 3-17 Procedure for experimental work.

Figure 3-18 Images showing various stages of the methodology a) application of particles into delivery arm b) coated particles evenly distributed along delivery arm length and inserted into drum, c) inserting delivery arm into drum through protective cage and inverting.

Figure 3-19 Experimental set-up of Luminera Infinity 3 camera with a Navitar 12X zoom lens and diffuse lighting.

Figure 3-20 Labview process for obtaining labelled image (example using Alumina 1 particles).

Chapter 4

Figure 4-1 Coating evolution of Alumina 1 particles with 179 mPa.s viscosity PEG solution at various time points (some time points removed for clarity).

Figure 4-2 CoV (%) red values as a function of tumbling time.

Figure 4-3 CoV (%) red values fitted using the exponential function, Equation 4.2.

Figure 4-4 CoV as a function of time for the 179 mPa.s viscosity coating solution for Alumina 1 (red) and Alumina 2 (blue).

Figure 4-5 Normalised CoV as a function of time for the 179 mPa.s viscosity coating solution for Alumina 1 (red) and Alumina 2 (blue). Exponential functions for each data set are displayed as dashed lines.

Figure 4-6 CoV as a function of time for the 4,080 mPa.s viscosity coating solution for Alumina 1 (red) and Alumina 2 (blue).

Figure 4-7 Normalised CoV as a function of time for the 4,080 mPa.s viscosity coating solution for Alumina 1 (red) and Alumina 2 (blue). Exponential functions for each data set are displayed as dashed lines.

Figure 4-8 CoV as a function of time for the 20,200 mPa.s viscosity coating solution for Alumina 1 (red) and Alumina 2 (blue).

Figure 4-9 Normalised CoV as a function of time for the 20,200 mPa.s viscosity coating solution for Alumina 1 (red) and Alumina 2 (blue). Exponential functions for each data set are displayed as dashed lines.

Figure 4-10 a) Coating rate constants (s^{-1}), and b) CoV_{∞} (%), for all combinations of the Alumina 1 and Alumina 2 material and the three coating solutions. Blue = 179 mPa.s, Orange = 4,080 mPa.s, Grey = 20,200 mPa.s.

Figure 4-11 Images and corresponding CoV (%) red values of Alumina 1 and Alumina 2 particles at varying time points (179 mPa.s).

Figure 4-12 Images and corresponding CoV (%) red values of Alumina 1 and Alumina 2 particles at varying time points (20,200 mPa.s).

Figure 4-13 Fractured Alumina 1 coated with a 10 % red dye solution.

Figure 4-14 Fractured Alumina 2 coated with a 10 % red dye solution.

- Figure 4-15** SEM images taken at 1,100 magnification showing the surface structure of a) Alumina 1 and b) Alumina 2.
- Figure 4-16** Comparison of fits for modelling the change of CoV as a function of time. Circles are experimental data points, the solid line represents the exponential function as detailed in equation 2 ($R^2 = 0.97$), and the dotted line represents a power law function ($R^2 = 0.85$).
- Figure 4-17** Mean red (%) as a function of tumbling time.
- Figure 4-18** CoV as a function of time using (a) actual mean red values, and (b) a higher averaged mean red value.
- Figure 4-19** Images of (a) raw white particles, (b) untumbled red particles, and (c) and (d) particles from the zero second time point analysis.
- Figure 4-20** Log-log plot of the critical rupture distance as a function of the liquid bridge volume for different coating solutions. ● represent Alumina 1 particles, and ▲ represent Alumina 2 particles.
- Figure 4-21** Comparison of the viscous force computed with the Adams & Perchard model and the Pitois model over the range of separation distances used in this work.
- Figure 4-22** Log-normal plot of the Collision number calculated using two separate methods against the coating completion time. Alumina 1 particles using three different viscosity coating solutions.
- Figure 4-23** Co number shown alongside coating completion times for Alumina 1 (blue) and Alumina 2 (orange). ● = 0.179 Pa.s, ■ = 4.08 Pa.s, ▲ = 20.2 Pa.s.

Chapter 5

- Figure 5-1** CoV data for 179 mPa.s PEG solution with Alumina 1 in Drum A, B and C. The legend shows which drum was used with the experiment number given in brackets.
- Figure 5-2** Normalised CoV data for 179 mPa.s PEG solution with Alumina 1 in Drum A, B and C. Exponential functions for each data set are displayed as dashed lines.
- Figure 5-3** CoV data for 4,080 mPa.s PEG solution with Alumina 1 in Drum A and B. The legend shows which drum was used with the experiment number given in brackets.
- Figure 5-4** Normalised CoV data for 4,080 mPa.s PEG solution with Alumina 1 in Drum A and B. Exponential functions for each data set are displayed as dashed lines.
- Figure 5-5** CoV data for 20,200 mPa.s PEG solution with Alumina 1 in Drum A, B, C and D. The legend shows which drum was used with the experiment number given in brackets.
- Figure 5-6** Normalised CoV data for 20,200 mPa.s PEG solution with Alumina 1 in Drum A, B, C and D. Exponential functions for each data set are displayed as dashed lines.
- Figure 5-7** CoV_{∞} values as a function of drum size for Alumina 1 particles using 179 mPa.s, 4,080 mPa.s and 20,200 mPa.s viscosity solutions.
- Figure 5-8** Coating rate constants as a function of drum size for Alumina 1 particles using 179 mPa.s, 4,080 mPa.s and 20,200 mPa.s viscosity solutions.

- Figure 5-9** Time for coating completion as a function of drum size for Alumina 1 particles using 179 mPa.s, 4,080 mPa.s and 20,200 mPa.s viscosity solutions.
- Figure 5-10** Normalised coefficient of variation as a function of drum revolutions for coating solutions viscosities of 179 mPa.s in Drum A, B and C. Exponential functions for each data set are displayed as dashed.
- Figure 5-11** Normalised coefficient of variation as a function of drum revolutions for coating solutions viscosities of 4,080 mPa.s in Drum A and B. Exponential functions for each data set are displayed as dashed.
- Figure 5-12** Normalised coefficient of variation as a function of drum revolutions for coating solutions viscosities of 20,200 mPa.s in Drum A, B, C and D. Exponential functions for each data set are displayed as dashed.
- Figure 5-13** CoV data for 179 mPa.s PEG solution with Alumina 2 in Drum A and B. The legend shows which drum was used with the experiment number given in brackets.
- Figure 5-14** Normalised CoV data for 179 mPa.s PEG solution with Alumina 2 in Drum A, B and C. Exponential functions for each data set are displayed as dashed lines.
- Figure 5-15** CoV data for 4,080 mPa.s PEG solution with Alumina 2 in Drum A and B. The legend shows which drum was used with the experiment number given in brackets.
- Figure 5-16** Normalised CoV data for 4,080 mPa.s PEG solution with Alumina 2 in Drum A and B. Exponential functions for each data set are displayed as dashed lines.
- Figure 5-17** CoV data for 20,200 mPa.s PEG solution with Alumina 2 in Drum A and B. The legend shows which drum was used with the experiment number given in brackets.
- Figure 5-18** Normalised CoV data for 20,200 mPa.s PEG solution with Alumina 2 in Drum A, B and C. Exponential functions for each data set are displayed as dashed lines.
- Figure 5-19** CoV_{∞} values as a function of drum size for Alumina 2 particles using 179 mPa.s, 4,080 mPa.s and 20,200 mPa.s viscosity solutions.
- Figure 5-20** Coating rate constants as a function of drum size for Alumina 2 particles using 179 mPa.s, 4,080 mPa.s and 20,200 mPa.s viscosity solutions.
- Figure 5-21** Time for coating completion as a function of drum size for Alumina 2 particles using 179 mPa.s, 4,080 mPa.s and 20,200 mPa.s viscosity solutions.
- Figure 5-22** Normalised coefficient of variation as a function of drum revolutions for coating solutions viscosities of 179 mPa.s with Alumina 2 in Drum A and B. Exponential functions for each data set are displayed as dashed lines.
- Figure 5-23** Normalised coefficient of variation as a function of drum revolutions for coating solutions viscosities of 4,080 mPa.s with Alumina 2 in Drum A and B. Exponential functions for each data set are displayed as dashed lines.
- Figure 5-24** Normalised coefficient of variation as a function of drum revolutions for coating solutions viscosities of 20,200 mPa.s with Alumina 2 in Drum A and B. Exponential functions for each data set are displayed as dashed lines.
- Figure 5-25** Percentage of total Alumina 1 particle mass present as agglomerates at several time points for three different viscosity solutions.

- Figure 5-26** Mean red % values for Alumina 1 particles tumbled with 20,200 mPa.s viscosity solution.
- Figure 5-27** Mean red % values for Alumina 1 particles tumbled with 4,080 mPa.s viscosity solution.
- Figure 5-28** Percentage of total Alumina 2 particle mass present as agglomerates (○) at several time points for three different viscosity solutions with Alumina 1 shown for comparison (●).
- Figure 5-29** Colour comparison of agglomerates and bulk particles of Alumina 2 particles coated with 20,200 mPa.s PEG solution at three time points.
- Figure 5-30** Comparison of percentage of agglomerates found in experiments completed in Drum A and Drum B as a function of time for Alumina 1 using 20,200 mPa.s viscosity coating solution.
- Figure 5-31** Co number against the coating completion time for all experiments completed in this chapter with Alumina 1. Labels show drum sizes, and viscosity of coating solution.
- Figure 5-32** Co number against the number of drum revolutions needed to reach coating completion for all experiments completed in this chapter with Alumina 1.
- Figure 5-33** Co number against the coating completion time for all experiments completed in this chapter with Alumina 2.
- Figure 5-34** Co number against the number of drum revolutions needed to reach coating completion for all experiments completed in this chapter with Alumina 2.
- Figure 5-35** Co number against the coating completion time for all experiments completed in this chapter with Alumina 1 (●) and Alumina 2 (■).

Chapter 6

- Figure 6-1** Experimental set-up of particle-particle collision experiments.
- Figure 6-2** Sodium percarbonate particles coated with 179 mPa.s viscosity PEG solution and tumbled for a) 0 seconds, b) 30 seconds, c) 60 seconds and d) 300 seconds.
- Figure 6-3** CoV as a function of tumbling time for unsieved sodium percarbonate coated with 179 mPa.s viscosity solution in Drum A.
- Figure 6-4** Unsieved sodium percarbonate compared to sieved sodium percarbonate (size fractions as per Table 6-4) in Drum A.
- Figure 6-5** CoV as a function of tumbling time for sieved sodium percarbonate (>850 μm) coated with 179 mPa.s viscosity coating solution in Drum A. Brackets in legend refer to experiment repeat number.
- Figure 6-6** Percentage of agglomerates as a function of tumbling time for the full size range unsieved and sieved compared with experiments where the fines have been removed (179 mPa.s coating solution) in Drum A.
- Figure 6-7** Comparison of the effect of particle material on the CoV as a function of time, all coated with 179 mPa.s viscosity PEG solution in Drum A. Legend shows particle material and experiment repeat number in brackets.

- Figure 6-8** Sodium percarbonate particles greater than 850 μm coated with 179 mPa.s viscosity 50 % PEG solution and tumbled for a) 0 seconds, b) 30 seconds, c) 60 seconds and d) 300 seconds.
- Figure 6-9** Effect of initial particle size on the CoV as a function of tumbling time using 179 mPa.s viscosity PEG solutions in Drum A. Legend shows particle size range and experiment repeat number in brackets.
- Figure 6-10** Comparison of images of different sodium percarbonate particle sizes coated with 179 mPa.s viscosity PEG solutions.
- Figure 6-11** Percentage of agglomerates present at each time point for systems using various sized particles.
- Figure 6-12** Effect of solution viscosity on liquid contact spreading for the 50 % PEG in 10 % ethanol / water solutions.
- Figure 6-13** Agglomeration as a function of tumbling time for four different 10 % ethanol /water PEG solutions.
- Figure 6-14** Dissected sodium percarbonate particles coated with 102 mPa.s viscosity PEG solution.
- Figure 6-15** Dissected sodium percarbonate particles coated with 2,920 mPa.s viscosity PEG solution.
- Figure 6-16** Dissected sodium percarbonate particles coated with 14,600 mPa.s viscosity PEG solution.
- Figure 6-17** SEM images of surfaces of a) Alumina 1 and b) Sodium percarbonate.
- Figure 6-18** CoV as a function of tumbling time for a number of different drum speeds in Drum A. Coated using 179 mPa.s viscosity PEG solutions. Legend indicates tumbling speed with experiment repeat number shown in brackets.
- Figure 6-19** CoV as a function of number of drum revolutions for a number of different drum speeds in Drum A. Coated using 179 mPa.s viscosity PEG solutions. Legend indicates tumbling speed with experiment repeat number shown in brackets.
- Figure 6-20** Log-normal plot of percentage of agglomerates as a function of tumbling time for 30, 70 and 90 rpm. Legend indicates tumbling speed with experiment repeat number shown in brackets.
- Figure 6-21** Normalised CoV as a function of time for sodium percarbonate tumbled in Drum A (70 rpm) and Drum C (45 rpm) and coated with 102 mPa.s viscosity PEG solution.
- Figure 6-22** Effect of collision velocity for two different drop sizes of the 179 mPa.s solution. \blacklozenge are 0.52 mm^3 and \blacksquare are 0.30 mm^3 droplet volumes.
- Figure 6-23** Effect of liquid viscosity on liquid bridge width as a function of time (0.3 mm^3 drop volume and 1.7 m/s collision velocity).
- Figure 6-24** Effect of liquid viscosity on liquid bridge width as a function of time ($\sim 0.5 \text{ mm}^3$ drop volume and 1.7 m/s collision velocity).

Figure 6-25 Co number as a function of tumbling time for all the experiments completed using sodium percarbonate.

Chapter 7

Figure 7-1 Basic regime map for understanding contact spreading.

Figure 7-2 Log-log plot of the Co number and coating completion time for all experiments completed in this thesis.

Figure 7-3 Log-log plot of the Co number and coating completion time for all experiments completed in this work, and experimental data from Yusof et al. (2018).

Figure 7-4 Flow speed as a function of the normalised direction in the radial direction through the powder bed (Jarray et al., 2018).

List of Tables

Chapter 2	
Table 2-1	Summary of research on fluidised bed coaters.
Table 2-2	Differences in pan speed and pan radius needed to maintain an approximately constant Froude number for two different batch sizes. Adapted from Chen et al., 2010.
Table 2-3	Regimes predicted as a result of differences in the Stokes number with regard to the critical Stokes number.
Table 2-4	Summary of various techniques used in analysis of tablet / particle coating.

Chapter 3	
Table 3-1	Particle size data measured using laser diffraction.
Table 3-2	Particle size data measured using sieve analysis.
Table 3-3	Densities of the three types of particles.
Table 3-4	Particles and their calculated porosities.
Table 3-5	Solution density measurements for PEG 4,000, PEG 10,000, PEG 20,000 and PEG 35,000 (and the equivalent 10 % ethanol / water solutions).
Table 3-6	Surface tension measurements for PEG 4,000, PEG 10,000, PEG 20,000 and PEG 35,000 (and the equivalent 10 % ethanol / water solutions).
Table 3-7	Viscosity results for 50 % PEG solutions and 10 % ethanol solutions made with 4,000 MW, 10,000 MW, 20,000MW and 35,000 MW PEGs.
Table 3-8	Drum dimensions.

Chapter 4	
Table 4-1	Particle properties for Alumina 1 and Alumina 2.
Table 4-2	Coating liquid properties.
Table 4-3	Particle and liquid coating combinations used in this chapter.
Table 4-4	Example of data obtained from Labview.
Table 4-5	Recalculated porosity values.
Table 4-6	Comparison of R ² values for the exponential and power law models along with particle type and viscosity of the coating solution.

Table 4-7 Solution viscosity, surface tension and capillary number for the three solutions used, calculated using Equation 4-9.

Table 4-8 Summary of liquid bridge volumes at the beginning and end of the coating process for Alumina 1 and Alumina 2.

Chapter 5

Table 5-1 Particle properties for Alumina 1 and Alumina 2.

Table 5-2 Coating liquid properties.

Table 5-3 Drum dimensions.

Table 5-4 Particle and liquid coating combinations used in this chapter for effect of drum size.

Table 5-5 Images of Alumina 1 agglomerates larger than 2mm sieve size, for a variety of time points and solution viscosities.

Chapter 6

Table 6-1 Particle properties for sodium percarbonate.

Table 6-2 Coating liquid properties for the 50 % PEG aqueous solutions and 50 % PEG in 10 % ethanol /water PEG solutions.

Table 6-3 Size fractions of sodium percarbonate used in experiments with corresponding liquid volumes.

Table 6-4 Dimensions of drums used in this chapter.

Table 6-5 Sodium percarbonate size fractions.

Table 6-6 Updated size fractions with fines < 850 μm removed.

Table 6-7 Liquid bridge development for 179 mPa.s, 810 mPa.s and 4,080 mPa.s viscosity PEG solutions over various time points.

List of Symbols

Symbol	Meaning
D	Drum diameter
dh/dt	Half gap velocity
e	Coefficient of restitution
f	Drum fill level
F_B	Capillary bridge force calculated via the Boundary method
F_{BG}	Bagnold force
F_G	Capillary bridge force calculated via the Gorge method
F_v	Force due to the viscous component of the liquid
F_V^*	Dimensionless bridge force
g	Acceleration due to gravity
h	Half separation distance
h_a	Height of asperities on a particle surface
h_l	Height of liquid on a particle surface
L	Drum length
L_{SPW}	Spanwise length of the spray zone
P_C	Coated particles
P_U	Uncoated particles
ΔP	Capillary suction pressure
R	Distance from the axial line joining the two particles to the edge of the liquid bridge as it connects with the particle
R_i	Radius of the i^{th} particle
R_D	Drum radius
r_g	Granule radius
r_p	Particle radius
r_1	Radius of curvature of the liquid bridge profile
r_2	Liquid bridge radius at midpoint (for equisized particles)
R^*	Harmonic mean radius
S	Separation distance
S_c	Critical rupture distance
S_c^*	Dimensionless critical rupture distance
S_{initial}	Initial particle segregation index

t	Coating time
t_c	Coating completion time
V	Particle velocity
V_b	Liquid bridge volume
V_b^*	Dimensionless liquid bridge volume
V_D	Drum volume
V_L	Liquid volume
v	Relative particle velocity
V_f^*	Dimensionless drum fill volume

Dimensionless numbers	Meaning
Bo	Bond number
Ca	Capillary number
Co	Collision number
Fr	Froude number
Stv	Viscous stokes number
Stv*	Critical viscous stokes number

Greek letters	Meaning
γ	Liquid surface tension
γ_{LV}	Liquid-vapour interfacial tension
γ_{SL}	Solid-liquid interfacial tension
γ_{SV}	Solid-vapour interfacial tension
δ	Particle flowing layer thickness
δ^*	Dimensionless separation distance
ε	Porosity
ϕ	Half filling angle
λ	Coating rate constant
μ	Viscosity
ζ	Mean of the red intensity
ζ_c	Mean of the cycle time distribution
ζ_M	Mean of the coating mass
ζ_N	Mean of the number of passes a tablet makes through the spray zone
ζ_w	Mean of the coating received per pass through the spray zone
v	Separation speed
π	Pi

θ	Liquid-solid contact angle (radians)
θ_r	Receding phase contact angle (radians)
ρ_e	Envelope density
ρ_B	Bulk density
ρ_l	Liquid phase density
ρ_s	Solid phase density
ρ_t	True density
σ_c	Standard deviation of the cycle time distribution
σ_M	Standard deviation of the coating mass
σ_N	Standard deviation of the number of passes a tablet makes through the spray zone
σ_w	Standard deviation of the coating received per pass through the spray zone
ω	Drum speed (rpm)

Abbreviations	Meaning
CoV	Coefficient of variation
CoV _{Inter}	Inter-particle coefficient of variation
CoV _{Intra}	Intra-particle coefficient of variation
CoV _{Norm}	Normalised CoV
CoV _∞	Asymptotic CoV
CoV ₀	Initial CoV

1. Introduction

1. Introduction

1.1 Project background.....	2
1.2 Introduction to industrial coating.....	2
1.3 Aims and objectives.....	4
1.4 Thesis Outline.....	5

1.1 Project background

Coating is the process of applying a layer of material onto another material (Saleh & Guigon, 2006). This can include the application of liquid coating solutions (bleaches, perfumes etc.) onto powdered detergents, the fine coating of liquids onto pharmaceutical tablets, the application of paint particles onto a surface, or the coating of foodstuffs with different flavourings, to name but a few. Liquid spray coating is clearly an important process for many industries and has benefitted from numerous studies e.g. Pandey et al. (2006), Saleh et al. (2003), Basu et al. (2013) and Kumar & Wassgren (2014). Yet, regardless of this fact, the coating process still presents several difficult challenges, namely, understanding the role of liquid bridges in liquid distribution. Because of gaps in the process understanding, scale up and design of coaters can often be based on trial and error with predictive tools not being readily available.

This first chapter will summarise the state of the current understanding in the coating field and highlight the areas which this research will seek to address. The main aims and objectives of the work will be presented, alongside a description of the content of future chapters.

1.2 Introduction to industrial coating

Coating of powders and particles is often the final step in a manufacturing process e.g. pharmaceutical tablet coating, and is done for myriad reasons, e.g. taste, functionality, handling issues (flowability), and as a protective barrier (Basu et al., 2013). The uniformity of these coating solutions is of extreme importance for quality assurance; in the pharmaceutical industry, for example, heterogeneous coating layers have the potential to either speed-up or delay the release of the active ingredient, making drugs ineffective. Coatings can be applied in one of several different manners; dry coating, wet coating, melt coating, or encapsulation, with the process chosen being a function of the end product specification. Research is available on all of these methods and covers a wide range of processing equipment (Ye & Chi, 2018; Sauer et al., 2013). However, recently, more and more processes are favouring tumbling drums as a quick and cheap method of coating particles with liquids and, therefore, an understanding of the

underlying mechanisms is quickly becoming of high importance; powdered detergent manufactured in this way accounted for 31 % of the total global sales (€ 133.3 billion) of detergents in 2016 (Grand view research, 2017).

Mechanistically speaking, coating within a tumbling drum can be conceptualised as two separate processes; first is the initial liquid deposition and spreading on the primary particles, and second is the transfer of this liquid to other particles through contact spreading (seen visually in Figure 1-1). The initial liquid deposition has benefitted from a vast amount of research; work proposed by Litster et al. (2001), detailing the dimensionless spray flux, is now widely accepted and used to characterise binder distribution in terms of the solution flowrate, the powder flux and the solution droplet size.

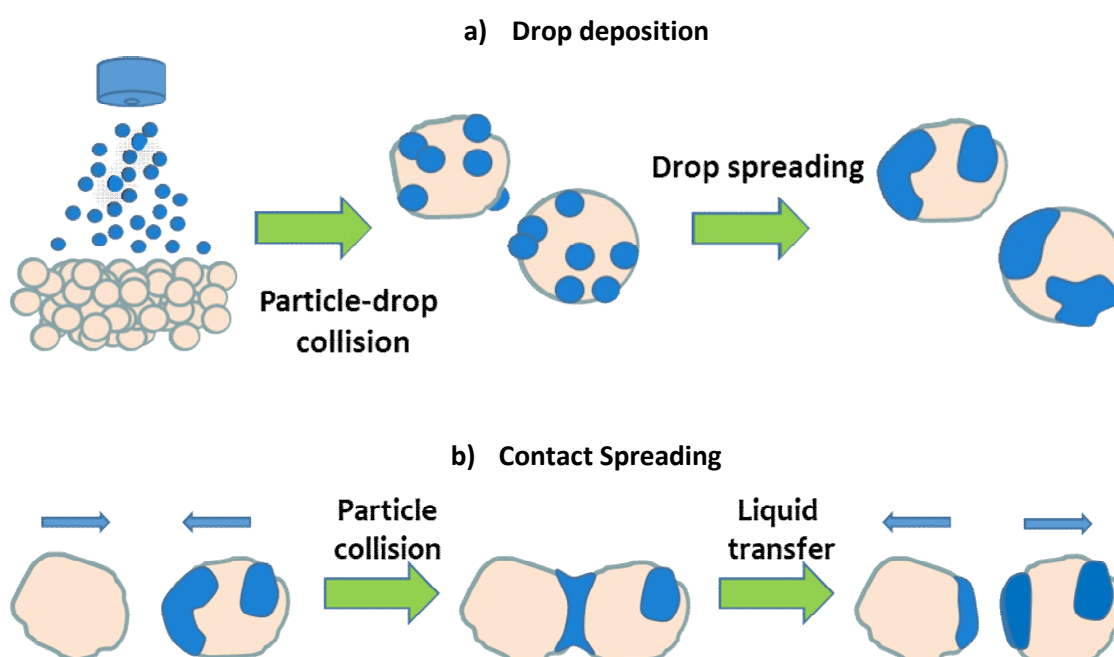


Figure 1-1. The two conceptualised mechanisms for liquid coating, a) initial drop deposition and spreading, b) distribution of liquid through contact spreading. Blue drops represent liquid and cream represents powder particles.

Contact spreading is understood to refer to the distribution of liquid around the bulk powder bed via the formation and subsequent rupture of liquid bridges. Research into liquid bridge behaviour has made great advances in understanding the interaction between two particles (Mazzone et al., 1987; Willett et al., 2000; Pitois et al., 2000; Mu & Su, 2007), and occasionally three particles (Rynhart et al., 2003; Murase et al., 2004;

Murase et al., 2008; Lievano et al., 2017), joined by liquid bridges. However, research into contact spreading in production scale interactions is lacking. Recently, several authors have published research on modelling the contact spreading in drums (Shi & McCarthy, 2008; Washino et al., 2016), but simplifications mean the models often overpredict the amount of liquid transfer seen in a system and / or are unable to account for changes in system properties. The work here will seek to address this knowledge gap by advancing the understanding of the contact spreading mechanism through an experimental investigation of several operational parameters and material properties.

It is hypothesised that values extracted from analysis of the experimental data can be correlated with some dimensionless number as a way of describing the controlling mechanisms. In this way, the main factors which prevail in the systems studied here can be determined.

1.3 Aims and objectives

The overall aim of this research is to develop a mechanistic understanding of contact spreading in tumbling drums and understand and relate the effect of changes in material properties and operational parameters to the coating uniformity. As this is the first time this phenomenon has been investigated on a lab scale, an appropriate methodology must first be determined for both the experimental execution and for quantifying the coating uniformity in the following analysis. This aim will be met by completing the following objectives:

1. Investigating various material properties and operational parameters using two model systems consisting of spherical, mono-sized alumina ceramic particles and a range of different molecular weight polyethylene glycol solutions as the coating liquids.
 - 2.1. Investigate liquid viscosity
 - 2.2. Investigate material density
 - 2.3. Investigate drum size
2. Investigating realistic coating systems specific to the detergent industry to determine whether trends identified when using model materials are still

applicable. Here, sodium percarbonate particles will be used instead of alumina. In contrast to the model alumina particles, these particles are non-spherical, porous and exhibit a large size distribution. This will allow for the effect of these different properties to be studied. The effect of the aforementioned parameters on coating uniformity will be quantitatively determined using colourimetric analysis

- 3.1. Investigate coating of a realistic powdered material (sodium percarbonate)
 - 3.2. Investigate size distribution
3. Consolidating this new information to create a tool to help predict the coating behaviour of various systems in tumbling drums. These rules can be potentially extended to cover other pieces of coating equipment.

1.4 Thesis outline

Chapter 2 of this thesis is given to a review of the existing literature in the area of coating, with particular emphasis on contact spreading and tumbling drums. Here, various aspects of liquid bridges (the method through which liquid is transported around the powder bed) will be detailed, and gaps in the existing knowledge will be highlighted.

Chapter 3 discusses all the materials used in the experimental works, and gives a description of the techniques used to characterise both the powders and coating solutions. The methodology for the general experimental work is also presented.

Chapter 4 is the first results chapter and presents the development of the data analysis technique with which to quantify coating uniformity/behaviour. Various experiments are completed using the two model materials and results give an insight into the effect of material porosity and solution viscosity on contact spreading.

Chapter 5 looks at operational parameters, specifically the effect of drum size, on the contact spreading. Again, the same two model materials are used.

Chapter 6 utilises a more realistic powdered material; sodium percarbonate. The material is present in a large number of detergents, and its shape and composition offer an insight into a more realistic coating scenario. The particle-liquid interactions are

Chapter 1
Introduction

influenced by the surface structure, a fact which is reflected in the ultimate coating variability.

Chapter 7 provides a final discussion on all aspects of the data presented, presenting a map developed from the understanding of the contact spreading mechanism gained through this research.

Chapter 8 is the final chapter and concludes the thesis, and also gives recommendations for further study.

2. Literature review

2. Literature review	
2.1 Introduction.....	8
2.2 Coating methods.....	9
2.3 Coating equipment.....	11
2.4 Liquid bridges.....	21
2.5 Wetting and spreading.....	37
2.6 Coating behaviour: Coefficient of variation.....	39
2.7 Previous work on contact spreading.....	51
2.8 Conclusions.....	54

2.1 Introduction

The transfer of liquid and binders between surfaces is important in many industrial processes and its efficiency can greatly influence the final product quality. Inkjet printing, particle agglomeration, tablet coating and detergent manufacture are just a few examples of processes that incorporate liquid transfer. Liquid bridges are present in a number of particle unit processes; agglomeration utilises liquid bridges to hold several constituent particles together as an agglomerate, coating uses liquid bridges to facilitate the transfer of liquid from one particle to another. In none of those industries is the formation and rupture of liquid bridges well understood at the process scale. In this thesis, the surface will always be a particle and the liquid being transferred will be a coating agent. Coating agents are applied for any number of reasons; to mask undesirable tastes and / or odours, to aid with release of active ingredients from pharmaceutical tablets, to improve flow and bulk handling properties and to distribute liquid ingredients (e.g. bleaches and perfumes) evenly around the particle population. Coating of powders and particles can be done in one of several forms; a liquid (wet coating), a fine solid (dry coating) or as a 'melt' (melt coating). The study of liquid bridges is mainly applicable to wet coating where the main critical product parameter to be controlled is the coating variability, both within a batch (inter-), and on individual coated media (intra-). If these values are not within specified limits, entire batches of product, e.g. tablets, can face rejection. To date, this has been achieved through research focused on the initial droplet deposition, where atomised liquid droplets first contact the powder bed. There is a small amount of work that has been done on contact spreading, where liquid is transferred between particles by liquid bridge, however, a more comprehensive understanding of this mechanism is needed.

This chapter will introduce the relevant science associated with liquid coating and presents justifications for the research conducted in this thesis, namely the investigation of the contact spreading mechanism through the formation and rupture of liquid bridges. The following main topics will be reviewed;

- The methods of coating and the main equipment used in the process

- The mechanisms of liquid transfer between particles, including the initial droplet deposition and the contact spreading, with a focus on the properties of liquid bridges and the wetting and spreading of the liquids themselves.
- Previous research on coating uniformity and variability, including existing methods used to quantify the particle coating variability (both inter and intra), and a look at the methods used to track particles inside processing equipment.
- And finally, previous work looking at the mechanism of contact spreading

2.2 Coating methods

There are several methods through which the coating agent can be introduced into the processing system (Saleh & Guigon 2006), with different processes being favoured for different applications. In this section, four methods of coating technique will be discussed.

2.2.1 Dry coating

The coating agent used in dry coating consists of fine solid particles. As stronger forces associated with the addition of liquid binders are absent, the adherence of the fine particles is due to van der Waals forces and electrostatic forces (Saleh & Guigon 2006). However, this means the adhering particles must be smaller than approximately 1 μm to ensure the adhesive forces are greater than the conflicting disruptive forces. Qiao et al. (2010) developed a novel coating process that used electrostatic forces to dry coat pharmaceutical powders. This method is beneficial as it reduces the energy input needed to dry aqueous based coatings in conventional systems, and it was able to produce coatings of a similar uniformity to that gained via the conventional method.

2.2.2 Melt coating

This process uses a coating agent which is made molten either prior to addition or during the coating step. The solidification of the solution is achieved via cooling of the bed, as opposed to the drying technique used for wet coating. The most commonly used substances are high molecular weight compounds such as polyethylene glycols, silicone, paraffins etc., and do not include a solvent (Saleh & Guigon 2006).

Application of the coat can be achieved in one of two ways; molten coating solution can be sprayed against a cooled bed of particles, whereby the chosen bed parameters ensure sufficient time for spreading before solidification. Alternatively, the mixture, including the fine powdery coating agent and the host particles, is heated to a temperature close to the melting point of the coating agent at limited regions in the bed; this causes the coating agent to soften and spread over the particle bed, after which the deposited layer can be solidified by further cooling (Saleh & Guigon 2006).

2.2.3 Liquid encapsulation

Liquid phase encapsulation is an alternative method for liquid coating, and has seen a recent surge in development due to increasing interest in the immobilisation of enzymes, live cells and biocatalyst systems (Saleh & Guigon 2006). The process involves coating small liquid droplets in a microcapsule wall, generally made from one of four materials; ethyl cellulose, polyvinyl alcohol, gelatine or sodium alginate. The liquid requiring encapsulation is dispersed in an immiscible liquid, where polymerisation reactions form continuous microcapsule walls around the active liquid phase. There are multiple techniques that can be used for microencapsulation, each depending on the physical and chemical properties of the material to be encapsulated (Jackson & Lee 1991). For liquid phase encapsulation, there are four main techniques; interfacial polymerisation, polymer phase separation, polyelectrolyte complex formation, and solvent evaporation.

2.2.4 Wet coating

In the wet coating process, a coating agent is dissolved in an easily evaporable solvent. The solvent is applied, usually via spray nozzles, to the powder / particle bed (Saleh & Guigon 2006). After coating the particles, heat, introduced via a hot gas or through the mixer wall, is used to evaporate the solvent, leaving behind a solidified layer of coating agent (Saleh & Guigon 2006). Wet coating makes up most industrial coating processes, with a large variety of coats available; sugar coating, film coating of drugs, colouring and flavouring of food etc.

In the case of wet (and melt) coating, the spreading of liquid can be split into 2 distinct areas: 1) the initial drop addition and impact on the particle bed and, 2) the contact spreading of the liquid around the bed. The initial drop impact has been much more extensively covered than contact spreading, but it is the summation of the impact from both mechanisms which affects the final liquid movement.

2.3 Coating equipment

There is a multitude of equipment available for industrial spray coating of products. In the food industry, products, for example crisps, are dispensed onto a horizontal conveyor belt upon which a liquid is sprayed, and popcorn is tumbled in a drum with additional components to give the desired taste. In the pharmaceutical industry, a coating is commonly applied to tablets in a tumbling drum for the purposes of taste / identification / to improve the ease of swallowing (R. Muliadi & E. Sojka 2010). In 1950, Yen & Stirn (1950) proposed a method of coating tablets which consisted of simply dipping the tablets in the coating solution. In other industries, coatings are applied to powders using fluidised beds (see Figure 2.1).

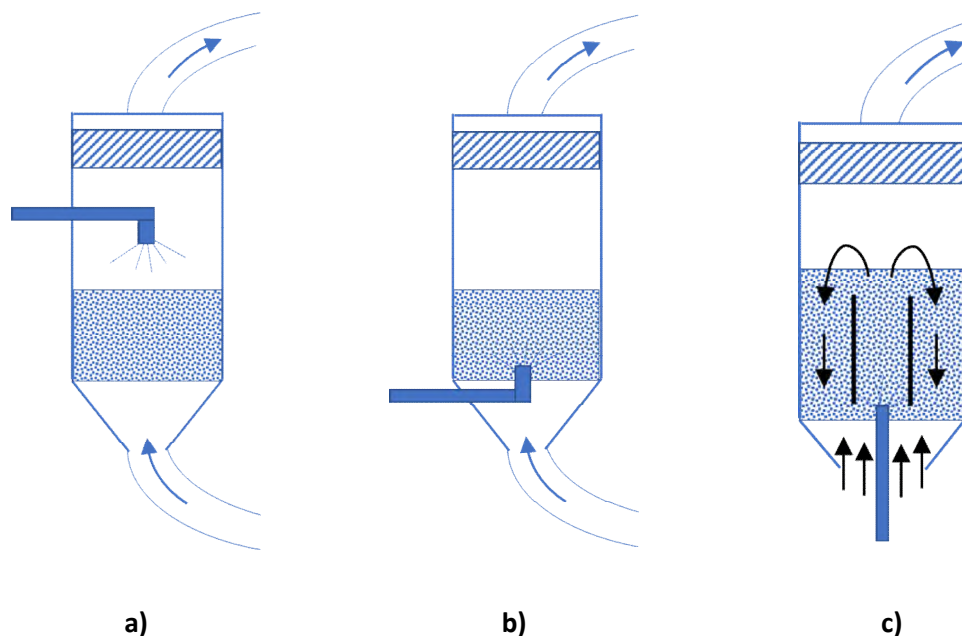


Figure 2-1. Different configurations of the fluidised bed coating equipment a) top spray, b) bottom spray, c) Wurster coater. Adapted from Toschkoff & Khinast (2013).

The final choice of equipment is heavily dependent on several factors, discussed more in the coming sections. Here, several pieces of processing equipment will be discussed in depth, with a focus on tumbling drums.

2.3.1 Fluidised bed coaters

Fluidised beds are the most common piece of equipment used in the coating industry. Particles are fluidised within a conical chamber, and a coating agent is applied from above the fluidised bed, or from inside it. It is usually done so with the aid of a spray nozzle which atomises the coating solution to produce very fine droplets. Fluidised beds are available in several configurations, as seen in Figure 2-1. Although the fluidised bed process benefits from excellent heat and mass transfer, and good particle mixing, it also suffers from defluidisation due to the undesired formation of large agglomerates and attrition (the process of producing extremely fine particles through breakage or fragmentation). Many researchers have tackled the effect of various parameters on the coating mass distribution, a few of which are summarised in Table 2-1.

A more in-depth overview of two particular types of fluidised bed will now be given.

2.3.2 Spouted bed coaters

Spouted beds, named after the central spout zone within the beds caused by high gas velocity and a dilute particle region, offer an alternative to traditional fluidised beds for coarse materials exceeding approximately 1 mm in diameter. They have been successfully used to coat a wide variety of materials (Epstein & Grace 2010), and offer the benefit of providing a uniform coating layer in a short period of time (Kmieć 1980; Kucharski & Kmieć 1983). Spouted coaters consist of 3 distinct regions; zone 1 is the central spouting region whereby high gas velocities entrain particles upward at a similar speed which results in short contact times between the gas and solid phases and high bed voidage. Zone 2 is the fountain, where particles move almost cross-currently to the gas stream and move towards the vessel walls, and zone 3 is the down-comer (annulus) which is characterised by high solids concentrations and low gas and solid velocities, which results in higher contact times.

Table 2-1. Summary of research on fluidised bed coaters.

Reference	Summary
Botterill et al. (1982)	Showed the minimum fluidisation velocity decreased with increasing operating temperature . However, this behaviour is also dependent on the initial size distribution of the material.
Iley (1991)	Investigated the effect of particle size and porosity on particle film coatings in a 20 cm diameter fluidised bed, showing smaller particles capture more coating but have thinner coats. Porous particle coatings were poor due to liquid ingress. To improve coating, particles should be spherical with zero porosity and have a high density.
Abe et al. (1998)	Glass beads (149 – 297 μm and 350 – 500 μm) coated with sodium chloride and dextran. Each particle weighed with coating and after removal of coating via dissolving in water to find coating mass per particle. The variation in the coating mass decreased with increased coating time, increased seed particle size, and decreased seed holdup . Variation considered to be dominated by average number of droplets colliding with a particle.
Dewettinck & Huyghebaert (1998)	Investigated the effect of coating sodium chloride crystals with protein concentrates and found that higher coating masses were obtained when using a lower average particle size. The nozzle atomisation showed more influence on the droplet size than on the coating mass, although this in turn led to the coating of particles via the layering mechanism as opposed to the production of agglomerates
Saleh et al. (2003)	Coated sand particles with NaCl to investigate the effect of particle size . Showed the distinction of the two growth mechanisms; particles under 200 μm tended to agglomerate whereas larger particles grew by layering. They used this information and a population balance model to predict the evolution of the particle size distribution, incorporating both agglomeration and layering.
(Naz et al. 2015)	Starch dispersions were used to coat urea granules (3.45 mm) with the effect of the solution temperature being varied from 50 to 80 degrees. As coating solution temperature increased, dissolution time increased, surface hardness increased, and coating thickness also increased. Coating temperature effects hard to uncouple from solution composition effects.

In spouted beds, particle growth happens by layering; droplets are deposited on the particles in zone 1 and subsequently dry in zones 2 & 3. The particles then repeat this process until the desired coating content has been achieved. de Oliveira et al. (1997)

coated nearly spherical porous alumina particles with a sucrose and talc water suspension, and analysed the increase in particle mass and mass fraction of atomized solids as a function of the spouting gas temperature, the mass flow rate of the atomised suspension, and the gas flow rate. The authors showed that over the range studied there was no dependence of the measured properties on the temperature of the spouting gas, but proposed empirical correlations with the gas flow rate and suspension feed flow rate. Kiani et al. (2017) looked at the effect of particle size and density on the mixing and segregation in a pseudo 2D spouted bed. They used sand, gypsum and polyurethane and an image processing technique to determine the mixing and segregation of the particles in the bed. They showed that air velocities larger than the minimum spouting velocity resulted in decreased segregation and a decreased time to reach equilibrium. In Section 2.3.3, the Wurster coater, a type of spouted bed, will be discussed in further detail.

2.3.3 Wurster coaters

The Wurster coater, potentially the most common piece of equipment used for film coating pharmaceutical tablets since its introduction in the early 1950's (Wurster 1953), is a circulating fluidised bed with a bottom spray. It is a variant of a spouted bed coater, but has a gas distributor at its base (Palmer et al. 2010). As noted by Karlsson et al. (2011), there are 5 regions within the bed, each of which has a distinct function in the coating process. Zone 1 corresponds to the spray zone and is located just above the distributor plate. Spraying from the bottom works to increase the number of droplet-tablet collisions thereby increasing coating efficiency, and provides increased particle agitation which prevents agglomeration (Teunou & Poncelet 2002). Zone 2 is the Wurster tube, inside which the particles travel upwards at accelerated speeds (Li 2015). At the top of their fluidisation, the particles enter zone 3, the fountain region, and begin to move outwards and fall, entering the downbed region (zone 4). Zone 5 is the horizontal transport region on top of the distributor plate where particles are recirculated into the central tube to be fluidised once again. Wurster coaters have been used in pharmaceutical coating almost since their inception. Coletta & Rubin (1964) used ethyl- and methylcellulose to successfully coat aspirin tablets on a commercial scale and showed that sustained-release of the drug was possible due to the coating homogeneity achievable in the coater. In a study utilising SEM and mercury porosimetry

to determine the coating thickness of polymer latex spray on inorganic particles, Iley (1991) showed that smaller particles were capturing more of the coating, but also had thinner coating layers due to their higher specific surface area. Cheng & Turton (2000a) and Cheng & Turton (2000b) investigated the effect of process parameters on the coating uniformity, predicting the mass coating uniformity from an understanding of the cycle time distribution (the time taken for 1 particle to pass from zone 1 to 5), and presenting a model which tried to explain the variation in coating received per pass per particle, respectively. The main research concerning Wurster coaters focuses on fluidisation regimes, particle size and moisture content. da Silva et al. (2014) presented a study which reviewed all of these parameters, and the methods used for monitoring and controlling them. As well as monitoring and controlling processes, an increasing number of studies look to predict them. Šibanc et al. (2013) used CFD simulations to analyse the effect of the fluidising flow rate on the gas-solid flow and compared these to experimental data, showing good agreement. KuShaari et al. (2006) presented a Monte Carlo model for predicting the mass coating variability based on the fact of particle sheltering (some particles are sheltered by other particles in the coating region) and showed good agreement with experiments completed in the same equipment when the number of discretised elements was greater than 3,000. They showed that gas velocity and gap height impact on the coating uniformity; lower values of each parameter lead to wider coating distributions due to the increased effect of particle sheltering.

2.3.4 Tumbling drums

Tumbling drums, one of the oldest methods used for applying coatings, were originally developed in the confectionary industry and adopted by the pharmaceutical industry for applying sugar coatings to drugs (Florence & Attwood 2015). They are one of a number of rotary devices also including pans (Sahni & Chaudhuri 2012) and discs (Sacher & G. Khinast 2015). They are extremely versatile in function, can handle considerable throughputs and a wide range of products (Saleh & Guigon 2006). As can be seen in Figure 2-2, the drum rotates maintaining an inclined powder front, over which a spray is applied. A hot air stream is sometimes used to aid with drying of the coating layer. Unlike the fluidisation techniques discussed previously, tumbling drums (and rotary

devices in general) suffer from poor heat and mass transfer, and have poor axial mixing when unbaffled (Saleh & Guigon 2006). Tumbling drums can be operated either continuously or in batch, with a continuous coater being inclined around 3-10° (Ennis 2010) to promote movement of material along the drum length.

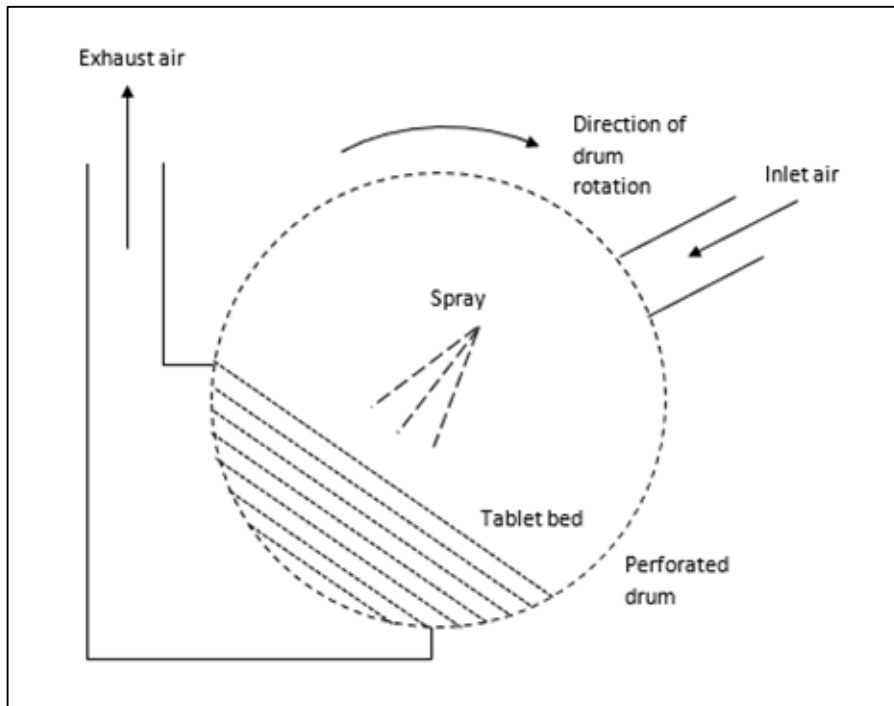


Figure 2-2. Schematic of tumbling drum spray coater. Adapted from Freireich et al., 2015.

Arntz et al. (2008) used Discrete Element Method (DEM) to model the effect of fill level and drum rotation velocity on the segregation of bidisperse granules and presented bed behaviour diagrams as a function of the Froude number (see Equation 2-1). They showed that segregation in this bidisperse model was a result of small particles falling through the larger particles in the drum bed, causing size segregation after a number of revolutions. The velocity and fill level determine the segregation pattern by influencing the location, size and density of the top mobile particle layer. To encourage particle mixing, baffles can be employed. Jiang et al. (2011) looked at three configurations of baffles in rotating drums and showed that selection of the size of the baffles is crucial in not only increasing mixing quality, but also in ensuring a decrease in mixing quality is not introduced. They stated that any baffle drastically improves the mixing over an equivalent non-baffled system; enhancing inter-particle mixing and reducing size segregation. The powder regime within a drum is a parameter which can be easily

manipulated, mainly being a function of the drum rotation speed, and greatly affects the coating efficiency. At low rotational speeds, the powder bed is relatively static at the bottom of the drum, minimising agitation and reducing interaction between the particles. At the other extreme, known as the 'critical speed', the powder is carried around the drum as a result of centrifugal forces. A total of 6 regimes exist; slipping, slumping, rolling, cascading, cataracting and centrifuging, in order of increasing rotational speed (Figure 2-3).

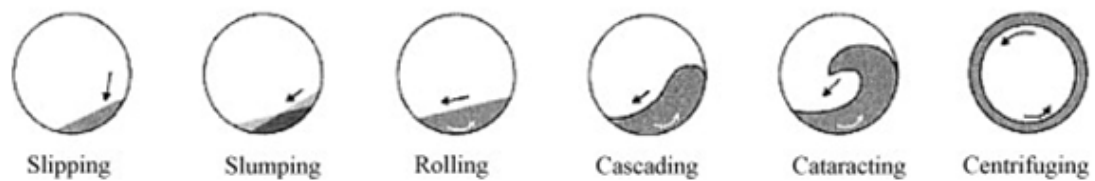


Figure 2-3. Mode of granular motion in a rotating drum (Pirard et al. 2009). Reprinted from Chemical Engineering Journal, 146, S.L. Pirard., G. Lumay., N. Vandewalle., J.P. Pirard., Motion of carbon nanotubes in a rotating drum: The dynamic angle of repose and a bed behaviour diagram, pp.143-147, (2009), with permission from Elsevier.

Cascading occurs at approximately half the critical speed, and a motion is induced whereby the powder bed rises a significant way up the drum wall and is substantially agitated when falling back to the base. As well as altering the rotational speed, differences in the internal surface roughness will significantly alter the powder regime seen in the drum; greater levels of friction are likely to induce more agitation and carry particles further up the drum wall, increasing the likelihood of seeing a cascading motion. Also affecting the flow regime is the particle surface roughness. Coarse particles increase friction, whereas smooth particles increase wall slippage (Li 2005). As a result of this influence on the flow regime, particle surface roughness and shape can impact heavily on segregation and mixing within the drums. Their impact is, however, poorly understood (Ottino & Khakhar 2000). Because of the different flow regimes within drums, and their dependence on the material and coating liquid interaction as well as the drum geometry, sizing of process drums is based on the scale up of lab sized experiments; making informed alterations to increase liquid transfer is still difficult. Across numerous industries, lack of knowledge at scale up can be financially trying; Paul et al. (2004) estimated costs of \$500 million per year were spent on scale up and mixing issues in the pharmaceutical industry alone.

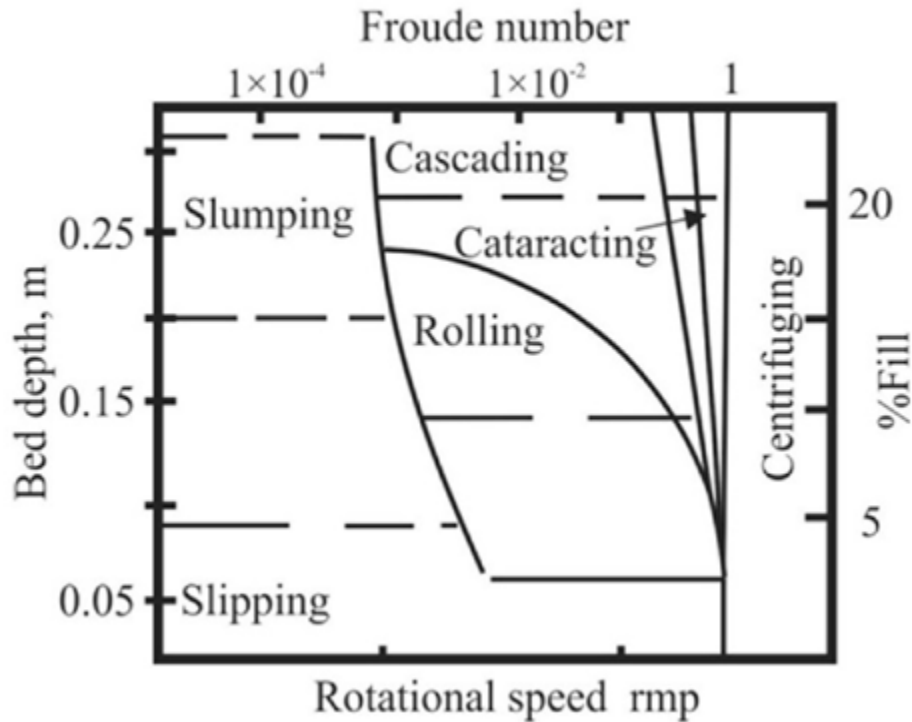


Figure 2-4. Example of a bed behaviour diagram (Shariati et al., 2015).

Developed by Henein et al. (1983), bed behaviour diagrams (an example is given in Figure 2-4) allow for the prediction of the bed behaviour under given operational parameters. The Froude number (Fr) is a dimensionless number, representing the ratio of inertia to gravitational forces, which dictates the dynamics of drum coating systems:

$$Fr = \frac{\omega^2 D}{g} \quad \text{Equation 2-1}$$

where ω is the pan speed (rpm), g is acceleration due to gravity, and D is the pan diameter. It is often used when scaling up drum coaters to ensure dynamic similarity across the two systems, as can be seen by the work conducted by Chen et al. (2010). Here, they showed similarity of a 50 kg batch and a 400 kg batch could be achieved by varying the pan speed and the radius. The data in Table 2-2 shows the differences in these parameters for a nearly constant Froude number.

Table 2-2. Differences in pan speed and pan radius needed to maintain an approximately constant Froude number for two different batch sizes. Adapted from Chen et al., 2010.

Batch size	Pan speed (rpm)	Pan radius (cm)	Froude number
50 kg	18	35	0.00321
400 kg	12.5	71.5	0.00316

However, the Froude number takes no account of particle properties, or the properties of the drum wall (as earlier mentioned). Ding et al. (2001) conducted work which looked at a combination of these parameters and were able to propose a single dimensionless number, valid for Froude numbers above 0.003 but only applicable in the rolling regime. Interestingly, they also showed differences between drum sizes; larger drums operated at medium rpms exhibit quasi-static movement, whereas small drums at medium rpms are found to be in the transition flow regime. Turton & Cheng (2005) discussed the scalability of rotating drums (and fluidised beds), and offer several laws for maintaining product attributes (given the same material and spray qualities) based on maintaining the coating mass, discerning the maximum batch size, and calculating a scaled coating time. For example, the Froude number, as previously discussed, is often kept constant. However, this often results in abrasion and so it is beneficial to instead maintain a constant ωD (*rotational speed (rpm) * Diameter*).

There are many individual parameters which can affect the coating quality in a tumbling drum, as shown in Figure 2-5; however, they can all be grouped into five overarching themes; 1) the spray, 2) the coater, 3) the inlet air, 4) the medium being coated, and 5) the coating medium. Various limits are imposed which dictate whether or not products are able to pass quality assessments; in the pharmaceutical industry, the residual standard deviation (RSD) of the content uniformity must be less than 6 % (United states pharmacopoeial commision 2016). When active ingredients are being sprayed onto the tablet surface this translates directly to restrictions on coating uniformity. Rege et al. (2002) showed that lower atomisation pressure, higher pan speed and longer coating duration were all critical in achieving an acceptable level of coating uniformity. No upper limits on these parameters were suggested; once the coating has reached a uniform level within the specified RSD, further coating will not improve the uniformity but will

incur a significant additional cost. For this reason, it is important to be able to predict the end of the coating process accurately, and understand how parameters affect both the level of coating uniformity and time at which this point is reached.

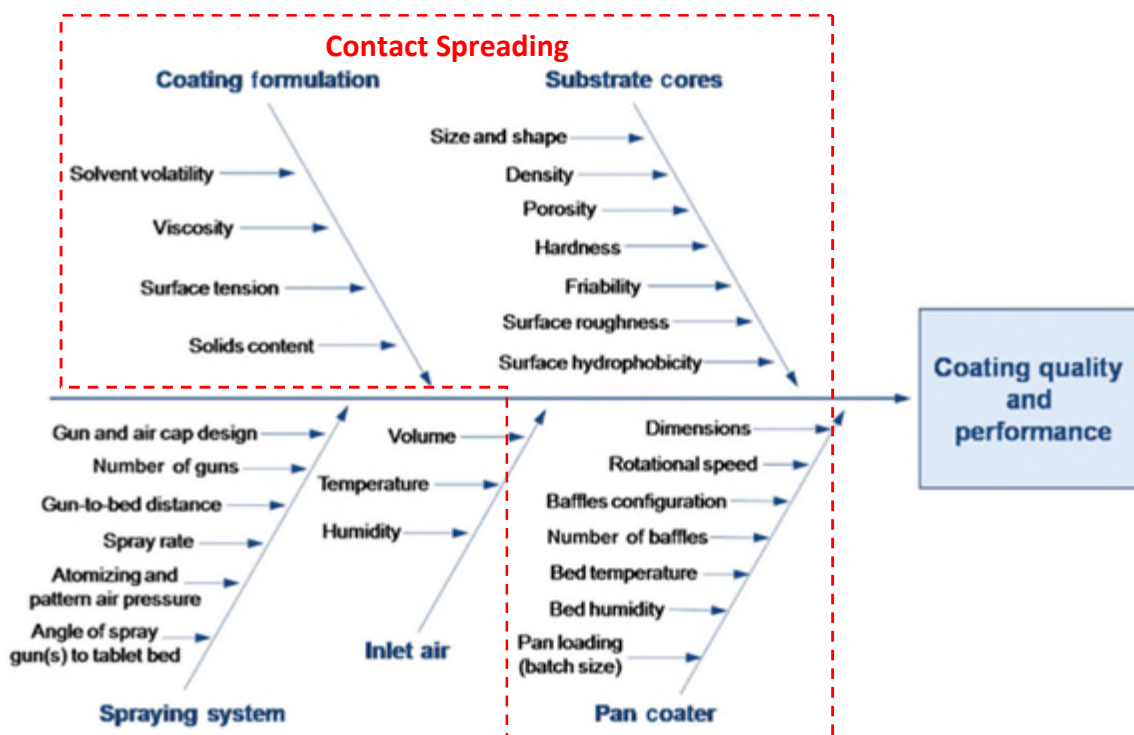


Figure 2-5. Fish-bone diagram of the tumbling drum coating process. Reprinted from *Journal of Pharmaceutical Sciences*, 104, A.M. Agrawal., P. Pandey., *Scale up of pan coating process using quality by design principles*, pp. 3589-3611, (2015), with permission from Elsevier.

Although numerous parameters are identified in this diagram, the way in which these parameters interact is not considered. As seen in Chapter 1 (Figure 1-1), there are two mechanisms for liquid transfer; 1) the initial droplet deposition, and 2) the particle-particle interactions which transfer liquid around the bed. The first mechanism, having benefited from considerable research, is governed largely by the spray system, and bed properties. However, the second mechanism has not been the subject of a great amount of attention and, being controlled by the formation and rupture of liquid bridges, will greatly depend on the properties of the coating agent, the media to be coated and certain drum properties. In the next section, liquid bridges will be introduced and an overview of several controlling parameters will be given.

2.4 Liquid bridges

This section will first give an overview of the development of liquid bridges, the different methods that can be used to model liquid bridges, and the differences between static and dynamic bridge strength. The theory will then be developed to include the rupture of liquid bridges, bridges between three particles, and how the collision success rate can influence the spreading of liquid between particles.

2.4.1 Introduction

Liquid bridges form when some volume of liquid is present in a solid particle system. The associated liquid-solid structures can be placed into four categories: pendular, funicular, capillary and droplet, with each type containing more liquid than the last (Figure 2-6). For coating applications, the focus is on the pendular and funicular structures; the structures associated with higher liquid loading are more relevant to agglomeration processes. Figure 2-6 shows an example of the pendular state; there is a thin liquid bridge between particles, and each bridge is independent of one another. The addition of more liquid, creating either the funicular, capillary or droplet state, decreases the attractive forces between the particles as the liquid bridges merge and begin to disappear. The attractive force is a result of surface tension of the liquid and the capillary pressure resulting from the curvature of the bridges (Domike & Cooney 2015). The liquid bridges that form in the pendular and funicular states can generate both static surface tension forces and dynamic forces due to the liquid viscosity (Iveson et al. 2001).

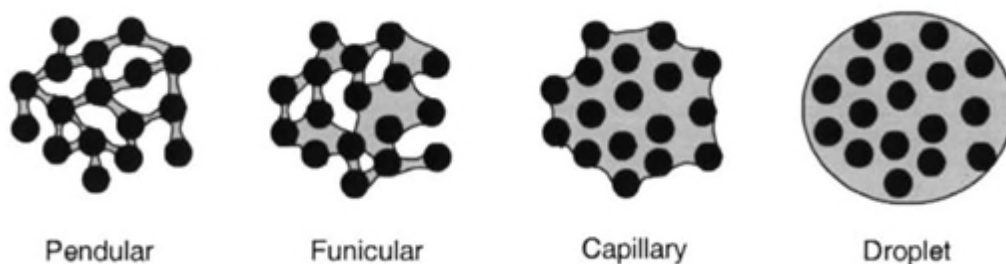


Figure 2-6. The four types of structure seen in liquid particle interactions. Reprinted from Powder Technology, 117, S.M. Iveson., J.D. Litster., K. Hapgood., B.J Ennis., Nucleation, growth and breakage phenomena in agitated wet granulation processes: a review, pp. 3-39, (2001), with permission from Elsevier.

These structures can be affected by a number of process parameters, as described in Section 2.3; influencing the likelihood of coating versus agglomeration, the strength of liquid bridges, and the strength of agglomerates etc. The various outcomes from a liquid spray coating process can be seen in Figure 2-7.

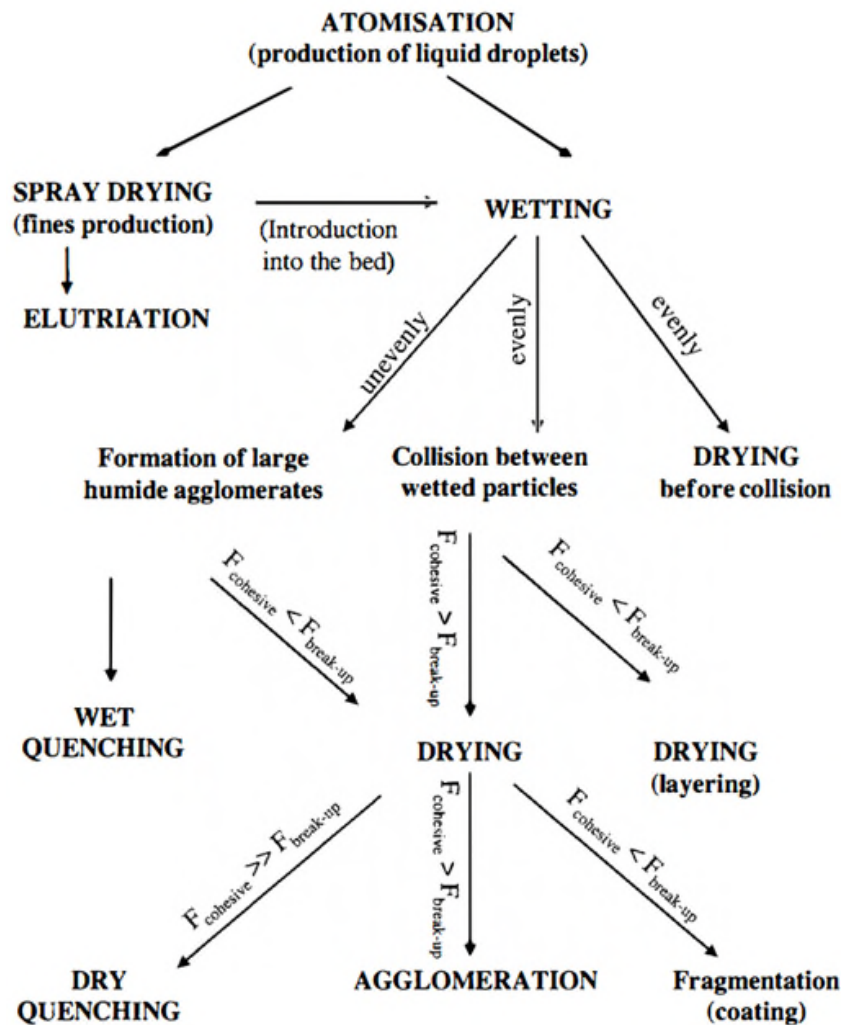


Figure 2-7. Phenomena occurring during wet coating. Reprinted from Handbook of Powder Technology, K. Saleh., P. Guigon., Coating and Encapsulation Processes in Powder Technology, pp. 323-375, (2007), with permission from Elsevier.

If the droplet size is smaller than the particle size in the powder bed and the particle achieves a successful collision before the liquid dries, a liquid bridge has the potential to form between the particles involved, creating wet agglomerates. If the liquid bridge ruptures before drying, liquid may be transferred from one particle to another and transported around the powder bed (contact spreading). However, if the bridges dry before being disrupted, solidified agglomerates will be formed (agglomeration on Figure

2-7). The formation and rupture of liquid bridges are, therefore, of critical importance when considering the transfer of liquid through the powder bed and will be considered now in greater detail.

2.4.2 Young-Laplace equation

Liquid bridges comprise both a static and dynamic force. The former is composed of the capillary and surface tension effects, and the latter represents a viscous component which arises under dynamic conditions. To analyse any aspect of the liquid bridge, some method of studying the bridge geometry is needed. The profile of a liquid bridge at rest can be described theoretically by the Young-Laplace equation (Equation 2-2); the curvature of the capillary bridge is related to some function, $y(x)$, that describes the liquid bridge profile, and its derivatives (De Bisschop & Rigole 1982). This equation can only be used when the effect of gravity is negligible, indicated by a small gravitational Bond number ($Bo = gr_p^2\rho_l/\gamma$), leading to a nearly uniform curvature of the bridge profile. The Bond number relates the gravitational forces to those of the surface tension (γ), where g is the acceleration due to gravity, r_p is particle radius, and ρ_l is the density of the liquid.

$$\frac{\Delta P}{\gamma} = \frac{1}{y \left[1 + \left(\frac{dy}{dx} \right)^2 \right]^{\frac{1}{2}}} - \frac{\frac{d^2y}{dx^2}}{\left[1 + \left(\frac{dy}{dx} \right)^2 \right]^{\frac{3}{2}}} \quad \text{Equation 2-2}$$

Here, ΔP is the capillary suction pressure, γ is the liquid surface tension and $y(x)$ is a curvature of the capillary bridge. Orr et al. (1975) solved the Laplace-Young equation using elliptical integrals. However, due to the complexity of solving these equations, normally a numerical solution is required. This was attempted by Lian et al. (1993), however, the bridge profiles were evaluated using a constant liquid bridge volume and a constant contact angle. These assumptions are questionable; contact angle depends heavily on the wettability and spreading of the liquid, and the volume of the liquid bridge is again dependent on these liquid properties. Although the Young-Laplace equation does offer the ability to describe the liquid geometry, several simplified models now exist which can also define the bridge geometry and allow for the determination of the

rupture distance, the rupture energy, and the liquid distribution, for example. These models will be discussed in Section 2.4.5 after the bridge forces for both static and dynamic bridges have been reviewed.

2.4.3 Static liquid bridge strength

The static liquid bridge strength has been shown to consist of three components: the capillary suction pressure, the surface tension force, and buoyancy forces. Princen (1968) showed that the buoyancy forces are negligible for particles with a diameter less than 1 mm, thereby reducing the liquid bridge strength to a combination of the capillary pressure and the surface tension only. Numerous researchers (Hotta et al. 1974; Lian et al. 1993; Willett et al. 2000) have measured the liquid bridge strength at low and/ or invariant strain rates, i.e. static liquid bridge measurements.

As stated by Iveson et al. (2001), there are two common methods for calculating the static liquid bridge force: the gorge method and the boundary method. These involve the evaluation of the surface tension and capillary pressure terms at the mid-point of the bridge, and at the contact line with one of the spheres, respectively. Hotta et al. (1974) presented experimental data which showed that the boundary method gave more accurate results, whilst Lian et al. (1993) presented data which showed that the Gorge method was capable of evaluating a wide range of bridge volumes with errors < 10 %. The total forces predicted by each of these models is the sum of the capillary force acting in the interior of the bridge, and the surface tension acting at the three-phase contact line, as can be seen from Equation 2-3 and Equation 2-4:

$$F_G = \pi r_2^2 \Delta P + 2\pi r_2 \gamma \quad \text{Equation 2-3}$$

$$F_B = \pi r_p^2 \sin^2 \phi \Delta P + 2\pi r_p \sin(\phi) \sin(\theta + \phi) \gamma \quad \text{Equation 2-4}$$

Here, γ is the liquid surface tension, ΔP is the capillary suction pressure and all other variables are identified on Figure 2-18. The locations used for the calculations of the forces from Equation 2-3 and Equation 2-4 have been highlighted on Figure 2-8; the capillary term and the surface tension term are determined by multiplying these forces by the area and the circumference at the relevant location.

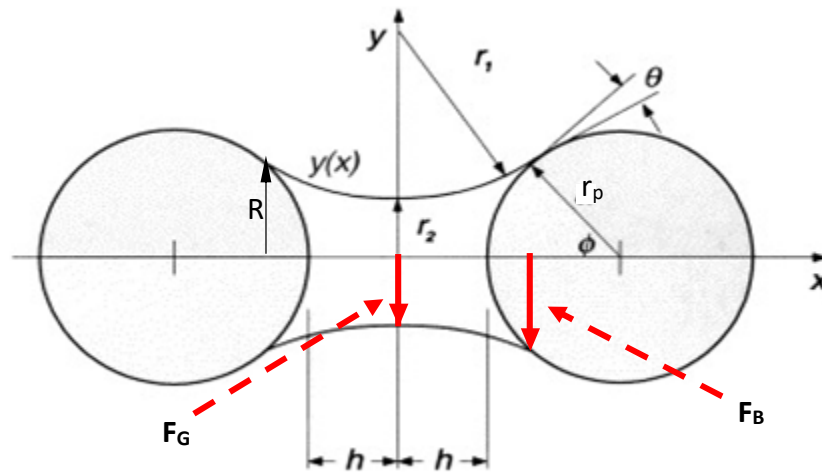


Figure 2-8. Schematic of a pendular bridge between two equi-sized spheres. Adapted from Iveson et al., 2001. Reprinted from Powder Technology, 117, S.M. Iveson., J.D. Litster., K. Hapgood., B.J Ennis., Nucleation, growth and breakage phenomena in agitated wet granulation processes: a review, pp. 3-39, (2001), with permission from Elsevier.

As both of these equations are analytical, and based on an approximation that is known to be flawed, Willett et al. (2000) fitted empirical expressions to the results gained from numerically solving the Laplace-Young equation. They produced the following equation which gave a good fit to the solutions for $V_b/r_p^3 < 0.001$ and for when the 2 particles were of the same size:

$$F_{Static} = \frac{2\pi r_p \gamma_{LV} \cos \theta}{1 + 2.1 \left(\frac{h^2 r_p}{V_b} \right)^{1/2} + 10 \left(\frac{h^2 r_p}{V_b} \right)} \quad \text{Equation 2-5}$$

where r_p is the particle radius (as seen in Figure 2-8), γ_{LV} is the liquid surface tension, θ is the liquid-solid contact angle, h is the half distance between the two particles, and V_b is the bridge volume (Willett et al. 2000).

2.4.4 Dynamic liquid bridge strength

Dynamic bridge strength is defined as the interaction generated when a particle is set to move (Murase et al. 2004). Although there is significantly less research on dynamic bridges than static ones, understanding the dynamic bridge strength becomes much more significant when impact velocities are high, and when the binders are of a higher viscosity. Mazzone et al. (1987) and Ennis et al. (1990) showed that the dynamic liquid

bridge strength can exceed the static bridge strength by several orders of magnitude for viscous binders. The strength of a dynamic pendular bridge (F_v) between two spherical surfaces can be approximated using lubrication theory (Adams & Edmondson 1987):

$$F_v = \frac{3\pi\mu r_p^2}{2h} \frac{dh}{dt} \quad \text{Equation 2-6}$$

and is justified in the limit of small capillary numbers, small gap distances, and sufficient bridge volumes (Pepin, Blanchon, et al. 2001). In Equation 2-6, $2h$ is the gap distance, μ is the liquid viscosity, r_p is the particle radius, and dh/dt is the time derivative of h , i.e. the half-gap velocity. A correction factor was proposed to Equation 2-6 by Matthewson (1988) which makes the equation applicable when considering a finite volume of liquid, as is the case for all liquid bridges, and proposes a cylindrical liquid bridge. Pitois et al. (2000) validated the corrected formula (Equation 2-7) using data obtained in the 'viscous' regime, whereby the viscous force is much larger than the capillary force, and showed good agreement between the theoretical and experimental values.

$$F_v = \frac{3\pi\mu r_p^2}{2h} \left(1 - \frac{2h}{H(R)}\right)^2 \frac{dh}{dt} \quad \text{Equation 2-7}$$

Here, $H(R)$ is determined from the liquid bridge volume (V_b) via Equation 2-8;

$$H(R) = \sqrt{h^2 + \frac{2V_b}{\pi R}} \quad \text{Equation 2-8}$$

where R is the distance from the axial line joining the two particles to the edge of the liquid bridge as it connects with the particle (see Figure 2-8) (in the case of a cylindrical bridge, R is equal to the radius of the bridge). If the equation for the viscous contribution (either inclusive of the modification or not) is added to either Equation 2-3 or Equation 2-4, an expression for the total bridge force can be written. Here, the viscous contribution (not inclusive of the modification) is added to the capillary forces as calculated using the Gorge method, i.e. at the neck of the liquid bridge, to give Equation 2-9;

$$F = \pi r_2^2 \Delta P + 2\pi r_2 \gamma + \frac{3\pi \mu r_p^2}{2h} \frac{dh}{dt} \quad \text{Equation 2-9}$$

Pitois et al. (2000) combined a simplified expression for the static component of the liquid bridge force calculated using the gorge method and the modified viscous component to accurately predict the bridge force in the region where the capillary forces are approximately equal to the viscous forces. They showed a change in the bridge force from attractive to repulsive as the separation distance became smaller, moving from the capillary to the viscous regime.

Washino et al. (2017) used direct numerical simulations (DNS) of liquid bridges to suggest a further adaption to the Pitois model for use at large particle separation distances. Only the normal component of the force was analysed, and Washino et al. showed that only the dimensionless versions of the separation distance (δ^*), liquid bridge volume (V_b^*) and contact angle (θ) could influence the dimensionless force (F_v^*). As both the Adams & Perchant and Pitois model are based on lubrication theory, they do not hold true at large separation distances, hence the development of the new model, Equation 2-10;

$$F_{Vcorrected}^* = \frac{\pi}{\delta^*} \left[\left(1 - \frac{\delta^*}{H^*(r_p^*)} \right)^2 + \frac{A}{\delta^*} \left(\frac{1}{\delta^*} - \frac{1}{H^*(r_p^*)} \right) + \frac{B}{\delta^*} (H^*(r_p^*) - \delta^*) \right] \quad \text{Equation 2-10}$$

Here, the parameters A and B are determined from the fitting of a correction function, g , which is dependent only on the dimensionless separation distance and dimensionless radial distance of the bridge. To solve any of the above equations, a number of parameters must be known and some expression for the pressure difference (ΔP) across the interface must be found. The calculation of the relative velocity and the separation distance will be further discussed in Section 2.6.4 and Section 2.4.8 respectively. As was seen earlier, one option for expressing the pressure difference is through numerically or analytically solving the Young-Laplace equation. However, there are now simplified

models which can approximate the curvature of the liquid bridge. These will now be discussed.

2.4.5 Bridge profile approximations

If the shape of a liquid bridge profile satisfies the Young-Laplace equation (Equation 2-2), its profile can be classified as either nodoid ($\Delta P > 0$), catenoid ($\Delta P = 0$) or unduloid ($\Delta P < 0$) in shape (Plateau 1863). Orr et al. (1975) gave exact solutions to these profiles, however, due to their complexity many researchers now favour some method of approximating the bridge profile. There are two main methods by which this can be done; the toroidal and the parabolic method. Fisher (1926) proposed the toroidal approximation for the solution of the Laplace-Young equation which treated the profile of the liquid-air interface as an arc of a circle. As shown by Mehrotra & Sastry (1980) and Orr et al. (1975), this approximation gives good results with small separation distances and small bridge volumes. The toroidal approximation can be further split into a concave and convex method, as shown in Figure 2-9 and Figure 2-10, respectively. The concave method is often seen in the literature and is often assumed in many research studies.

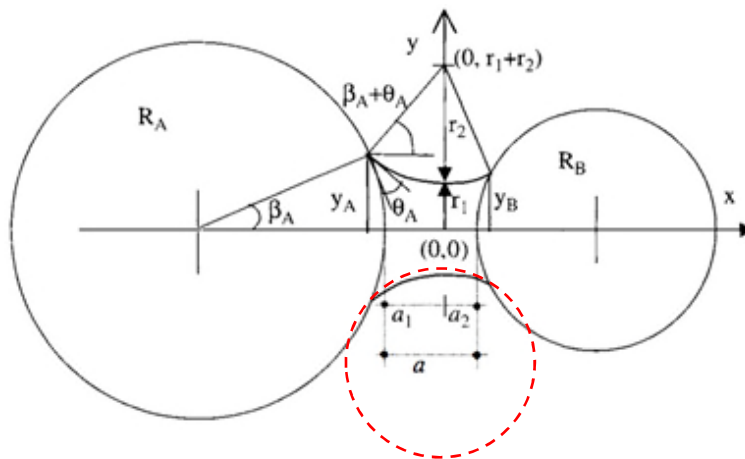


Figure 2-9. Schematic of the toroidal approximation of a liquid bridge for a concave profile. Red dotted line shows the arc of the circle used to approximate the bridge profile. Reprinted from Handbook of Powder Technology, S. Simons., Liquid Bridges in Granules, pp. 1257-1316, (2007), with permission from Elsevier.

The convex approximation is used when adjoining particles are close together and/or when large contact angles are formed. In this case, the upper and lower bridge parameters are usually described by the circumference of two different circles. Megias-Alguacil & Gauckler (2010) completed a theoretical study on convex liquid bridges using

the toroidal approximation in terms of the liquid bridge volume and the contact angle, and showed that convex bridges can occur even when the contact angle is less than 90° , i.e. hydrophilic. Megias-Alguacil & Gauckler (2011) then did further studies looking at both concave and convex liquid bridges. They showed that for equally sized spheres, the maximum errors associated with the respective toroidal approximations were below 10 % and approximately 30 % respectively, in comparison to the exact solution of the Young-Laplace equation. Although these errors are large, the errors associated with experimental measurement of the bridge shape are likely to have larger errors and, therefore, for ease, the use of an approximation is sensible.

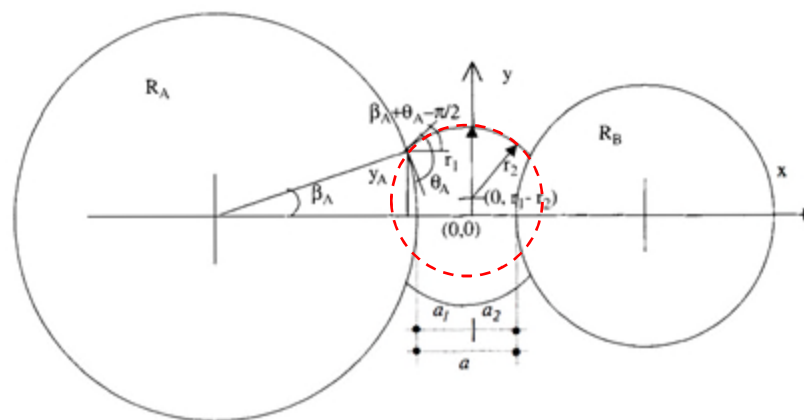


Figure 2-10. Schematic of the toroidal approximation of a liquid bridge for a convex profile. Red dotted line shows the arc of the circle used to approximate the bridge profile. Reprinted from Handbook of Powder Technology, S. Simons., Liquid Bridges in Granules, pp. 1257-1316, (2007), with permission from Elsevier.

Pepin et al. (2000) used both a toroidal and parabolic approximation to model the evolution of the bridge shape, the rupture distance and the liquid distribution upon rupture, and stated that the parabolic approximation was slightly more accurate and easier to use. In the case that a liquid bridge profile turns from concave to convex, or vice versa, the bridge will assume a cylindrical shape at some point. This will not be solvable using the toroidal approximation and, furthermore, would involve solving two sets of equations for the initial and end conditions. As the parabolic method can solve both concave and convex profiles with the use of one equation, it offers a much simpler and more robust mathematical model (Figure 2-11).

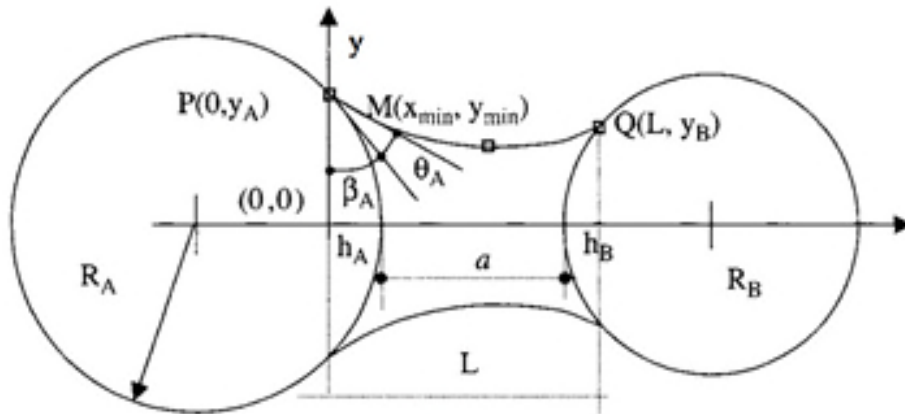


Figure 2-11. Schematic of the parabolic approximation of a liquid bridge. Reprinted from Handbook of Powder Technology, S. Simons., Liquid Bridges in Granules, pp. 1257-1316, (2007), with permission from Elsevier.

2.4.6 Experimental methods for measuring bridge strength

The measurements of liquid bridge strength are generally split into two groups; direct tensile tests or uni-axial compression tests. Uniaxial compression tests involve applying a load to two ends of a sample and measuring both the axial and radial deformation at the failure point or some other prescribed level. Direct tensile tests measure the elongation of a specimen under tension and compare it to the force applied. Each test is capable of outputting the information in the form of a stress-strain curve. Schubert et al. (1975) developed a model to predict the stress-strain behaviour of agglomerates held together by liquid bridges and validated it experimentally using a new instrument for measuring tensile stress. They modified a commercial tensile tester to be able to determine the stress strain behaviour under uniaxial tension, and from this were able to develop a model which predicts the stress-strain behaviour of agglomerates held together by liquid bridges. Mazzone et al. (1987) attached a magnetic sphere permanently below an electromagnet, added a small volume of liquid and then placed a second identical sphere below the first to study the evolution of dynamic liquid bridges. The second sphere is retained in place as long as the electromagnet is turned on. A light source and high speed camera were then utilised to watch the evolution of the liquid bridge when the electromagnet was turned off and the second, lower sphere was no longer held in place. Because this method cannot directly measure the bridge force, the force was taken as the equivalent static bridge force, knowing the bridge volume and separation distance. They showed for the first time the large difference in

the strength of a dynamic bridge in comparison to a static one. More recently, Simons & Fairbrother (2000) developed a novel experiment to study the liquid bridge force using an optical microscope and a stage to support two micromanipulators with particles attached to the end. They termed this a micro force balance (MFB) which relies on the deformation of a pipette attached to the stationary particle to calculate the force of adhesion from the liquid bridge. Three distinct methods of forming the bridge were employed based on the method of liquid introduction; liquid was either added after the particles were brought into contact, used to coat both particles before interaction occurs, or used to coat one particle and second dry particle was then introduced. From this, they were able to propose an adjustment to the standard Gorge and Boundary methods for the case of a catenoidal bridge geometry (as opposed to the standard toroid), and also showed that the movement of liquid around the particles, or even adjacent particles, is dependent on the liquid viscosity.

2.4.7 Liquid bridges between three particles

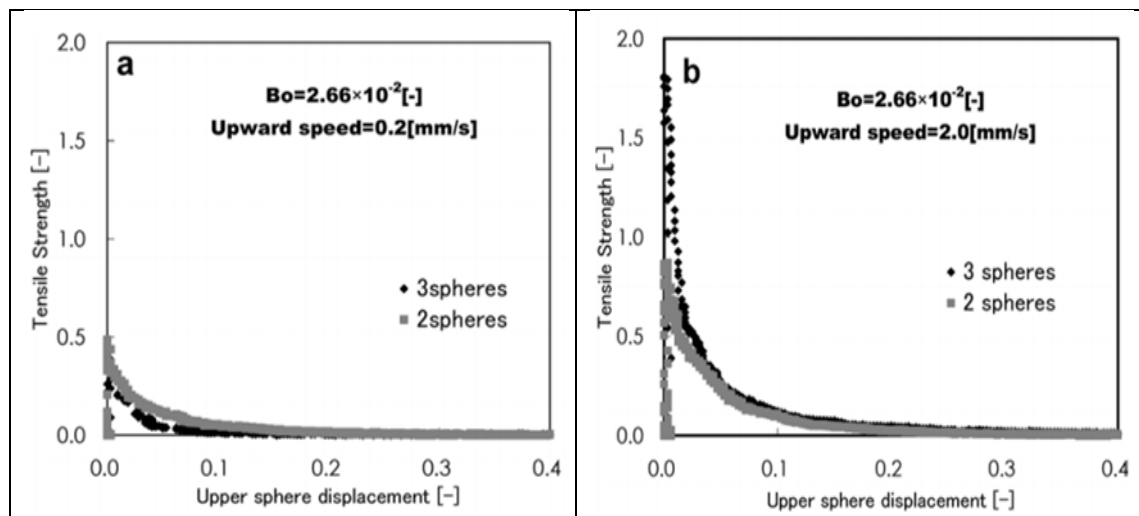


Figure 2-12. Experimental tensile strength profiles at a) 0.2 mm/s stretching speed and b) 2.0 mm/s stretching speed. Reprinted with permission from Springer: Nature, Granular Matter, Experimental and numerical studies on liquid bridge formed among three spheres, K. Murase., T. Mochida., H. Sugama., (2004).

A few authors have tried to model the bridge strength, both static and dynamic, between three particles. Rynhart et al. (2003) numerically solved the Laplace-young equation to give a solution for capillary state liquid bridges between three equally-sized, equally-spaced particles in three dimensions. The authors were able to calculate the

surface area, volume, and inter-particle force of the liquid bridges. They got agreement within 0.5 % for the liquid volume determined experimentally compared to that based on the model. Murase et al. (2004) showed that, similar to a two-particle interaction, the surface tension is the dominant force at slow speeds, i.e. static bridges. As the speed of the separation is increased, viscous forces become more relevant, and Murase et al. (2004) showed that the maximum tensile strength for the liquid bridge between three particles is almost double that of a two-particle system, as can be seen in Figure 2-12.

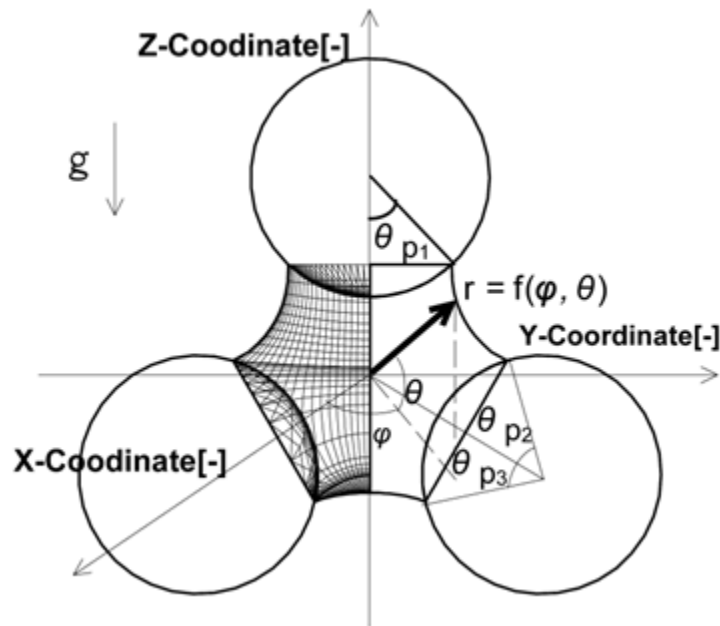


Figure 2-13. Schematic of a static liquid bridge between three particles with grid generation for simulation purposes in spherical co-ordinates (Murase et al. 2008). Reprinted from *Advanced Powder Technology*, 19, K. Murase., T. Mochida., Y. Sagawa., H. Sugama., Estimation on the Strength of a liquid bridge adhered to three spheres, pp. 349 – 367, (2008), with permission from Elsevier.

Both papers note additional strength in the three particle agglomerate (Figure 2-13) which is to be expected due to the greater perimeter of contact at the interface boundary. Murase et al. (2008) used numerical simulations to estimate the static strength and experimental data to estimate the dynamic strength of pendular liquid bridges composed of various viscosity asphalt KPI solutions adhered to three quartz spheres (7.5 mm radius). They investigated the effects of bridge volume, stretching speed and liquid viscosity on the maximum bridge strength and showed that the dimensionless bridge strength decreases with increasing sphere displacement following

a power law function with a -1.2 exponent. They found that the numerical simulations underpredicted the force of the identical experimental dynamic bridges.

2.4.8 Rupture distance

As well as calculating the liquid bridge force, the liquid bridge rupture distance is an important parameter which has been extensively studied. As the particles are separated, the liquid meniscus is displaced until a critical bridge distance is achieved, beyond which the bridge becomes unstable and ruptures (Simons 2007). The minimum separation distance, or the closest distance the particles can get to each other, must only account for the surface roughness of the particles; a value in the range of tens of microns is generally accepted and used for modelling purposes (Liu et al. 2011). Defining the rupture distance is not as easy; generally research in this area utilises high speed cameras to analyse the rupture of liquid bridges, tracking the narrowing of the bridge as the two adjoined surfaces are separated. Padday (1978) showed that during this process, although the bridge separates into two liquid masses, due to the formation of some satellite drops the bridge volume may not be exactly preserved. De Bisschop & Rigole (1982) analysed the separation distance as a function of the half-filling angle, and showed that rupture of the bridge occurs as the half-filling angle is at a minimum. Mazzone et al. (1987) developed this work to show that a stable liquid bridge can exist beyond the minimum half-filling angle, and that the half-filling angle increases before rupture. Lian et al. (1993) developed Equation 2-11, relating the dimensionless bridge volume, $V_b^*(=V_b/R^3)$ to the dimensionless rupture distance;

$$S_C^* \cong (1 + 0.5\theta)^3 \sqrt[3]{V_b^*} \quad \text{Equation 2-11}$$

where θ is the solid-liquid contact angle in radians, and S_C^* is S_C/R , and R is the radius of the spheres. At low contact angles ($<40^\circ$), this equation shows that the critical rupture distance is approximately equal to the cube root of the liquid bridge volume. Interestingly, Pitois et al. (2000) showed the dynamic bridge rupture distance to be up to 20 % larger than the corresponding static rupture distance, showing that the percentage increase of the dynamic rupture distance compared to the static rupture distance is proportional to the square root of the separation velocity. Song & Turton

(2007) investigated liquid bridges between two colliding tablets; dropping one tablet from height onto a stationary tablet below and using image analysis to record the interactions. They varied the amount and location of the liquid in the experiments and showed that if only one surface is wetted, a bridge will not form due to the contact time being less than the time needed for bridge formation (for the specific liquid in question). This highlights the importance of collision timescales and shows how important wetting and spreading phenomena are in the coating process.

2.4.9 Liquid distribution upon bridge rupture

After the critical rupture distance is reached and the liquid bridge breaks, liquid is redistributed between the involved particles. This can be affected by the contact angles of the particles, the size of the spheres, the volume of liquid in the bridge, gravitational effects (Darabi et al., 2010b) and a number of liquid properties. Salcudean et al. (2010) varied the solid-liquid contact angle between two equally sized particles to identify the volume of liquid transferred as a function of the capillary number and identified three zones; 1) the dynamic zone, where the liquid is almost equally distributed (high capillary numbers), 2) quasi-static zone, where liquid transfer depends on the contact angles (low capillary numbers), and 3) transition zone, the middle portion of the S-shaped curve which connects the two extreme zones (intermediate capillary numbers). These areas have been identified on Figure 2-14, however the boundaries have been arbitrarily chosen and are there for illustrative purposes only. In the region which is dependent on contact angle, smaller contact angles always result in more liquid being retained; according to the sessile test, a smaller contact angle signifies a more hydrophilic surface which will be naturally favoured during liquid redistribution. For the case of identical contact angles and equally sized particles, the liquid distribution is equal, as shown by Lian et al. (1993), amongst others. Darabi et al. (2010) used a simplified mathematical model and numerical simulations to show an increase in the volume of liquid transferred with increasing liquid bridge volume, and increasing Bond number (for equi-sized particles).

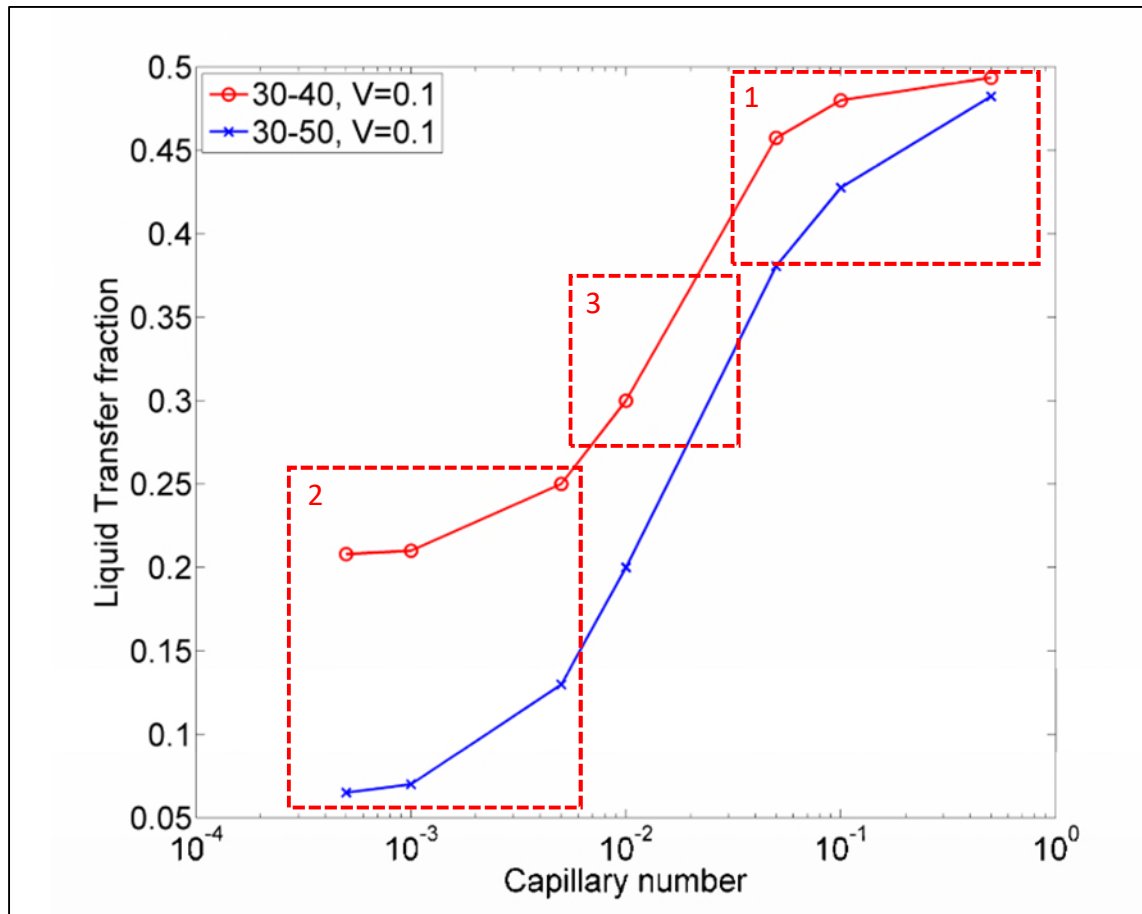


Figure 2-14. Liquid transfer fraction as a function of capillary number for two different contact angles. Adapted from Salcudean et al., 2010.

Chen et al. (2015) completed a systematic experimental study looking at the effect of multiple parameters on the evolution of liquid bridges using a high-speed camera (5,000 f/s). For systems with negligible effects of inertia, they showed that the transfer of liquid from one particle to another is a function of the capillary number (Ca), the contact angle and the minimum separation distance between two surfaces, and eventually tends towards 0.5 for high Ca values. As the minimum separation distance decreases, the footprint of the liquid droplet on the top surface converges to that of the footprint on the bottom surface. This means as the top plate is accelerated away from the bottom, there is a larger contact area for the liquid to be moved with the surface, thereby increasing the transfer ratio. For systems which include the effects of inertia, large values of Ca do not result in the convergence of the transfer ratio to 0.5; high Reynolds numbers result in an increased number of satellite drops which eventually return to the lower surface and result in asymmetric bridge formation.

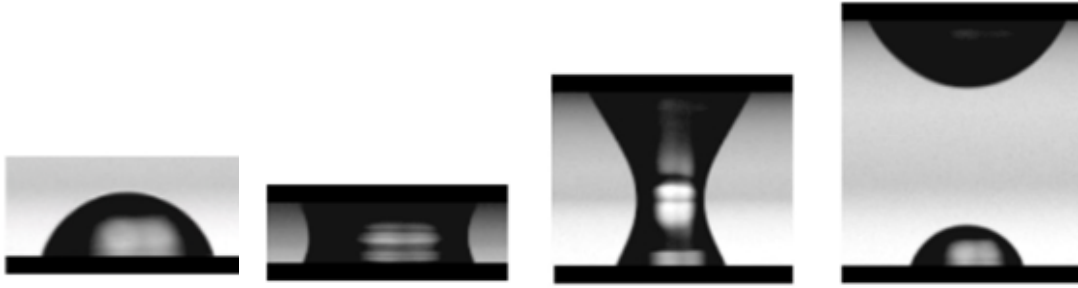


Figure 2-15. Evolution of a liquid bridge for liquid transfer between two surfaces (. Reprinted with permission from Langmuir, H. Chen., T., Tang, A. Amirfazli., Fast liquid transfer between surfaces, Breakup of stretched liquid birdges. Copyright (2015) American Chemical Society.

2.4.10 Success of particle collisions

As well as trying to determine the formation/ rupture point of liquid bridges, work on predicting the strength of collisions and, therefore, the success of the coating application, has been noted by Simons & Fairbrother (2000) and Iveson et al. (2001). The viscous Stokes number, a ratio of the relative kinetic energy between colliding particles and the viscous dissipation brought about by pendular bonds, can be used to predict the chances of a collision being successful in a coater. Three regimes exist (Table 2-3); 1) non-inertial regime - the viscous Stokes number is less than the critical Stokes number and all collisions are successful, 2) inertial regime - the two numbers are approximately equal and some collisions are successful, and 3) coating regime - the Stokes number is greater than the critical Stokes number and no collisions are successful. The viscous Stokes number relates the density of the particles, the relative velocity of the particles, the particle diameter, and the viscosity of the binder. It does assume knowledge of the relative velocity of the particles, but several models exist that can predict this parameter in different appliances; e.g. fluidised bed, tumbling drum etc (this is covered further in section 2.6.4). Regime 3 is desirable for particle coating, where the liquid bridges will break and the liquid will be available for transfer.

Table 2-3. Regimes predicted as a result of differences in the Stokes number with regard to the critical Stokes number.

Stokes value	Regime
$St_v < St_v^*$	Non-inertial
$St_v \approx St_v^*$	Inertial
$St_v > St_v^*$	Coating

There are various forms of the viscous Stokes number; Equation 2-12 shows a modified form for use with drum granulation, proposed by Walker et al. (2000). The modification calculates the velocity as the linear velocity at the drum periphery.

$$St_v = \frac{8\rho_g r_g \omega R_D}{9\mu} \quad \text{Equation 2-12}$$

where ρ_g is the granule density (kg/m^3), r_g is the radius of the granule (m), ω is the granulator speed (s^{-1}), R_D is granulator radius (m), and μ is binder viscosity (kg/m.s). Equation 2-13 gives the critical viscous Stokes number. It is determined by the ratio of binder layer height (h_l) to asperity height (h_a), and the coefficient of restitution of the granules(e).

$$St_v^* = \left(1 + \frac{1}{e}\right) \ln(h_l/h_a) \quad \text{Equation 2-13}$$

2.5 Wetting and Spreading

It has been shown that that parameters of interest when describing liquid bridges are all dependent, to a greater or lesser degree, on the contact angle of the solid-liquid pairs, and that this variable is most often used to capture a liquid's wettability. The wetting of liquids on solid surfaces has been the topic of much research over a number of years and the depth of the topic is too great to cover everything sufficiently here. The main points of interest will be detailed, but a more detailed explanation is provided by Starov et al. (2007) who give a more comprehensive review of the subject. The equilibrium contact angle, θ , is the angle formed at the 3 phase line; the point at which the surface,

droplet, and surrounding fluid all meet, and is described by Young's equation, Equation 2-14, as first described by Thomas Young (Young 1805).

$$\cos \theta = \frac{\gamma_{SV} - \gamma_{SL}}{\gamma_{LV}} \quad \text{Equation 2-14}$$

Here, γ_{SV} , γ_{SL} and γ_{LV} are the solid-vapour, solid-liquid and liquid-vapour interfacial tensions, respectively. As shown in Figure 2-16, contact angles can be classified into 3 groups; complete wetting (droplet spreads completely on surface (Figure 2-16c)), non-wetting (contact angle $> 90^\circ$ (Figure 2-16a)) and partial wetting ($0 < \text{contact angle} < 90^\circ$ (Figure 2-16b)). However, knowing the equilibrium contact angle is not enough to characterise a drop. For example, when a drop is expanding or contracting, the contact angles measured are the advancing and receding contact angles, respectively. These are examples of dynamic contact angles; measurements which are not at equilibrium but rather are taken when the droplet is still in motion. Hysteresis is the difference between these two contact angles but is often neglected in liquid bridge calculations. It is particularly important on rough surfaces and therefore relevant for the materials studied here. Shuttleworth & Bailey (1948) showed that the roughness of a normal solid surface was enough to account for the hysteresis seen with contact angle measurements. Willett et al. (2003) looked experimentally and theoretically at the effects of wetting hysteresis on liquid bridges between rigid spheres.

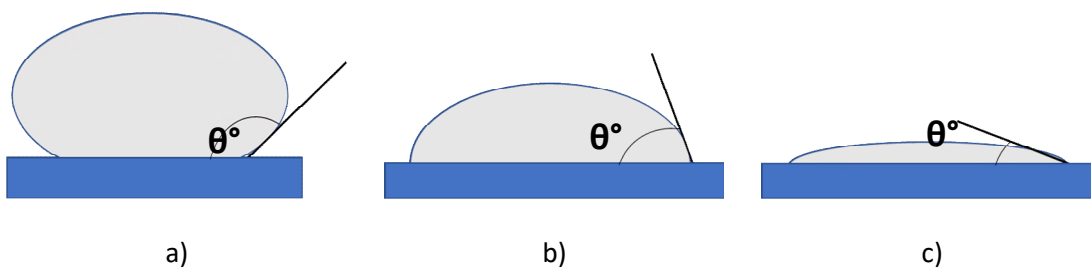


Figure 2-16. Contact angles for droplets on a surface showing a) non-wetting, b) partial wetting, and c) complete wetting.

They formed liquid bridges of various solutions between two sapphire stones, measuring the capillary forces using a microbalance and captured images to investigate the bridge volume; their work was limited to separation speeds less than $1 \mu\text{m/s}$ and therefore was not inclusive of viscous forces. They showed that wetting hysteresis has

the potential to dissipate additional energy during particle-particle collisions, and that the bridge rupture distance is increased over calculations that did not account for hysteresis. They showed the contact angle at rupture to be well approximated by $0.3 + 0.9\theta_r$ (where θ_r is the receding contact angle (radians)). To try and prevent hysteresis in measurements, most researchers try to form a flat deposition surface; for powders, this involves compression to form a tablet. Buckton & Newton (1986) examined the contact angles on powders after they had been compressed to form tablets; they found that the contact angle reduced with increasing compression force until some critical value was reached, and explained that this was a result of plastic deformation at the powder surface. As well as surface roughness and compression force, the porosity of powders can also adversely affect contact angle measurements, as shown by Cassie & Baxter (1944). All of these phenomena mean that measurement of the contact angle is very rarely the equilibrium contact angle; it is complicated by surface roughness, chemical composition and heterogeneity, and hysteresis.

Also dependent on the liquid wettability is the liquid bridge volume. If the liquid is extremely wetting, bridge formation can draw liquid from external reservoirs, i.e. liquid located on adjacent particles, or on the other side of a particle in a liquid bridge. As the wettability decreases, this movement is likely to take much longer, if it happens at all. However, as the time increases, so do the chances that the liquid bridge will once again rupture, forcing the liquid to redistribute. Pepin et al. (2001) proved this, and showed that the rupture mechanism was dependent on the saturation of the liquid reservoirs. Liu et al. (2011) found that about 5 % of liquid was contributing to liquid bridges made between glass beads, much higher than the 0.1 % recorded by Hornbaker et al. (1997) between sand particles. Hornbaker et al hypothesised that only such a small amount was contributing to the liquid bridges due to surface roughness, explaining the difference seen in the two studies (glass beads are much smoother and pose less resistance to liquid movement).

2.6 Coating behaviour: Coefficient of Variation

As reviewed in the previous section, liquid bridge behaviour is an important factor that controls the coating process, and ultimately the coating uniformity. As mentioned

previously, coating uniformity is often critical for product quality. The coefficient of variation (CoV) is often used to quantify the coating variability in a system. Here, it represents the level to which the coating is evenly distributed over either an individual particle's surface (CoV_{Intra}) or throughout the batch (CoV_{Inter}) and, therefore, how successful the coating has been. A number of authors have dedicated time to assessing both of these values, with such studies often being pharmaceutically related, e.g. Freireich et al. (2011) and Ketterhagen (2011). In recent years, the coating process has benefitted from simulations and models which are able to offer a deeper mechanistic understanding of the process. This section will first give an overview of the experimental characterisation techniques used to quantify the inter and intra tablet coating uniformity and will then give a more detailed review of intra- and inter-particle coating variation. Finally, a review of particle tracking techniques will be given before a review of the literature specifically on contact spreading is summarised.

2.6.1 Experimentally characterising coating uniformity

Quantifying the distribution of the coating quality, both intra- and inter-particle, is extremely important; heterogeneous coatings have the potential to cause serious issues, especially in pharmaceutical operations where irregularly coated pills could lead to mistimed release of an API. To quantify and characterise this variability, various analytical technologies have been developed. They take advantage of changes in the particle mass and the surface structure and are both invasive and non-invasive. Although many have been used to successfully quantify the inter-particle coating uniformity, several restrictions do exist. For example, mass gain experiments are limited by the number of particles that can be reasonably analysed in a given timeframe, some are restricted to large particle and/or large volumes of coating agents, some require time consuming sample preparation (e.g. FM) and calibration procedures (e.g. NIRS) and some are destructive (e.g. LIBS). Several of the more commonly used methods and examples of the work in which they have been used are given in Table 2-4.

Table 2-4. Summary of various techniques used in analysis of tablet / particle coatings.

Technique	Reference	Summary
Mass gain experiments and population balance modelling.	Liu and Litster 1993	Rape seed and Lucerne particles coated with fertiliser and water in a spouted bed coater. Manually removed coating layer and calculated coating mass – showed strong dependence on the initial particle size distribution. Model showed good agreement with size dependent growth term – larger particles coated preferentially.
Mass gain experiments	Abe et al. 1998	Glass beads (149 - 297 μm and 350 to 500 μm) coated with sodium chloride and dextran in a fluidised bed. Coating removed via dissolving in water and particles reweighed. CoV decreased with coating time and size of seed particle.
Scanning Electron Microscopy (SEM)	Wesdyk et al. 1990	Coated particles in a bottom spray fluidised bed; showed that larger particles were receiving a thicker film in comparison to smaller particles. Hypothesised this was result of fluidisation pattern experienced by different sized particles.
	Wesdyk et al. 1993	Sliced pellets in half and photographed to determine the average coating thickness using top, bottom and tangential spray units. Conclusions from previous work (1990) did not hold true for fluidised bed operated with a top or tangential spray i.e. larger particles were not receiving more coating.
Fluorescence microscopy (FM)	Andersson et al. 2000	Sliced pellets (400 – 500 μm) coated with ethyl cellulose in an ethanol solution and took fluorescent images. Used Matlab to separate the particle from the coating and calculate the coating height thickness. Useful for calibration of NIR spectra for determining coating height.
Laser induced breakdown spectroscopy (LIBS)	Mowery et al. 2002	Showed a change in coating thickness of less than 2.5 % is detectable and can measure both inter and intra tablet uniformity.
	Dubey et al. 2011	Measured inter-tablet variability – showed it is avoidable in pan coaters. Measured intra-tablet coating and showed it was a result of tablet structure

Chapter 2
Literature Review

Terahertz pulse imaging (TPI)	Ho et al. 2007	Fully imaged the surfaces of 10 tablets with 10 mg / cm ² of coating. They showed measurements of coating layer thickness and uniformity agreed with results from optical microscopy imaging. Variation on the tablet surface was noted in most cases because of tablets having preferred orientation through the spray zone.
	Maurer and Leuenberger 2009	Monitored coating application at different time points and created a map of coating thickness over the entire tablet surface. Showed good comparison to NIR imaging. Able to provide info about the curved edges of the tablets and to give a direct thickness value.
	Lin et al. 2015	Inline measurement of film-coating thickness and inter-tablet variability. Assessed effect of baffles, addition of uncoated tablets, blockage of spray guns on coating thickness variation. Current limitation is at 30-40 µm.
Confocal laser scanning microscopy (CLSM)	Ruotsalainen et al. 2003	Used to image surface defects of film-coated particles. Could image whole surface with results comparable to those of a laser profilometer and an optical roughness analyser.
	Depypere et al. 2009	Determined coating thickness of microparticles. Showed good agreement with a chemical method down to a coating thickness of 1 – 1.5 µm.
Micro-computed x-ray tomography (XRT)	Sondej et al. 2015	Determined coating layer thickness and porosity of alumina coated with sodium benzoate and HPMC in a fluidised bed. Showed simpler and quicker method (using only 1 X-ray) gave comparable results to a more complicated method. Also noted method can be used for multiple particles at once.
Near-infrared spectroscopy (NIR)	Perez-Ramos et al. 2005	Analysed in-line the coating thickness of tablets in a pan coater and developed a model to account for different growth rates on face and sides of tablets. Showed good correlation of their model with measured values.
	Römer et al. 2008	Used NIR to validate a calibration model for scaling up a pan coater. Determined thickness of 100 tablets using a digital micrometer and showed that the predicted coating thickness from the NIR model was

		only 30 μm greater than the measured average (210 μm).
Colourimetric image analysis	Yusof et al. 2018	Determined the inter-particle coating uniformity of particles in lab scale tumbling drum experiments using colourimetric image analysis. Coating variability of alumina particles coated with PEG solutions determined. Showed that coating rate is a function of PEG viscosity and rum speed.

2.6.2 Intra-particle coating variability

More recently, a number of researchers have developed simulations or modelling tools to try and predict the intra-tablet coating variation with a spray component. Freireich & Wassgren (2010) used Monte-Carlo simulations of single particles alongside an analytical model to predict the variation in the coating thickness, investigating both orientations and rotations as particles pass through the spray zone. They showed that the $\text{CoV}_{\text{intra}}$ is proportional to the inverse square root of the coating time for convex particles exhibiting no preferred orientation in the spray zone. If a particle does have a tendency for a particular orientation, the $\text{CoV}_{\text{intra}}$ will approach some non-zero value, or an asymptotic CoV, and the greater this preferred orientation, the quicker the asymptotic value will be reached. They showed that increased surface layer speed (the rate at which a particle moves from the top to the bottom of the exposed powder surface) results in increased particle-particle coating uniformity as there is more chance of uniform exposure to the spray. DEM simulations were used to model spherical particles, and this showed that even though they lack preferred orientations, preferred rotations about an axis are evident. Similar to the convex particles, the CoV will eventually approach the $1/t^{1/2}$ behaviour, but greater degrees of preferred rotation will delay this approach more significantly. Freireich et al. (2011) extended this work and looked at 5 non-spherical tablet shapes coated in a rotating drum. They used DEM simulations to determine the tablet orientations and then used Monte-Carlo simulations to coat the particles. For all the shapes tested, they again showed that the CoV decreases with the square root of the number of coating trials and eventually approaches some asymptotic value. A coat was when the Monte Carlo algorithm samples a tablet

orientation from the DEM simulation and applied a coating to the tablet surface. The asymptotic value is dependent on the extent of the tablets' preferred orientation; greater preferences lead to higher asymptotic CoVs which are reached in shorter times. This can be seen in Figure 2-17 which shows the CoV_{intra} values approaching some non-zero limiting value as the experimental run time increases. They could find no correlation between the tablets' asymptotic CoV and either the tablet sphericity, aspect ratio or band-to-tablet area ratio. In this work, the effect of shadowing (the effect of neighbouring tablets reducing a tablet's exposure to the spray) was not considered.

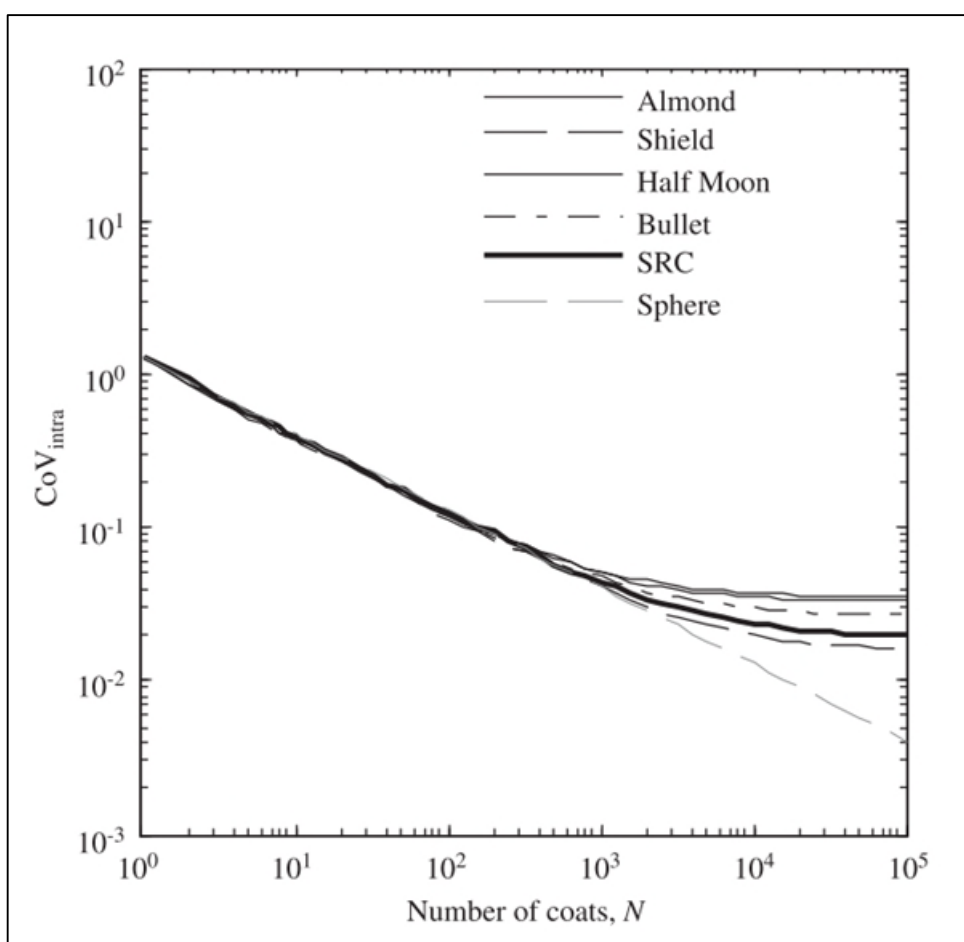


Figure 2-17. DEM predictions of intra-tablet coefficient of variation plotted as a function of number of coats for six tablet shapes. Reprinted from Chemical Engineering Science, 66, B. Freireich., W.R. Ketterhagen., C. Wassgre., Intra-tablet coating variability for several pharmaceutical tablet shapes, pp. 2535 – 2544, (2011), with permission from Elsevier.

Hilton et al. (2013) presented a CFD-DEM approach to model spray coating in a fluidised bed, presenting the first model which incorporated particles, spray droplets and gas flow. A spherical harmonic formulation maps the coating coverage of each particle and

allows for the evaluation of the intra-particle (and inter-) coating uniformity. Unlike Freireich et al., Hilton et al. showed a divergence from the -0.5 power law relationship between CoV and coating passes. The CoV starts out following this idealised trend, but their model predicts greater divergences at longer times, with a power law exponent between -0.4 and -0.3. Similar deviations have been recorded in the literature for experimental works investigating the inter-particle coating uniformity. Freireich et al. (2015) built on their earlier work and included the effect of shadowing in their new DEM simulations, showing that without incorporating this effect the CoV intra values would always be over-predicted. When shadowing was included, a fair correlation was made between the asymptotic CoV and tablet sphericity; increased sphericity results in increased coating uniformity due to the ability of the particles to roll as they pass through the spray zone and hence be less likely to present a preferred orientation. They showed qualitative similarities between the coating thickness distributions from the simulations and from terahertz thickness measurements. The intra-particle variation is very difficult to determine experimentally for large volumes of particles, requiring in-depth and time-consuming analysis of individual particle surfaces.

Unlike the intra-particle coating, which asymptotes to some constant value, inter-particle coating variability will continue to decrease with more passes through the spray zone, and is more readily analysed. This will be discussed in greater detail in the next section.

2.6.3 Inter-particle coating variability

Inter-particle coating uniformity (CoV_{inter}) is an important quality control measurement and has benefitted from a lot of research. It is shown in Equation 2-15 and represents the ratio of the standard deviation (σ_M) to the mean of the total coating mass (ζ_M);

$$CoV_{inter} = \frac{\sigma_M}{\zeta_M} \quad \text{Equation 2-15}$$

In a batch tumbling drum process, the amount of material accumulated by a particle over time is given by the summation of the random amount of coating accumulated on each pass for all the random number of passes that the particle makes through the spray

zone. If the mean coating mass and the standard deviation of the coating mass are then obtained in terms of the coating mass a tablet receives per pass (subscript W), and the number of passes a tablet makes (subscript N), the CoV can be written as follows (Mann et al, 1979);

$$CoV_{Inter} = \sqrt{\frac{\sigma_W^2}{\zeta_W^2 \zeta_N} + \frac{\sigma_N^2}{\zeta_N^2}} \quad \text{Equation 2-16}$$

Matt (1983) then used renewal theory to relate the number of passes to the distribution of the cycle time, and ultimately showed that;

$$CoV_{Inter} = \sqrt{\frac{\mu_C}{t} \left[\left(\frac{\sigma_M}{\zeta_M} \right)^2 + \left(\frac{\sigma_C}{\zeta_C} \right)^2 \right]} \quad \text{Equation 2-17}$$

where ζ_M and σ_M are the mean and standard deviation of the distribution of coating mass deposited on a particle per pass through the coating zone, ζ_C and σ_C are the mean and standard deviation of the cycle time distribution, and t is the coating time (Kumar et al. 2015). This clearly shows that the CoV_{Inter} is proportional to $1/t^{0.5}$ for spray coating systems. This equation can, however, only be used for batch coaters; continuous coating would result in different coating times for different particles. Freireich & Li (2013) showed that the approach taken by Mann et al was flawed in that the assumption of independence between the coating mass per visit and the cycle time is not true for large spray to cycle time ratios. They instead proposed Equation 2-18, which assumes that the coating mass per visit (W) has a linear relationship with the cycle time (C), and that the bed and spray times are independent. As they highlighted, industrially the two equations should show small variance since small spray areas and long coating times are common. In Equation 2-18, ρ_{WC} is the correlation coefficient of W and C .

$$CoV_{Inter} = \sqrt{\frac{\zeta_C}{t} \left[\left(\frac{\sigma_W}{\zeta_W} \right)^2 + \left(\frac{\sigma_C}{\zeta_C} \right)^2 - 2\rho_{WC} \frac{\sigma_W \sigma_C}{\zeta_W \zeta_C} \right]} \quad \text{Equation 2-18}$$

Population balance modelling offers an alternative approach; Denis et al. (2003) developed a population balance to predict the coating mass distribution based on a

model of surface renewal, modelling the cascading layer of the powder bed in a tumbling drum as a stirred tank reactor. The remaining particle mass (below the particle-liquid interface) is approximated using a number of stirred tanks connected in series. Their model showed that the coating mass distribution is well approximated as a normal distribution which centres around the mean coating mass and is dependent only on the size of the feed zone, the rate of application of the coating solution and the turnover of the bed. They compared their model with results from a rotary drum (diameter 25.4 cm, length 25 cm) used to coat 3.7 mm diameter tablets, showing an increase in the percentage of particles coated with increasing rotational speed and decreasing fill ratio. Kalbag & Wassgren (2009) combined DEM with experiments and proposed a semi-empirical equation to determine the CoV_{Inter} (Equation 2-19);

$$CoV_{Inter} = 4.49 \sqrt{\left(\frac{2\pi}{\omega t}\right) \left(\frac{L}{L_{SPW}}\right) V_f^{*0.68} Fr^{-0.1}} \quad \text{Equation 2-19}$$

Here, ω is the drum speed, t is the coating time, L is the drum length, L_{SPW} is the spanwise length of the spray zone, V_f^* is the dimensionless drum fill volume and Fr is the Froude number. However, the equation shows limited accuracy, with errors +/- 30 % compared to measured values. Sahni & Chaudhuri (2011) coated lactose with aqueous Opadry solutions in a pan coater to investigate the effect of spray variables, drum speed (10, 20 and 30 rpm), drum fill level and drum tilts (0°, 16° and 32°). A DEM model based on the experimental conditions was used to calculate the residence time distributions of the particles in the spray zone. They showed a decrease in coating variability with increasing drum tilt, increasing coating time and optimisation of the rotating speed. Unlike previous studies, the spray characteristics had minimal effect on the coating uniformity. Kumar & Wassgren (2014) looked at the influence of particle axial motion on inter-particle coating variability and showed that the CoV_{Inter} value for continuous coaters is strongly dependent on the particle residence time.

Kumar et al. (2015) used DEM simulations, a compartment model, and a population balance to predict inter-particle coating variability in a horizontally rotating drum. They built on the work of Denis et al. (2003) and included a third region, a passive bed region, as well as the active region and the spray zone region. The inclusion of the passive zone

(Figure 2-18), which represents the particles outside of the circulating loop, becomes important at high coater volumes, and has a significant impact on the inter-tablet coating variability. A new compartment model, which does not require the use of area or time thresholding, but looks to represent the motion of particles in the drum, is proposed. They noted significantly less computational time compared with previous DEM simulation only models and found excellent agreement between the proposed model and DEM simulations with a relative error of less than 5%.

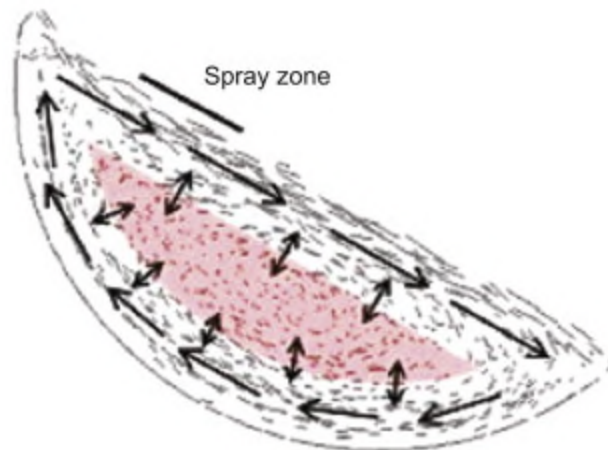


Figure 2-18. Simulated flow of particles in an un-baffled horizontal rotating drum. The black arrows represent the particles general circulating loop, the solid black line represents the spray zone, and the passive bed zone is indicated by the red region. Reprinted from Chemical Engineering Science, 125, R. Kumar., B. Freireich., C. Wassgren., DEM-compartment-population balance model for particle coating in a horizontal rotating drum, pp. 144-157, (2015), with permission from Elsevier.

Pasha et al. (2017) used DEM to model the coating of 4200 7.1 - 8 mm corn seeds in a vertical rotating coater, capturing the shape of the corn seeds via X-ray tomography and modelling it using a combination of 5 spheres. The simulation does not account for contacts between particles; as soon as a droplet touches a particle, its mass is removed from the system. They then investigated the effect of several parameters, stating the ones which had significant effect of the coating variation to be atomiser disc position and baffle arrangement.

Monte-Carlo simulations have also been successfully used to determine coating uniformity; KuShaari et al. (2006) obtained velocity and voidage data from a 22.6 cm diameter Wurster coater and used these variables as input parameters in their model, also incorporating the effect of sheltering in the spray zone. They noted a very large

dependence of the coating variability on the spray shape, but were unable to quantify their findings, and also showed that a wider coating distribution was found for lower gas velocities and lower gap height. Pandey et al. (2006) completed similar experiments but used a pan coater instead of a Wurster. They investigated the effect of pan speed, pan loading, tablet size, coating time, spray flux distribution and spray area and shape. They used a video imaging technique which traced a coloured particle around the bed to collect data on the dynamics of the tablet movement and then used this data as a model input. Unlike the Wurster coater, the coating uniformity was not found to depend heavily on the spray shape, however, an increase in the spray area led to lower CoVs. Similar to many previous authors, they also showed a dependence on the inverse square root of the coating time. Overall, the model underpredicted the CoV in comparison to experiments coating round tablets (6.3 mm, 7.9 mm and 10.4 mm) with various colours of Opadry solution in a 57.5 cm diameter and 10 cm long perforated tumbling drum. Wang et al. (2012) showed the droplet size and the spray velocity were important parameters for improving the coating efficiency in their study.

2.6.4 Particle tracking: velocity profiles

For a number of models, the cycle time distributions are a required input parameter. To measure this, Parker et al. (1997) used positron emission particle tracking (PEPT) to trace a radioactive particle around a rotating drum (136 mm diameter) filled with 1.5 mm glass spheres. They also investigated larger particles (3mm) in larger drums (100 and 144 mm diameter) and rotational speeds from 10 to 65 rpm, clearly showing a distinction between an active surface layer and an underlying bed layer in each experimental set. The technique allows a very detailed understanding of the axial and radial positions of the tracer particle with time, and from this a cycle time can be found. Jain et al. (2002) used particle tracking velocimetry to experimentally determine the flow of particles in the active surface layer of a quasi-2D rotating drum (28 cm diameter). They showed very large discrepancies between the velocities in the top layer compared with the bottom layer, using spherical glass beads of 1 mm, 2mm and 3 mm to maintain a constant dimensionless thickness of the tumbler. The velocity profile throughout the top layer was shown to be linear in the direction parallel to the flow of the tumbling bed,

but becomes logarithmic when the bulk layer is entered due to the slow rearrangement of particles.

Nakagawa et al. (1993) used magnetic resonance imaging (MRI) to measure the velocity of 1.5 mm mustard seeds in two rotating drums (internal diameters 88 mm and 70 mm). They were the first to use this technique, and proved its capabilities for measuring the velocity profiles in rotating drums. In 1997, Nakagawa again used MRI to study the flow at the centre of a cylindrical rotating drum, and proposed an equation to model the velocity profile which depended on the velocity at the free surface, the depth of the layer from the free surface, the radial position and the rotation rate. This was later verified by Sanfratello et al. (2007) using the same technique. Pandey et al. (2006) developed a DEM model to study the particle velocity in the cascading layer of a pan coater, both axially and parallel to their powder bed surface and compared their results with video analysis of 9 mm polystyrene balls in a 58 cm diameter pan. They showed good agreement between the simulations and experiments and built on the work of Alexander & Muzzio (2001), proposing Equation 2-20 which includes a parameter allowing for the scaling of the particle velocity by different fractional fill volumes. Particles were found to reach their maximum velocity at approximately the mid-point of the cascading bed surface.

$$V = kR_D\omega^{2/3}\left(\frac{g}{r_p}\right)^{1/6}f^{1.8} \quad \text{Equation 2-20}$$

Here, V is the velocity of the particles, k is a constant, R_D is the pan radius, ω is the pan speed, g is acceleration due to gravity, r_p is the particle size and f is the drum fractional fill volume. Mueller & Kleinebudde (2007) used this model to scale up experiments from laboratory (31.6 and 39.6 cm diameter) to pilot (66 cm diameter) and production scale (110 cm diameter). They measured tablet velocities at 5 drum speeds using video imaging of a tracer particle and proved that velocities at the production scale can be accurately predicted from the velocities measured at the lab scale. They also proposed an alternative method for predicting the scaled-up velocities of two coaters at the same speed and with the same spray zone but of different sizes, which does not require calculation of k at various pan speeds. They related the ratio of the tablet velocities to

the radius of drum 2 divided by drum 1 to the power 1/3, and showed excellent agreement with their experimental work. There has been a lot of work completed in this field, however, all have been inclusive of or focused on the spray component of coating systems. Few authors have completed work on contact spreading, but this work will now be reviewed.

2.7 Previous work on contact spreading

All the previous work mentioned in this chapter has included a spray, and so drawing comparison between it and the work completed in this thesis is difficult. As has been previously mentioned, the work which has been completed on contact spreading has been limited to modelling. The first work in this area was attempted by Shi & McCarthy (2008) who developed a liquid transfer model for contact spreading in DEM and presented results from a simulation of a rotating drum spray coating process to test their model. One key assumption of their work is that the liquid is evenly distributed over the particle surface; as has previously been shown, this is highly dependent on the solution viscosity and so their assumption is only valid for very low viscosity and highly wetting liquid-solid systems. The liquid bridge volume is determined as a summation of the liquid stored in the spherical caps of the two adjacent particles (as indicated in Figure 2-19).

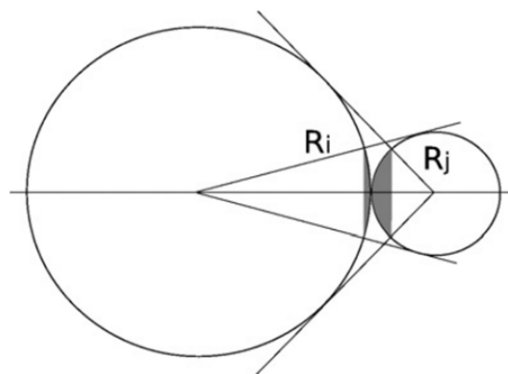


Figure 2-19. Schematic of liquid bridge spherical caps used to determine the liquid bridge volume. Reprinted from Powder Technology, 184, D. Shi., J.J. McCarthy., Numerical simulation of liquid transfer between particles, pp. 64-75, (2008), with permission from Elsevier.

This also neglects the earlier mentioned point of liquid reservoirs ‘feeding’ liquid into the bridge, and supposes that the volume stays constant. Their model produced the result that CoV_{inter} increases with the inverse square root of the coating time, with the curve having a positive intercept for Bond numbers greater than 1 and no intercept for Bond numbers less than 1 (see Section 2.4.2 for more information on the Bo number). Mani et al. (2013) produced a simple model to redistribute liquid over particle surfaces at bridge rupture, assuming the bridge volume is the sum of the total liquid film volume on each particle, and the distribution of the liquid is equally split between the two particles if the critical separation distance is exceeded. They showed that this redistribution affects the velocity profiles in a sheared granulator.

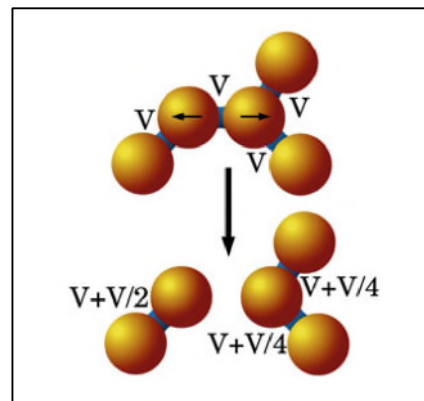


Figure 2-20. Post-rupture liquid distribution model. Reprinted by permission from Springer: Nature, Granular Matter, Liquid migration in sheared unsaturated granular media, R. Mani., D. Kadau., H.J. Herrmann., (2012).

Mohan et al. (2014) tested four liquid dispersion models; the first assumes the liquid transfer is analogous to heat conduction between two particles in contact, with the liquid transfer rate being dependent on the difference of the liquid content between the two particles and a transfer coefficient. The second model is the one which Shi & McCarthy proposed, as previously detailed (the liquid transfer takes place at the time point when the particles separate and no separation distance is considered). In the third model, the liquid exchange is assumed to occur after the particle surfaces come into contact; the liquid bridge forms instantaneously, the bridge ruptures after reaching some critical distance and the subsequent redistribution is based on some transfer coefficient. The fourth model assumes a certain and finite volume of liquid on the particle surface will drain into the liquid bridge. Their simulations did not however

include the effects of particle roughness, bridge volume, or wetting effects, all of which are known to be extremely important. Recently, Washino et al. (2016) developed a new model which subdivides the particle surface into a number of sections with the liquid being stored in these areas. This does not assume instantaneous spreading, a mechanism which has been a main feature of other models. They compared their model with the Shi & McCarthy (2008) and showed that their instantaneous spreading assumption is applicable at low viscosities but that it becomes very important to take into account liquid spreading at higher viscosities. This is shown in Figure 2-21 where the left hand image shows agreement of the two models for a low viscosity coating solution, and the right hand image shows the Shi & McCarthy model underpredicts the variation in the system as compared to the model developed by Washino et al.

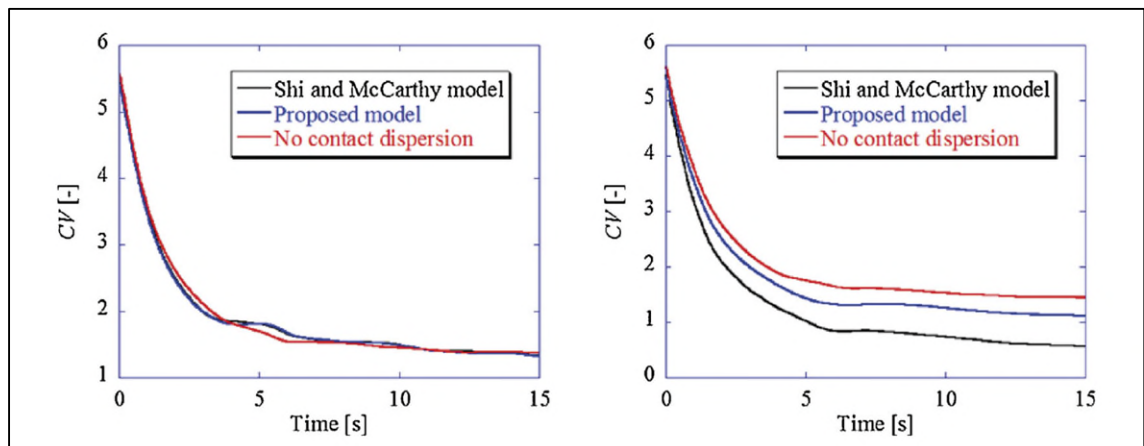


Figure 2-21. Graphs showing the coefficient of variation as a function of time as predicted by three models; left) liquid viscosity = 0.001 Pa.s, and right) liquid viscosity = 0.1 Pa.s. Reprinted from Chemical Engineering Research and Design, 110, K. Washino., K. Miyazaki., T. Tsuji., T. Tanaka., A new contact liquid dispersion mode for discrete particle simulation, pp. 123-130, (2016), with permission from Elsevier.

Schmelzle et al. (2018) built on the work of Washino et al. (2016) and their particle surface discretisation method and included partial wetting and drop formation in their DEM simulations of a solid mixing process (Figure 2-22).

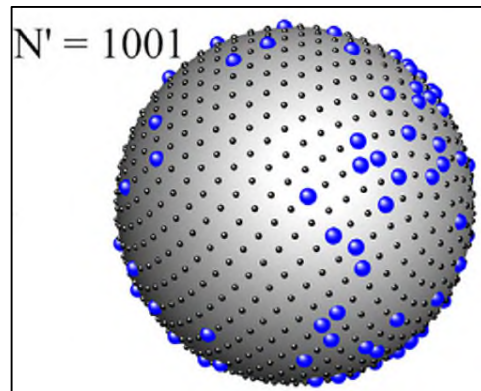


Figure 2-22. Example of discretisation method used by Schmelzle et al with 1001 discretised potential liquid storage points. Reprinted from Powder Technology, 338, S. Schmelzle, E. Asylbekov., B. Radel., H. Nirschl., Modelling of partially wet particles in DEM simulations of a solid mixing process, pp, 354-364 (2018), with permission from Elsevier.

Unlike Washino et al. who only considered contact points, Schmelzle et al. implemented liquid spreading to other discretised points on the particle surface to a greater or lesser extent based on the contact angle; lower contact angles result in greater liquid spreading. They did not however, include the viscous forces. The accuracy of their model improved as the number of discretisation points increased, but this obviously comes at the expense of drastically increased computing power.

2.8 Conclusions

In the context of wet spray coating, two mechanisms are generally widely accepted; the initial droplet deposition, and the further movement of liquid due to particle-particle interactions (contact spreading). This second stage is dependent on the formation and subsequent rupture of liquid bridges, and to date, no relatively large scale experiments focusing only on contact spreading have been completed. A great number of studies have analysed one-to-one particle interactions, and several studies have gone as far as reporting the behaviour of liquid bridges connecting three particles. Yet even these interactions differ greatly when under the stresses of agitation within industrial processing equipment. A number of computational methods have attempted to model the contact only spreading of liquids, but due to a lack of experimental data, have made unjustified assumptions. As the focus of this research is to develop a mechanistic understanding of the movement of liquid due to contact spreading, the equipment

chosen should have high particle-particle interaction and provide an easy means of removing the spray component. A tumbling drum meets these requirements. A comprehensive experimental study of coating bulk material with liquid coating agents will develop the mechanistic understanding of contact spreading. Of the coating characterisation techniques described in Section 2.6.1, most are not able to process large volumes of data necessary to produce a large scale study. However, a new technique developed at the university of Sheffield (Yusof et al. 2018) based on colourimetric analysis addresses this limitation and will be used to quantify the particle coating uniformity.

3. Materials and Methods

3. Materials and Methods

3.1 Introduction.....	58
3.2 Material systems.....	58
3.3 Material characterisation.....	59
3.4 Methods.....	79
3.5 Summary.....	85

3.1 Introduction

This chapter will outline the materials used in this research, the main experimental procedures, and material characterisation. Any characterisation, or methodologies, which are specific to individual results chapters, will be discussed in the relevant chapter. The general procedure of the majority of the experimental works can be seen in Figure 3-1.

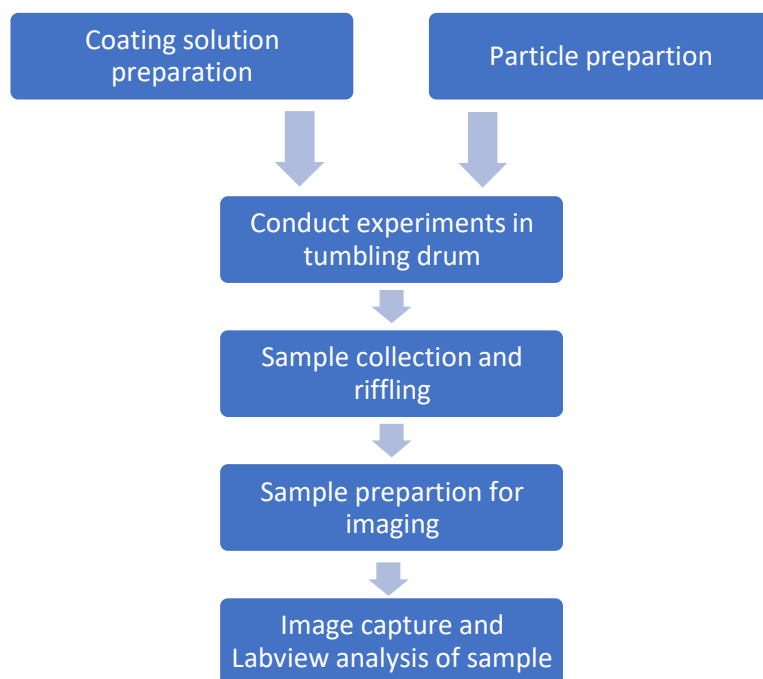


Figure 3-1. Flowchart showing an overview of the experimental procedure.

3.2 Material systems

A simple model system was used for the first experimental works, allowing complexity from realistic coating systems to be gradually introduced at a future date. Although detergent materials are available, their complexity, i.e. liquids with rheology that is dependent on the temperatures the liquids have previously been exposed to, particle surface roughness and non-uniform colour distributions, makes it difficult to analyse the effect of changing individual variables. On the other hand, a model system with known variables, i.e. smooth surface, narrow size distribution, uniform colour etc., will make understanding and quantifying the impact of individual parameters much easier. As

outlined in Chapter 1, a non-model, more realistic system using sodium percarbonate as the particles will be subsequently investigated.

3.3 Material characterisation

This section will describe the characterisation methods undertaken for both the particles and coating liquids. Methods for characterisation of products are given in the relevant results chapters.

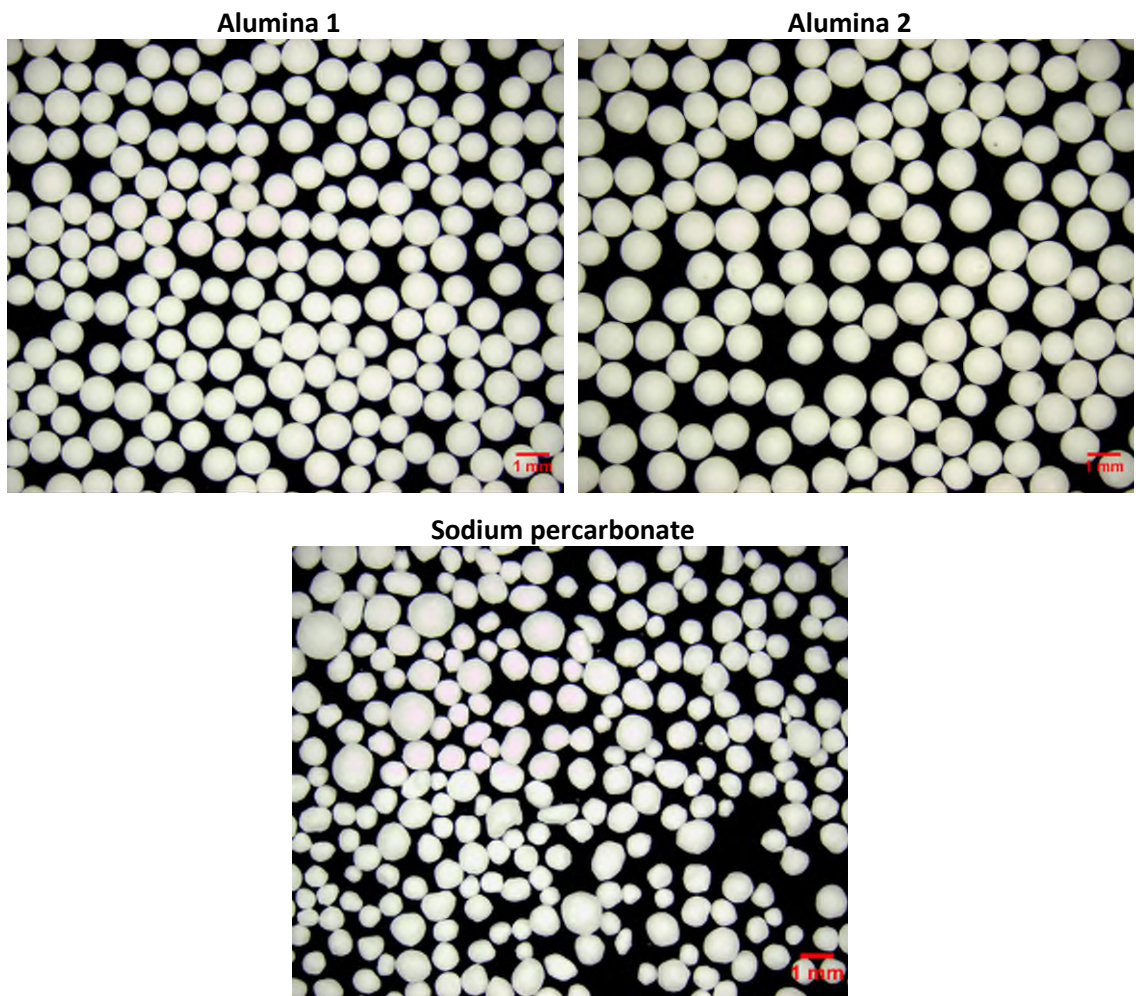


Figure 3-2. Images of the particles employed in this research.

Two types of alumina ceramic particles (Anderman-ceramics, UK) were used as a simple model system; Alumina 1 and Alumina 2. They are white and spherical with a narrow size distribution and allowed for the analysis of the effect of particle density, liquid viscosity, and drum parameters. Sodium percarbonate (Solvay, UK) (SPC) was later introduced as a more complex system, consisting of non-spherical particles and being a

constituent of many industrial detergents. Furthermore, sodium percarbonate has a wide size distribution, has rough surfaces, and has a much lower density than the simple model system due to its increased porosity. This allows investigation into both the effect of the particle size distribution (PSD), and the effect of particle density. Figure 3-2 shows a comparison of the particle appearance for the three materials investigated.

Polyethylene glycol (PEG) aqueous solutions (BioUltra, Sigma-Aldrich) of varying molecular weights were used throughout this work. They were chosen to represent a large range of viscosities (~100 - 20,000 mPa.s), covering the viscosities of realistic detergent solutions (~400 - 10,000 mPa.s). The viscosity was varied by using different molecular weight PEG solutions, all made up at a 50 % w/w concentration in distilled water. The PEG flakes were dissolved in a 1 % w/w solution of Acid red dye (Sigma Aldrich) in distilled water. The addition of red dye was important for the subsequent colourimetric analysis which allowed the quantitative determination of coating uniformity, as described in section 3.4.2.

A second batch of solutions were made for use with the sodium percarbonate experiments. In this case, the red dye solution was composed 9.9 % w/w ethanol, 89.1 % w/w distilled water, and 1 % w/w Acid red dye. The reason for this was that when adding the original solution to sodium percarbonate, the higher molecular weight PEGs were forced out of solution and precipitation of PEG was observed. The SPC is more soluble in water compared to the higher chain length PEGs, forcing the PEGs to precipitate. SPC is not as readily soluble in ethanol/water solution, and therefore the PEG remains in solution form and is available for coating of the particles.

3.3.1 Particle Size

Two methods were used to measure the size of the particles; laser diffraction and sieving. For laser diffraction, a Malvern Mastersizer 3000 with a dry cell was used to measure the size distribution of particles. A sample of approximately 20 g was placed in the top hopper. The approach platform down which the particles are fed is vibrated to encourage movement. The technology then measures the intensity of the light scattered as a laser beam passes through the dispersed sample. The scattering patterns produced can then be used to calculate the size of particles in the sample (Rawle et al., 2003).

Results are presented in terms of a volume frequency distribution, from which several parameters can be extracted. The $d_{3,2}$ (surface area mean diameter, also known as the Sauter mean diameter) is of particular interest when the surface area of the population is important; representing the diameter of a sphere that has the same volume to surface area ratio as the particle in question. The $d_{4,3}$ (volume moment mean diameter, also known as the De Brouckere mean diameter) shows where the majority of the volume is located within the bulk and can therefore be less useful when a large number of fines are present which can heavily influence the distribution (Merkus, 2009).

Sieving allows a large number of particles to be analysed relatively quickly; sieves (Retsch) with increasingly smaller mesh sizes were placed in a column and a known mass of material (5 kg) was poured in the top. Because the material was supplied in very large quantities, it was difficult to ensure that a representative sample had been taken. To overcome, it was necessary to use a large quantity of the material to ensure a representative size distribution was obtained. The ratio between adjacent sieve mesh sizes is equal to the fourth root of 2, meaning the aperture size doubles every 4th size. A Retsch AS 200 Sieve Shaker was then used to agitate the material for two minutes at an amplitude of 1.05 mm, after which the various fractions were collected and weighed to give a size distribution. These conditions were chosen to ensure that the particles were properly separated; any further sieving resulted in no further movement of particles between the sieves. From this, a cumulative size distribution can be created and the values of the d_{10} , d_{50} and d_{90} can be extracted. The d_{90} represents the diameter of which 90 % of the sample is smaller than (by volume), the d_{10} is the diameter of which 10 % of the sample is smaller than, and the d_{50} is the median size of the distribution. The span was calculated using Equation 3-1, and gives some indication of the spread of the data.

$$Span = \frac{d_{90} - d_{10}}{d_{50}} \quad \text{Equation 3-1}$$

Table 3-1 summarises the data from the laser diffraction, and Table 3-2 shows the data from the sieving analysis.

Table 3-1. Particle size data measured using laser diffraction.

Particles		d_{10} (μm)	d_{50} (μm)	d_{90} (μm)	Span	$d_{3,2}$ (μm)	$d_{4,3}$ (μm)
Alumina 1		857	1014	1222	0.360	1006	1026
Alumina 2	Batch 1	983	1077	1225	0.225	1082	1089
	Batch 2	1149	1337	1570	0.315	1331	1348
Sodium percarbonate		874	1508	2469	1.06	1335	1594

Table 3-2. Particle size data measured using sieve analysis.

Particles		d_{10} (μm)	d_{50} (μm)	d_{90} (μm)	Span	$d_{3,2}$ (μm)	$d_{4,3}$ (μm)
Alumina 1		868	1034	1155	0.278	1041	1050
Alumina 2	Batch 1	954	1077	1164	0.195	1080	1084
	Batch 2	1182	1422	1646	0.326	1447	1462
Sodium percarbonate		370	840	1314	1.12	1115	1219

The data from the two alumina particles compares very well between the two methods; this is to be expected as the material has a reasonably narrow size distribution and is highly spherical. The sodium percarbonate, on the other hand, shows a very large difference in the measurements; sieving shows a far greater proportion of smaller particles. This could be due to the fact that the material does have a much wider size distribution and, therefore, collecting a representative sample to feed to the mastersizer can be difficult. Sieving allows a much larger mass of material to be processed, increasing the likelihood of sampling a representative sample. The particle size distribution and the cumulative distribution for the sodium percarbonate particles are shown in Figure 3-3 and Figure 3-4, identifying the d_{10} , d_{50} , d_{90} , $d_{3,2}$ and $d_{4,3}$. Figure 3-3 show a very wide size distribution for the sodium percarbonate material, ranging from 53 to 2,180 μm with a high proportion of fines.

When plotting the cumulative particle size distribution, the upper size in each bin is plotted, whereas when plotting the normal size distribution, the midpoint of the bin is plotted. This is why the size distribution graphs are all slightly offset from the cumulative

distribution graphs and explains why the $d_{3,2}$ and $d_{4,3}$ are slightly different from the Malvern data.

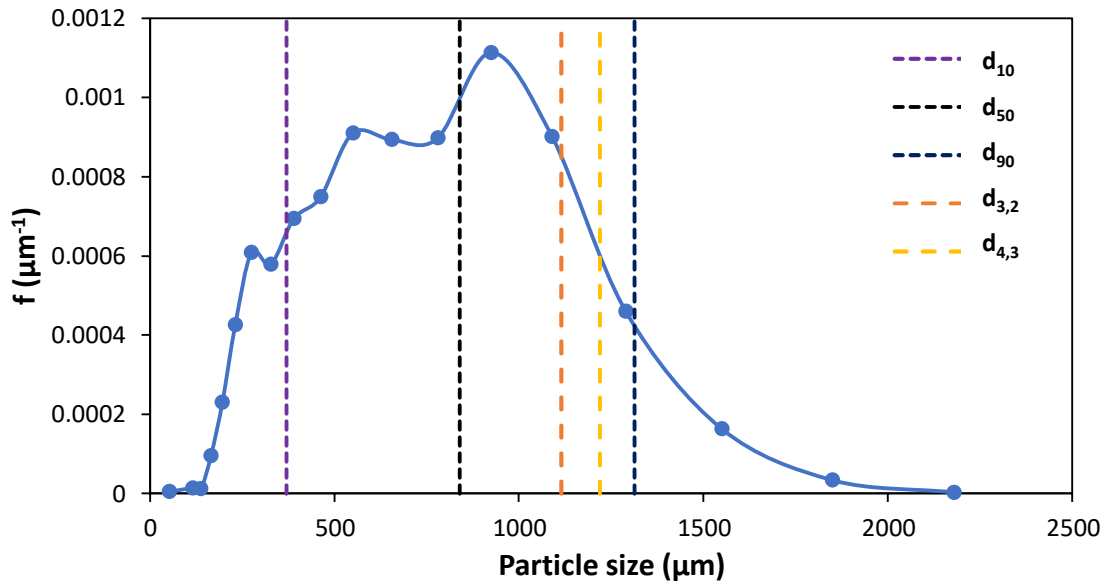


Figure 3-3. Particle size distribution of sodium percarbonate obtained via sieve analysis.

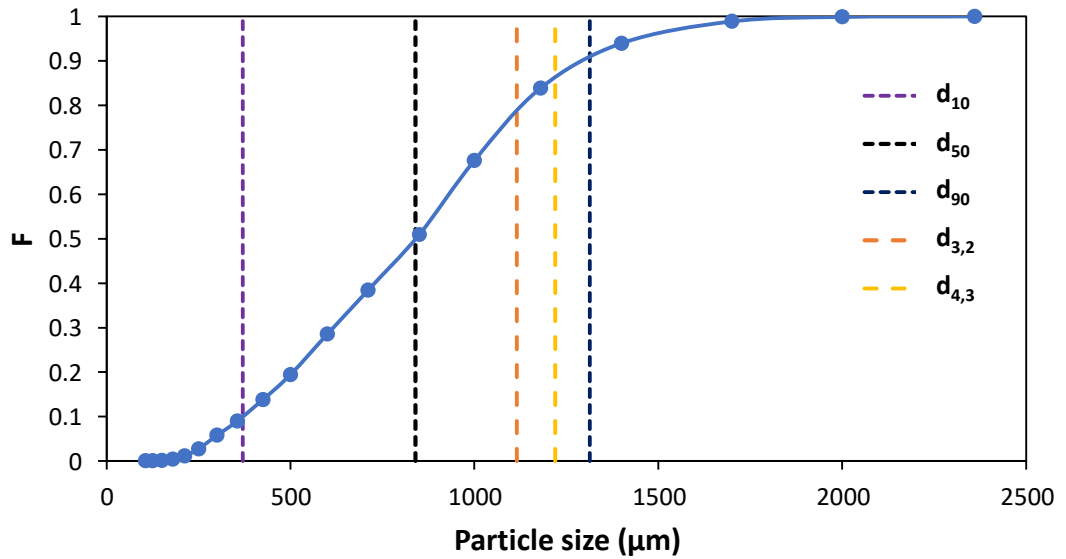


Figure 3-4. Cumulative particle size distribution of sodium percarbonate obtained via sieve analysis.

The size distribution and cumulative size distributions are shown on the same graph for Alumina 1 (Figure 3-5), Alumina 2 – batch 1 (Figure 3-6), and Alumina 2 – batch 2 (Figure 3-7) and identify the same parameters.

Unlike the sodium percarbonate, Alumina 1 and Alumina 2 (both batches) have much narrower size distributions. Alumina 1 spans from 655 to 1550 μm , showing neither the fines or oversized particles that are present in the sodium percarbonate.

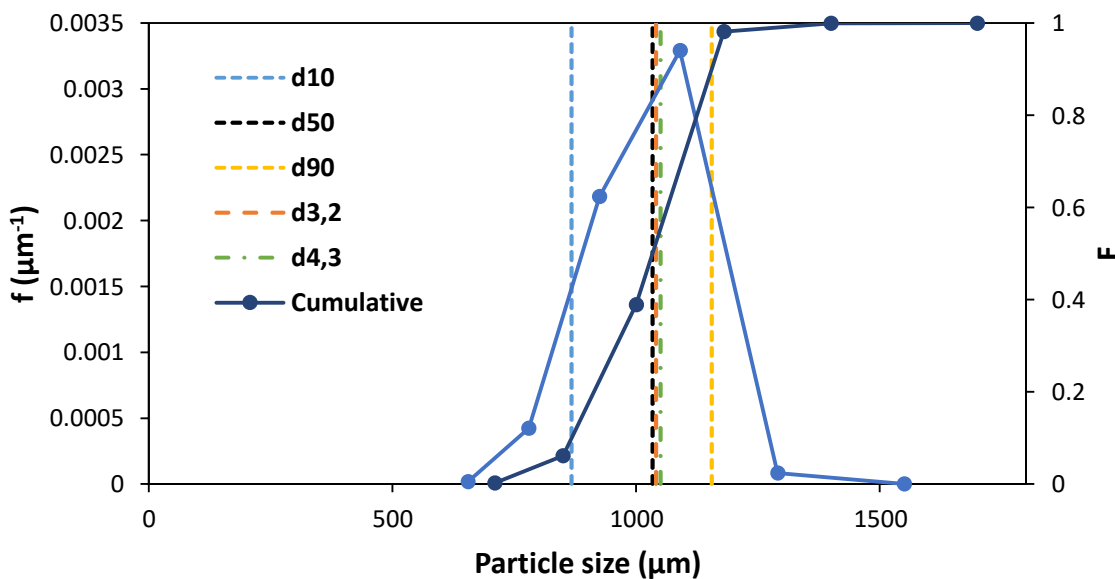


Figure 3-5. Particle size and cumulative particle size distribution of Alumina 1 obtained via sieve analysis.

Batch 1 of the Alumina 2 particles displayed the narrowest size distribution of all the materials studied. As can be seen from Figure 3-6, the particles span from 780 to 1290 μm , and follow a very unimodal pattern, as indicated by the tight grouping of the d_{50} , $d_{3,2}$ and $d_{4,3}$. From Figure 3-7 it can be seen that the second batch of Alumina 2 particles has a wider span, ranging from 925 to 1850 μm . The median value (d_{50}) is the highest of all the materials tested. It should be noted that this material was only used for a small number of experiments, and any results pertaining to this material are clearly highlighted.

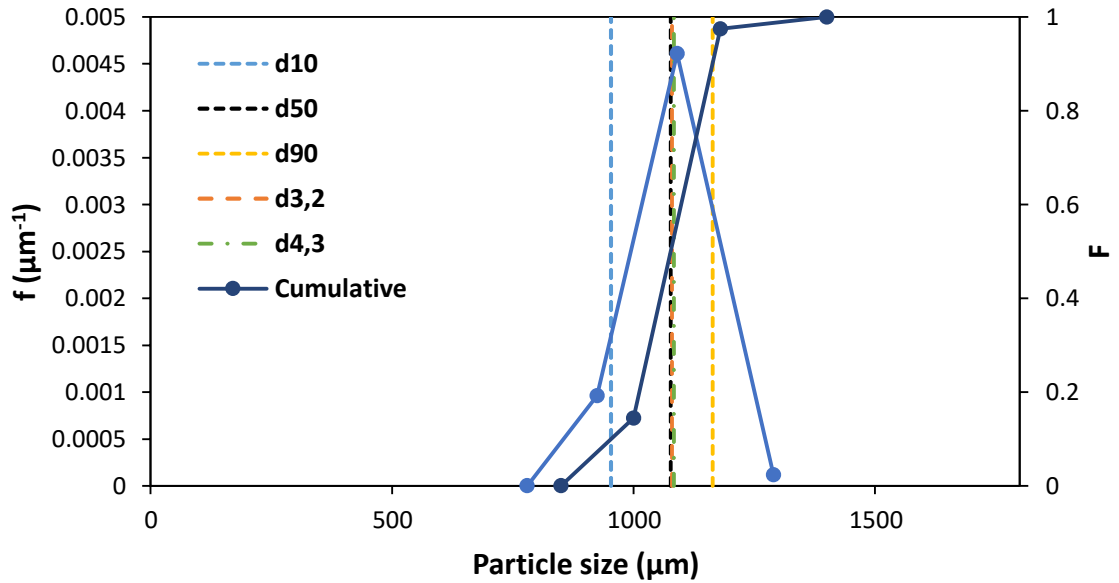


Figure 3-6. Particle size and cumulative particle size distribution of Alumina 2 (Batch 1) obtained via sieve analysis.

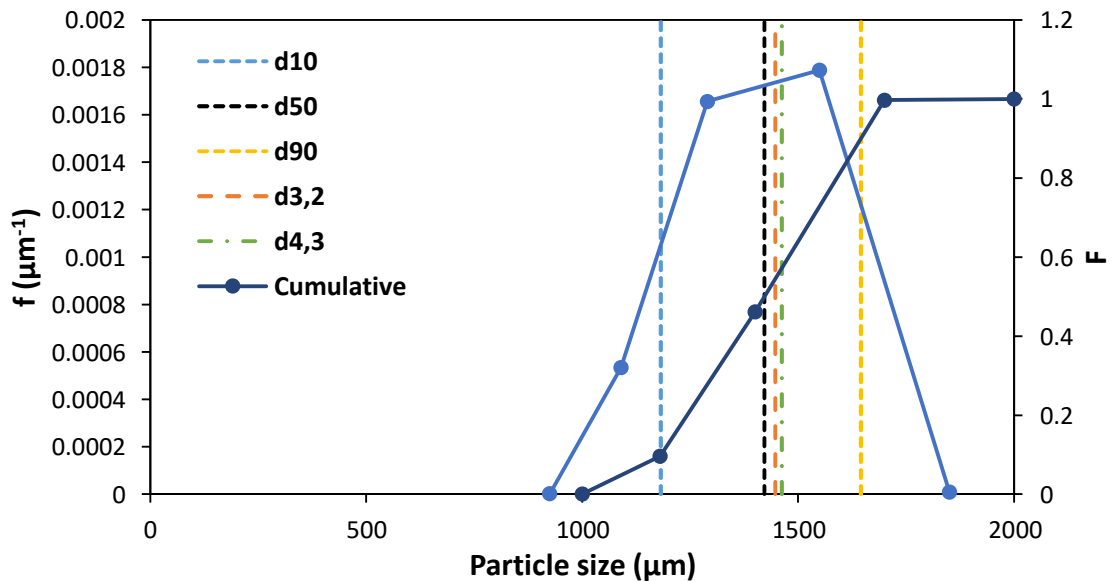


Figure 3-7. Particle size and cumulative particle size distribution of Alumina 2 (Batch 2) obtained via sieve analysis.

3.3.2 Density

The bulk, true and envelope densities are summarised in Table 3-3. The bulk density is the weight of material in a given volume and includes the interparticulate voids. True density is the weight of the solid material divided by the volume of the material minus

any internal pores and space between particles. The envelope density is the weight of a particulate material divided by the volume of the material inclusive of the internal pores.

The true density of the materials was measured using gas displacement on a Micromeritics AccuPyc II 1340 helium pycnometer (Micromeritics, 2018). A chamber of known volume containing the particle, is filled with helium. The helium is then passed to a second container, where the helium's volume is measured. Knowing the volume of gas that should theoretically fit in the chamber, and the volume of gas that actually fit in the chamber, the volume of any additional material in the chamber (i.e. that of the particle) can be calculated. The mass of the sample was measured using a microbalance Toledo XS3DU-series. From this, the density of the material can then be calculated. Helium fills all pores down to one angstrom in diameter, and hence the density calculated is that of the material only, minus any pores (i.e. the true density). The measurement was completed 10 times per sample, and three samples were completed for each material.

Envelope density is a useful parameter, especially in determination of particle porosity, and was measured using a Micromeritics GeoPyc 1360 Microbalance pycnometer. The equipment uses a free-flowing dry powder (*DryFlo*) as the displacement medium. A cylinder (12.7 mm diameter) was filled with approximately 1 cm of the *DryFlo* powder, and the volume was then measured. The sample, after being weighed, was then added to the cylinder and the volume remeasured. The dry powder is unable to enter the pores of the sample but captures the irregularity of the particle shape, thereby increasing the cylinder volume by a volume equal to the particle plus internal and external pores (Micromeritics, 2009). The volume was measured 10 times per sample, and 10 samples were completed for each material. The sample weight was approximately 0.9 g, fulfilling the requirement of the sample occupying 20-50 % of the total sample space.

Bulk density is of particular importance as industries commonly use this value to quantify particles and, therefore, makes comparisons relatively easy. The bulk density was determined by filling a 100 ml glass cylinder with particles using a funnel and recording the mass needed to fill the space. This value can easily be influenced by the

degree to which the sample is compacted and, therefore, every effort was made to simply fill the cylinder to the correct height, and not apply any further external pressure.

As can be seen from Table 3-3, the true density of all the materials is the highest, followed by the envelope density and the bulk density.

Table 3-3. Densities of the three types of particles.

Particles		Density (g/cm ³)		
		True	Envelope	Bulk
Alumina 1		3.56 (0.0029)	3.37 (0.049)	2.09 (0.078)
Alumina 2	Batch 1	2.72 (0.0025)	2.55 (0.17)	1.56 (0.049)
	Batch 2	2.69 (0.0012)	2.64 (0.021)	1.55 (0.067)
Sodium percarbonate		2.09 (0.0064)	1.62 (0.027)	1.16 (0.028)

Although it was originally believed that Alumina 1 and Alumina 2 particles were made from the same material, analysis of the true density shows obvious differences. This suggests that perhaps that Alumina 2 consists of a different structure; a core which has an increased porosity, enclosed by a shell of non-porous alumina. Because of this impenetrable external shell, the Helium gas would not be able to penetrate the internal pores and the AccuPyc true density measurement would also include the internal pores and give a lower density measurement than the true value. Images showing the internal structure of the particles in Chapter 4, section 4.4.2, support this theory.

3.3.3 Porosity

Particle porosity is an important parameter to define; in coating systems, the mass of liquid needed could be affected by the rate at which liquid is able to penetrate the particles. In high porosity particles, less liquid will be held on the surface and, therefore, it is likely that the contact spreading experienced in these systems will be lower than when using non-porous systems. Porosity can be directly measured using porosimetry or calculated using the true and envelope density. The former produces unreliable data due to limitations of the technique; highly spherical samples means the mercury flows

freely into the particles without external pressure being needed, which is a requirement of the technique.

$$\varepsilon = 1 - \frac{\rho_e}{\rho_t} \quad \text{Equation 3-2}$$

The latter, using Equation 3-2, gives the values as seen in Table 3-4. However, as previously discussed, with questions regarding the accuracy of the true density measurements, these values should be treated with caution. If it is assumed that Alumina 1 and Alumina 2 are in fact the same material and the difference in the recorded true density is due to experimental error, the porosity values for Alumina 2 can be recalculated using the true density value of Alumina 1. Both Alumina 2 and the sodium percarbonate are clearly significantly more porous than the Alumina 1 ceramic particles.

Table 3-4. Particles and their calculated porosities.

Particles		Porosity (%)
Alumina 1		5.32
Alumina 2	Batch 1	28.4
	Batch 2	25.8
Sodium percarbonate		24.2

3.3.4 Flowability

Flowability is a measure of how easily a powder can be poured and is important as it can affect the powder regime within a drum. In this instance, the flowability of the particles was captured through a combination of two measurements; the angle of repose and the angle of wall friction. The angle of repose (AoR), or angle of incline, was measured using the powder pile test; i.e. a mass of particles was placed on a horizontal surface, added to the top of the pile using a funnel so as to not adversely affect the shape of the pile. The height of the pile (h) was then measured using a ruler and a camera, along with the x and y diameter, allowing the angle of the incline to be measured. This set-up can be seen in Figure 3-8, with blue representing the particle pile from a top and side view.

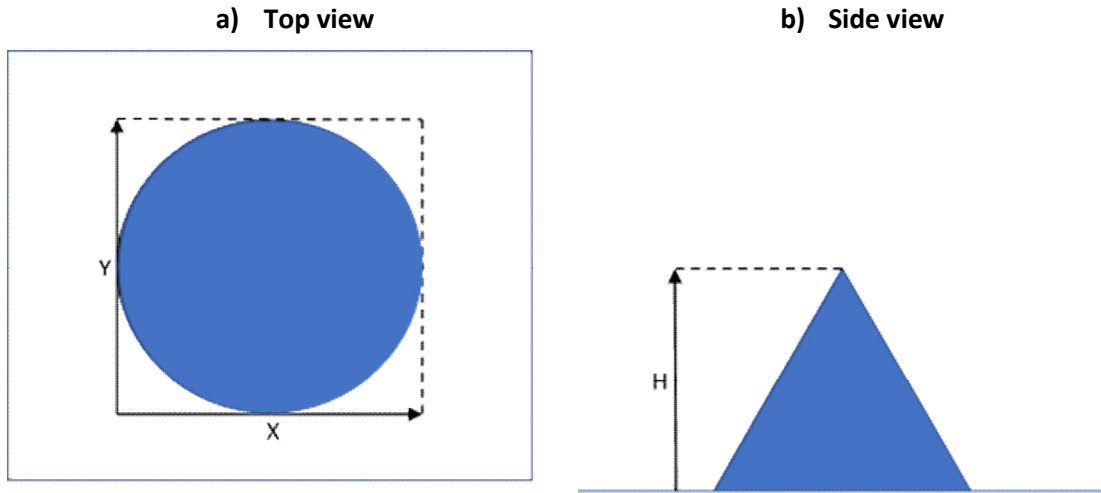


Figure 3-8. Schematic diagram of experimental work for angle of repose a) top view showing the x and y dimensions of the particle pile, and b) side view showing the height (h) of the particle pile.

The angle of wall friction is the angle at which the material starts to slip on an inclined surface of material. The drum used for the coating experiments was upended, and the flat end covered with a small particle pile. The drum was then inclined and the height at which the particles began to slip was recorded. Knowing the length of the drum, the angle at which the particles started to roll can be easily calculated.

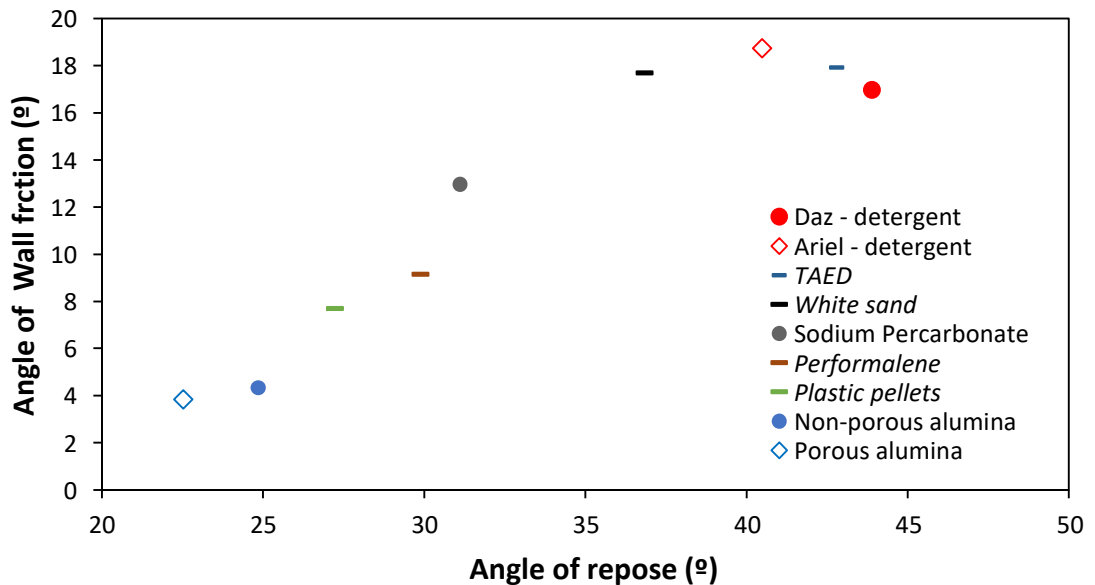


Figure 3-9. Angle of repose and angle of wall friction for all materials used in this research and other materials used for reference.

This was repeated several times for each of the particles, and plotted against the AoR, as can be seen in Figure 3-9. A number of particles not used in this work (shown in *italics* on the legend of Figure 3-9) were also investigated for comparison and understanding of the particle properties on the effect of the wall friction and the angle of repose.

The detergent particles occupy the top right corner of the graph having a high AoR and a high angle of wall friction, suggesting poor flowability. The initial model material (alumina ceramic particles) have both a low angle of wall friction and angle of repose as a result of their smoothness and sphericity. Sodium percarbonate sits half way between the detergents and the model materials and goes some way to more fully representing the powdered detergents in terms of their flowability. Both the angle of wall friction and AoR give some understanding of the surface roughness and particle shape; lower values indicating smoother, better-flowing particles.

These tests were only completed on the steel surface of the drum and did not consider the interaction of the particles with the acrylic drum lid. From visual observations made during the various experiments, the friction seemed to be increased at the acrylic end compared with the steel end.

3.3.5 Scanning Electron Microscopy (SEM)

SEM was used to observe the surface structure of the particles. Electrons are fired at a sample, off which secondary electrons are emitted and collected. These secondary electrons are produced very close to the sample surface and hence a very high resolution image of the sample surface can be obtained. Images of the particles will be shown in the relevant results chapter.

3.3.6 Solution densities

Solution densities were measured using a 25.112 cm³ glass pycnometer, and used in the measurement of interfacial tension. A pycnometer consists of a glass vial with a fitted top which has a thin capillary running through its central vertical axis. In this way, a very specific volume of liquid can be contained; anything which does not fit in the vial will pass through the capillary and can be removed from the top. Densities of all the solutions used in this work are presented in Table 3-5.

Table 3-5. Solution density measurements for PEG 4,000, PEG 10,000, PEG 20,000 and PEG 35,000 (and the equivalent 10 % ethanol / water solutions).

Liquid	Density (g/cm ³)	Std dev (g/cm ³)
PEG 4,000 MW 50 % Solution	1.084	0.0013
PEG 10,000 MW 50 % Solution	1.088	0.0010
PEG 20,000 MW 50 % Solution	1.087	0.0010
PEG 35,000 MW 50 % Solution	1.081	0.0008
10 % ethanol / water solutions		
PEG 4,000 MW 50 % Solution	1.075	0.0006
PEG 10,000 MW 50 % Solution	1.072	0.0013
PEG 20,000 MW 50 % Solution	1.063	0.0005
PEG 35,000 MW 50 % Solution	1.071	0.0004

For each fluid, this process was repeated three times, with the vial being weighed before and after addition of the liquid. As would be expected, the liquids are all very similar in density, with the 10 % ethanol / water solutions being marginally different from the pure water-based systems.

3.3.7 Surface tension measurements

The ability of a liquid to wet or spread on a solid surface is a strong function of the surface tension. This is clearly an important parameter in coating operations, where the aim is to force liquids to spread over solid surfaces. Fifteen measurements were completed for each liquid using the Pendant drop method on an Edmund Optics goniometer (Woodward, 2008). A 22 Gauge needle was used to create the pendant droplets, after which a still frame was taken to analyse the image (Figure 3-10).

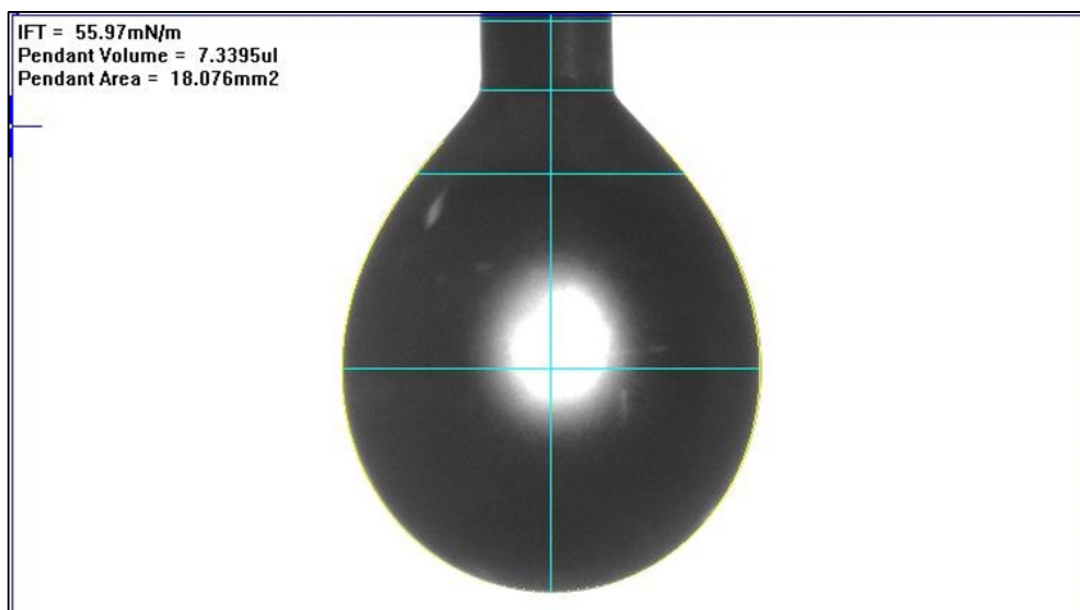


Figure 3-10. Snapshot of pendant droplet (810 mPa.s viscosity PEG solution) used to measure interfacial tension.

The accompanying software utilises the Young-Laplace equation, the densities of the droplets and surrounding fluid (in this case air), and the radii of curvature of the droplets to calculate an interfacial tension. Table 3-6 shows the surface tension measurements, and shows no significant difference is seen between the four coating solutions. The 10 % ethanol / water solutions have very similar surface tension values. All the tests were completed at room temperature (21 °C).

Table 3-6. Surface tension measurements for PEG 4,000, PEG 10,000, PEG 20,000 and PEG 35,000 (and the equivalent 10 % ethanol / water solutions).

Liquid	Surface Tension (mN / m)	S.D. (mN / m)
PEG 4,000 MW 50 % Solution	56.07	0.47
PEG 10,000 MW 50 % Solution	56.14	0.82
PEG 20,000 MW 50 % Solution	56.78	0.81
PEG 35,000 MW 50 % Solution	56.00	0.76
10 % ethanol / water solutions		
PEG 4,000 MW 50 % Solution	55.14	0.55
PEG 10,000 MW 50 % Solution	56.89	0.98
PEG 20,000 MW 50 % Solution	57.74	1.27
PEG 35,000 MW 50 % Solution	55.33	0.99

3.3.8 Solution viscosity measurements

An Anton Paar MCR502 rheometer equipped with a variable temperature Peltier plate and a 50 mm 2° aluminium cone was used for the measurement of the viscosity of the coating solutions. Solution viscosity was measured at 293 K as a function of shear rate, which was varied from 1,000 s⁻¹ to 1 s⁻¹. For all measurements, the distance between the cone and plate was 207 μm. In this method, liquid is held between the bottom stationary plate and the top cone. The shear rate is dependent on a relationship between the velocity of the rotation of the cone and the gap height between the plate and the cone. The shear stress is the force applied divided by the area, and the viscosity is then calculated as the shear stress divided by the shear rate (Barnes et al., 1989).

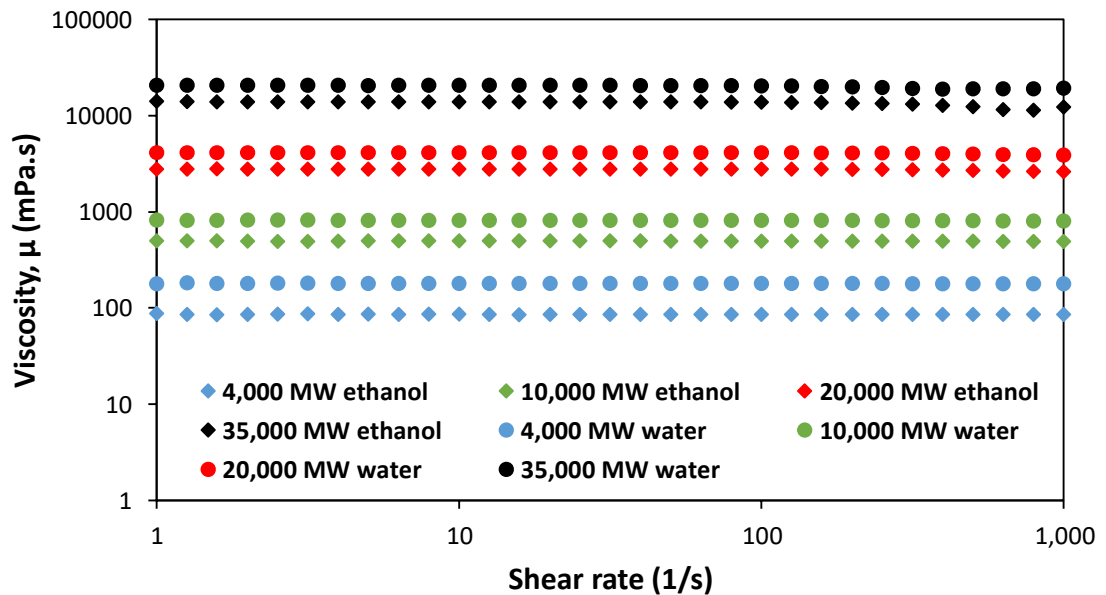


Figure 3-11. Viscosity as a function of shear rate for all solutions. Circles represent the PEG/water solutions used with alumina particles. Diamonds represent the PEG/water/ethanol solutions used with sodium percarbonate particles.

Figure 3-11 shows the viscosities of the 4,000, 10,000, 20,000 and 35,000 MW 50 % PEG solutions over a range of shear rates (summarised in Table 3-7). The results closely match a previous report of PEG solution viscosities by Gonzalez-Tello et al. (1994), and the solutions all behave as Newtonian fluids over the range of shear rates tested. Shear rates in tumbling drums have been shown to be well within this range (Govender et al. (2011); Shi & Napier-Munn (1999)). The PEG solutions made up in 10 % ethanol / water are also shown, represented with diamonds. They match the viscosities of the solutions

without the ethanol and, therefore, comparison between systems which used ethanol and no ethanol can be made.

Table 3-7. Viscosity results for 50 % PEG solutions and 10 % ethanol solutions made with 4,000 MW, 10,000 MW, 20,000MW and 35,000 MW PEGs.

Molecular Weight	4,000	10,000	20,000	35,000
50 % PEG solutions				
Viscosity (mPa.s)	179.3 ± 0.947	810 ± 4.43	4,080 ± 69.9	20,200 ± 630
10 % ethanol solutions				
Viscosity (mPa.s)	102 ± 3.57	512 ± 5.80	2,920 ± 55.7	14,600 ± 528

3.3.9 Solution contact angle measurements

To describe the wetting behaviour of the three different powders, contact angle (CA) measurements were completed using the sessile drop method. Because of the non-flat nature of powders and particles, conventional measurements of contact angle can be difficult, i.e. placing a single drop onto a single particle surface. The powder must first be either crushed and applied to a glass slide as a monolayer (material monolayer method) or compressed into a cake to form a flat surface (tablet method); however, this also presents challenges (Alghunaim et al. 2016). The compression can be irregular, leaving a porous architecture within the cake which can lead to spontaneous drop penetration when droplets are first deposited, giving untrue measurements. Even the compression itself will alter the surface energy of the particles, altering the contact angle. However, regardless of this, the sessile drop technique is still regularly used to report the contact angle.

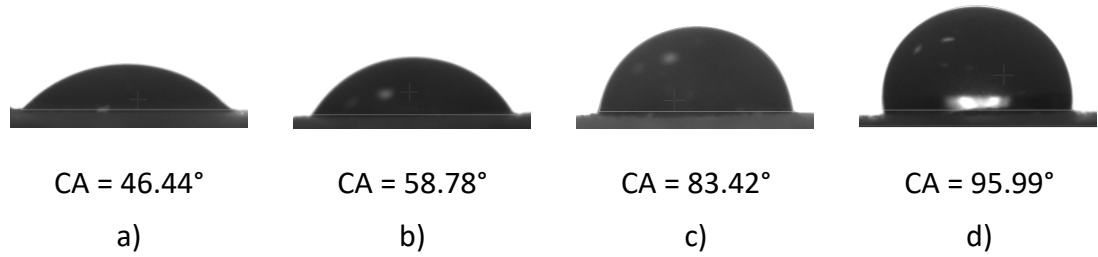


Figure 3-12. Example of the initial contact angles formed on sodium percarbonate tablets using a) 179, b) 810, c) 4,080, and d) 20,200 mPa.s PEG solutions.

The sessile drop tests were completed using a goniometer (Edmund Optics) and FTA 32 software (First Ten Angstroms). 10 g of powder was compacted to form a tablet (diameter 30 mm, height 9 mm) using a Specac pellet press under a compression of 10 mm/min up to a maximum load of 30 kN, with a pre-compression of 10 mm/min up to 1 kN to remove trapped air and prevent tablet fractures. A droplet was then added to the particle surface using a 22 gauge needle (internal diameter 0.413 mm) attached to a 2 ml syringe (Gilmont Instruments). Figure 3-12 shows droplets of the four different viscosity solutions on sodium percarbonate tablets; the contact angle clearly increases with increasing solution viscosity.

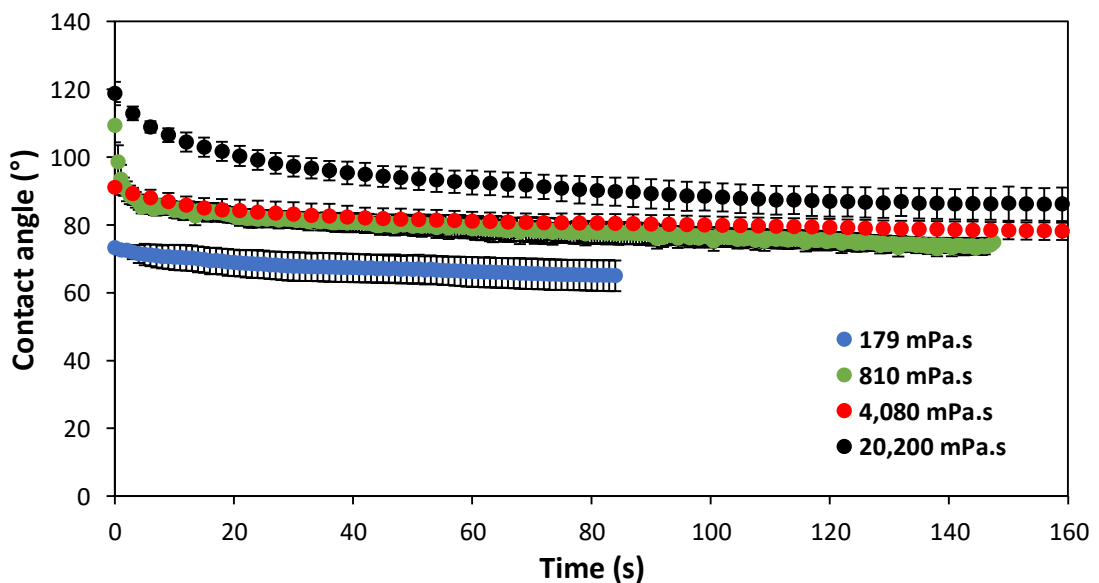


Figure 3-13. Contact angle as a function of time for four different viscosity coating solutions on a powdered bed of Alumina 1 material.

When using Alumina 1 and 2, as the material is extremely strong, forming a tablet to complete the sessile drop measurement is very difficult. Instead, a very thin layer of the

powder was formed using a pestle and mortar to crush the starting material into a fine powder, onto which the liquid drops were deposited. The resulting contact angles can be seen in Figure 3-13 for the Alumina 1 particles and Figure 3-14 for Alumina 2 particles. Alumina 1 has the highest contact angle with each of the solutions of all the particles tested. This could perhaps be because the material was crushed to a different extent resulting in a powder with a different size distribution, or the possibility of a different chemical composition between Alumina 1 and Alumina 2. For these reasons, the difference in contact angle seen between Alumina 1 and Alumina 2 should be treated with caution. After approximately 160 seconds, the droplets began to dry on the particle surface; the contact angle subsequently started to increase again as the droplet receded and its shape distorted, hence data collected after this point is not shown. The rate at which different droplets reach equilibrium can be seen; the lowest viscosity material does not appear to spread at all after the initial deposition, whereas the highest viscosity liquid moves from a contact angle of 118° to approximately 86°, but only after 60 seconds of spreading.

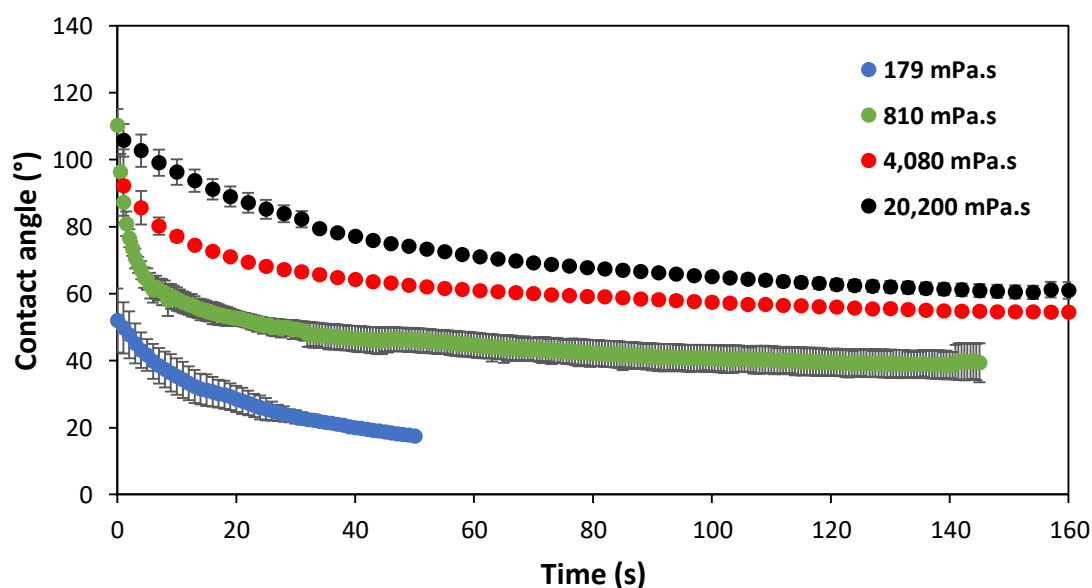


Figure 3-14. Contact angle as a function of time for four different viscosity coating solutions on a powdered bed of Alumina 2 material.

Alumina 2 shows the same behaviour beyond the 160 second time point, however, the spreading rates of the liquid are very different; the lowest viscosity liquid eventually fully wets the particle surface, decreasing from ~50° to ~17°. Because of inaccuracies with

the technology, any measurements of a contact angle below 20° are thought to indicate completely wetting liquids; the software struggles to identify the tangent line when the drop profile is almost flat (Yuan & Lee, 2013). The highest viscosity liquid spreads from ~100° to ~60°, but this process takes nearly 2 minutes.

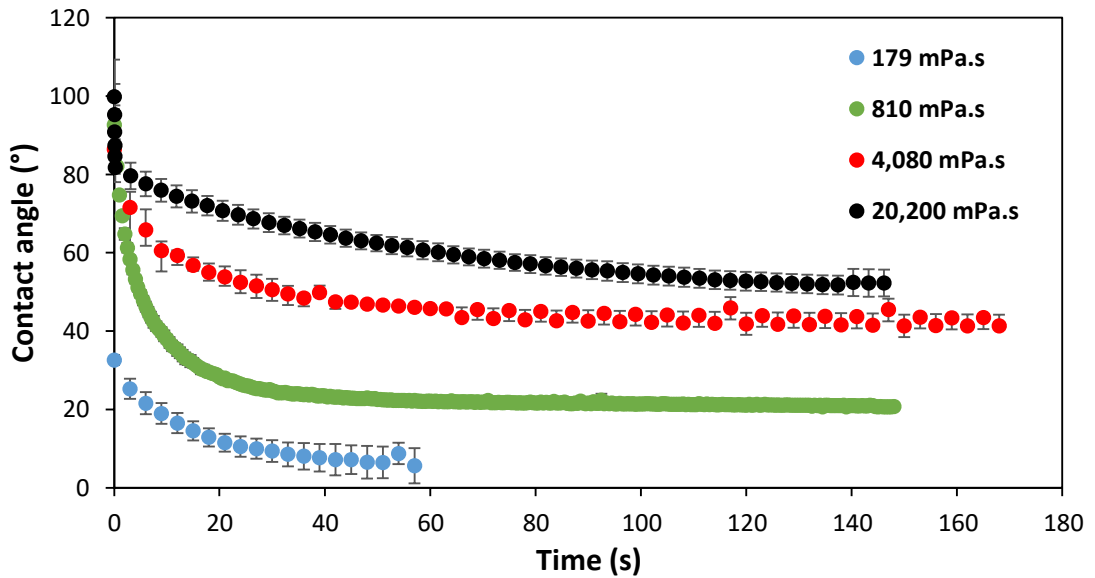


Figure 3-15. Contact angle as a function of time for four different viscosity coating solutions on a powdered bed of sodium percarbonate particles.

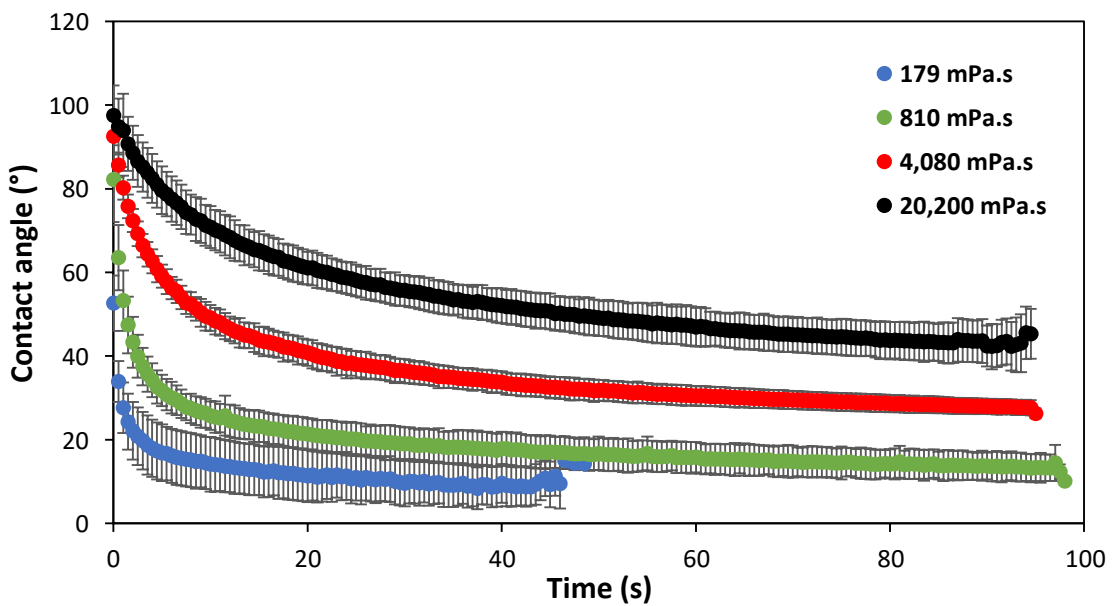


Figure 3-16. Contact angle as a function of time for four different viscosity coating solutions on sodium percarbonate tablets.

Figure 3-15 shows the contact angle of the four PEG solutions on a powdered monolayer of sodium percarbonate. For comparison, and to check the method was giving reliable data, the contact angle was also measured using sodium percarbonate tablets. Figure 3-16 shows the contact angles recorded on the tabletted sodium percarbonate, using the method described above. The liquids all show a very fast rate of spreading (the 179 mPa.s viscosity PEG solution fully wets the particle in 3 seconds), and eventually decreases to equilibrium values lower than those seen for either of the alumina particles. The 179 mPa.s and 810 mPa.s solutions decrease to less than 20° in 3 and 25 seconds, respectively, and the 4,080 and 20,200 reach equilibrium values of ~28° and ~43°, respectively. This very fast spreading rate could be to do with the particle-liquid interaction, but also to do with the method of measurement i.e. the material monolayer method as opposed to the tablet method. The compaction of the tablet provides a more even surface which is less likely to fall foul to liquid penetration than the material monolayer method. Conversely, if the powder is sparse in certain regions, the liquid may interact with the adhesive tape beneath the powder layer, resulting in an increased contact angle. However, even though the recorded spreading rate is different between the two methods, the final contact angles are very similar for the sodium percarbonate using the two methods i.e. material monolayer (Figure 3-15) and the tablet method (Figure 3-16).

3.4 Methods

The experimental system used in this work consisted of a horizontally positioned batch drum, a ball mill (Glen Creston model CA3) and control unit, and an image analysis unit for quantitative determination of coating behaviour. The methodology had been developed by work preceding this research at Sheffield university (Yusof et al, 2018), and is described in the following sections. The quantitative analysis of data has been further developed during this current research and will be described fully in Chapter 4, section 4.3.

3.4.1 Tumbling drum

Four differently sized tumbling drums have been used in this research. The four drums were constructed from stainless steel and made with various dimensions (Table 3-8), and designed to run on two 750 mm (long) by 44 mm (diameter) rollers, separated by 245 mm. The rollers, powered by a ball mill (Glen Creston model CA3), on which the drums ran were rubber coated to reduce noise and prevent slippage. One of the drum end plates was constructed from acrylic and attached with bolts. The acrylic end plate allowed the cross-sectional tumbling regime of the material to be viewed as the experiments were underway. The rollers were powered by a 750 W motor and gave the capability to run the drum in the range of 0 to 95 rpm, generating all of the regimes commonly seen in industrial tumbling drums, e.g. rolling, cascading, cataracting.

Table 3-8. Drum dimensions.

Drum	Diameter (m)	Length (m)	Volume (m ³)	L/D ratio
A	0.11	0.17	0.0016	1.55
B	0.21	0.325	0.0113	1.55
C	0.265	0.408	0.0225	1.54
D	0.315	0.49	0.0382	1.55

For this research, Drum B was the standard drum used for the effect of material characteristics (Chapter 4). The other drums (A, C and D) were used to study the effect of drum size in Chapter 5. Drum A was used as the standard for a large number of sodium

percarbonate experiments in Chapter 6 to reduce material consumption, as material availability was limited.

The general procedure (Figure 3-17) involves coating a percentage of the total mass outside of the drum and adding it to the uncoated mass using a delivery arm (as seen in Figure 3-18), through an orifice in the centre of the acrylic end plate. A fixed 10 % drum fill level was used throughout the work. Based on the material bulk density, the correct mass was weighed to occupy the 10 % desired fill level.

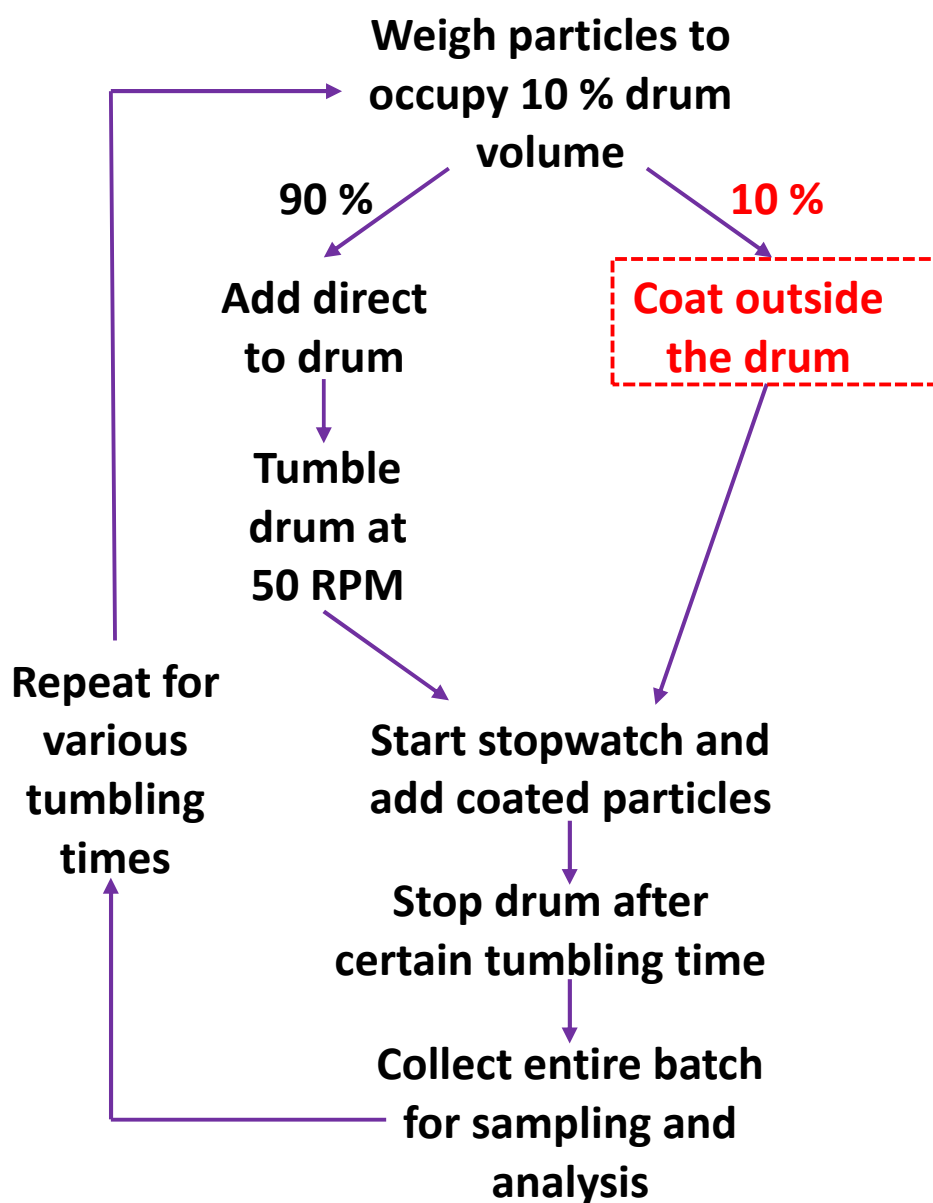


Figure 3-17. Procedure for experimental work.

Of this mass, a further 10 % was removed, placed in a plastic bag and manually agitated with the liquid solution to achieve a homogenous coating. After adding the coating solution to the plastic bag, the time taken to add the particles to the drum was minimised (maximum 1 minute) and kept constant between experiments for consistency.

With the uncoated mass in the drum, the drum was run for 20 seconds to achieve a good particle distribution across the drum length. The coated particles were then emptied from the plastic bag into a delivery arm, and evenly spread across the delivery arm length (Figure 3-18 a). The arm was then inserted into the drum whilst the drum was running (Figure 3-18 b), through a protective cage. The delivery arm was then inverted (Figure 3-18 c), emptying the coated particles into the drum whilst simultaneously starting the timer. After the desired time, the drum was stopped. The drum contents were emptied into a tinfoil tray and left to dry for 24 hours, minimising further particle agitation as far as possible to prevent liquid spreading outside the drum. To mitigate the effect of contact spreading experienced between the particles as a result of emptying the drum and transporting the particles, an experiment to obtain a 'background' point (i.e. no tumbling), was conducted to obtain a starting point for the series of tumbling times. The uncoated particles were placed in the drum and, without tumbling, the coated particles were emptied into the drum. Subsequently, the whole batch was removed.

After the drying time, the entire sample was emptied from the tinfoil tray and riffled using a chute splitter, which separates the sample into two smaller roughly equally sized samples with the same distribution as the original sample. One half of the first riffle was then passed through the splitter again, further producing two smaller samples. The sample was riffled 4 times until a sample size of approximately 20 g was remaining. Studies have shown that the chute splitting method of powder sampling produces samples with relative standard deviations of approximately 1 % (Allen (2013)) and, therefore, the author confidently believes that the samples obtained via the chute splitter are representative of the bulk.

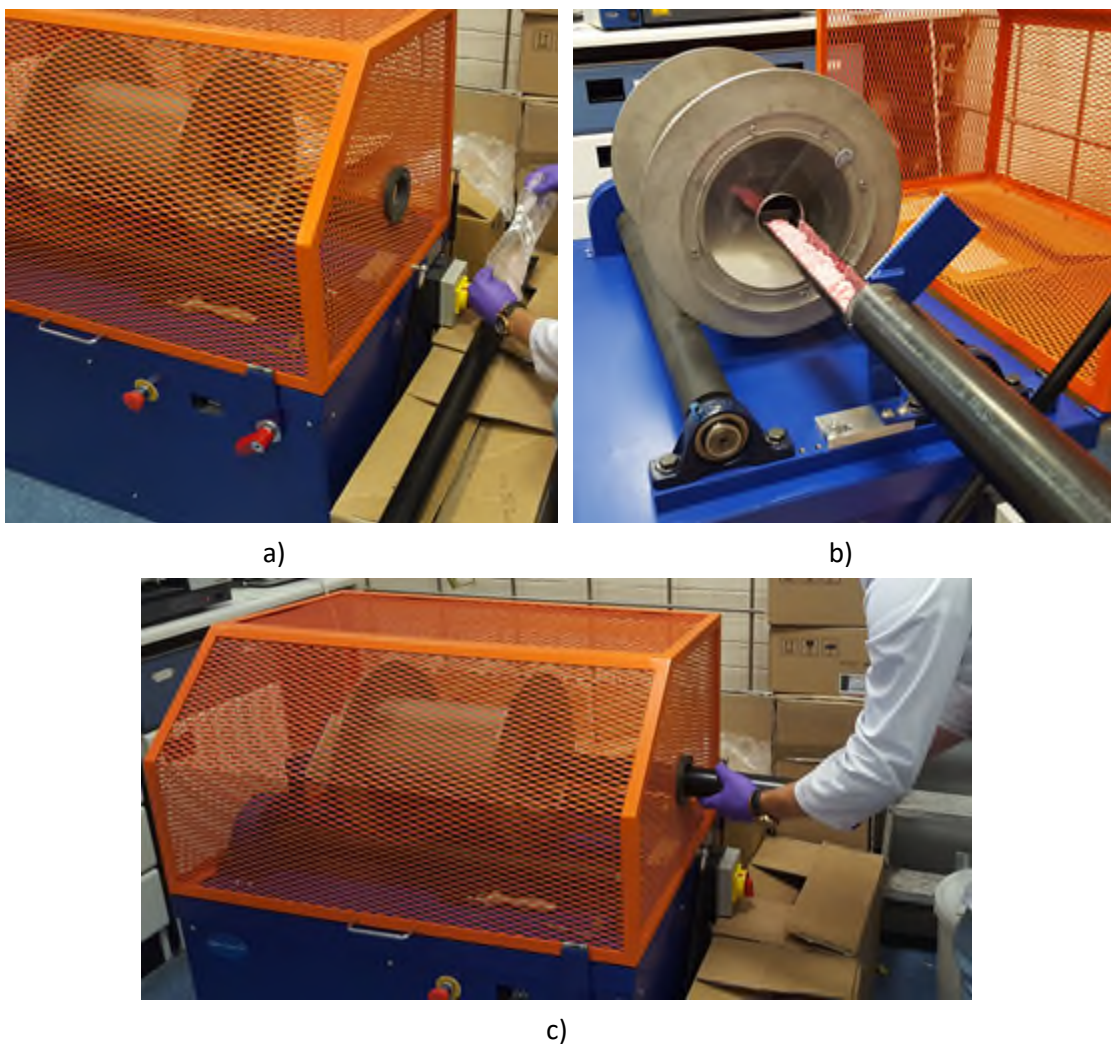


Figure 3-18. Images showing various stages of the methodology a) application of particles into delivery arm b) coated particles evenly distributed along delivery arm length and inserted into drum, c) inserting delivery arm into drum through protective cage and inverting.

Prior to image analysis, one side of a 5 cm by 5 cm piece of sticky black vinyl (Anchor Magnets, UK) was removed and was attached to a larger supporting piece of card. The second side of black vinyl tape was then removed and was placed face down in the riffled particles, entirely coating the surface of the vinyl with particles. The particles were then placed under a Navitar 12X zoom lens (Image Optics, UK) with a LGT.19.MF2d LED dome diffuser light (Haishu Honyu Opto-Electro Co., Ltd), Figure 3-19) and four 24-bit colour images were captured using a Luminera Infinity 3 camera and Infinity Capture software. Each image was of a different corner of the black vinyl, with every effort made to not image the same particles more than once. Four vinyl pieces were made per time point, resulting in 16 images per time point for analysis. The number of images taken (16) was

chosen arbitrarily; it was believed that this number provided a large enough sample size but was not overly time intensive.



Figure 3-19. Experimental set-up of Luminera Infinity 3 camera with a Navitar 12X zoom lens and diffuse lighting.

3.4.2 Colourimetric image analysis

The addition of acid red dye meant the appearance of coating solution on a particle was easily identifiable from the captured images. Colourimetric image analysis, looking at the distribution of the liquid over the particles, was used to quantify the coating uniformity, and was expressed as a coefficient of variation (CoV).

Approximately 3,000 particles were analysed at each time point to determine the CoV red. The total number of particles used per experimental point can be approximated at 1,200,000, using the known bulk mass and averaged individual particle weight. The sample analysed therefore represents approximately 0.25 % of the total mass. Although this value is small, greater numbers would have been logistically infeasible, increasing

both material consumption and data analysis time, and it has been previously shown (Allen, 2013) that the sampling method has been proven to provide representative samples.

Image analysis was used to give a quantitative determination of the coating variation between a batch of particles. To calculate the coefficient of variation and, therefore, the extent of contact spreading, the mean red value of the particles (ζ) in each image and the standard deviation (σ) found in this value must be known (Equation 3-3).

$$CoV = \frac{\sigma}{\zeta} \times 100 \quad \text{Equation 3-3}$$

Labview was the computer programme used to determine these values. The software produces a RGB value for each of the particles in the sample, which can be averaged over 16 images to give representative colourimetric information for each time point. Three 8-bit arrays of pixel values for red, green and blue intensities constitute each 24-bit image. A value ranging from 0 to 255 denotes the recorded colour intensity of red, green and blue light in that portion of the image. For a purely white bead, the intensities of red, green and blue will each be 1/3. Where the red dye concentration is applied, the intensity of the red value will be greater than 1/3. To collect the information relating to red dye intensity, several steps were taken in the Labview software (Figure 3-20). The particles were first separated from the background and converted to an 8-bit greyscale image. The particles were then separated from their neighbours using an erode and dilate function, and labelled using a Labview function. The RGB intensity fractions can then be calculated from the pixels in each particle, and averaged to give a value for each particle. This process is then repeated for each of the 16 images per time point, and the mean red value is then averaged for each time point. Along with the standard deviation of the mean red value, the coefficient of variation in the sample can then be calculated using Equation 3-3. More detailed information about the Labview software and analysis process can be found in Yusof et al. (2018).

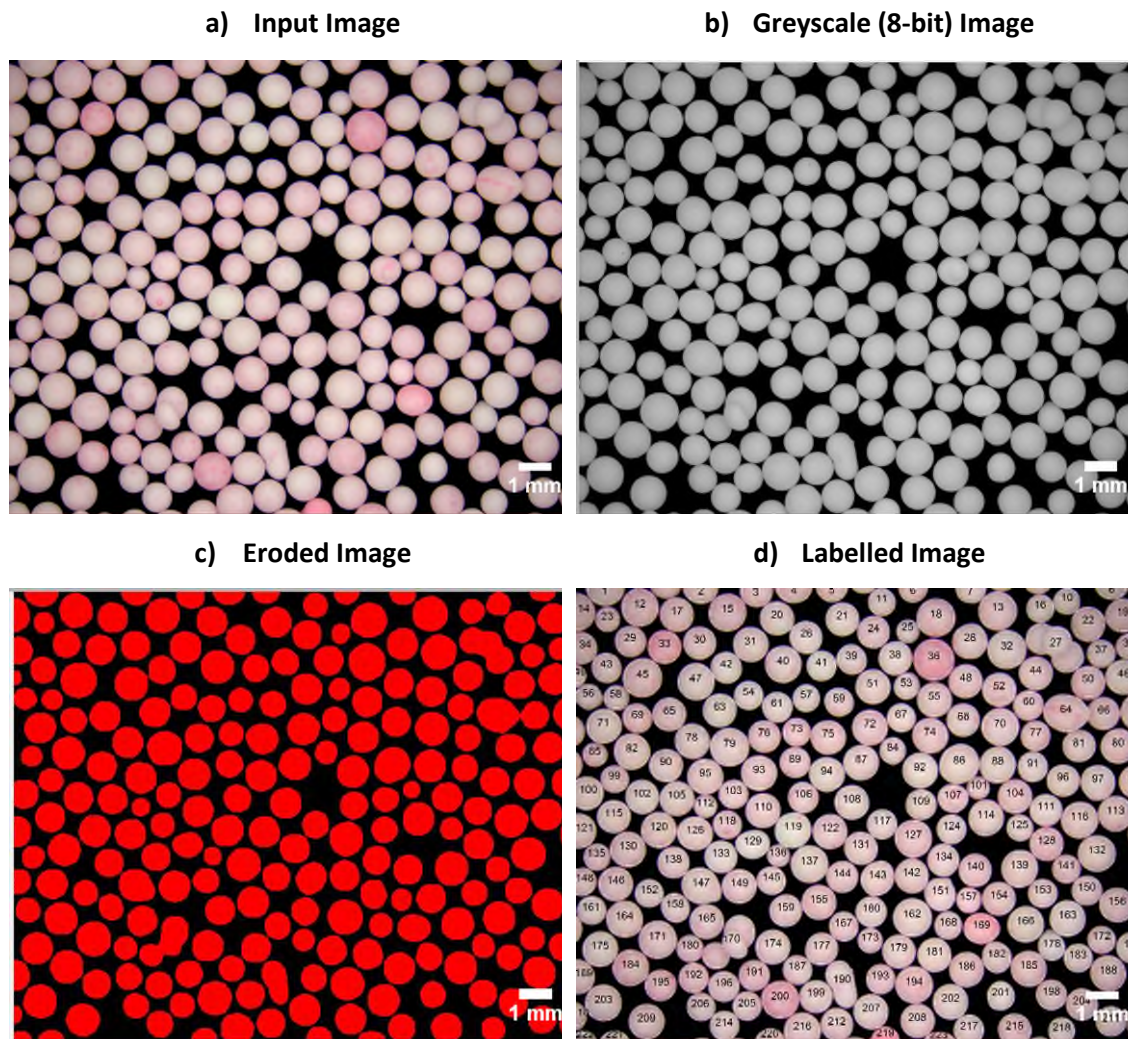


Figure 3-20. Labview process for obtaining labelled image (example using Alumina 1 particles).

3.5 Summary

Methods for characterising the particles and coating liquid properties have been discussed in this chapter. The experimental methodology has been described, along with the method for image analysis and determination of the coefficient of variation; the parameter which will be used to quantify coating behaviour. Chapter 4 will use the information generated by LabView and outline the method used for processing the raw data to give quantitative information about the coating process.

4. Mechanistic understanding of contact spreading: Study of material properties

A data processing methodology is developed and presented with which the extent of contact spreading in a system can be quantified. The effects of material characteristics are considered; two types of ceramic alumina particles with different densities are investigated with three different viscosity coating solutions. Contact spreading is observed for all the systems investigated and the asymptotic values indicate nearly uniform inter-particle coating is achieved. There is very little difference seen between the coating rates of the two alumina types when using a low viscosity solution. The difference between the two types of alumina is greatest when using the highest viscosity coating solution. The energy of low-density particle-particle collisions was not enough to overcome the high viscosity liquid bridge forces holding the particles together, and therefore the liquid could not as easily redistribute around the particle bed. As with high density, these systems do eventually reach an asymptotic condition. However, many more collisions are necessary, and therefore a much longer coating time is required to achieve the same coating uniformity. A viscous collision number is proposed which relates the viscous component of the liquid bridge force to the collision energy of particle-particle interactions and appears to correlate well with the time for coating completion.

4. Mechanistic understanding of contact spreading: Study of material properties

4.1 Introduction.....	88
4.2 Methods.....	89
4.3 Data processing: Typical data set.....	91
4.4 Results.....	97
4.5 Discussion.....	108
4.6 Conclusions.....	121

4.1 Introduction

Material characteristics are well known to effect the properties of a wide variety of powder processing operations (Li et al. (2013); Abberger et al. (2002); Kan et al. (2017)). They include a number of different properties (particle density, porosity, surface roughness, liquid viscosity, drop size etc.) which are ultimately a result of the material formulation. Many authors have looked at the effects of various material characteristics in spray coating systems (Wesdyk et al. (1993); Wnukowski & Setterwall (1989); Turton & Cheng (2005); To & Davé (2015)). However, none have looked at the impact of material characteristics on the effect of contact only liquid spreading, specifically in tumbling drums. Most studies focus on the interaction of the particle droplet and the powder as the latter passes through the spray zone. In tumbling drums, although the spray zone is important, the particles are constantly interacting with each other and the liquid moves through a series of liquid bridge formations and ruptures. For this reason, it is important to understand how these material characteristics effect the contact only spreading of liquid between particles, and identify systems where contact spreading is likely to have a large influence. The main objectives for this chapter are;

- Identification of a suitable model material
 - The ideal model material should have uniformity across individual particles and across the entire particle batch in terms of colour, shape, size and material composition. This level of particle uniformity ensures only the intentional change of variables will be affecting the results.
- Development of analytical methodology
 - This should allow quantification of the rate of coating as well as the extent of the coating achieved, and provide an easy method for comparison of these values across different systems.
- Development of mechanistic understanding of contact spreading within coating processes
 - Specifically, quantify the effect of liquid viscosity and material density on contact spreading, and identify systems in which contact spreading will be dominant.

In this chapter, development of the data processing methodology is presented which allows the effect of various parameters on the coating rate to be investigated. A study into the effect of using three different viscosity coating solutions and two types of alumina particles of different densities will be presented.

4.2 Methods

As described in Chapter 3 (Materials and Methods), a suitable model material was identified which would allow the comparison of material characteristics. Two types of alumina ceramic particle were used; Alumina 1 and Alumina 2, with Alumina 1 having the higher density. This allows for the investigation of the effect of particle density. These alumina particles are white, allowing easy image analysis, have a narrow size distribution, and do not chemically react with coating PEG solutions. Throughout this work, polyethylene glycol (PEG) of varying molecular weights are used. This allows for an investigation into the effect of viscosity. Solutions of PEG in distilled water were dyed with acid red to allow for colourimetric analysis to quantify the coating (as described in Chapter 3, section 3.4). Tables 4-1 and 4-2 give a brief recap of the relevant material properties; particles and liquid, respectively. It should be noted that two different batches of Alumina 2 were supplied. Particle characterisation revealed these to have slightly different particle sizes, but showed that the densities were very similar.

Table 4-1. Particle properties for Alumina 1 and Alumina 2.

Property	Alumina 1	Alumina 2	
		Batch 1	Batch 2
Envelope density (g/cm ³)	3.37 ± 0.049	2.55 ± 0.17	2.64 ± 0.021
d ₁₀ (µm)	868	954	1,182
d ₅₀ (µm)	1,034	1,077	1,422
d ₉₀ (µm)	1,155	1,164	1,646

Drum B (length 0.325 m, diameter 0.21 m) was used for all of the experiments, with a 10 % drum fill level and run at 50 rpm (cascading regime). All the experiments completed here were done so *without a spray component*, isolating the contact spreading mechanism. Before being placed in the drum, 10 % of the total particle volume was

coated as evenly as possible with a PEG solution outside the drum. The remaining 90 % of the uncoated particles were added to the drum and tumbled to allow the cascading flow regime to develop. The coated particles were then added to the uncoated particles in the tumbling drum through the use of a delivery arm inserted into a hole in one of the drum ends, and a stopwatch was simultaneously started.

Table 4-2. Coating liquid properties.

Property	Molecular weight (Da)		
	4,000	20,000	35,000
Viscosity (mPa.s)	179.3 ± 0.947	4,080 ± 69.9	20,200 ± 630
Surface tension (mN/m)	56.1 ± 0.47	56.8 ± 0.81	56.0 ± 0.76

After a certain tumbling time, the drum was stopped and the entire batch was removed for sampling and analysis. To do this, a tray was placed underneath the drum and the drum as carefully tilted to allow the particles to run into the tray below. Undoubtedly some further agitation will have occurred, however this was minimised as far as possible by using a smooth motion. A fresh batch of particles was then added to the drum, and the procedure was repeated for a number of different tumbling times, ranging from zero seconds through to 1,000 seconds. After allowing each batch to dry, the particles were riffled using a chute splitter to obtain a representative sample of approximately 20 g. Sixteen images were then taken of each sample, and Labview software was used to determine the RGB value of each individual particle. As was described in Chapter 3, Section 3.4.2, the coating variability is quantified by the coefficient of variation seen in the red value, and is calculated as the standard deviation seen in the red intensity value divided by the mean red intensity value. The coefficient of variation was calculated for each of the 16 images and averaged to give a representative value for each time point. The CoV can then be plotted as a function of tumbling time to give an indication of how the coating uniformity changes with time. A more detailed description of the methodology and imaging analysis can be found in Chapter 3 (Materials and Methods), Section 3.4. Table 4-3 gives a full list of all the experimental combinations of particles and liquids used in this chapter.

Table 4-3. Particle and liquid coating combinations used in this chapter.

System	Materials	
	Particles	Solution viscosity (mPa.s)
1	Alumina 1	179
2	Alumina 1	4,080
3	Alumina 1	20,200
4	Alumina 2 (Batch 1 & 2)	179
5	Alumina 2 (Batch 2)	4,080
6	Alumina 2 (Batch 2)	20,200

Once the experiments were completed, a methodology was devised to treat the data and extract useful parameters. The development of this data processing is described and detailed in the following section.

4.3 Data processing: Typical data set

Here, a typical data set is presented. The frequency distribution is first presented, followed by the data showing the coefficient of variation as a function of time. Subsequently, an exponential function is fitted to the data, allowing a coating rate constant to be determined. This will allow for the comparison of coating behaviour between experiments. The data set used is a combination of Alumina 1 particles with a 179 mPa.s viscosity PEG solution. This data processing has been completed for each of the experiments.

4.3.1 Frequency distribution data

Figure 4-1 shows the coating evolution for a typical experiment. Each distribution on the graph represents one time point in an experiment, and shows the number of particles as a function of the % red value. For perfectly white particles, the % red value would be a straight vertical line at 33.3 %. The raw particles, represented by the grey line in Figure 4-1, show a slight deviation around this value, indicating they are nearly perfectly white in colour. At the early stages, for example 0 seconds, there is a shift in the % red toward higher values, and a much larger distribution, between approximately 34 – 43 %. This

curve is made up of a large, relatively narrow peak at approximately 34.5 %, representing the bulk of the material which has not contacted the red coating liquid, and a long tail from approximately 35 – 43 % red, representing the smaller number of particles which are coated in various levels of coating agent (expressed as intensities of red dye detected).

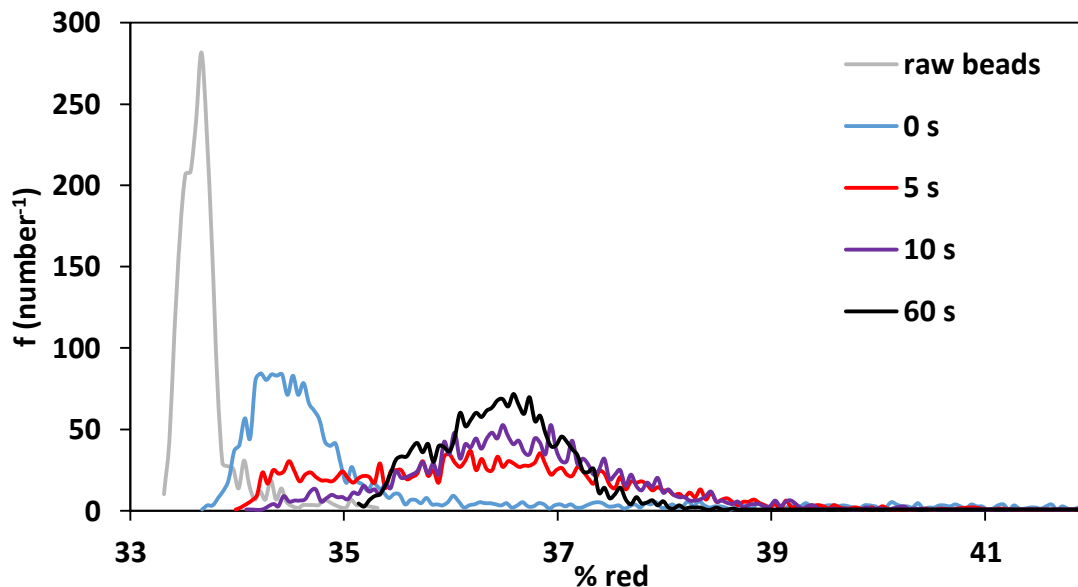


Figure 4-1. Coating evolution of Alumina 1 particles with 179 mPa.s viscosity PEG solution at various time points (some time points removed for clarity).

As the experiment continues, the coating distribution is skewed towards higher red % values with narrower peaks. This is indicative of a more uniform coating across the particles. Ideal coating would show a tall narrow peak at a high % red intensity, representing a body of particles that are homogeneously coated. The 60 second distribution, the longest time this system was run for, shows the real life distribution of the previously described ideal. The peak is not narrow, but is a more uniform, normal distribution with the mode value being approximately 36.5 %, a significant increase from the 0 second time point. The data from each of these distributions can be expressed as a single value and plotted as a function of time, as is described in the next section.

4.3.2 Coefficient of Variation

In this study, the coating uniformity is quantitatively expressed as the coefficient of variation (CoV); a lower CoV value indicating greater coating uniformity. From the

frequency distribution graphs previously described, both the mean red value and the standard deviation for each data set is calculated. The CoV is then defined as;

$$CoV = \frac{\sigma}{\zeta} \times 100 \quad \text{Equation 4-1}$$

where ζ is the mean value of red intensity values, and σ is the standard deviation of the data. This information - the mean red, the standard deviation, and the CoV % red - are all shown in Table 4-4. The standard deviation of the data decreases with time whilst the mean red stays relatively constant, meaning that the CoV % value decreases with time as the coating becomes more uniform. The slight increase that is seen in the mean red value is clearly seen on Figure 4-1; the zero and 2 second distributions have peaks at obviously lower values. This observation will be addressed further in the Discussion, Section 4.5.1.

Table 4-4. Example of data obtained from Labview.

Time (s)	Mean red	Standard deviation red	COV % red
0	0.356	0.0257	7.23
2	0.359	0.0188	5.57
5	0.364	0.0137	3.78
7	0.364	0.0135	3.71
10	0.367	0.0106	2.90
15	0.367	0.00837	2.28
20	0.366	0.00749	2.04
25	0.365	0.00754	2.07
30	0.364	0.00645	1.77
35	0.364	0.00624	1.71
40	0.363	0.00628	1.73
45	0.363	0.00660	1.82
50	0.363	0.00674	1.86
60	0.365	0.00660	1.81

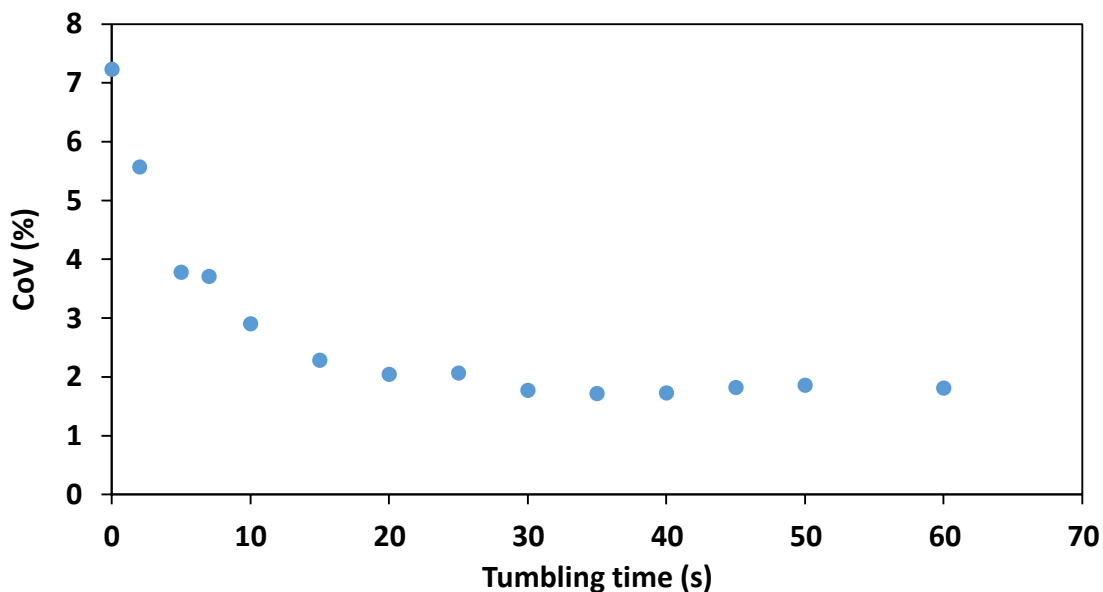


Figure 4-2. CoV (%) red values as a function of tumbling time.

Figure 4-2 is a graphical representation of the CoV as a function of tumbling time; the initial CoV % red value represents the greatest degree of coating variation in the experiment, as the liquid has not had time to spread between the particles. As the time increases, the drum tumbles and induces particle interactions, causing contact liquid spreading. This results in a decrease in the variation in the coating as the liquid becomes more evenly distributed. The data also appears to decay to some non-zero value following an exponential function. This does not agree with the findings of Freireich et al. (2011) who showed that for systems including a spray component, the inter-particle coefficient of variation would constantly decrease with time, eventually approaching homogeneity. Unlike the systems employed by Freireich et al. (2011), here, no spray component has been used and only a finite volume of liquid is introduced; it is therefore unlikely that the CoV will approach 0 in such a short period of time. Although for most of the experiments completed an asymptote does exist, the value is not constant across different experiments, indicating some coating systems are capable of producing inherently better homogeneity than others. Currently no methodology exists for predicting the CoV based on either drum or material properties, or a combination of the two. However, several authors have proposed models to predict the intra-tablet asymptotic coating limit for non-spherical tablets (Freireich et al. (2015); Pei & Elliott (2017)).

4.3.3 Coating rate constant

To determine a coating rate constant, an exponential function of the form given in Equation 4-2 was fitted to each data set. The coating rate constant describes the rate at which the value of the coefficient of variation decays from its initial starting value to the value at the asymptote.

$$COV(t) = CoV_{\infty} + (CoV_0 - CoV_{\infty}) * \exp(-\lambda t) \quad \text{Equation 4-2}$$

Here, CoV_{∞} represents the coefficient of variation when the system reaches equilibrium, CoV_0 is the initial variation in the system, t is the tumbling time, and λ is the coating rate constant. Determination of the equilibrium CoV value, CoV_{∞} , is extremely important. As can be seen from Figure 4-2, the variation in the coating reaches some asymptotic value after approximately 30 seconds, after which the value is considered constant. Therefore, to more accurately determine the CoV_{∞} value, an average CoV value is taken from the experiments run at the longest times, and where no further decrease of the CoV is seen. In this example, the values used to determine the average final value are those found at 40, 45, 50 and 60 seconds. The average CoV_{∞} value clearly depends on the number of CoV values and, therefore, ensuring enough experimental points at the asymptote have been completed is essential.

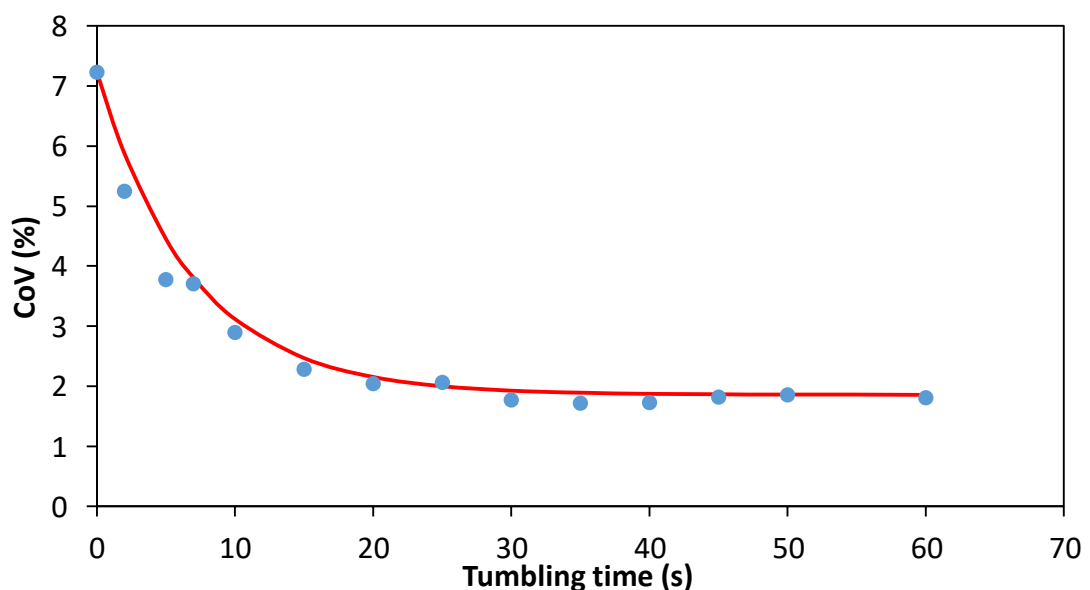


Figure 4-3. CoV (%) red values fitted using the exponential function, Equation 4.2.

Figure 4-3 shows a graphical representation of the CoV % red values with an exponential function (Equation 4-2) fitted. A rapid decay leads into an asymptotic plateau after approximately 30 seconds. By fitting the exponential function, it is then possible to compare coating behaviour under different experimental conditions, in the rate at which the data decays, the time at which the asymptote is reached, and the value of the asymptote itself.

4.3.4 Exponential function optimisation

The coating rate constant was initially determined by fitting a curve which looked to best represent the data. This was subsequently improved using an excel solver function. To determine the goodness of the exponential fit to the experimental data, an R^2 value was calculated. An average value of the CoV data was first determined; the sum of the squared differences between this value and the y values (SS_{Tot}) were calculated using Equation 4-3. SS_{Reg} is the sum of the squared difference between the CoV data points and the predicted y values (Equation 4-4). The R^2 value is then calculated using Equation 4-5, giving a fitting value between 0-1.

$$SS_{Tot} = \sum_{i=1}^n (CoV_{Average} - Y(solver)_i)^2 \quad \text{Equation 4-3}$$

$$SS_{Reg} = \sum_{i=1}^n (CoV_i - Y(solver)_i)^2 \quad \text{Equation 4-4}$$

$$R^2 = 1 - \left(\frac{SS_{Reg}}{SS_{Tot}} \right) \quad \text{Equation 4-5}$$

By using a solver function in Microsoft Excel to minimise the sum of the SS_{Reg} value by altering λ , a R^2 value as close as possible to 1 can be found, forcing the best fit in each case and giving a fitting constant which best represents the data set. This method has been used to determine exponential decay constants for all of the experiments conducted. The coating rate constant for this system is 0.174 s^{-1} ($R^2 = 0.988$).

4.3.5 Time to reach asymptote

As the function fitted to the data is exponential in nature, it will by definition never truly reach the asymptotic value towards which it is tending. The tumbling time associated with this value would therefore be infinite. To overcome this issue, the time to completion is taken as the point at which 98 % of the coating was completed. This can be written mathematically as;

$$CoV(t) = 0.02(CoV_0 - CoV_\infty) + CoV_\infty \quad \text{Equation 4-6}$$

By rearranging Equation 4-2, and substituting in Equation 4-6, the following equation for the time of complete coating can be reached (Equation 4-7);

$$t_c = \frac{\ln \left[\frac{0.02(CoV_0 - CoV_\infty) + CoV_\infty - CoV_\infty}{CoV_0 - CoV_\infty} \right]}{-\lambda} = \frac{\ln 0.02}{-\lambda} \quad \text{Equation 4-7}$$

In this case, 22.48 seconds is found to be the time at which the coating process can be considered 'complete'.

4.4 Results

The aim of the work in this chapter is to understand the mechanisms affecting the contact liquid spreading, with particular focus on the impact made by different viscosity liquids and different material densities. The following section shows data which quantifies these effects, images to give a qualitative understanding, and images of fractured particles to determine if any liquid pore penetration has occurred. The experiments were all completed in the same drum and at the same rotational speed.

4.4.1 Coating behaviour: Effect of material density and coating liquid viscosity

Firstly, the lowest viscosity solution was used to coat the particles, the data for the CoV as a function of time being presented in Figure 4-4.

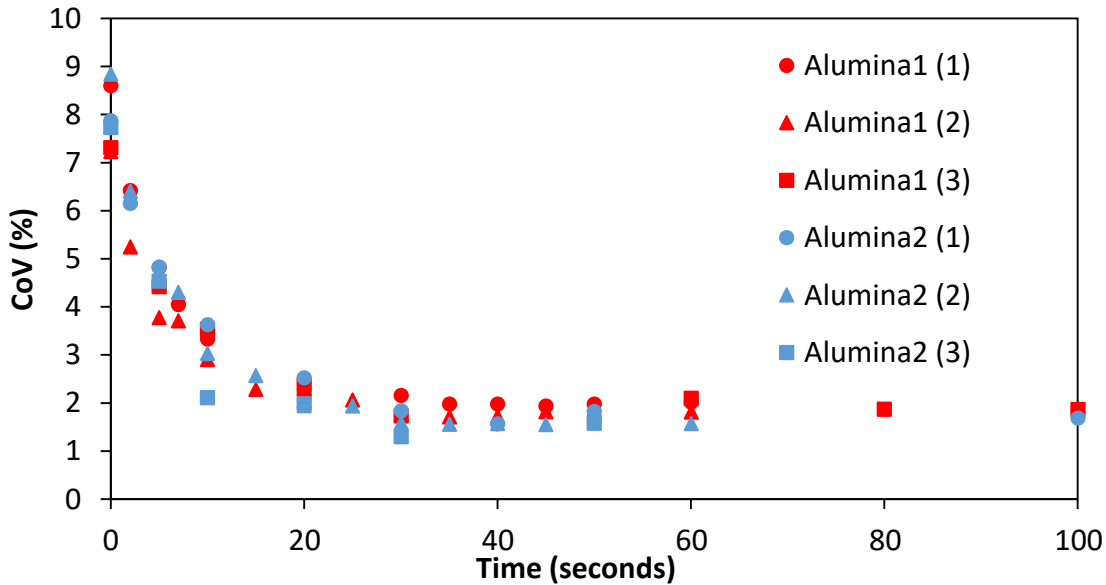


Figure 4-4. CoV as a function of time for the 179 mPa.s viscosity coating solution for Alumina 1 (red) and Alumina 2 (blue).

Here, the differences seen between the Alumina 1 and Alumina 2 particles is minor. Both sets of data decay at a similar rate, and decay to a very similar asymptotic value (2 %) after approximately 25 seconds. As was previously discussed, the Alumina 2 particles came in two different batches and although all the other material properties were the same, the size did vary slightly (refer to Table 4-1, Section 4.2). In Figure 4-4, both the batches have been used. There is no quantifiable effect of the slight difference in particle size. (It should be noted that batch 2 of the Alumina 2 particles were only used due to a limited availability of batch 1. A more detailed study of the effect of particle size is given in Chapter 6.) There are, however, slight differences in the initial CoV value, perhaps due to slight differences in the colour of the solution, the colour of the particles, or the sampling. To make comparisons of the different data sets easier, all the data was normalised per Equation 4-8;

$$CoV_{Norm} = \frac{CoV(t) - CoV_{\infty}}{CoV_0 - CoV_{\infty}} = \exp(-\lambda t) \quad \text{Equation 4-8}$$

Normalisation allows a coating rate constant which can be compared across data sets to be determined, and allows for a quick examination of how variables affect the coating. Figure 4-5 shows the normalised coefficient of variation as a function of tumbling time for the 179 mPa.s viscosity solution. The red data points represent experiments

completed using the heavier Alumina 1 material, and the blue data points represent the lighter Alumina 2 material. The dashed lines are the best fit exponential decay curves for each of the data sets. The coating curves for this low viscosity solution are extremely similar for both the light and heavy material.

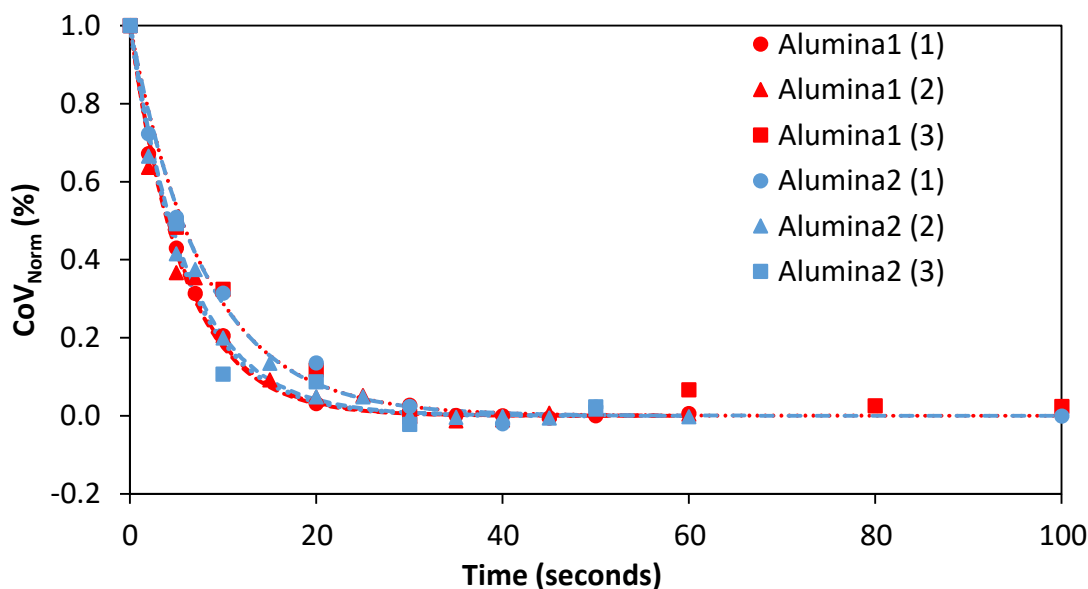


Figure 4-5. Normalised CoV as a function of time for the 179 mPa.s viscosity coating solution for Alumina 1 (red) and Alumina 2 (blue). Exponential functions for each data set are displayed as dashed lines.

Figure 4-6 uses the 4,080 mPa.s viscosity coating solution and shows a marked difference in the coating rate between the Alumina 1 and Alumina 2 particles. The denser Alumina 1 reaches a CoV_{∞} value after approximately 75 seconds, whereas the lighter Alumina 2 reaches an asymptote only after around 400 seconds. The rate at which the two systems approach this asymptotic value is very different (Figure 4-7), the lighter particles take much longer to become uniform. The combination of the material density and solution viscosity clearly influences the liquid contact spreading behaviour. The CoV_{∞} value for both of these systems is approximately 1 %, slightly lower than that seen with the 179 mPa.s coating solution viscosity. Inconsistencies in the number of repeats, both here and throughout the rest of this research, are due to limited material availability.

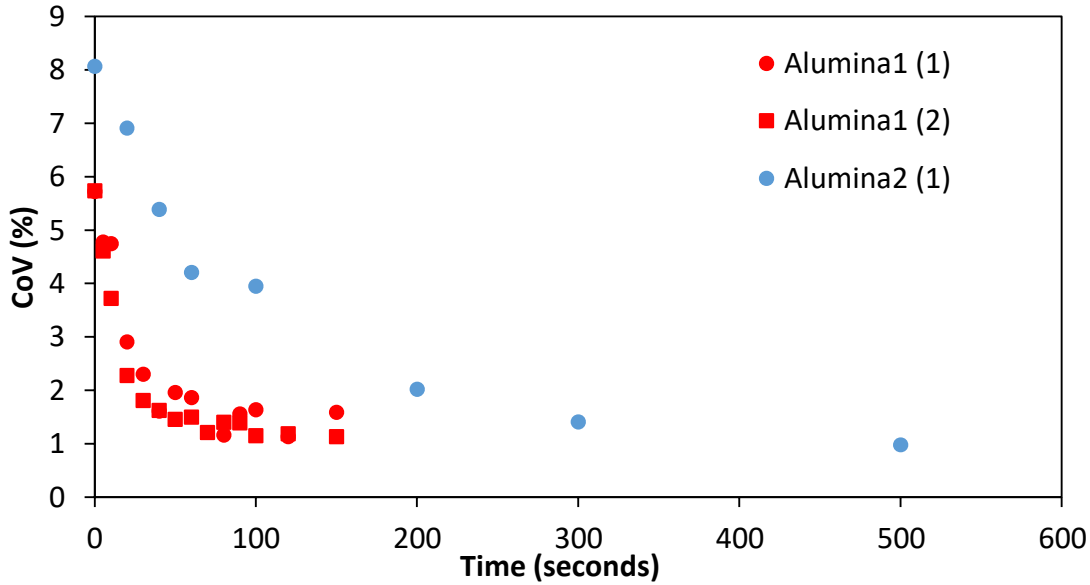


Figure 4-6. CoV as a function of time for the 4,080 mPa.s viscosity coating solution for Alumina 1 (red) and Alumina 2 (blue).

Figure 4-7 shows the normalised CoV data for the 4,080 mPa.s solution as a function of the tumbling time. The rate of decay is drastically different; the heavy Alumina 1 coating much faster than the light Alumina 2.

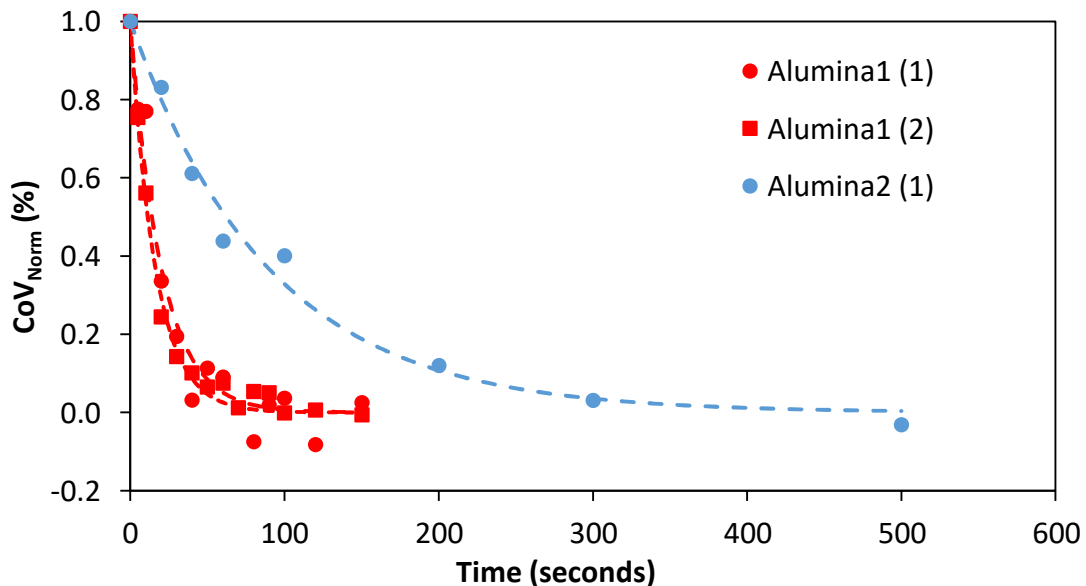


Figure 4-7. Normalised CoV as a function of time for the 4,080 mPa.s viscosity coating solution for Alumina 1 (red) and Alumina 2 (blue). Exponential functions for each data set are displayed as dashed lines.

Figure 4-8 shows the results using a high viscosity coating solution (20,200 mPa.s) and shows a much greater difference when comparing the effects of Alumina 1 and Alumina

2 particles, further reinforcing the effects seen in Figure 4-6. The rate at which the CoV decays differs drastically; the Alumina 1 particles reach an asymptotic value after approximately 140 seconds, whereas the Alumina 2 particles take around 1,000 seconds (even at this long time it is hard to know if the asymptote has been reached). The Alumina 1 particles asymptote at a CoV value of approximately 1.1 %, yet due to the nature of the Alumina 2 experiments, this value is also hard to determine. If an average of the two data points at the 1,000 second mark is taken, the Alumina 2 experiments can be thought to asymptote at approximately 1.7 %, considerably higher than that of the Alumina 1 experiments. The variation seen when using the Alumina 2 particles is likely due to the fact that the particles are not very dense and become easily agglomerated when using such a high viscosity solution. When and if agglomerates form and break can have a large impact on the variation of the system.

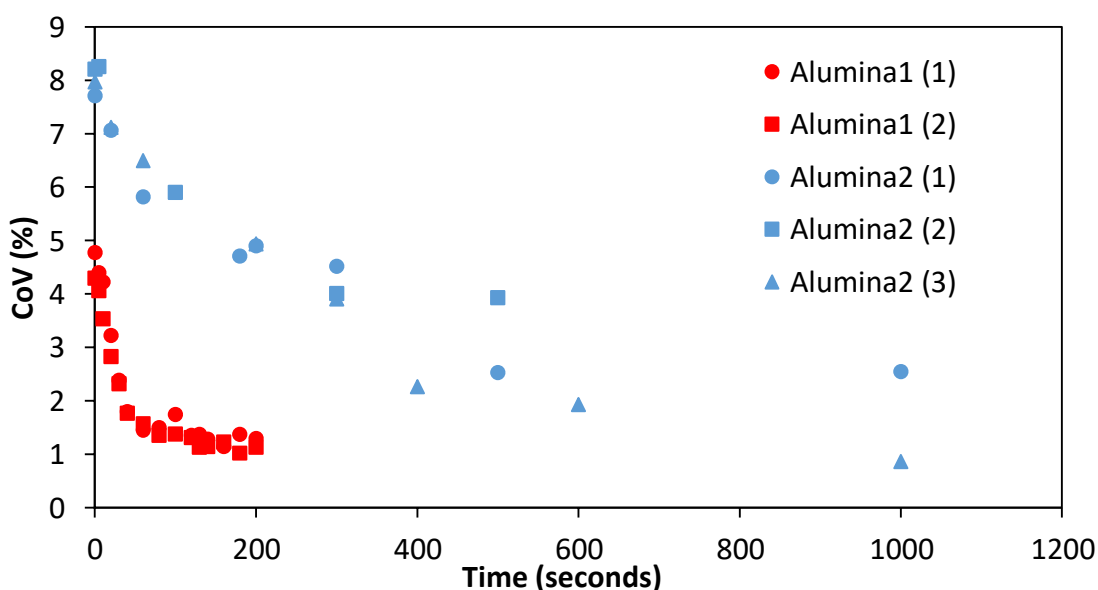


Figure 4-8. CoV as a function of time for the 20,200 mPa.s viscosity coating solution for Alumina 1 (red) and Alumina 2 (blue).

Figure 4-9 shows the normalised coefficient of variation as a function of tumbling time for the highest viscosity coating solution; 20,200 mPa.s. The difference between the two materials becomes more pronounced with increases in solution viscosity; much longer coating times are seen for the lighter Alumina 2 with increases in solution viscosity. Because of the variation in the asymptotic value for the Alumina 2 particles using the 20,200 mPa.s solution, there appears to be large variation in the coating rate curves, as

seen in Figure 4-9. Regardless of this, the rates are still considerably slower and the completion times considerably longer than for any of the other systems investigated.

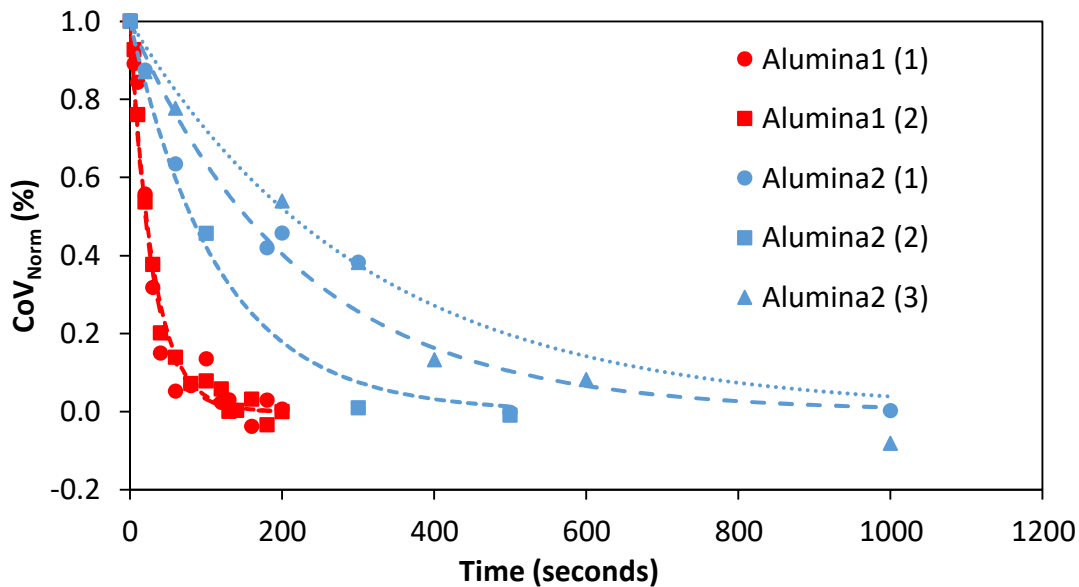


Figure 4-9. Normalised CoV as a function of time for the 20,200 mPa.s viscosity coating solution for Alumina 1 (red) and Alumina 2 (blue). Exponential functions for each data set are displayed as dashed lines.

Figure 4-10 (a) shows firstly how the coating rate constant decreases with increased solution viscosity, for both Alumina 1 and Alumina 2. The 179 mPa.s solutions show no difference in the coating rate constant between Alumina 1 and 2, whereas for both the 4,080 mPa.s and 20,200 mPa.s, the coating rate constant is considerably smaller for Alumina 2. Figure 4-10 (b) shows how the CoV_{∞} value for the Alumina 1 particles decreases slightly with increased viscosity, whereas the Alumina 2 material shows no identifiable trend. Many more experimental repeats would be needed to more accurately determine the asymptotic value and reduce the error, allowing any trends to be more easily identified.

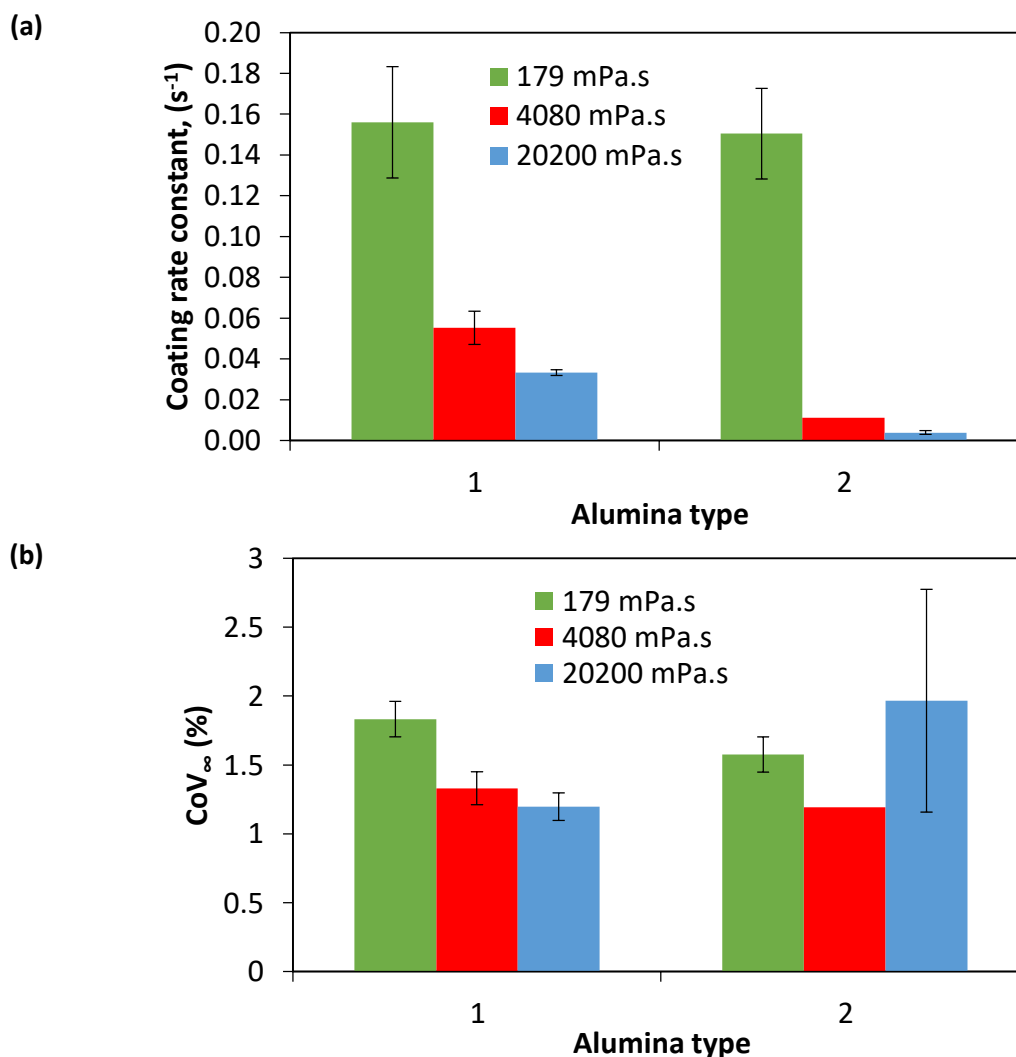


Figure 4-10. a) Coating rate constants (s^{-1}), and b) CoV_{∞} (%), for all combinations of the Alumina 1 and Alumina 2 material and the three coating solutions. Blue = 179 mPa.s, Orange = 4,080 mPa.s, Grey = 20,200 mPa.s.

Figure 4-11 shows images of Alumina 1 and Alumina 2 particles coated with a 179 mPa.s solution and shows the corresponding CoV values at differing time points. The CoV values decrease with time, showing an increase in coating uniformity which agrees with quantitative data. Qualitative analysis of the images in Figure 4-11 suggests a difference in intra-particle coating variability, seen as intense spots of red dye more noticeable on the Alumina 2 particles; this type of analysis is recommended for future work but is outside the scope of this work. If the red dye is being absorbed into the pores, the concentrated red dye spots visible on the Alumina 2 particles could be a result of concentrations of PEG solution around the pores when there is no more room for excess

fluid. Alternatively, the spots could be a result of liquid bridges forming and being ruptured in transit.

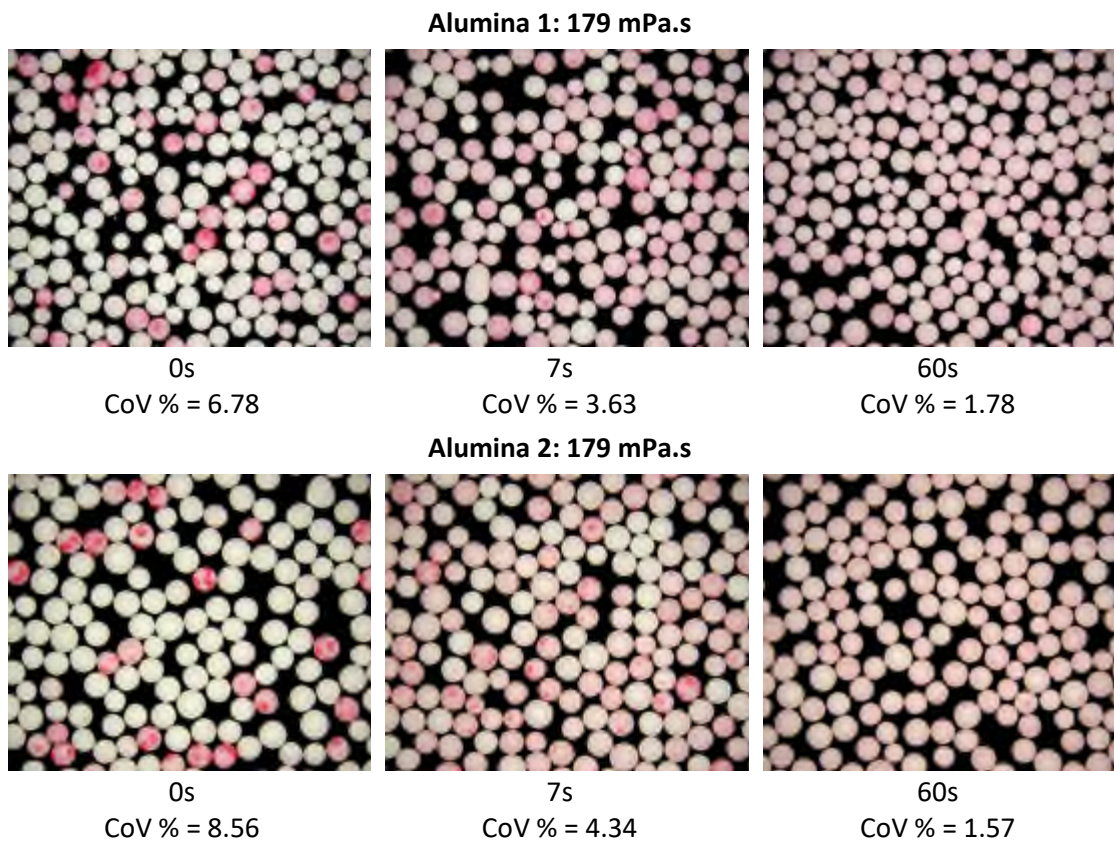


Figure 4-11. Images and corresponding CoV (%) red values of Alumina 1 and Alumina 2 particles at varying time points (179 mPa.s).

Figure 4-12 shows the difference seen between the two alumina materials when using the highest viscosity coating solution. The presence of localised red spots are still visible at early time frames, and do appear to persist long after they have disappeared for the low viscosity solution with some being visible up to 300 seconds after the coating process has started. This could be due to a liquid property; the low viscosity solutions perhaps wet the particle surface more effectively, meaning as a liquid bridge ruptures, the liquid is quickly redistributed around the particle of the surface. Whereas, with high viscosity solutions, bridge ruptures could result in pockets of liquid sitting on the particle surface. It is interesting to note that in the cases of both the high viscosity and the low viscosity, the concentrated red spots are visible at longer times for the Alumina 2 particles. This could be a result of either differences in the formation of the liquid bridges themselves or differences in the surface structure of the different Alumina.

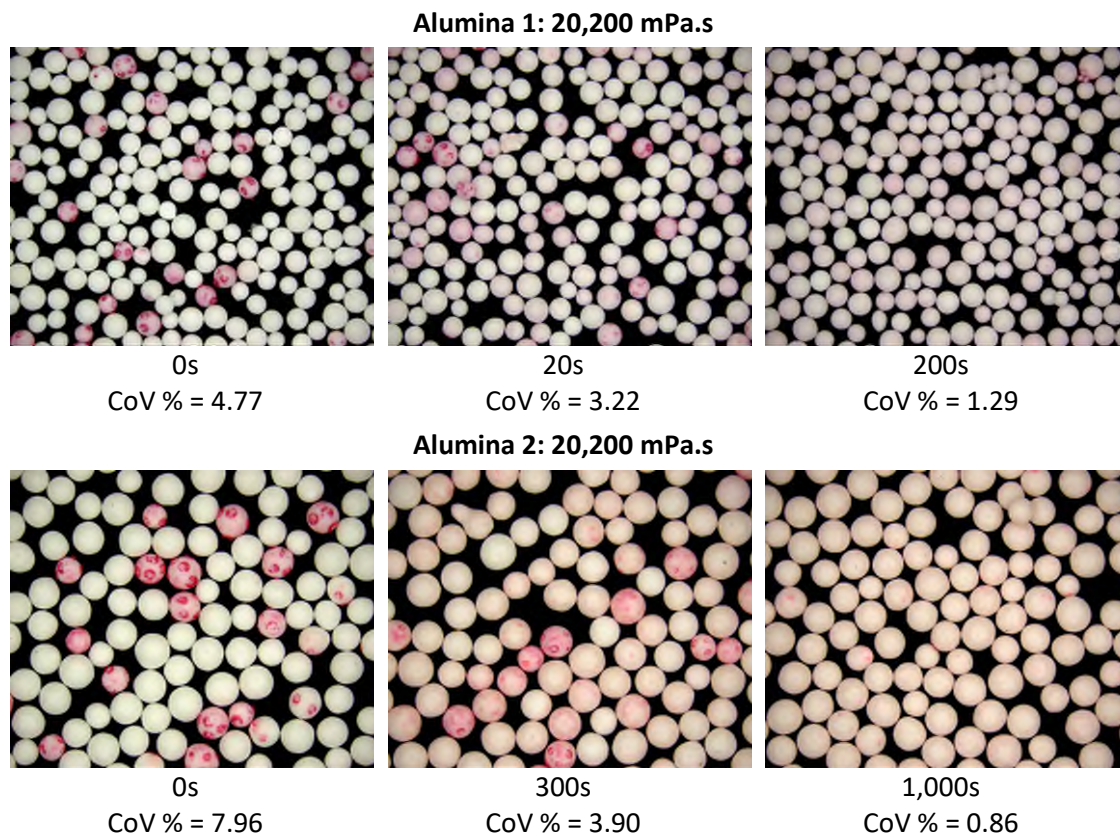


Figure 4-12. Images and corresponding CoV (%) red values of Alumina 1 and Alumina 2 particles at varying time points (20,200 mPa.s).

4.4.2 Analysis of fractured particles

To further investigate the localised red spots seen in Figure 4-11 and Figure 4-12, and understand to what extent the particles are being penetrated by the coating solutions, several particles were fractured to investigate the internal structure and to try and observe dye ingress. In order to fracture the particles, a piece of black vinyl with a number of particles attached was placed inside a sealable, see-through plastic zip-lock bag and an external force was applied to the particles using a hammer. It was not possible to quantify the exact force used, however, every effort was made to ensure a consistent approach was taken to fracture the particles. Firstly, several particles from experiments using both low and high density alumina coated with a range of viscosities were fractured, but no ingress was seen. To ensure this was not a function of the small dye percentage in the coating solutions, a solution of 10 % red dye was added to several particles of both Alumina to make any dye ingress more visible. Images of Alumina 1

coated with a 10 % red dye solution are shown in Figure 4-13, and Alumina 2 are shown in Figure 4-14.

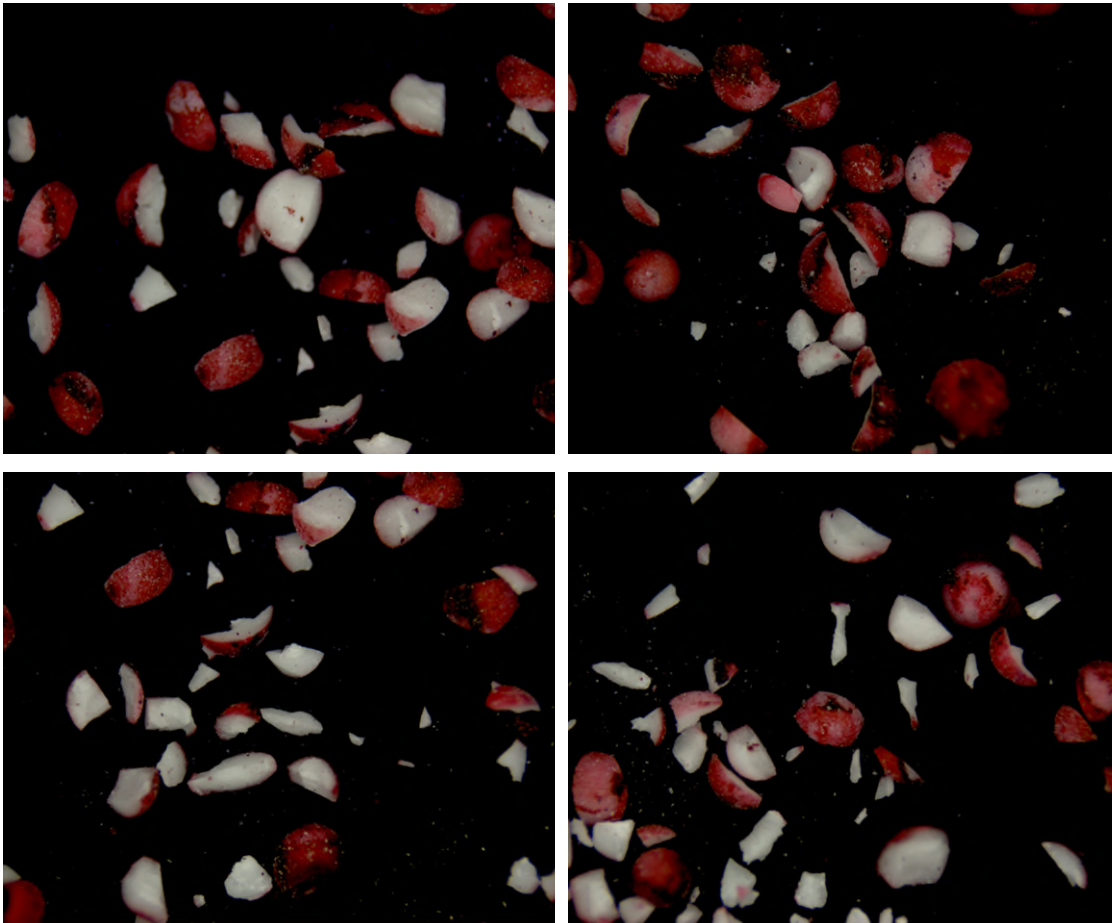


Figure 4-13. Fractured Alumina 1 coated with a 10 % red dye solution.

Although the ingress of the liquid is hard to numerically quantify, none is visible for Alumina 1, as evidenced in Figure 4-13. This suggests the material is highly non-porous, or if pores do exist, they are too small for the liquids to penetrate. This does suggest that the localised red spots are remnants of liquid bridge ruptures. In Figure 4-14 the lighter Alumina 2 particles, coated with 10 % red dye solution, have been crushed and imaged. There again appears to be no visible ingress. However, it is worth noting that the fracture pattern of the Alumina 2 particles is entirely different from that of Alumina 1; there are many more smaller fragments than seen with Alumina 1. This fracture pattern does suggest a degree of porosity; however, the lack of visible dye ingress could suggest that again the pores are too small for the liquid to penetrate. Alternatively, as was proposed earlier (Chapter 3, Section 3.3.2), the composition of the particles could be that of a

porous internal structure surrounded by a solid material. Evidence for this can be seen in Figure 4-14 where the particles tend to maintain their external structure very well; many small shards seem to be generated from the inside but the external shell breaks into several large structures, much like the Alumina 1 particles. If Alumina 2 is indeed porous, the microstructure of the pores and / or their location away from the particle surface is preventing the uptake of liquid and, therefore, porosity is not influencing the liquid contact spreading.

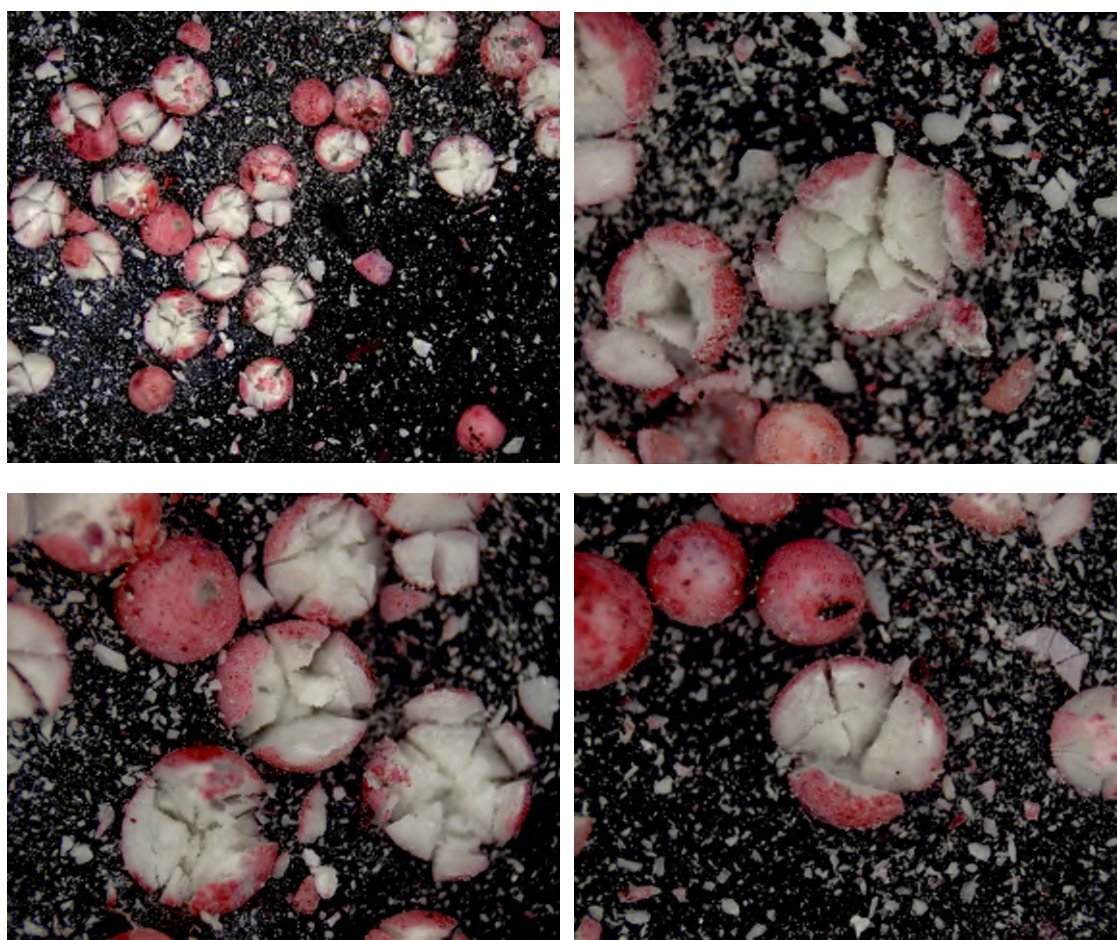


Figure 4-14. Fractured Alumina 2 coated with a 10 % red dye solution.

However, when attempting to reuse the Alumina 2 particles, they first had to be washed. This proved very difficult, with a lot of solution being retained on the particle surface, suggesting that either the shell is indeed porous compared to the Alumina 1 particles (some areas of nano-sized pores at the particle surface), or the particle has an increased surface roughness which in turn increases liquid retention. To investigate the surface structure, SEM was employed. Figure 4-15 shows a clear difference between the surface

structures; Alumina 2 (image b) appears to have a far greater number of peaks and valleys which increase the roughness.

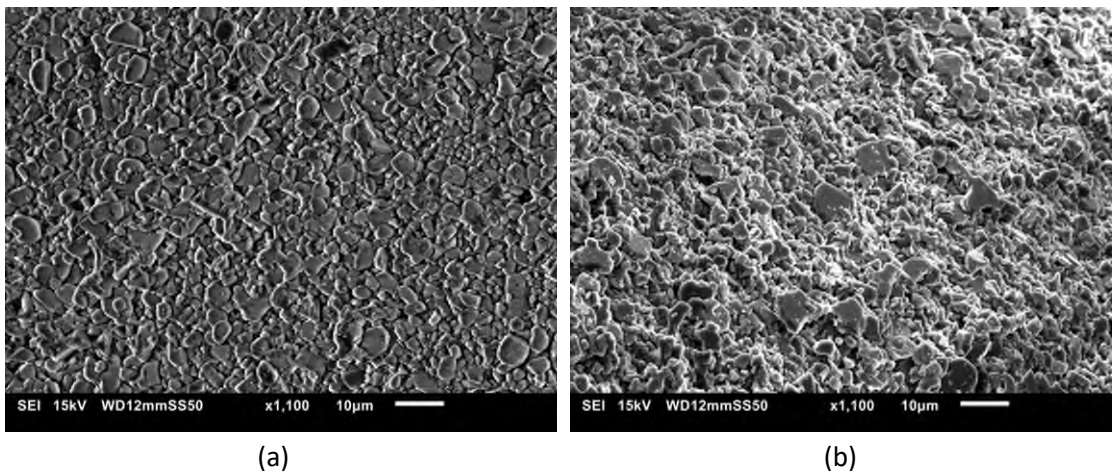


Figure 4-15. SEM images taken at 1,100 magnification showing the surface structure of a) Alumina 1 and b) Alumina 2.

As well as the surface roughness, if the shell and core structure hypothesis is correct, the porosity values calculated in Table 3-4 (Chapter 3) will be lower than the real values for Alumina 2. Here, the porosity values have been recalculated assuming the Alumina 2 has the same composition as Alumina 1, and therefore has the same true density values. These corrected values can be seen in Table 4-5, and are now much greater.

Table 4-5. Recalculated porosity values.

Material		Recalculated porosity (%)
Alumina 2	Batch 1	28.4
	Batch 2	25.8

4.5 Discussion

It has been shown that contact spreading does occur and can be an important mechanism for the transfer of liquid in powder processing units. Here, two effects have been investigated for their impact on contact spreading; the effect of particle density and the effect owing to the liquid viscosity. Both effects ultimately impact on the liquid bridges which form between particles, and which are the primary method of liquid distribution around the particle bed. The liquid viscosity impacts the strength of these

bridges; increased viscosity results in increased bridge strength and, therefore, slower liquid spreading. The particle density impacts on the probability of liquid bridge formation; higher density means increased chance of particles redounding upon collision and, therefore, faster liquid spreading. These two phenomena will be discussed to give an understanding of the mechanisms involved in contact spreading in section 4.5.2. Furthermore, an evaluation of the model and analysis method will be presented in the following section.

4.5.1 Exponential model and analysis evaluation

All the data obtained from experimental works has been determined from the fitting of an exponential function, as described in Section 4.3.3. This method has given good fits, and a way of comparing different data sets. However, several authors have modelled the decay in CoV of particle coverage for liquid spray systems using a power law function (Kadam (1990); Shi & McCarthy (2008)). The reasons for this are discussed in Chapter 2, Section 2.6. It has been shown here that an exponential function better describes the rate of decay for contact spreading only.

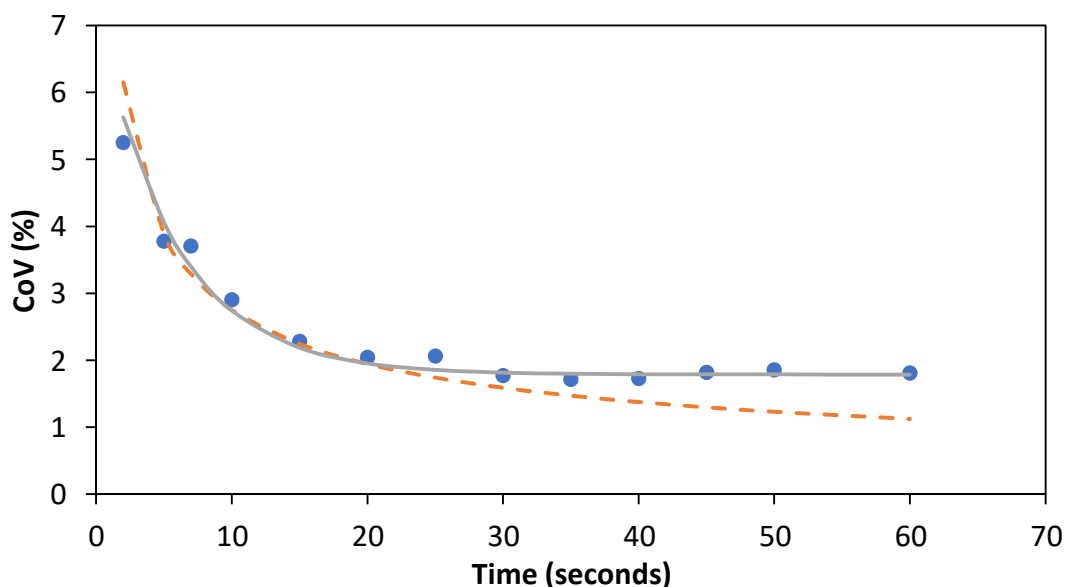


Figure 4-16. Comparison of fits for modelling the change of CoV as a function of time. Circles are experimental data points, the solid line represents the exponential function as detailed in equation 2 ($R^2 = 0.97$), and the dotted line represents a power law function ($R^2 = 0.85$).

Figure 4-16 shows the difference between the exponential and power law functions for one example experiment; this is amplified at long run times where the power law function approaches a CoV value of 0. For data generated in this work, this is not the case; the CoV for particle coating approaches some asymptotic value (Kumar & Wassgren (2014)).

Table 4-6 shows comparisons of the R^2 values for the exponential and the power law functions for all data in this chapter, with the exponential decay curve better predicting the data in all cases.

Table 4-6. Comparison of R^2 values for the exponential and power law models along with particle type and viscosity of the coating solution.

Experiment	Exponential	Power law	Particle type	Liquid viscosity (mPa.s)
1	0.998	0.921	Alumina 1	179
2	0.992	0.917	Alumina 2	179
3	0.991	0.968	Alumina 2	179
4	0.988	0.842	Alumina 1	179
5	0.971	0.849	Alumina 1	20,200
6	0.990	0.880	Alumina 1	20,200
7	0.988	0.437	Alumina 1	179
8	0.948	0.906	Alumina 2	20,200
9	0.986	0.962	Alumina 2	4,080
10	0.960	0.653	Alumina 2	20,200
11	0.982	0.906	Alumina 2	179
12	0.964	0.884	Alumina 1	4,080
13	0.992	0.973	Alumina 1	4,080

When considering the data generated by the Labview software, there are two points of importance; i) the initial increase in the mean red with time (seen for most every experiment), and ii) understanding the importance of the zero second time point.

Analysis of the data generated by the image analysis software shows a slight increase in the mean red value for each experiment performed (Figure 4-17). The slight initial increase in the mean red % can be attributed to the fact that at early time values the

red value reported will be lower due to several initial particles being thickly coated. The number of red points recorded will, therefore, be lower, but the high red intensity may not be representative of the coating thickness and therefore the mass of coating liquid. As time increases, the dye spreads and the number of thickly coated particles decreases; the red intensity stays relatively constant but the number of particles registering a value has increased. Here, the initial mean red value increases from 35.7 % to an average value of 36.5 %. This could be a potential limitation of this analysis technique. If the initial CoV values were adjusted to use a higher average mean red value which is more representative of the entire data set, they would be slightly lower than the current values.

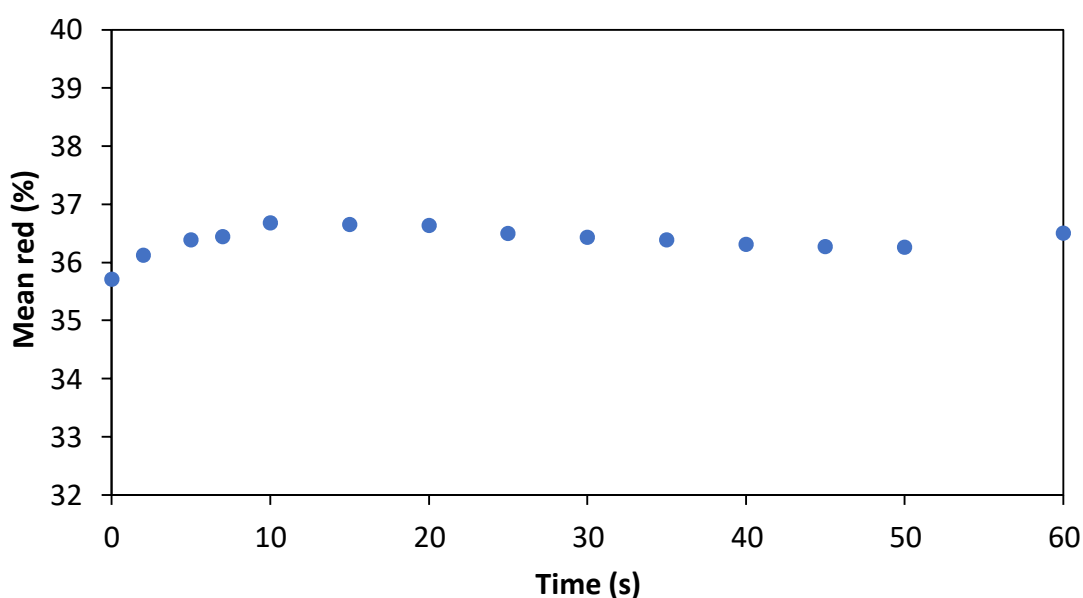


Figure 4-17. Mean red (%) as a function of tumbling time.

This can be seen in Figure 4-18; (a) shows the CoV data using the actual mean red data, and (b) shows the CoV using an averaged mean red value. Almost no difference between the two data sets can be seen; the standard deviation at the time points which have the lower mean red value are very high in comparison to the other data points. The CoV is influenced more by these large standard deviation values than the small mean red value. Therefore, this limitation is deemed to be negligible when analysing the results. To gain an understanding of the contact spreading occurring as a result of emptying the drum and analysing the samples, a further experiment was conducted. This involved coating particles with the coating solution and leaving them to dry without being tumbled

(Figure 4-19b). They were then imaged in the same way as an ordinary experiment. The same procedure was repeated using white particles that had not been coated (Figure 4-19a). A theoretical value of the CoV, calculated by combining the data from raw white particles and coated, untumbled red particles in a 90:10 ratio can be compared to the CoV value from the experiments (Figure 4-19 (c) and (d)) to give some indication of this variability. For the data presented in Figure 4-19 (a) and (b), the theoretical CoV value is 8.99 % (mean red value 0.347, standard deviation 0.0312), compared to the actual value of 7.22 % from the experiment (mean red value 0.356, standard deviation 0.0257).

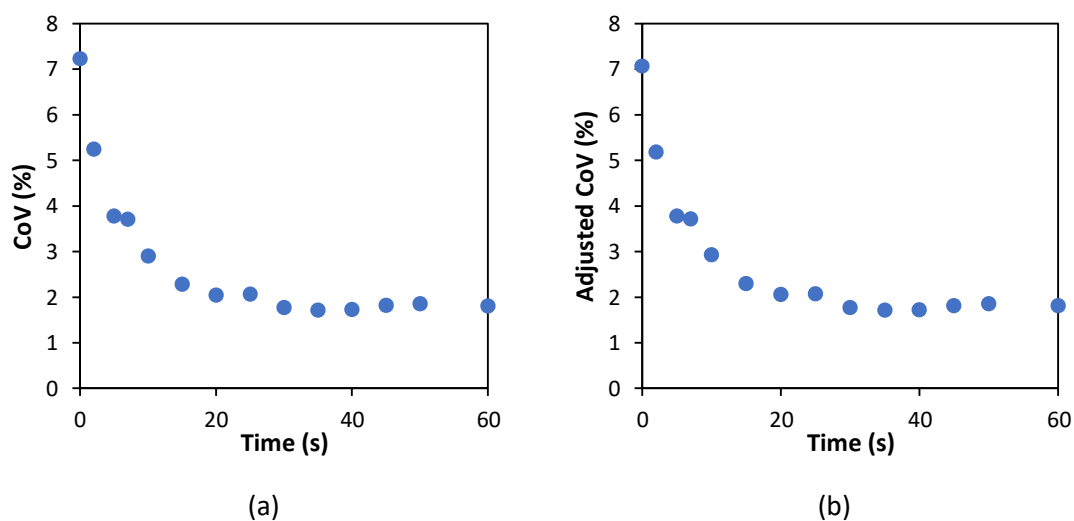


Figure 4-18. CoV as a function of time using (a) actual mean red values, and (b) a higher averaged mean red value.

A slightly lower value for the experimental value is to be expected; the red particles contact white particles in the drum, and contact more particles when the drum is emptied. This results in the lower standard deviation. The mean red value is higher for the experimental value because the theoretical calculation does not account for liquid transfer, and therefore the number of particles with red colouring is lower than would be experimentally expected. In the experiments, each red particle added to the drum is likely to contact a white particle, a fact which the theoretical calculation does not account for. Similar zero second CoV values for systems using the same PEG and Alumina type mean the drum is being consistently emptied, and no undue agitation resulting in excessive liquid transfer between particles is happening after the drum is emptied. Systems using different PEGs and Alumina types have different starting points due to the slight differences in colour of the PEG solutions dependent on the molecular weight

and the slight difference in colour of the alumina particles as received from the vendor, which is probably due to differences in the surface roughness.

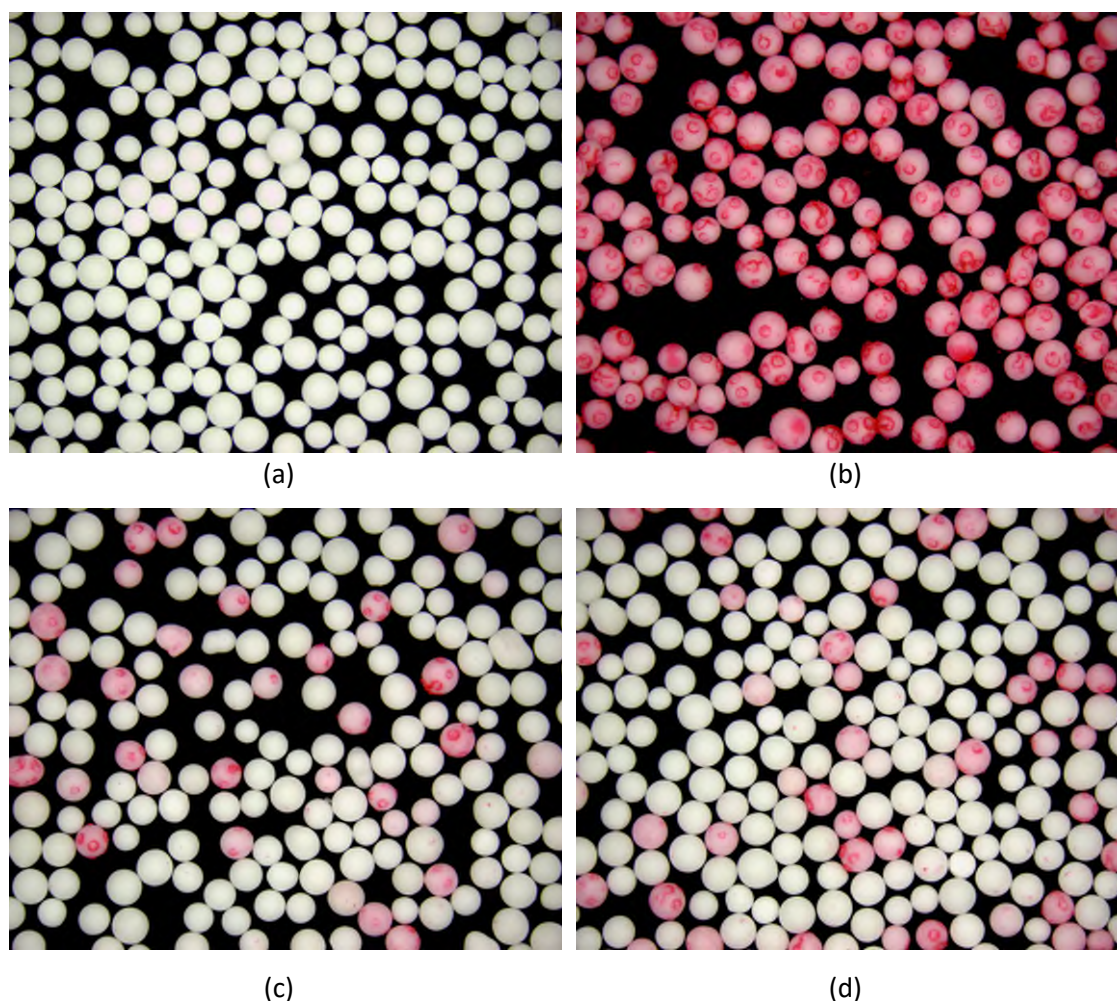


Figure 4-19. Images of (a) raw white particles, (b) untumbled red particles, and (c) and (d) particles from the zero second time point analysis.

Normalisation of the data helps overcome these slight differences and allows the rate of coating for different systems to be compared.

4.5.2 Understanding mechanisms effecting contact spreading

As has been previously discussed, contact spreading is the result of liquid bridges forming between two or more particles and subsequently rupturing to cause liquid redistribution around the tumbling bed. Many studies have tried to quantify myriad aspects of the liquid bridge; strength, size, rupture point, and liquid redistribution for example (Simons et al., 1994; Mazzone et al., 1987; Pitois et al., 2000, Darabi et al., 2010), but no studies have ever considered this phenomenon on a large experimental

scale. To understand how the kinetics of the liquid bridges impact the coating uniformity, the following section will discuss the bridge strength and the likelihood of liquid bridge formation, and try to understand how these phenomena are impacted by the liquid solution viscosity and the particle density.

Bridge Force

The total liquid bridge force is a summation of the contribution from the capillary forces and the viscous forces, with equations for each being well documented (refer to Chapter 2, Section 2.4 for more information). A capillary number (Equation 4-9) representing the ratio of these two forces was calculated for each of the systems to assess the contribution to the liquid bridge strength from the viscous forces; these can be seen in Table 4-7. If these values are high (above 1), the viscous force dominates and the capillary component of the liquid bridge force can be neglected. If the values are less than 10^{-3} , the dynamic bridge strength is of the order of a static bridge, and is insensitive to liquid viscosity (Ennis et al., 1990).

$$Ca = \frac{v\mu}{\gamma} \quad \text{Equation 4-9}$$

where γ is the liquid surface tension, v is the relative particle velocity, and μ is the liquid viscosity. To accurately determine the particle velocity, modelling or video image analysis should ideally be employed, but this was not available for this study. Here, the particle speed was approximated by the speed at the drum periphery (0.55 m/s). Parker et al. (1997) used positron emission particle tracking to develop velocity flow fields for spherical particles in rotating drums.

Table 4-7. Solution viscosity, surface tension and capillary number for the three solutions used, calculated using Equation 4-9.

Solution viscosity (mPa.s)	Surface tension (mN/m)	Capillary number (-)
179	56.1	1.8
4,080	56.8	39.5
20,200	56.0	198.4

Using 1.5 mm particles in a 0.136 m diameter drum, they found that the particle velocities at the free surface approximately matched the wall velocity (0.45 m/s). This shows the approximation of the particle velocity as the speed at the drum periphery is acceptable. Table 4-7 shows dominance of the viscous forces, particularly for the high viscosity solutions. As a result of this, the capillary contribution to the liquid bridge force can be neglected, and the strength can be approximated using Equation 4-10 (Adams & Perchard, 1985) or Equation 4-11 (Pitois et al, 2000). Here, only the normal component of the bridge force has been considered.

$$F_v = 6\pi\mu R^* v \frac{R^*}{S} \quad \text{Equation 4-10}$$

$$F_v = 6\pi\mu R^* v \frac{R^*}{S} \left(1 - \frac{S}{H(R)}\right)^2 \quad \text{Equation 4-11}$$

Where $1/R^* = 1/R_1 + 1/R_2$, μ is the fluid viscosity, v is the relative velocity of the spheres, R_1 and R_2 are the radii of the two particles, and S is the separation between the particles. For further information on the Pitois model, refer to Chapter 2, Section 2.4.2. To know which model is appropriate, the separation distance must first be determined. Lian et al. (1993) showed a simple correlation (Equation 4-12) relating the critical rupture distance (S_c) to the liquid bridge volume (V_b), where the contact angle, θ , is in radians and V_b is scaled using the particle diameter;

$$S_c = \left(1 + \frac{\theta}{2}\right) \sqrt[3]{V_b} \quad \text{Equation 4-12}$$

To know the rupture distance exactly, the bridge volume must be known. In small scale studies, which investigate liquid bridge evolution, the liquid bridge volume is usually a fixed parameter. However, in any process scale system, tracking the exact volume of liquid trapped between particles is extremely difficult; the volume in the bridges will change with the number of particle interactions as the liquid is distributed around the particle bed and is, therefore, a function of time. Here it is possible to estimate the liquid bridge volume at the beginning of the coating process and at the end when the liquid is more-or-less homogeneously distributed. At the beginning of the process, the 10 % of

particles coated outside the drum can be thought to be evenly coated in the coating solution. Knowing the mass of both particles and liquid and the relevant densities, the volume of liquid per particle can be calculated. Once this value is known, 10 % of the volume is taken as the bridge volume; 5 % of the liquid on a single particle was shown to contribute to the liquid bridge by Liu et al. (2011) and two particles are assumed to contribute to every bridge. This process can be completed again at the end of the coating process where it is assumed the liquid is evenly distributed cross the entire particle mass. These values have been summarised in Table 4-8.

Table 4-8. Summary of liquid bridge volumes at the beginning and end of the coating process for Alumina 1 and Alumina 2.

Particle	Liquid bridge volume at beginning of coating process (m ³)	Liquid bridge volume at end of coating process (m ³)
Alumina 1	3.9E-12	4.04E-13
Alumina 2	4.2E-12	4.02E-13

Darabi et al. (2010) used a liquid bridge volume of $1 \times 10^{-10} \text{ m}^3$ in their simulations, which agrees relatively well with the value calculated here.

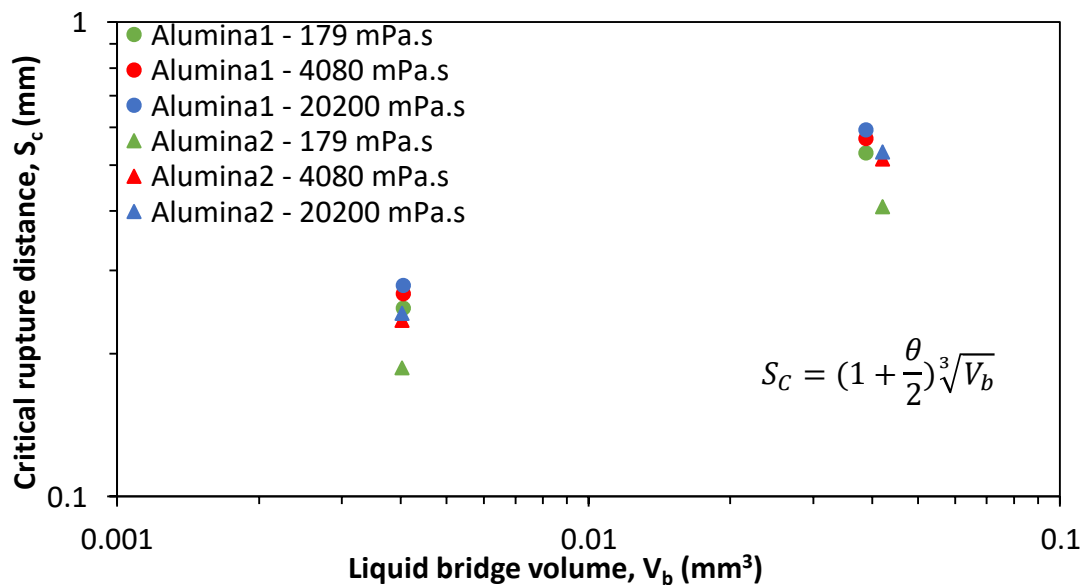


Figure 4-20. Log-log plot of the critical rupture distance as a function of the liquid bridge volume for different coating solutions. ● represent Alumina 1 particles, and ▲ represent Alumina 2 particles.

The relationship described by Lian et al. (1993) is shown in Figure 4-20 for the different contact angles seen between the coating solutions and particles and covering the range of liquid bridge volumes shown to be relevant to these systems. This shows that for the same liquid bridge volume, the bridge will achieve a greater distance before rupturing for liquid-solid combinations with greater contact angles; e.g. the Alumina 1 particles with the 20,200 mPa.s solution.

Having determined the separation distances corresponding to the liquid bridge volumes at the beginning and end of the coating process, the viscous component of the liquid bridge force can now be computed. Figure 4-21 shows a comparison of the Pitois and Adams & Perchard viscous force model over the range of liquid bridge volumes used here.

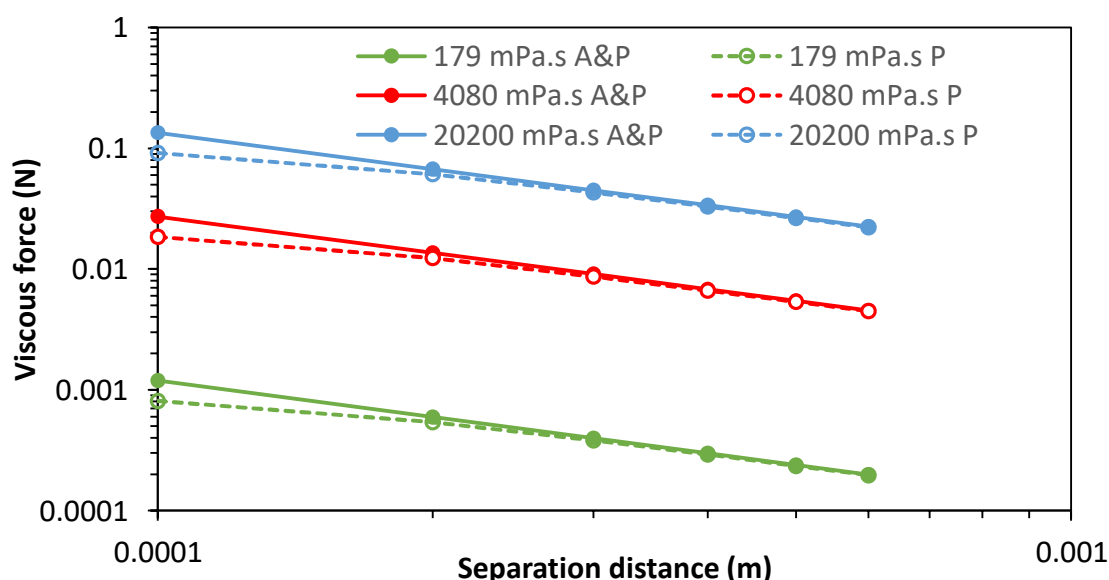


Figure 4-21. Comparison of the viscous force computed with the Adams & Perchard model and the Pitois model over the range of separation distances used in this work.

From this figure, it is evident that for the range of bridge volumes used here, the A&P model predicts the same viscous force and is the simpler equation. Hence, it will be used for all future viscous bridge force calculations. The viscous component of the bridge force is holding the particles together. To understand how the movement of liquid around the powder bed varies, the opposing force must also be examined. This is the energy which particles have when they collide; if the viscous term is much larger than this collision energy, the particles will adhere. If, however, the collision energy is much

greater than the viscous force, the particles will separate upon collision and liquid will be redistributed. Nase et al. (2001) defined a Collision number (Co) as the ratio of the bridge forces to the collision energy to help characterise the granular flow of grains (Equation 4-13), showing that the cohesion arising from liquid addition greatly influenced the outcome of mixing operations. Because of the low viscosity of the coating liquids chosen, they considered viscous effects negligible.

$$Co = \frac{F_c}{F_{Bg}} = \frac{2\pi r_p \gamma}{\pi \lambda^2 r_p^4 \rho \left(\frac{du}{dy}\right)^2} \quad \text{Equation 4-13}$$

Here, F_c is the capillary force and is a function of the particle radius (r_p) and the surface tension (γ) and F_{Bg} is defined below. However, as has been previously shown, the viscous component of the bridge force is much greater than the capillary component for the systems studied here, hence the capillary force in the Collision number proposed by Nase et al. (2001) has been replaced with the viscous bridge force, as shown in Equation 4-14.

$$Co_{vis} = \frac{F_v}{F_{Bg}} = \frac{6\pi\mu R^* v \frac{R^*}{S}}{\pi \lambda^2 r_p^4 \rho_p \left(\frac{du}{dy}\right)^2} \quad \text{Equation 4-14}$$

The collision energy was proposed by Bagnold (1954) and is a function of the particle density (ρ), the particle radius (r_p), a constant (λ) and the shear rate in the flowing layer (du/dy). Nase et al. (2001) assumed that the highest shear experienced within the drum was that seen between the two layers of particles; particles in a drum can be considered to be in two sections, a lower 'static' bed in which the relative particle motion is minimal, and a top flowing layer in which particles cascade from the top to the bottom of the powder surface. They proposed a method for calculating the shear rate in a rotating drum based on the drum radius (R_D), the thickness of the particle flowing layer (δ) and the drum rotational rate (ω);

$$\frac{du}{dy} \approx \frac{2u}{\delta} \quad \text{Equation 4-15}$$

where

$$u = \frac{\omega R^2}{2\delta} \quad \text{Equation 4-16}$$

and all other parameters are as defined in the text above. Without simulations of the system, it is difficult to calculate/measure the flowing layer thickness and hence Khakhar et al. (1999) proposed a relationship between the flowing layer thickness and the drum radius for drums in the cascading regime ($\delta / R_D = 0.03$) which allows for the shear rate to be calculated using Equation 4-15 and Equation 4-16. Here, the collision number was evaluated using the shear rate as calculated using this method (Co_1), but also using the linear velocity at the drum periphery divided by the particle diameter (Co_2) ($u = \omega R / 2r_p$). Figure 4-22 shows the collision numbers calculated via both these methods plotted against the coating completion time; as can be seen, there is a very minor difference between the two methods and so all further calculations will be completed using the wall speed method (Co_2).

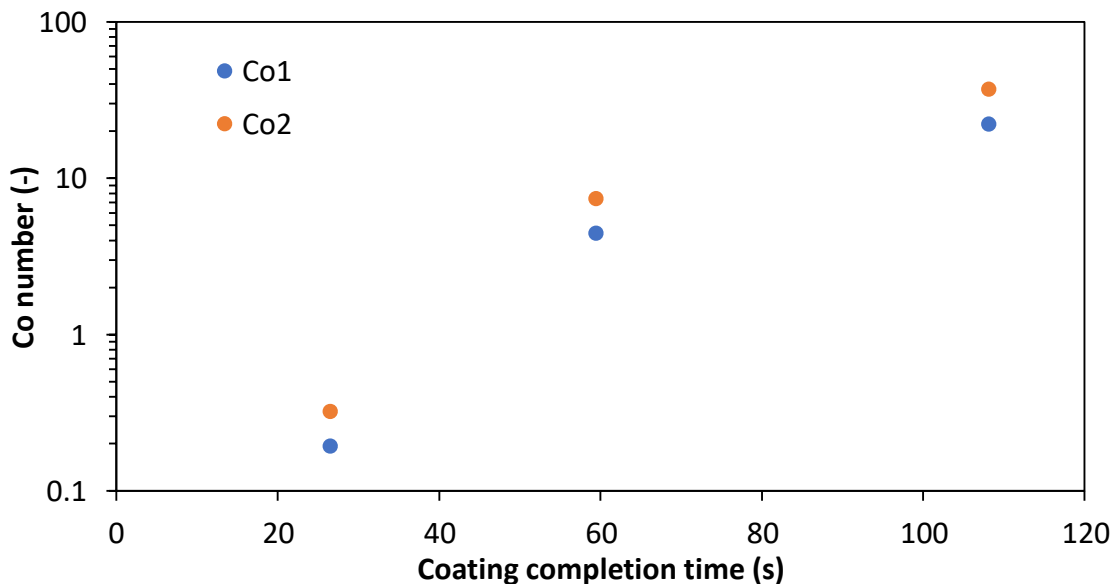


Figure 4-22. Log-normal plot of the Collision number calculated using two separate methods against the coating completion time. Alumina 1 particles using three different viscosity coating solutions.

The wall speed was chosen as the value was taken directly from the experiments completed here and does not rely on a relationship developed by other researchers. The

Chapter 4

Mechanistic understanding of contact spreading: Study of material properties

two points with a coating completion time of around 25 seconds correspond to a system using 179 mPa.s solution, the middle two data points were completed using 4,080 mPa.s viscosity solution and the final two used the highest viscosity solution, 20,200 mPa.s.

Figure 4-23 shows the Co numbers for all the experiments completed in this chapter plotted against the log coating completion times. It is evident that at lower Co numbers, the coating completion time is low. This makes sense; small Co numbers are a result of the collision energy being larger than the liquid bridge strength which results in low agglomeration and quick spreading. At higher values of Co, the coating completion time is very long. The denser Alumina 1 data is fitted remarkably well with a linear relationship; all the coating is relatively quick and is proportional to the Coating number. The Alumina 2 data is less easily fit with a curve; there appears to be more variables influencing the coating than are accounted for with the Co number. This could be particle mixing; the model does not incorporate anything to do with particle mixing in the bed. As has been previously shown, mixing, or the lack of, can have an extremely large impact on the particle coating. Lighter particles form agglomerates much more easily, which then prevent further spreading of liquid and lead to the development of new/different tumbling regimes. This will be explored further in the following results chapters.

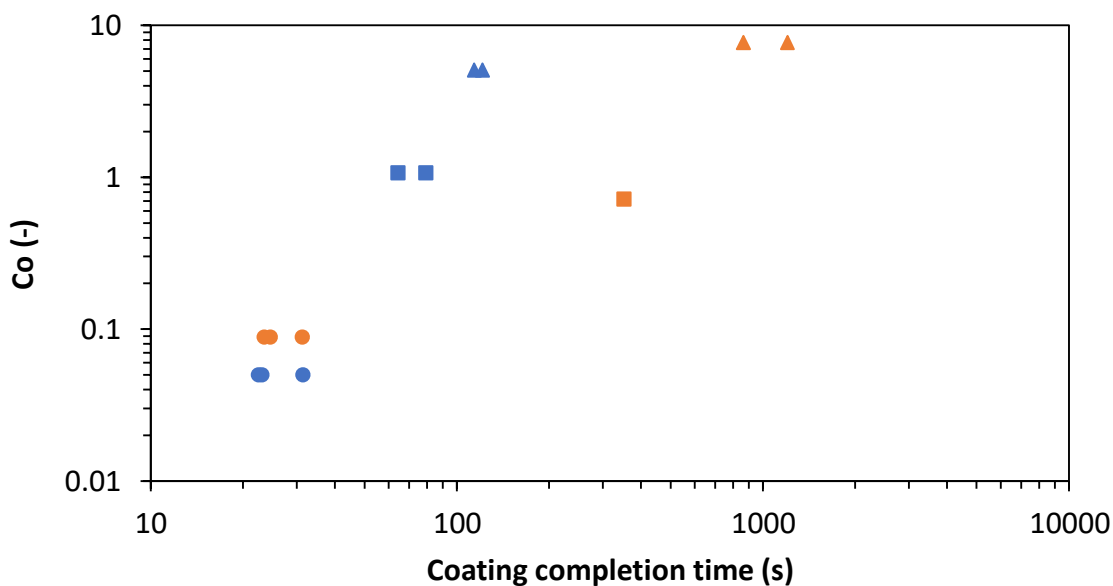


Figure 4-23. Co number shown alongside coating completion times for Alumina 1 (blue) and Alumina 2 (orange). ● = 0.179 Pa.s, ■ = 4.08 Pa.s, ▲ = 20.2 Pa.s.

4.6 Conclusions

In this chapter, results for the effect of material density and liquid viscosity on the liquid coating rate in a tumbling drum have been presented. The data from each experimental set has been expressed as the coefficient of variation in the red value as a function of time. For all the systems investigated, contact spreading occurred, and spread the liquid almost to uniformity. The only difference is the rate at which this uniformity is reached. An exponential function has been fitted to each data set to capture the rate of decay, and to allow a prediction of the time taken for 'complete' coating to occur. Comparison of the resulting coating rate constants across the different data sets showed how the coating is influenced by the material characteristics and the solution viscosity. The strong effect that material density had on the liquid coating was explained using a Collision number (Co), which can capture changes in particle properties, solution properties and drum properties. A capillary number showed how the viscous component of the liquid bridge strength dominates at each of the solution viscosities used, but especially for the high viscosity solutions. A collision number was proposed which accounts for the viscous component of the liquid bridge strength, and all the experiments completed so far were plotted using their Co number and coating completion time. Low Co numbers (below 1) correspond to quick coating times and high Co numbers correspond to long coating times. The number fails to account for particle mixing within the drum, and hence some data does not fall on the fitted line; specifically experiments which use high viscosity solutions and low-density particles are not well captured.

In the next chapter, whilst still using the model system, the effect of drum properties will be presented. Different drum sizes with different tumbling speeds will be introduced. Data from these operational parameters will be analysed in the same way i.e. through the use of a collision number.

Chapter 4

Mechanistic understanding of contact spreading: Study of material properties

5. Mechanistic understanding of contact spreading: Study of drum parameters

In this Chapter, the previously developed data processing techniques have been used to investigate the effect of drum size on the liquid contact spreading between Alumina 1 and Alumina 2 with the use of three different viscosity solutions. Contact spreading is observed in all cases, approaching a relatively homogenous coating in most systems. When using the denser Alumina 1 and the high viscosity coating solution, larger drums promoted quicker contact spreading. No change was seen when using lower viscosity solutions; particles in the smallest drum have the necessary collision energy to overcome the viscous bonds and so increases in the collision energy is superfluous. Similarly, the lighter Alumina 2 showed no difference in the rate of coating between the drum sizes when using the lowest solution viscosity. However, for both the higher solution viscosities, a considerable difference between the smaller and larger drums was seen; smaller drums promoted much faster coating. It is suspected that this is a result of particle mixing within the drum; smaller drums could mean that the effects of the walls, which promote particle mixing by increasing the friction and ‘pulling’ particles further up the drum wall, are felt further along the particle bed in the axial direction. The collision number was calculated for all the systems, and appeared to correlate linearly with the coating completion time for the majority of cases. However, systems which used high viscosity and low particle density did not correlate well with the Co number.

5. Mechanistic understanding of contact spreading: Study of drum parameters

5.1 Introduction.....	124
5.2 Methods.....	125
5.3 Results and discussion.....	127
5.4 Conclusions.....	157

5.1 Introduction

In Chapter 4, the effects of material characteristics were investigated. There was a strong correlation between material viscosity and the coating rate; higher liquid viscosity resulted in slower coating. In this chapter, three further sizes of drum will be investigated to see how scale affects the coating process. Understanding the effect of drum size is crucial. Industrially, new products are often made at lab scale before being scaled to accommodate commercial manufacture. If the way in which liquid is transferred between particles is affected by the drum size, it is important that this is understood. The agglomeration of particles in each of these situations will be studied alongside the coefficient of variation to observe how the drum size, particle type, and coating solution viscosity affect the coating / agglomeration boundary. As was seen in chapter 4, low viscosity solutions form the weakest liquid bridges, and a very minimal collision force is needed to overcome this which is easily achieved by the majority of interactions. The force that is needed is present in the smallest of the drums and, therefore, it is thought that increasing the drum size will have no impact on the spreading rate of the low viscous solutions. Conversely, it was seen that high viscosity solutions formed the strongest liquid bridges, and therefore these systems took the longest to homogenise. In this case, increasing the drum size could potentially improve the liquid spreading, increasing the collision energy and forcing bridges to rupture more readily. Many authors have studied the effect of processing parameters for liquid spray coating systems, yet none have quantified the effect of drum size on the liquid contact spreading. The main objectives for this chapter are;

- Identification of the effect of drum size on the rate of contact spreading for Alumina 1 and Alumina 2 using different viscosity coating liquids.
- Investigation into drum agglomeration, and identification of how this is likely to affect liquid contact spreading.
- Extension of the collision number proposed in Chapter 4 to include the effect of drum scale.

A brief recap of the methodology will first be presented, along with material and drum properties. The effect of drum size will then be presented, for the two types of alumina. Finally, the results of the agglomeration study will also be presented and discussed.

5.2 Methods

Similarly to Chapter 4, the results in this chapter pertain to two types of alumina particle, denser Alumina 1 and the lighter Alumina 2. Three different viscosity polyethylene glycol (PEG) solutions have been used to cover a range of viscosities. The solutions are dyed with red dye to allow colourimetric image analysis. A recap of the particle properties is presented in Table 5-1, and those of the liquid are presented in Table 5-2.

Table 5-1. Particle properties for Alumina 1 and Alumina 2.

Property	Alumina 1	Alumina 2	
		Batch 1	Batch 2
Envelope density (g/cm ³)	3.37 ± 0.049	2.55 ± 0.17	2.64 ± 0.021
d ₁₀ (µm)	868	954	1,182
d ₅₀ (µm)	1,034	1,077	1,422
d ₉₀ (µm)	1,155	1,164	1,646

Table 5-2. Coating liquid properties.

Property	Molecular weight (Da)		
	4,000	20,000	35,000
Viscosity (mPa.s)	179.3 ± 0.947	4,080 ± 69.9	20,200 ± 630
Surface tension (mN/m)	56.1 ± 0.47	56.8 ± 0.81	56.0 ± 0.76

Four different drum sizes will be investigated, shown in Table 5-3. All the drums maintain the same ratio of drum radius to drum length (0.32) and are run at a speed which correlates to a Froude number of 0.3, which is consistent with a cascading flow regime.

Table 5-3. Drum dimensions

Drum number	Diameter (m)	Radius (m)	Length (m)	Volume (m ³)
A	0.11	0.055	0.17	0.0016
B	0.21	0.105	0.325	0.0113
C	0.265	0.1325	0.408	0.0225
D	0.315	0.1575	0.49	0.0382

The drums were used with a 10 % fill level and run at speeds ranging from 41 to 70 RPM. *No spray component* was used in the drum. Before being added to the drum, 10 % of the total particles were coated with a PEG solution outside the drum, and then added to the uncoated 90 % of the particles remaining in the drum through the use of a delivery arm. At the same time, a stopwatch was started. After a certain tumbling time, the drum was stopped and the entire batch was removed for sampling and analysis. This process is then repeated for a number of different tumbling times. After the particles had dried, the batches were riffled and a sample obtained. Sixteen images were then taken of each sample and Labview software was used to determine the average RGB value of each individual particle. This data was then averaged at each time point to give a value for the coefficient of variation.

In certain systems, agglomeration of particles was observed to quantify the extent of agglomeration. The samples were sieved to produce a size distribution, and agglomerates were classified based on the starting particle size distribution. On a few occasions, the agglomerates were broken to allow colour analysis of individual size fractions.

The full methodology and imaging analysis can be found in Chapter 3 (Materials and Methods). Table 5-4 gives a full list of the experimental combinations of particles and liquids completed in this chapter.

Table 5-4. Particle and liquid coating combinations used in this chapter for effect of drum size.

System	Materials		Drum properties	
	Particles	Solution viscosity (mPa.s)	Size	Fr
1	Alumina 1	179	A, B, C	0.3
2	Alumina 1	4,080	A, B	0.3
3	Alumina 1	20,200	A, B, C, D	0.3
4	Alumina 2	179	A, B	0.3
5	Alumina 2	4,080	A, B	0.3
6	Alumina 2	20,200	A, B	0.3

The same data processing methodology as used in Chapter 4 has been employed.

5.3 Results and discussion

The results in this chapter pertain to the effect of drum size on the contact spreading mechanism. As identified in the previous chapter, agglomeration of the particles was observed, particularly for the lighter Alumina 2 particles with higher solution viscosities. This could affect the coating rate and extent of coating uniformity. Here, a more detailed overview of agglomeration will also be presented alongside data on the effect of drum size on the coefficient of variation as a function of both time and drum revolutions.

5.3.1 Alumina 1: Effect of drum size on coating variation

Alumina 1, the denser of the two alumina materials, was first investigated along with up to four different drum sizes, using 179 mPa.s, 4,080 mPa.s and 20,200 mPa.s PEG solutions. The un-normalised and normalised CoV graphs as a function of time for these solutions are presented. A smaller number of experiments were completed with the 4,080 mPa.s viscosity as the extremes were tested first and showed a minor effect of drum speed.

The lowest coating solution viscosity, seen in Figure 5-1, shows very little difference between the three drum sizes investigated. The CoV is plotted as a function of the tumbling time in three different drum sizes.

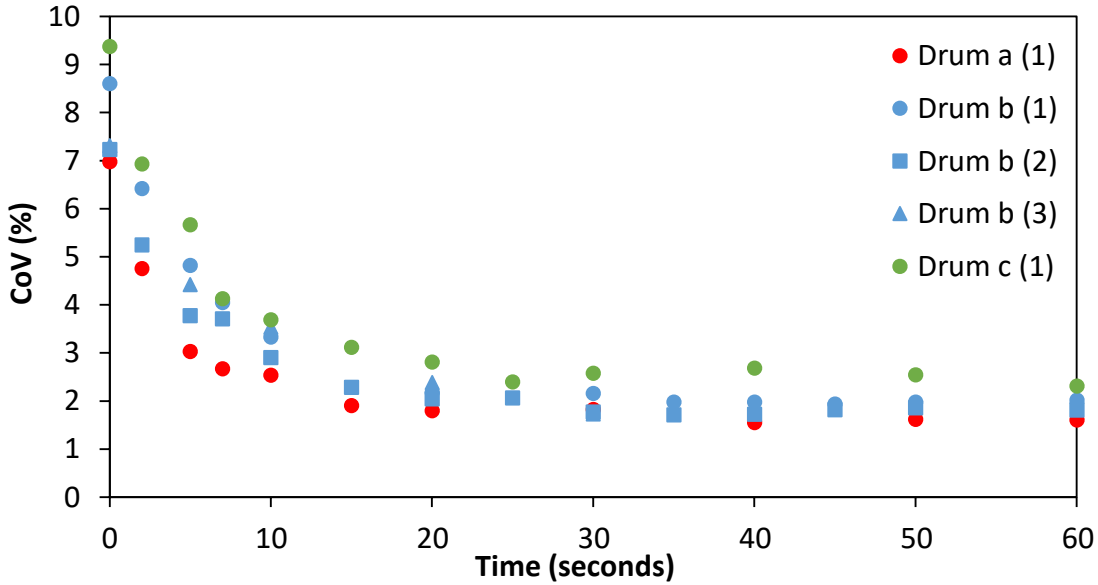


Figure 5-1. CoV data for 179 mPa.s PEG solution with Alumina 1 in Drum A, B and C. The legend shows which drum was used with the experiment number given in brackets.

Only one experiment using Drum A and Drum C were conducted; no further investigations were completed as the low viscosity results from Chapter 4 indicated very little difference in contact spreading upon varying parameters.

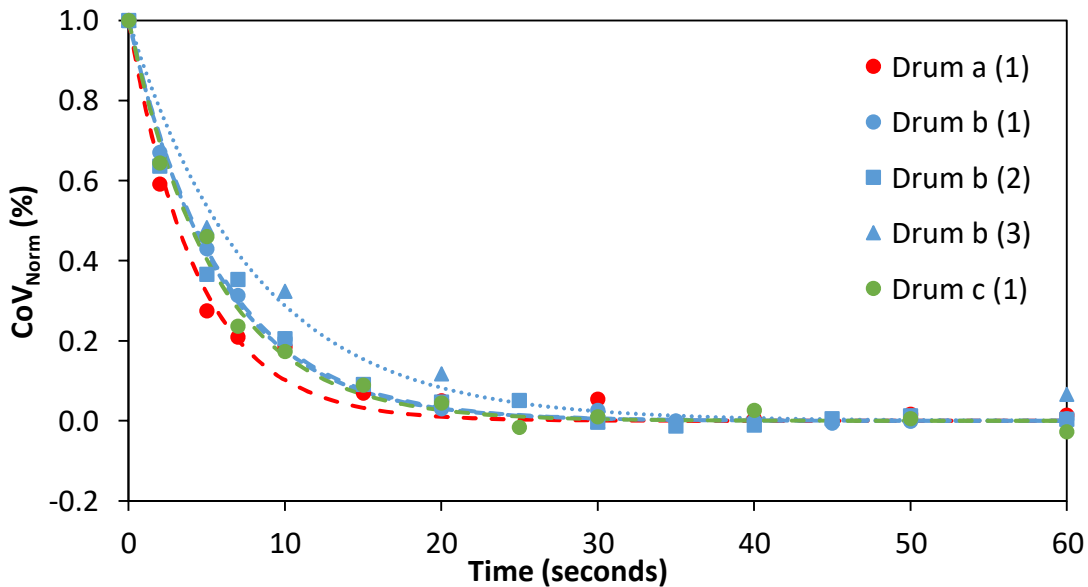


Figure 5-2. Normalised CoV data for 179 mPa.s PEG solution with Alumina 1 in Drum A, B and C. Exponential functions for each data set are displayed as dashed lines.

Although there may be some argument for stating the smaller drum size results in a faster coating rate, the normalised data shows no significant difference in the rate of

decay for any of the three drums sizes (Figure 5-2). The coating completion time is around 20 seconds for all three experiments.

Figure 5-3 shows the effect of drum size when using the 4,080 mPa.s coating solution. Again, there is very little variation between the two drum sizes. The coefficient of variation starts at approximately 6 % and decreases to around 1.5 %. Unlike the 179 mPa.s solution, there appears to be no effect of the drum size on the asymptotic value, although there is a lot more scatter in the data as compared with the 179 mPa.s solution. It is proposed that this is a result of stronger liquid bridges between the particles and hence more agglomeration in the systems.

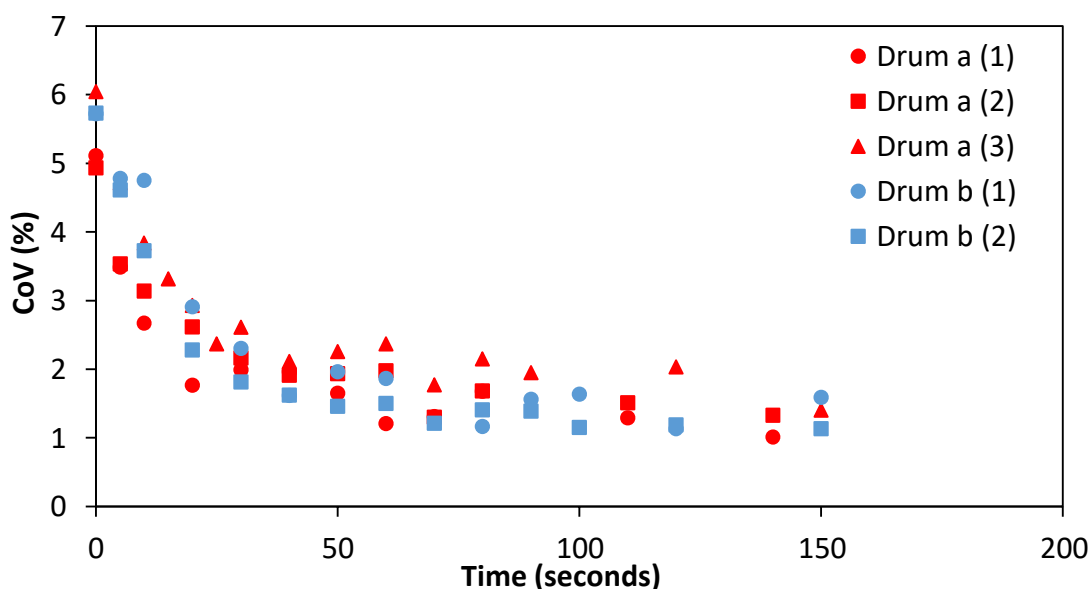


Figure 5-3. CoV data for 4,080 mPa.s PEG solution with Alumina 1 in Drum A and B. The legend shows which drum was used with the experiment number given in brackets.

Figure 5-4 shows the normalised CoV as a function of the tumbling time and again shows no discernible difference in the rate of coating for the two drums tested. Here, the coating completion time is around 50 seconds for both the drum sizes.

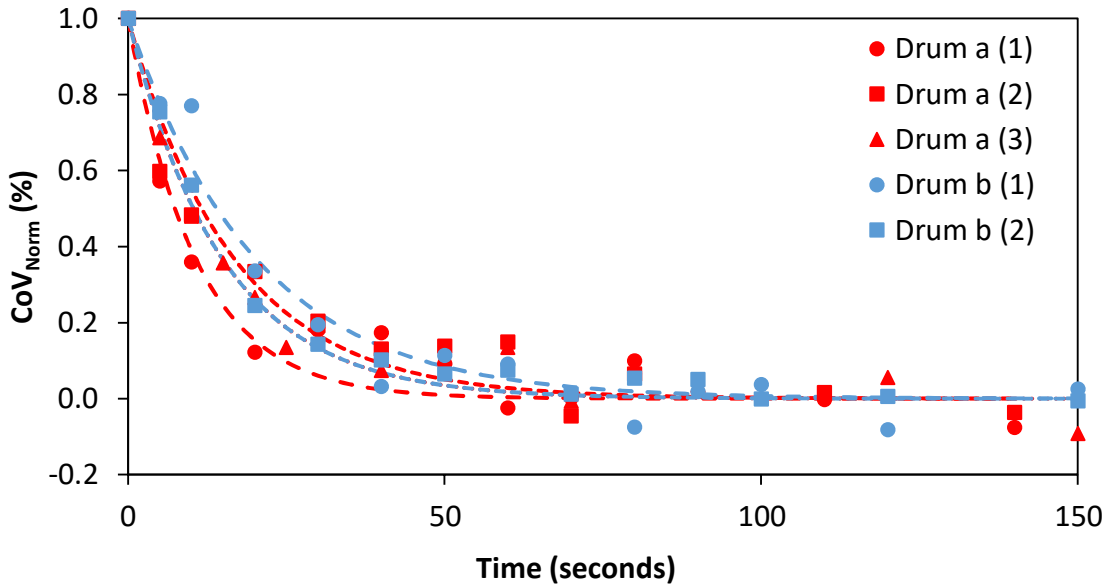


Figure 5-4. Normalised CoV data for 4,080 mPa.s PEG solution with Alumina 1 in Drum A and B. Exponential functions for each data set are displayed as dashed lines.

The 20,200 mPa.s solution, seen in Figure 5-5, shows a slight general trend indicating the larger drums coat more quickly.

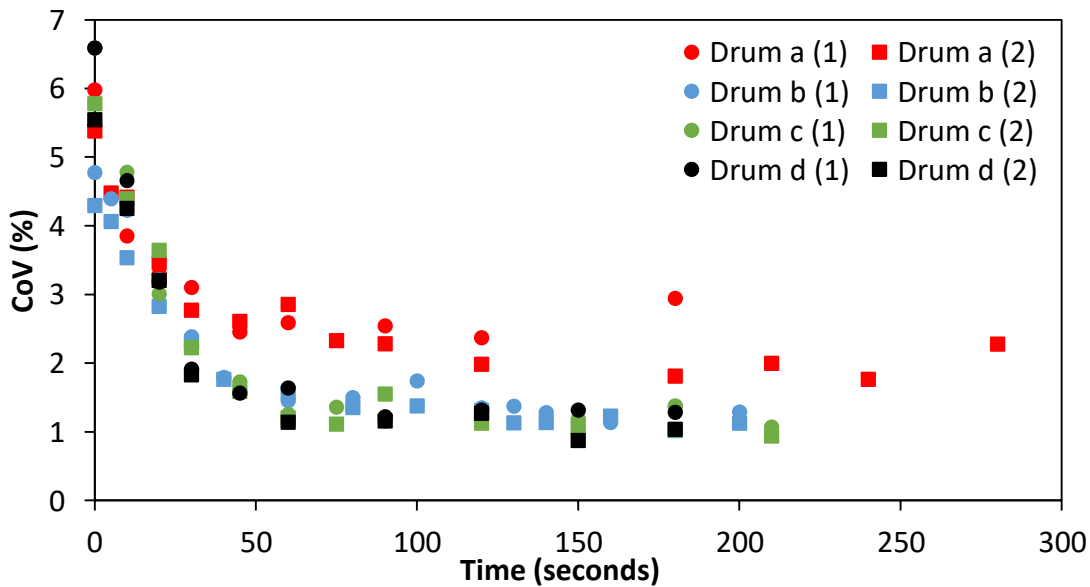


Figure 5-5. CoV data for 20,200 mPa.s PEG solution with Alumina 1 in Drum A, B, C and D. The legend shows which drum was used with the experiment number given in brackets.

This could be a result of the maximum collision velocity increasing with drum size and, therefore, the particles in these systems being more likely to rebound rather than coalesce. The CoV_{∞} value decreases from 2.5 % in the smallest drum to approximately

1.1 % in the largest of the drums, and the coating time decreases from approximately 120 seconds to 80 seconds. After normalisation, the data shown in Figure 5-6 does appear to show faster coating in the larger drums. For example, after 50 seconds, the normalised CoV in the largest drum is at approximately 0, whilst that of the smallest drum (A) is only at approximately 20 %. Summaries of the CoV_{∞} value, the coating rate constant and the time for coating completion can be seen in Figure 5-7, Figure 5-8 and Figure 5-9, respectively.

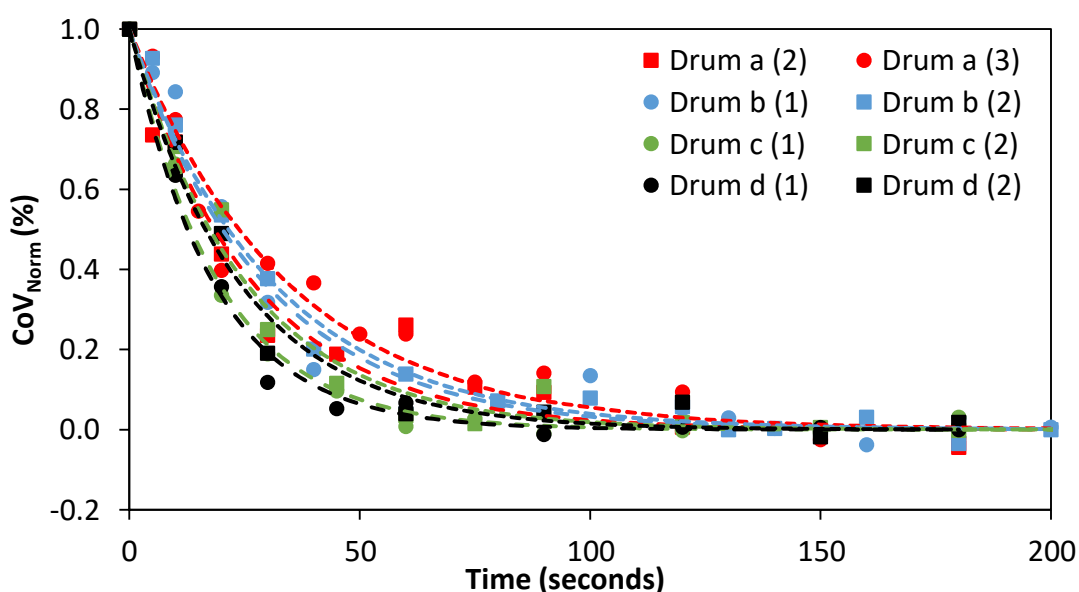


Figure 5-6. Normalised CoV data for 20,200 mPa.s PEG solution with Alumina 1 in Drum A, B, C and D. Exponential functions for each data set are displayed as dashed lines.

Figure 5-7 shows changes in the CoV_{∞} as a function of the drum volume for each of the three different coating solutions; the lowest viscosity solution (179 mPa.s) increases from 1.5 to 2.5 % with an increase in drum volume from 0.0016 m³ to 0.0225 m³. The two higher viscosity solutions, 4,080 and 20,200 mPa.s, however, both show a general decrease or no change in the asymptotic value with drum size, making it difficult to identify an overriding trend. It is noteworthy that there is a significantly higher asymptotic value for the 20,200 mPa.s solution when using Drum A compared to any of the other drums. This could be due to the fact that the smaller drum does not generate the large collision energies that are required to rupture the particles, especially when the viscosity of the liquid is so high. Agglomerates which form in the early stages of the experiments are likely to persist throughout the experiment, trapping the red dye and

preventing the solution from spreading before it dries. With the larger drums and lower viscosity solutions, a smaller collision energy is required to overcome the viscous bonds and therefore it is more likely that the solution will spread and not agglomerate, meaning less variation is seen at the end of the experiment.

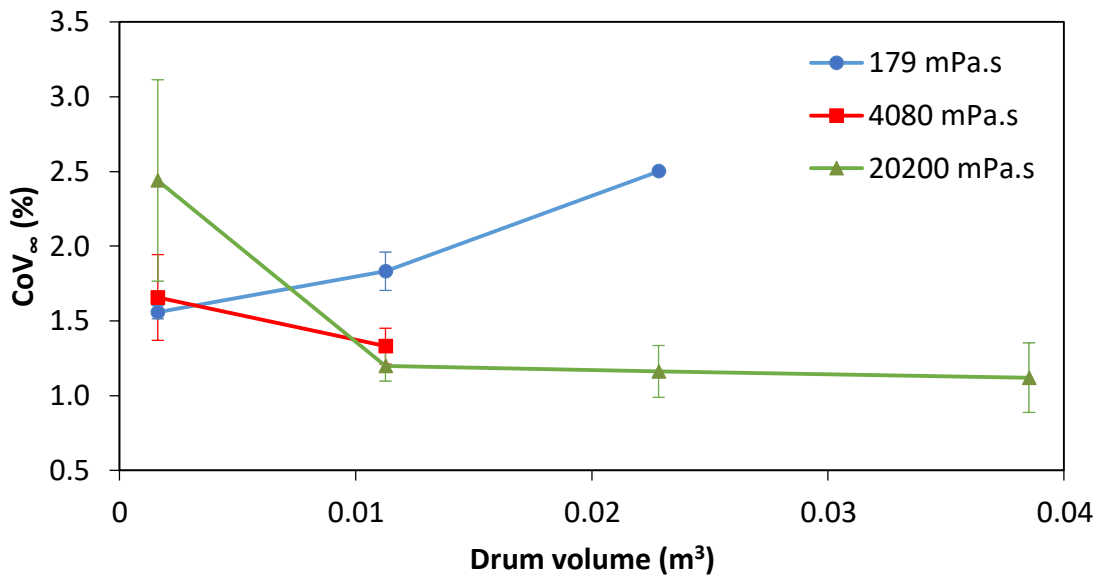


Figure 5-7. CoV_{∞} values as a function of drum size for Alumina 1 particles using 179 mPa.s, 4,080 mPa.s and 20,200 mPa.s viscosity solutions.

Figure 5-8 shows the coating rate constant as a function of drum size for the three solutions used. There is no general trend, other than the fact that the coating rate constant decreases with increasing viscosity at each drum size.

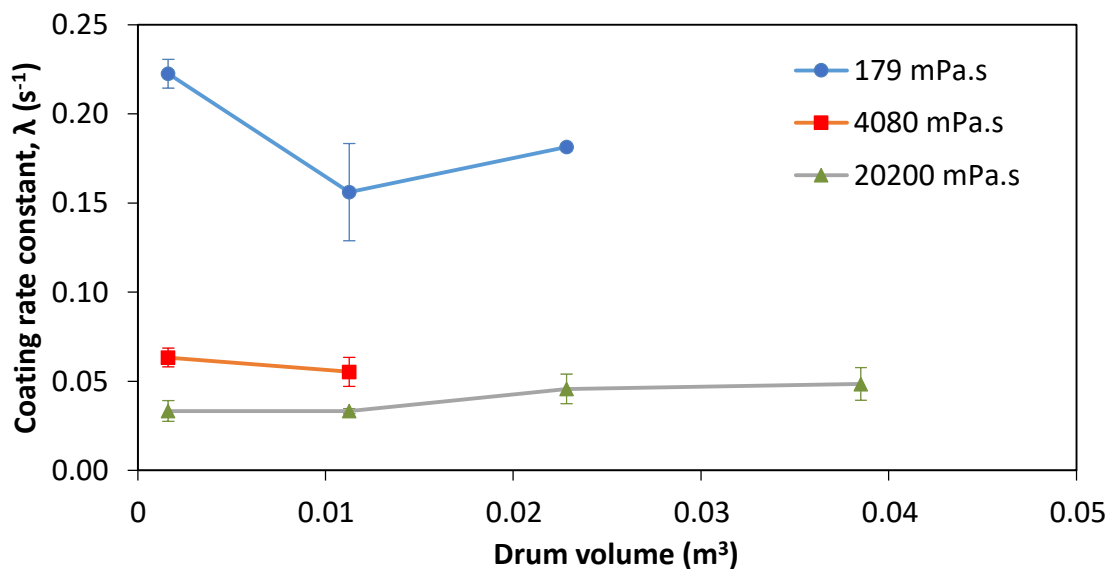


Figure 5-8. Coating rate constants as a function of drum size for Alumina 1 particles using 179 mPa.s, 4,080 mPa.s and 20,200 mPa.s viscosity solutions.

For the highest viscosity solution, there is a slight increase in the coating rate constant from approximately 0.03 to 0.05 as the drum size increases from 0.0113 m³ to 0.0385 m³. At the other extreme, the lowest viscosity solution shows a decrease in the coating rate constant from 0.22 to 0.18, with the drum size increasing from 0.0016 m³ to 0.0225 m³. However, due to the large error attached to the experiments completed in the middle drum size, no trend is identifiable. Figure 5-9 shows the change in time taken for coating completion as a function of drum volume for the three different viscosity solutions. As expected, longer coating times were recorded for higher coating viscosity solutions. For the highest viscosity solution (20,200 mPa.s), there does appear to be a slight decrease in the coating time with increases in drum size from approximately 120 seconds in Drum A and B to 87 seconds in Drum C and 82 seconds in Drum D. However, with the inclusion of the error bars, this is not conclusive. Similarly, the 4,080 mPa.s viscosity solution does not show any identifiable trend when the error bars are included. The lowest viscosity solution (179 mPa.s) shows no change in coating time with drum size, with all systems taking approximately 20 seconds to reach the asymptotic value.

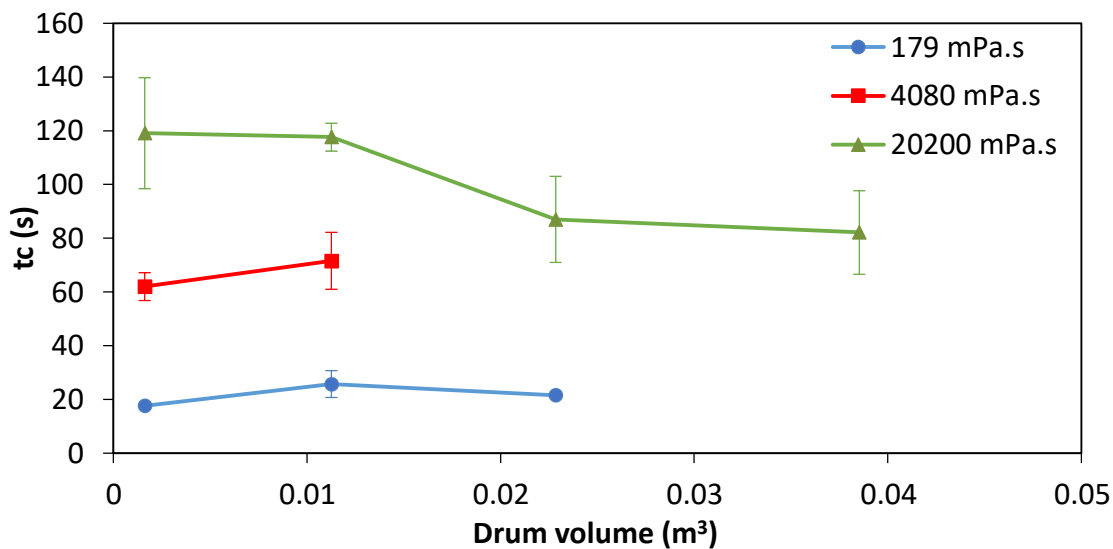


Figure 5-9. Time for coating completion as a function of drum size for Alumina 1 particles using 179 mPa.s, 4,080 mPa.s and 20,200 mPa.s viscosity solutions.

The CoV data from the investigation of the effect of drum size on Alumina 1 particles has been presented for three different viscosity solutions as a function of tumbling time. There is no discernible trend which is applicable to all the systems. The only observation which is true in all cases is that higher viscosity solutions take the longest to spread and have the smallest coating rate constants. To remove the influence of drum speed and only consider drum size, the normalised CoV data is now replotted as a function of the number of drum revolutions. Previously, each drum was run at a different speed to maintain the same Froude number. When the CoV is plotted as a function of drum revolutions, it is evident that there is no change for the low solution viscosity (179 mPa.s and 4,080 mPa.s) coating solutions, as seen in Figure 5-10 and Figure 5-11. All the normalised data for all the drum sizes could be easily represented by a single curve. Yet the 20,200 mPa.s shows a clear difference; the larger drums clearly promote quicker spreading at this high viscosity (Figure 5-12).

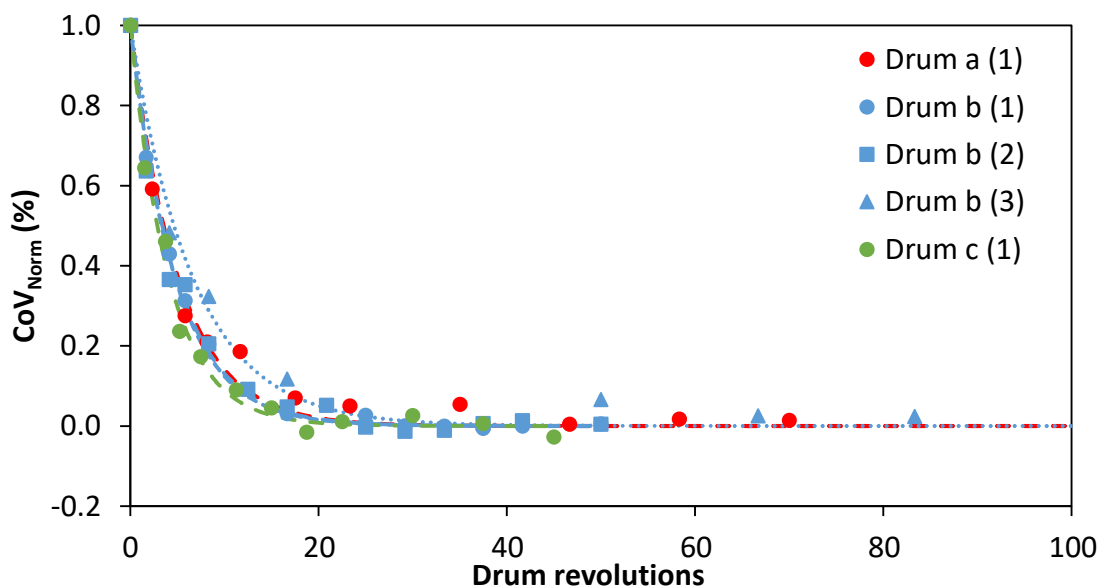


Figure 5-10. Normalised coefficient of variation as a function of drum revolutions for coating solutions viscosities of 179 mPa.s with Alumina 1 in Drum A, B and C. Exponential functions for each data set are displayed as dashed lines.

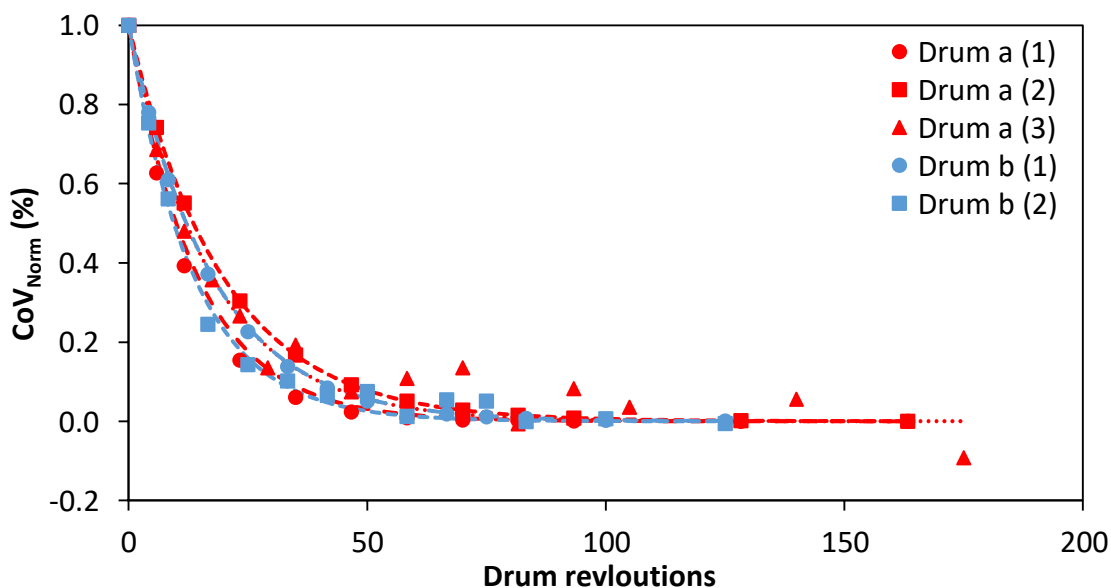


Figure 5-11. Normalised coefficient of variation as a function of drum revolutions for coating solutions viscosities of 4,080 mPa.s with Alumina 1 in Drum A and B. Exponential functions for each data set are displayed as dashed lines.

The difference highlighted earlier between the coating rate for the four different drum sizes when using the highest viscosity solution is clearly identified on Figure 5-12. For the same number of drum revolutions, the largest drum size coats considerably faster

than the smallest drum size. Again, very minimal difference is seen between the coating when using the 179 mPa.s viscosity solution (Figure 5-10). There is not enough data for the 4,080 mPa.s solution in the larger drums to conclusively identify a trend (Figure 5-11). This could be because at the 179 mPa.s viscosity solution, all the collisions, even in the smallest drum, have the energy required to overcome the liquid bridge strength and rebound, redistributing the liquid in the process. If all the collisions in the smallest drum (a) are considered to rebound, an increase in the drum size, and hence the speed of the collision, will have no impact on the contact spreading rate. With the 20,200 mPa.s solution, this is not the case; in the smallest drum, some proportion of the collisions have enough energy to overcome the bridge strength. However, when the drum size is increased, the collision force is also increased due to the increase in speed and hence a greater proportion of particles have the required energy to overcome the bridge strength. As well as the consideration surrounding collision energy, it should also be noted that perhaps the mixing within the drum is being altered with changes to the drum size. The drums are all unbaffled and therefore it is possible that some particles experience greater levels of segregation than others. This will be explored in more detail later in this thesis (see Chapter 7).

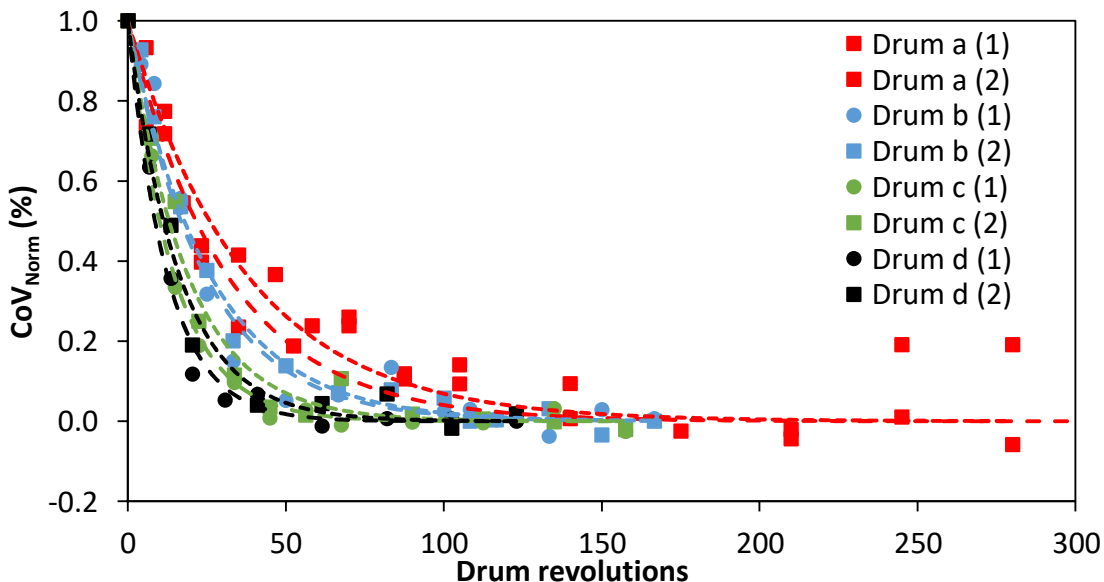


Figure 5-12. Normalised coefficient of variation as a function of drum revolutions for coating solutions viscosities of 20,200 mPa.s with Alumina 1 in Drum A, B, C and D. Exponential functions for each data set are displayed as dashed lines.

5.3.2 Alumina 2: Effect of drum size on coating variation

The same effect of drum size is now investigated using the lighter Alumina 2 particles. The effect on the coating rate is even more pronounced. However, due to material constraints, only Drum A and Drum B could be tested. In the future, it would be beneficial to complete more experiments using this material in even larger drum sizes.

In Figure 5-13, the CoV is plotted as a function of the tumbling time for Drum A and Drum B, using the 179 mPa.s coating solution. The 179 mPa.s coating solution shows very similar behaviour to the Alumina 1; there is no noticeable difference in the coating spreading between the two drum sizes. All the particle collisions possess a collision energy greater than that of the liquid bridge which is formed upon impact, and hence the particles rebound and distribute the liquid. Figure 5-14 shows the normalised CoV for the 179 mPa.s coating solution in Drum A and Drum B; virtually no difference in the coating rate can be seen.

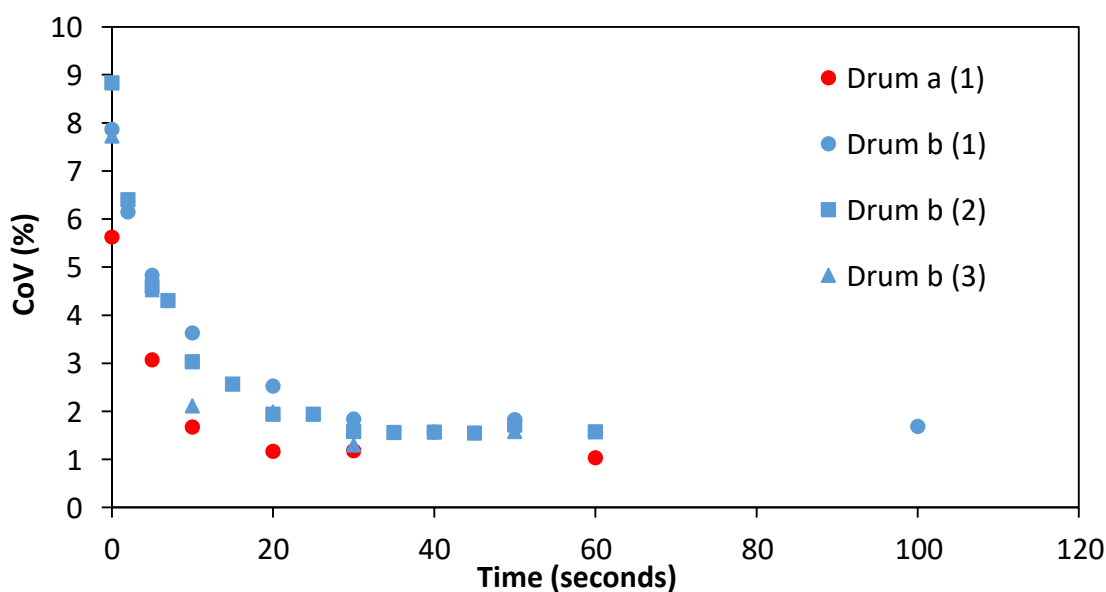


Figure 5-13. CoV data for 179 mPa.s PEG solution with Alumina 2 in Drum A and B. The legend shows which drum was used with the experiment number given in brackets.

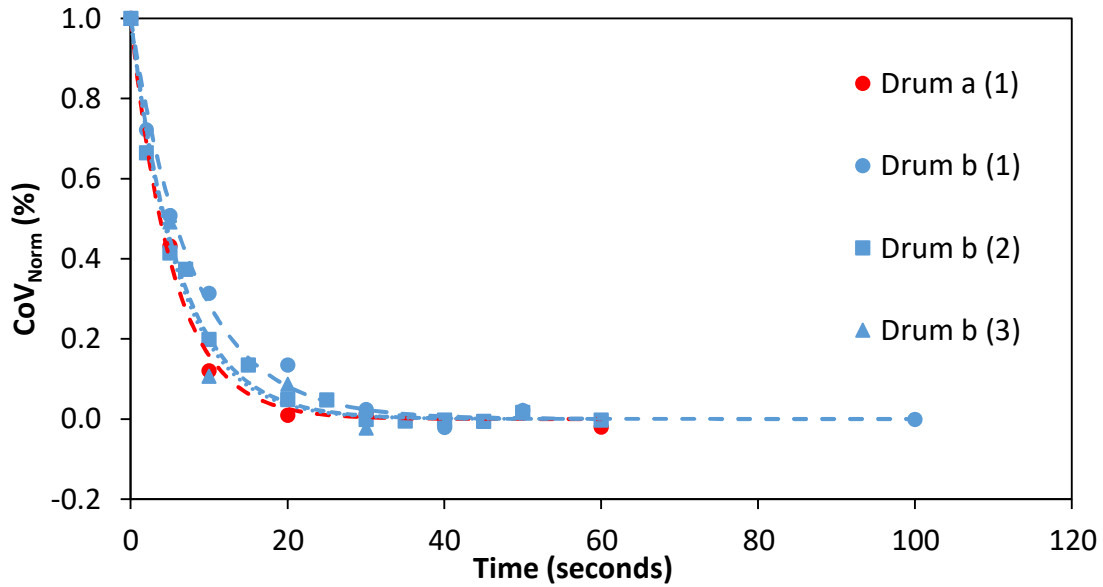


Figure 5-14. Normalised CoV data for 179 mPa.s PEG solution with Alumina 2 in Drum A, B and C. Exponential functions for each data set are displayed as dashed lines.

Figure 5-15 shows the CoV as a function of the tumbling time for the 4,080 mPa.s solution in Drum A and Drum B. The smaller drum shows a considerably quicker coating time, with the coating completing after approximately 100 seconds compared with approximately 300 seconds in Drum B.

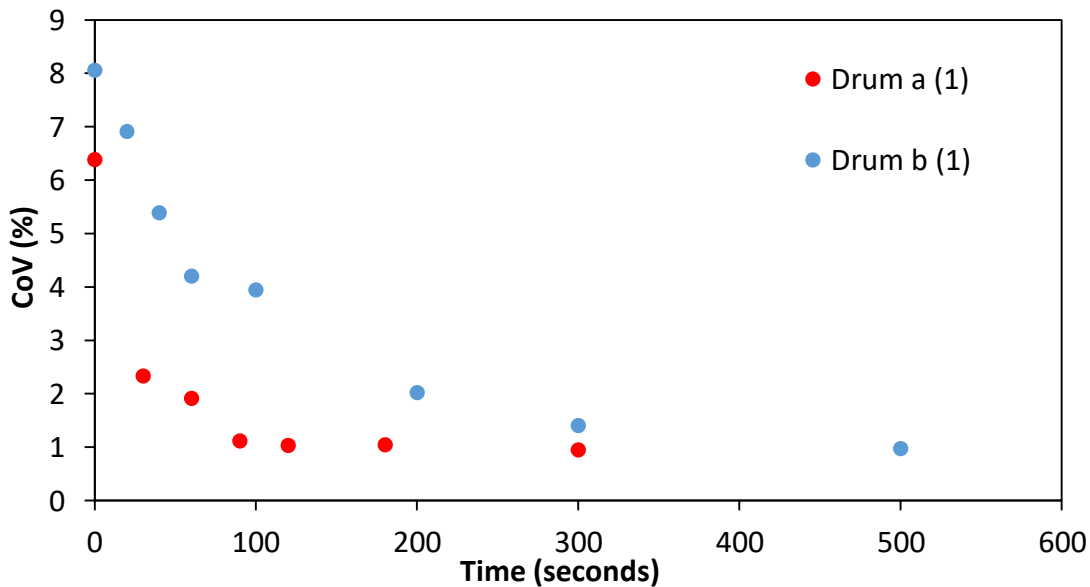


Figure 5-15. CoV data for 4,080 mPa.s PEG solution with Alumina 2 in Drum A and B. The legend shows which drum was used with the experiment number given in brackets.

Figure 5-16 shows the normalised rates of decay for the CoV in the two drums using the same solution viscosity (40,80 mPa.s). Even after normalisation, the smaller drum clearly promotes more contact spreading.

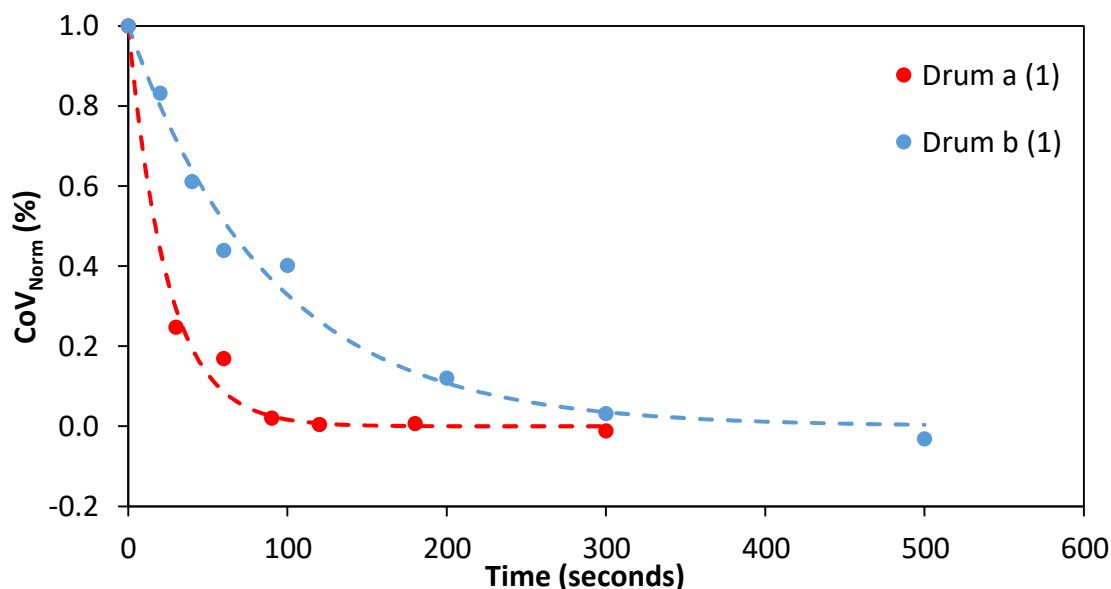


Figure 5-16. Normalised CoV data for 4,080 mPa.s PEG solution with Alumina 2 in Drum A and B. Exponential functions for each data set are displayed as dashed lines.

Figure 5-17 shows the CoV as a function of the tumbling time in Drum A and Drum B using the highest viscosity coating solution (20,200 mPa.s).

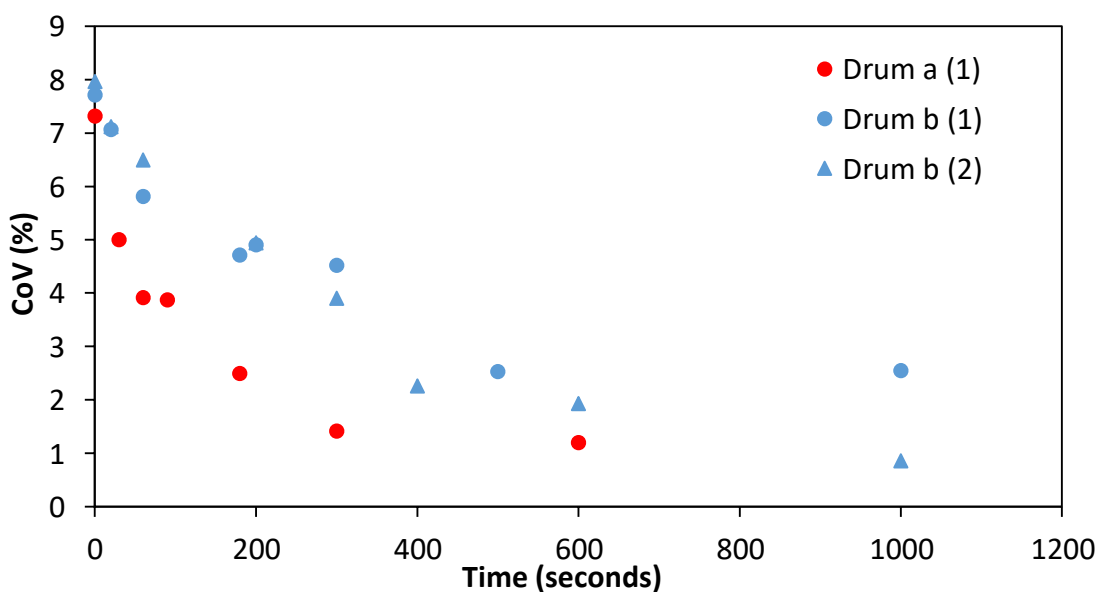


Figure 5-17. CoV data for 20,200 mPa.s PEG solution with Alumina 2 in Drum A and B. The legend shows which drum was used with the experiment number given in brackets.

A similar trend is seen; the 20,200 mPa.s solution finishes spreading after approximately 300 seconds in Drum A as compared with approximately 800 seconds in Drum B. In both cases, the lighter particles favour the smaller drums. The normalisation data (Figure 5-18) may not tell the entire picture. It is entirely dependent on the asymptotic value being correctly determined from Figure 5-17, however, there is clearly still a large amount of variation in the Drum B system even after 1,000 seconds. Further studies are recommended to look at the coating rate of the lighter Alumina 2 particles in even larger drum sizes. Here, experiments were limited to Drum A and Drum B due to material constraints.

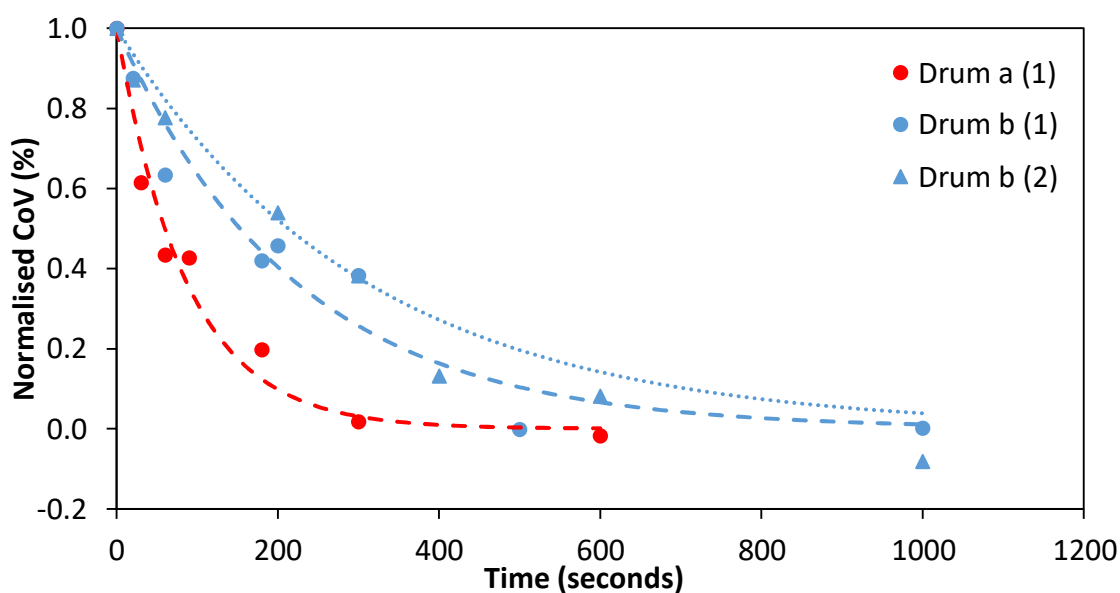


Figure 5-18. Normalised CoV data for 20,200 mPa.s PEG solution with Alumina 2 in Drum A, B and C. Exponential functions for each data set are displayed as dashed lines.

Figure 5-19, Figure 5-20 and Figure 5-21 show the asymptotic CoV values, the coating rate constants and the coating completion times, respectively, as a function of the tumbling time or drum volume for all the Alumina 2 experiments.

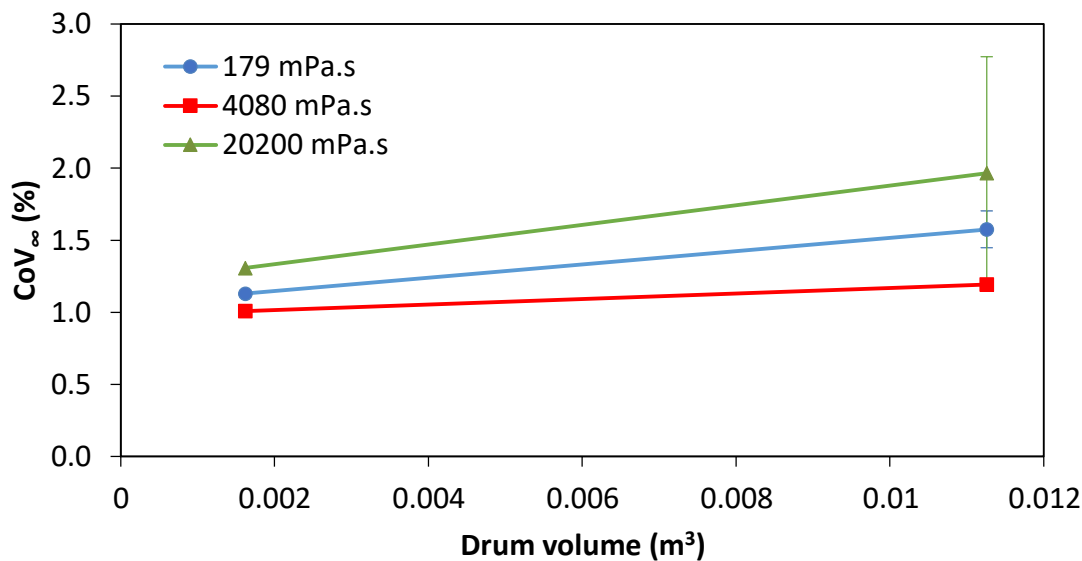


Figure 5-19. CoV_{∞} values as a function of drum size for Alumina 2 particles using 179 mPa.s, 4,080 mPa.s and 20,200 mPa.s viscosity solutions.

Clearly more experiments are needed to truly identify any trends, however, it is clear from Figure 5-21 that for the lighter Alumina 2 particles, larger drums result in longer coating times. This effect becomes more pronounced with increases in solution viscosity.

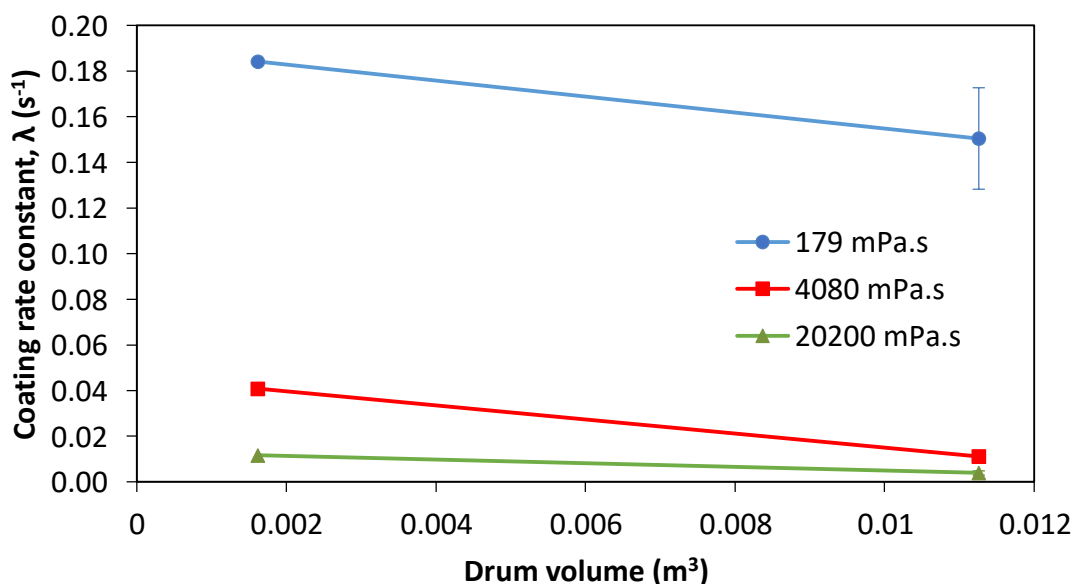


Figure 5-20. Coating rate constants as a function of drum size for Alumina 2 particles using 179 mPa.s, 4,080 mPa.s and 20,200 mPa.s viscosity solutions.

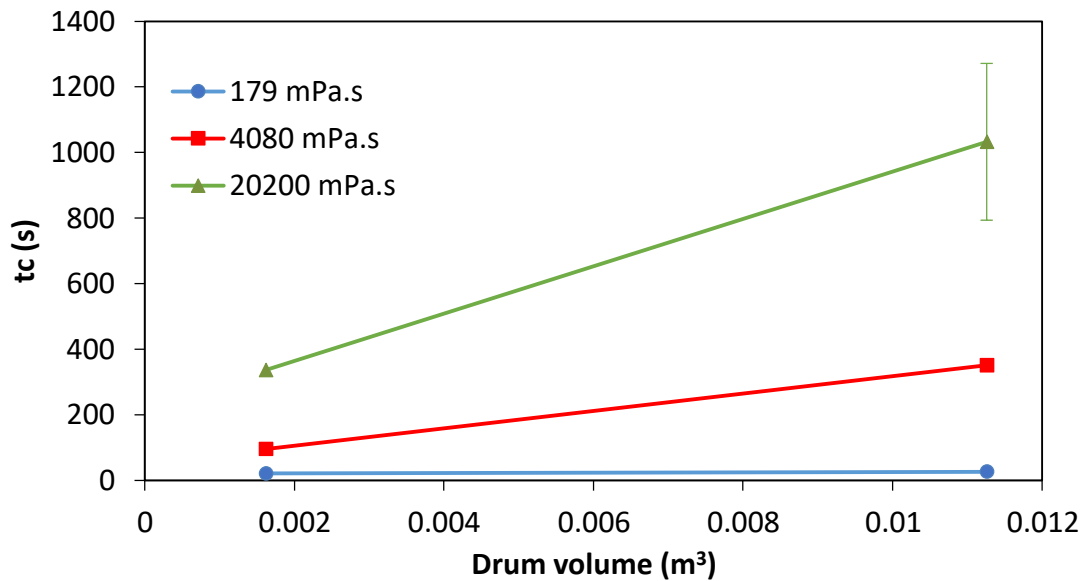


Figure 5-21. Time for coating completion as a function of drum size for Alumina 2 particles using 179 mPa.s, 4,080 mPa.s and 20,200 mPa.s viscosity solutions.

Here, the CoV data for the experiments completed using the lighter Alumina 2 particles and three different viscosity solutions have been presented, for both Drum A and Drum B. Unlike the Alumina 1, there is an obvious trend; smaller drums result in faster coating for both the 4,080 mPa.s and the 20,200 mPa.s solutions. However, there is no effect of drum size seen when using the 179 mPa.s coating solution. Again, for each drum size, increases in solution viscosity result in increased tumbling times and reduced coating rate constants. Plotting the data as a function of the drum revolutions offers the chance to isolate the impact of the drum size from the drum speed. Figure 5-22 shows the normalised CoV as a function of the number of drum revolutions for the lowest solution viscosity (179 mPa.s). There is no difference in the rate at which the coating approaches the asymptotic value. This is similar to the results seen when using the heavier Alumina 1 particles.

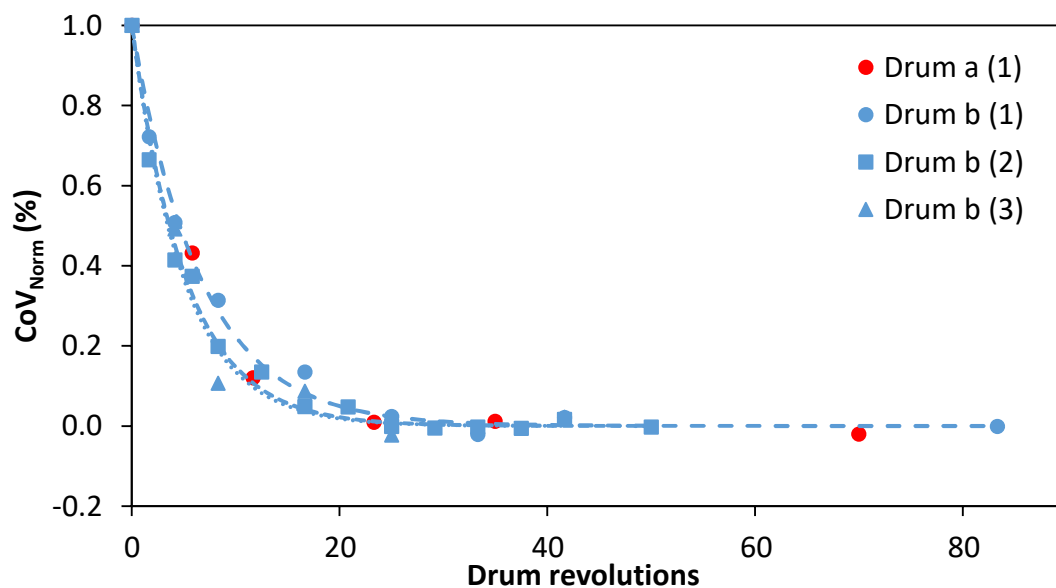


Figure 5-22. Normalised coefficient of variation as a function of drum revolutions for coating solutions viscosities of 179 mPa.s with Alumina 2 in Drum A and B. Exponential functions for each data set are displayed as dashed lines.

Figure 5-23 shows the comparison of the normalised CoV as a function of the number of drum revolutions for the 4,080 mPa.s viscosity solution; the speed at which the particles approach CoV_{∞} is much greater for the smaller drum.

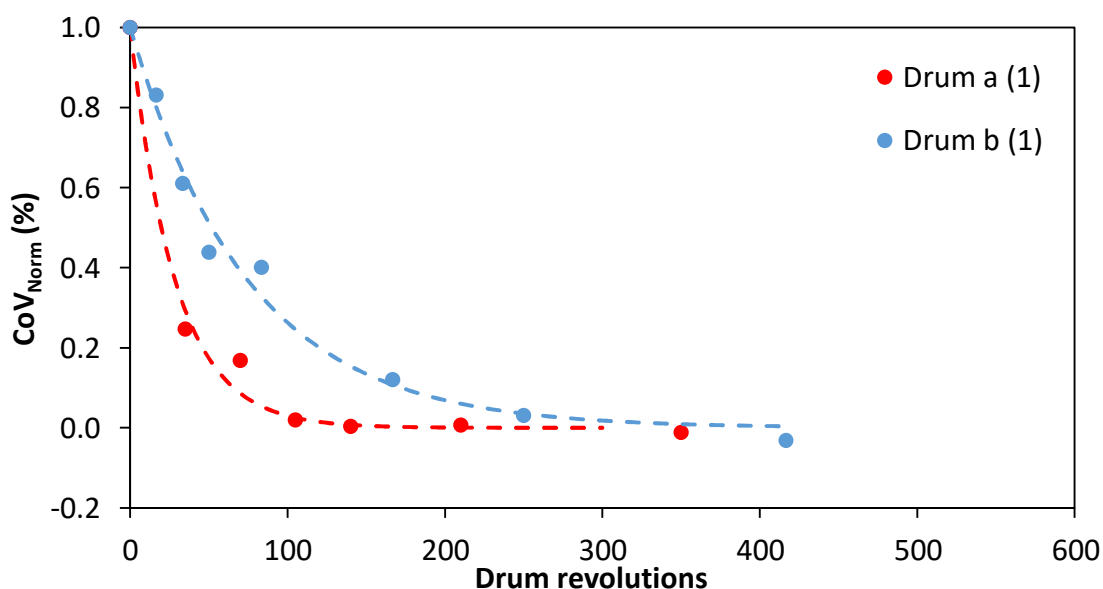


Figure 5-23. Normalised coefficient of variation as a function of drum revolutions for coating solutions viscosities of 4,080 mPa.s with Alumina 2 in Drum A and B. Exponential functions for each data set are displayed as dashed lines.

The smaller drum appears to reach the asymptotic value after 100 drum revolutions, whereas the larger drum (B) reached the asymptotic value after a much larger 300 revolutions (approximately).

In Figure 5-24, the same graph is displayed for the 20,200 mPa.s viscosity solution; the coating is much faster in Drum A (completing after approximately 360 drum revolutions) compared with the larger Drum B (completing after 900 drum revolutions).

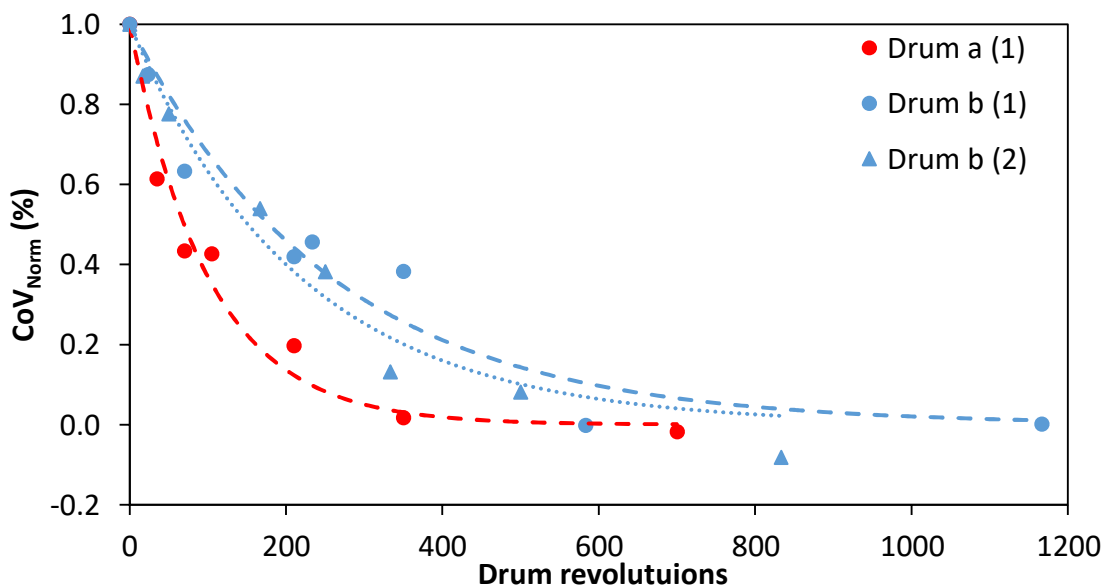


Figure 5-24. Normalised coefficient of variation as a function of drum revolutions for coating solutions viscosities of 20,200 mPa.s with Alumina 2 in Drum A and B. Exponential functions for each data set are displayed as dashed lines.

In the earlier section examining the effect of drum size on the heavier Alumina 1 particles (Section 5.3.2), it was suggested that the particles favour a larger drum due to the increased particle velocity and therefore collision energy. With the lighter particles used here, the opposite appears to be true; smaller drums promote faster spreading.

Unlike with the heavier Alumina 1, the differences seen here are unlikely to be explained as a result of the collision velocity. The differences seen in the drum sizes here could be a result of particle mixing. Although the drum is run at the same Froude number, meaning the same flow regime is developed, the mixing inside the drum, both radially (through the powder bed) and axially (along the powder bed), can be different. Several parameters can affect particle mixing; cohesion, baffles, particle size, particle density, flow regime, and end walls. Here, the only parameters which change from drum to drum

are the distance between the end walls and the particle cohesion. The flow regime, being scaled with the Froude number, should not affect the mixing, neither should the particle size or density as a very tight distribution of the same particle were used. The end walls increase the dynamic angle of repose of the particles at the walls relative to that of the particles in the centre of the drum, as shown by Santomaso et al. (2004). It is therefore reasonable to assume that smaller drums, having a higher percentage of their particles located in the region of an end wall, are likely to promote increased mixing as the particles are dragged up the wall. For larger drums, the percentage of particles that are affected by this effect reduces and there becomes a 'dead' zone between the two end walls which increases in width with increases in the drum size. As the drum used in this work was not transparent, this hypothesis is unfortunately hard to quantify, but many researchers have quantified the various effects of the drum walls on particle mixing, segregation and velocity profiles (Dury et al. (1998); Santomaso et al. (2004); Liu et al. (2018)).

The second factor which could change is the particle cohesion. If particles adhered to other particles are initially deposited in the centre of the drum, there is less chance these structures will be broken, and more chance they will solidify into agglomerates with increases in drum size. There is less chance they will be caught in the mixing effect associated with the wall ends, and they are likely to encounter less disruption. This could explain the increased rate of coating seen in the smaller drums. To test this hypothesis further, experiments in larger drums or in drums with more controlled mixing, i.e. through the use of baffles, would need to be completed. This phenomenon was not seen with the heavier particles because the end walls have a much smaller effect; the lighter particles are more susceptible to the increased friction and the distinction between the centre and edges of the drum is increased.

5.3.3 Agglomeration in coating processes

To help understand the differences in spreading between the different viscosity solutions, several experiments were conducted that looked at quantifying that mass of particles trapped in agglomerates. These structures, especially the larger ones, form relatively quickly on entry to the drum, and are gradually broken up as the process

progresses. It will be shown that the larger agglomerates have an ability to strongly effect the average red value being detected; they trap and hold several of the initial red-dyed particles and prevent the colour from being distributed around the bed, which results in localised, high concentrations of red colour. The formation of these agglomerates is seen more readily when using higher solution viscosities because of the increase in liquid bridge strength between particles. The lighter particles, as discussed in Chapter 4, have less kinetic energy in their collisions and, therefore, it is expected that they will agglomerate more readily.

5.3.3.1 Alumina 1: Effect of viscosity on agglomeration

For the initial agglomeration experiments, the smallest drum (A) and the denser Alumina 1 particles were used. Five sieve sizes were originally used to classify the particles; 2mm, 1.7 mm, 1.4 mm, 1.18 mm and 1 mm. In order that any agglomerates were not broken during the process, the material used in the agglomeration experiments were sieved by hand (not using the Retsch AS3000 machine). This prevented overly aggressive agitation of the particles and reduced the likelihood of agglomerates breaking. Small amounts of each batch were sieved at a time so that a visual inspection of the sieve fractions could determine whether the sieving process was finished or not. Weights and images were collected over each of these sieves for time points previously seen to be relevant to the coating for solutions with particular viscosities; i.e. it is known that the 179 mPa.s systems reach an asymptotic CoV value after a maximum of approximately 30 seconds, hence, studying agglomeration formation after this time would be of little benefit. Although the largest agglomerates were seen on the 2 mm sieve mesh, agglomerates containing 2 or 3 constituent particles were also seen on the 1.7 and 1.4 mm mesh sieves. To determine the percentage of the particles involved in agglomeration, the masses of particles on the 1.4, the 1.7 and the 2 mm sieves were summed and termed the weight of agglomerates. The d_{90} of both the Alumina 1 and Alumina 2 is approximately 1.2 mm; anything larger than this can be thought of as two particles stuck together which here constitutes an agglomerate. Figure 5-25 shows the change in percentage of agglomerates (by weight) as the process progresses for three solution viscosities. As predicted, the highest viscosity solution (20,200 mPa.s), shows the largest number of agglomerates at each of the time points, with several persisting long after

the two lower viscosity systems have no agglomerates remaining. At 5 seconds, approximately 21 % of the mass of the system was held in agglomerates, decreasing to 3 % after 180 seconds. Compared with the 179 mPa.s solution which has only 6 % agglomeration at 2 seconds decreasing to 0 after only a further 3 seconds, the 20,200 mPa.s solution clearly evidences relatively high agglomeration.

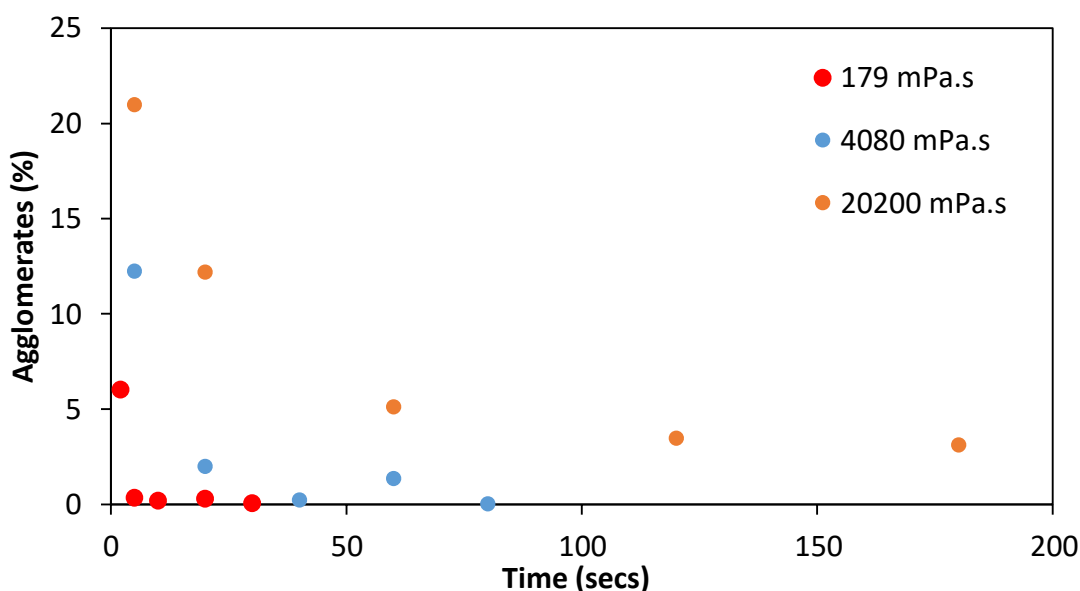


Figure 5-25. Percentage of total Alumina 1 particle mass present as agglomerates at several time points for three different viscosity solutions.

Table 5-5 is a visual representation of the data seen in Figure 5-25. An increase in time and a decrease in solution viscosity results in decreased likelihood of agglomeration formation; zero agglomerates were seen for the case of 179 mPa.s and a 60 second tumbling time. For shorter times and increased viscosities, agglomeration is highly likely; 20,200 mPa.s and a 5 second tumbling time saw agglomerates accounting for 21 % of the total mass. As well as an increase in the number of agglomerates, the size of agglomerates is considerably larger when using high viscosity solutions. For example, all the images taken of the 20,200 mPa.s system contain large agglomerates. It is however, unknown whether the agglomerates present at later tumbling times are being formed in the early stages of the experiments and persisting throughout the experiments, or whether the agglomerates are breaking and reforming within the system. Breakage and reformation seems unlikely considering the drying and distribution of the solution taking

place throughout the tumbling, seeming to suggest that large, strong agglomerates are formed in the early stages of the tumble and persist for long times.

Table 5-5. Images of Alumina 1 agglomerates larger than 2mm sieve size, for a variety of time points and solution viscosities.

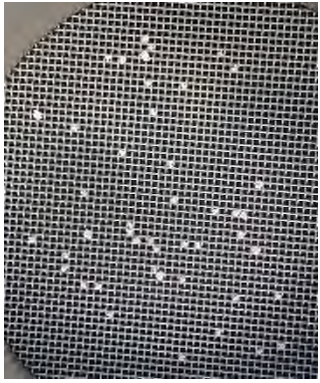
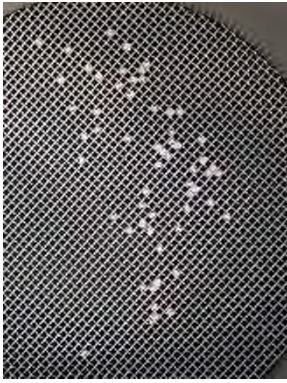
	Time (seconds)		
	5	20	60
179 mPa.s			-
4,080 mPa.s			
20,200 mPa.s			

Figure 5-26 shows the mean red % values for the agglomeration experiments conducted with 20,200 mPa.s viscosity solution. The agglomerates from the 2mm sieve were separated from the remaining material and analysed separately. The mean red value for

the particles constituting the agglomerates is much higher than that of the particles composing the bulk.

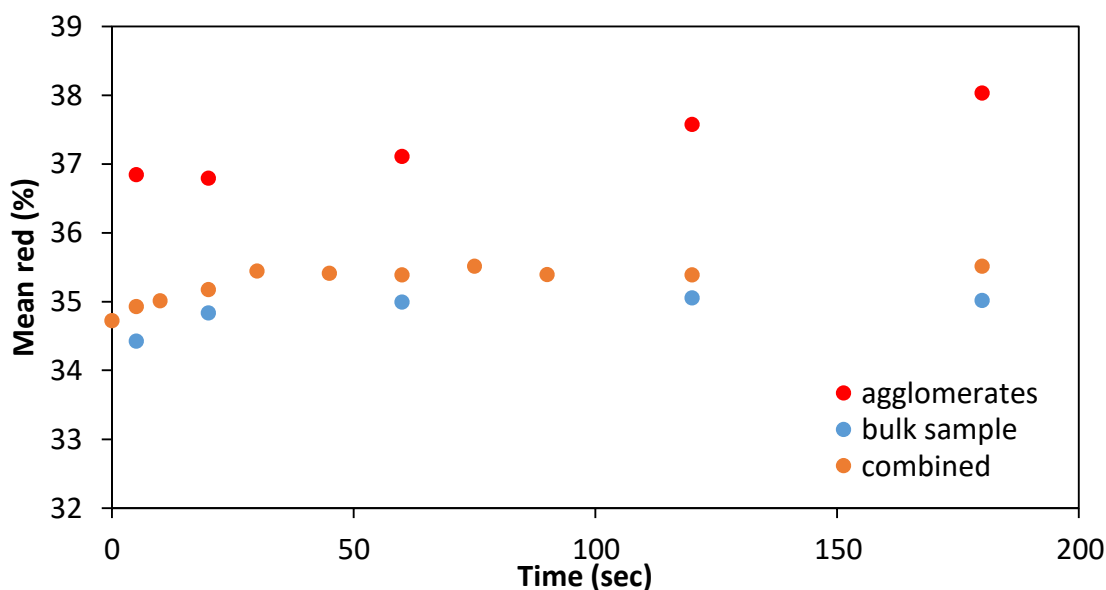


Figure 5-26. Mean red % values for Alumina 1 particles tumbled with 20,200 mPa.s viscosity solution.

An earlier experiment (called 'combined' on Figure 5-26) has been added to show the additive effect of the agglomerates along with the bulk sample. When considering the final application of this process, i.e. the desire to be able to distribute a material homogeneously around a powder bed, the formation of agglomerates is undesirable. Some understanding of the conditions in which they arise and how long they persist for in certain tumbling conditions is greatly important. Due to the small number of agglomerates generated when using the 179 mPa.s system, the colour from the agglomerate sample was hard to verify, and therefore no analysis data is presented.

It is interesting to note that in Figure 5-26, the mean red % of the agglomerates appears to slightly increase with time. One explanation for this could be that when agglomerates are first formed, there is excess liquid which coats the outside of agglomerates to which uncoated particles can loosely adhere. As time progresses, these more loosely adhered, whiter particles are more likely to be removed from the agglomerates, leaving a particle mass which has a higher red value (as the internal, very red particles are exposed when the whiter, external particles are removed). Figure 5-27 highlights a similar situation when using the 4,080 mPa.s solution. The agglomerates physically represent a much

smaller quantity of material, yet their red values are drastically increased compared with the bulk sample.

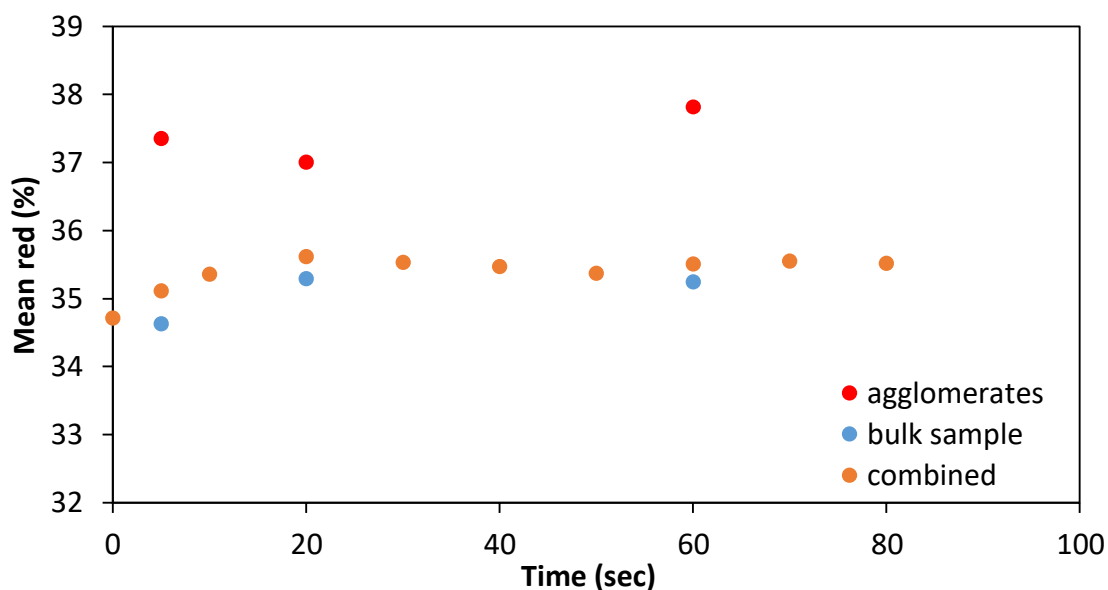


Figure 5-27. Mean red % values for Alumina 1 particles tumbled with 4,080 mPa.s viscosity solution.

5.3.3.2 Alumina 2: Effect of viscosity on agglomeration

The lighter Alumina 2 particles were then used to investigate agglomeration behaviour. The smallest drum (A) was again used to minimise material consumption. At the early time points, the agglomeration is expected to be similar to that seen with the Alumina 1. However, as the time increases and the collision impact becomes important, the number of agglomerates persisting in the system is expected to stay higher than that which is seen with Alumina 1. This was seen qualitatively when emptying the drum for the majority of the Alumina 2 experiments. The same sieving method was used to determine the mass of agglomerates at each time point.

As can be seen in Figure 5-28, the number of agglomerates formed with the 179 mPa.s and 4,080 mPa.s solutions is very low – they show a very similar trend to that seen with the Alumina 1 particles. With the 20,200 mPa.s solution a very similar trend is again identified; a high number of agglomerates decreases to give roughly zero agglomerates by 600 seconds.

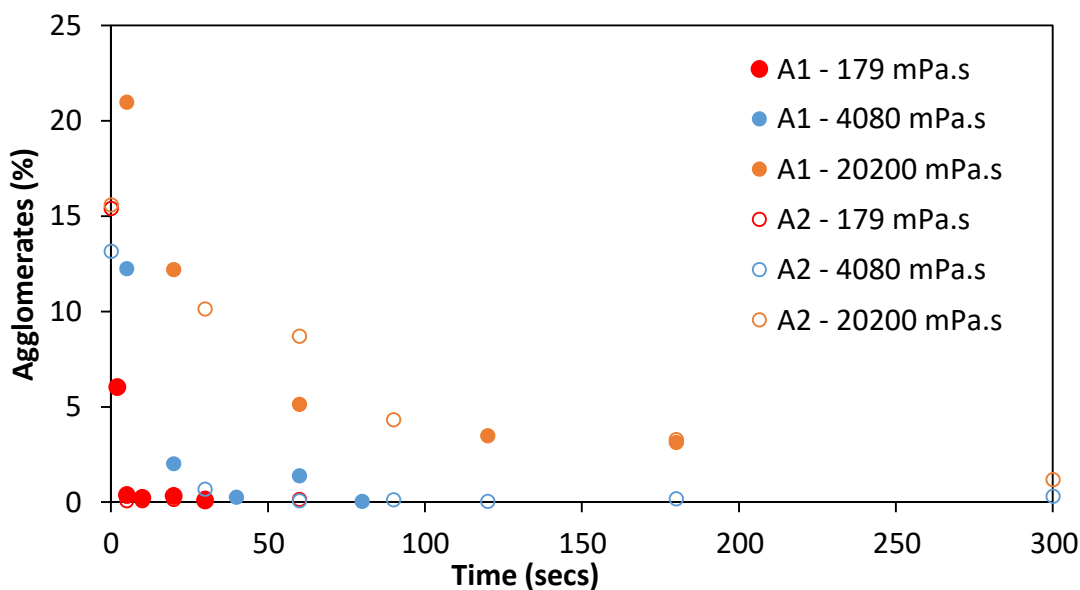


Figure 5-28. Percentage of total Alumina 2 particle mass present as agglomerates (o) at several time points for three different viscosity solutions with Alumina 1 shown for comparison (●).

However, the prediction that the experiments using Alumina 2 would show a much higher number of agglomerates appears to be incorrect. One possible reason for this could be experimental error. As the particles are left overnight to dry so that the image analysis can be successfully performed without altering the colour content on the particles, it can be difficult to determine which are the true agglomerates. The ones formed in the drum are more compact and spherical in nature whereas the ones which form as the particles are drying are much flatter and generally larger in nature. It was difficult to differentiate between the two, and hence this data should be treated with caution; it indicates a general trend but does not necessarily give a true reflection of absolute values. One method of doing this would be to immediately sieve the particles after the process. This would have given a truer representation of particle agglomeration. However, it could have also severely distorted the colour analysis for the determination of the CoV data which was the primary parameter of this investigation and so it was decided not to pursue this line of experimentation. Due to material constraints, the sieve fractions had to be remixed and the average CoV determined as opposed to analysing the colour of each individual fraction, as was done for the Alumina 1. Several images in Figure 5-29 show the difference between the agglomerates and the bulk colour. It appears that there is a slight change in the colour of the bulk material,

Chapter 5

Mechanistic understanding of contact spreading: Study of drum parameters

with an increasing red value with time. However, differences in the colour of the agglomerates are hard to determine from a purely visual analysis.



Figure 5-29. Colour comparison of agglomerates and bulk particles of Alumina 2 particles coated with 20,200 mPa.s PEG solution at three time points.

5.3.3.3 Alumina 1: Effect of drum size on agglomeration

Although the limitations of this method have been discussed, it has been shown to give a fairly accurate trend in terms of particle agglomeration. Here, data is presented which compares the agglomeration seen in Drum A and Drum B for Alumina 1 with 20,200 mPa.s viscosity solution. The lower molecular weight PEGs were not used in these experiments due to the fact that virtually no agglomeration was seen in Drum A. Figure 5-30 shows the agglomeration in Drum B is decidedly lower than that seen in Drum A for 20,200 mPa.s viscosity solution. Drum size is clearly influencing the collision energy; larger drums result in greater collision energy's which in turn result in less agglomerates. This fits with the work detailed in Section 5.3.1, the heavier particles coat slightly better in larger drums (see Figure 5-12). Unfortunately, due to material limitations, there was not enough material to perform the same experiment using Alumina 2. It would be interesting to investigate the agglomeration for these systems with respect to drum size; and help explain the earlier result that lighter particles coat more evenly and quicker in smaller drums.

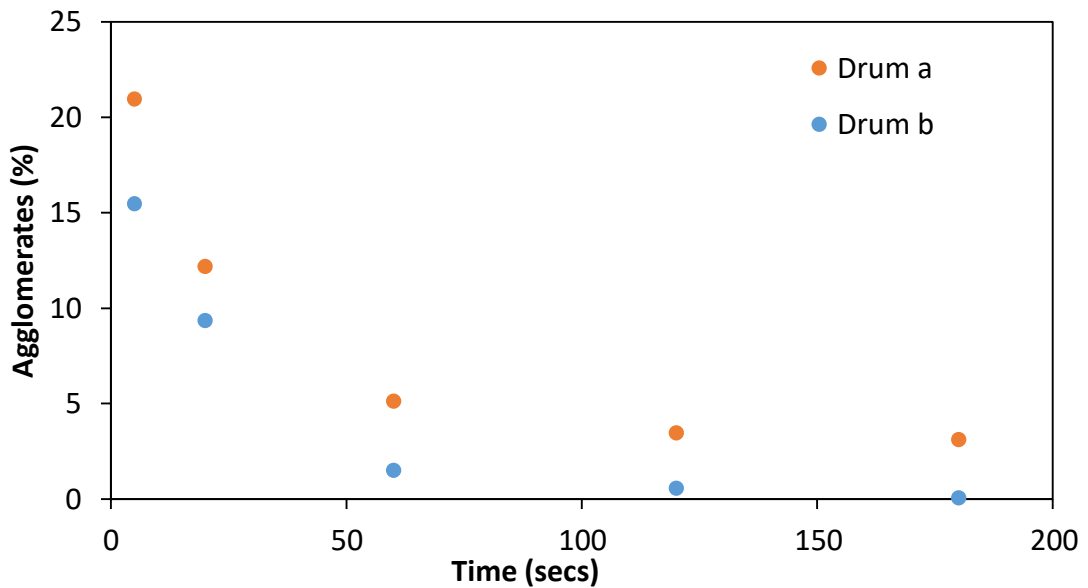


Figure 5-30. Comparison of percentage of agglomerates found in experiments completed in Drum A and Drum B as a function of time for Alumina 1 using 20,200 mPa.s viscosity coating solution.

5.3.4 Collision number

In this chapter, the effect of drum size has been considered, with experiments being conducted in four differently sized drums using three different viscosity coating solutions. The two different density particles exhibited opposing trends; the denser Alumina 1 particles coated quicker in the larger drums (but only for the 20,200 mPa.s coating solution) whereas the lighter Alumina 2 particles coated faster in the smaller drum. It is believed that these results can be explained as the result of two different mechanisms; firstly, the increased collision energy as a result of the increased drum size promotes particles rebounding upon collision and spreading of the liquid as a result. And secondly, the change in axial mixing which is increased with shorter and smaller drums as a result of the wall having an effect on a greater percentage of the particle bed.

The collision number (Co), calculated as described in Chapter 4, is shown in Figure 5-31 for all the experiments completed in this chapter using the denser Alumina 1 (log-normal plot). A linear trend is observed; coating time increases proportional to the Co number. The graph has been overlaid with squares which identify the viscosity of the coating solution used in the experiment.

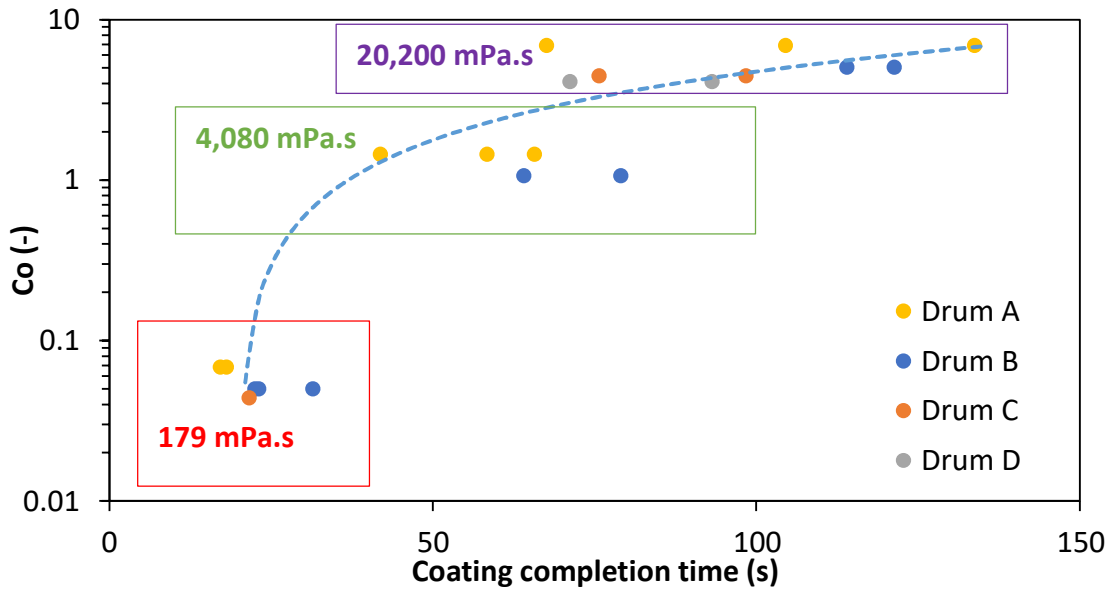


Figure 5-31. Co number against the coating completion time for all experiments completed in this chapter with Alumina 1. Labels show drum sizes, and viscosity of coating solution.

When using the 179 mPa.s coating solution, the coating completion times are similar regardless of the drum size. Again, this is very similar for the 4,080 mPa.s solution. The smaller drums may be coating slightly quicker as the collisions in all the drums have the necessary energy to rupture the liquid bridges, and the controlling mechanism therefore becomes the frequency of the interactions. These interactions are slightly more frequent in the smaller drums. However, with the highest solution viscosity (20,200 mPa.s), the opposite is true; larger drums appear to promote faster spreading. There is a large amount of spread in the experiments conducted in Drum A, but Drums B, C and D do show a trend. Here, it is more likely that fewer collisions in the small drum have the necessary energy to rupture a liquid bridge. There will be a distribution of collision energies, and if one experiment happens to contain a very narrow distribution of high collision energies, the smaller drums will promote more particle interactions and hence a very quick coating time may be possible. This could be one explanation for the data point representing the experiment in Drum A coated with 20,200 mPa.s with a completion time of approximately 70 seconds. As the drum size is increased, the number of collisions with this energy is increased, and hence the coating becomes quicker. If the Co is replotted against the number of drum revolutions needed to reach coating completion (Figure 5-32), this trend is easier to see. For a similar Co value, experiments

using the 20,200 mPa.s viscosity solution reach completion quicker when a larger drum is used.

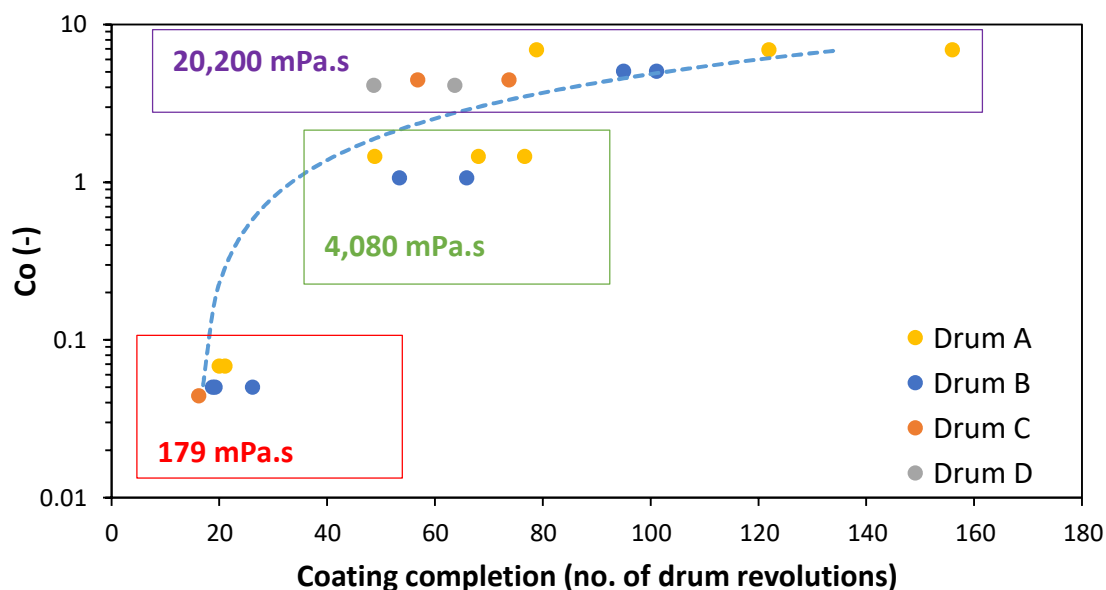


Figure 5-32. Co number against the number of drum revolutions needed to reach coating completion for all experiments completed in this chapter with Alumina 1.

Figure 5-33 shows the Co number plotted with the coating completion time for all Alumina 2 experiments completed in this chapter. The drum in which the experiment was completed is identified with a label, and the coating solution viscosity is also shown. Unlike Alumina 1, this data does not follow a linear trend (shown as the dotted line for justification). The data points from the 20,200 mPa.s experiments skew the data considerably; extremely long processing times are required to reach homogenous conditions.

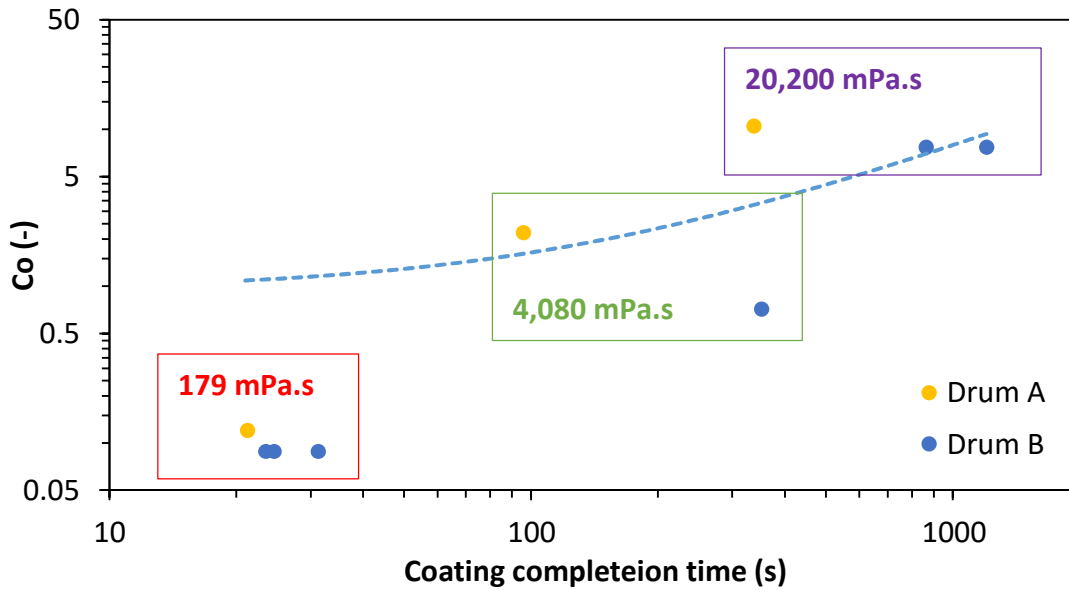


Figure 5-33. Co number against the coating completion time for all experiments completed in this chapter with Alumina 2.

Replotting the data against the number of drum revolutions needed to reach completion minimises the time difference between the a and b data points at each of the viscosities (Figure 5-34).

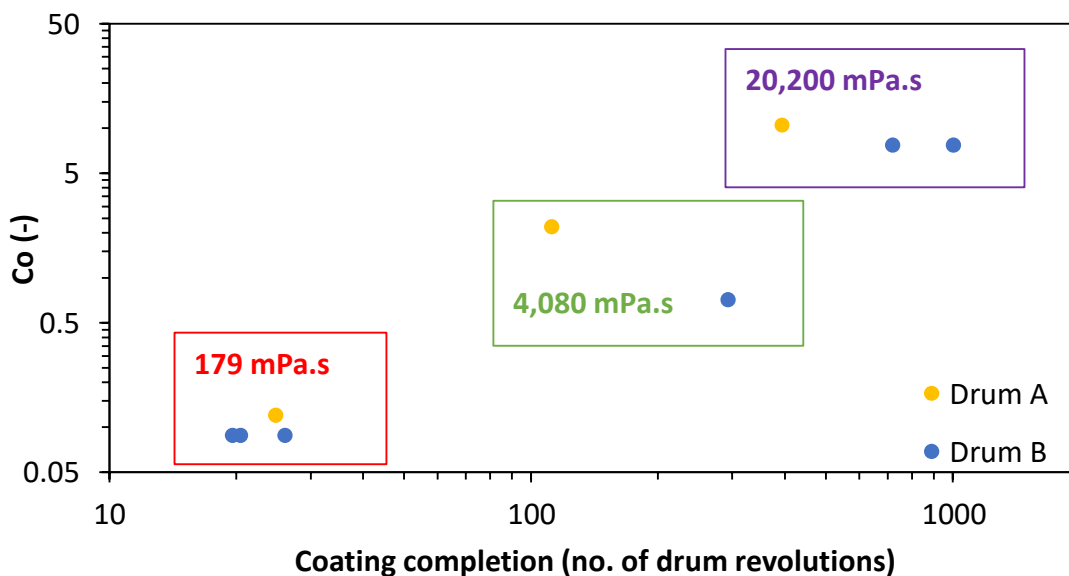


Figure 5-34. Co number against the number of drum revolutions needed to reach coating completion for all experiments completed in this chapter with Alumina 2.

However, for both the 4,080 mPa.s and the 20,200 mPa.s solutions, Drum A coats considerably quicker every time, requiring many less drum revolutions to reach the

same homogeneous coating. Clearly more data points and more drum sizes would be desirable, and give a more complete picture when using this lighter material.

Figure 5-35 shows the Co numbers for all the experiments completed in this chapter, Alumina 1 and Alumina 2. It appears that a linear relationship is capable of describing the majority of the experiment, apart from those which use a combination of high solution viscosity and low density material. In this region (highlighted with the blue box on Figure 5-35, other phenomena are clearly at play. This could include the differences in agglomeration, but it is also suspected that differences in the mixing regimes are also partly responsible.

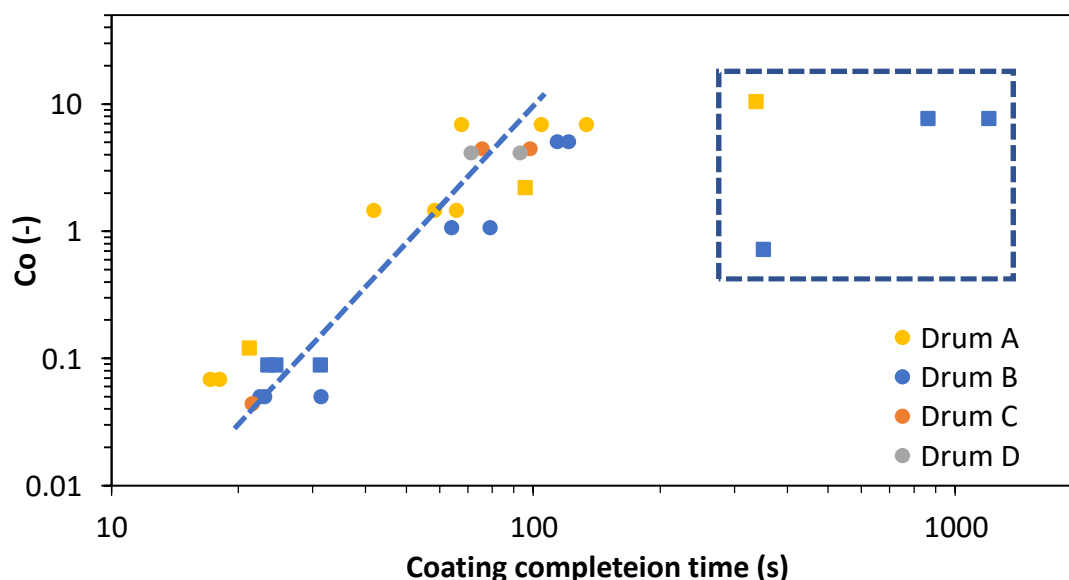


Figure 5-35. Co number against the coating completion time for all experiments completed in this chapter with Alumina 1 (●) and Alumina 2 (■).

5.4 Conclusions

In this Chapter, four different drum sizes have been used to investigate the effect on contact spreading, using Alumina 1 and Alumina 2 with three different viscosity solutions. All the experiments conducted here showed some form of contact spreading and reached a relatively high level of uniformity (low CoV value). The time taken for systems to homogenise differs drastically; the lighter Alumina 2 particles take much longer than the denser Alumina 1 particles. The Co number was used and plotted against both the time taken and the number of drum revolutions required to reach coating

Chapter 5

Mechanistic understanding of contact spreading: Study of drum parameters

completion; experiments taking below 200 seconds to reach uniformity were well captured by the Co number. Those taking long times i.e. the experiments which combine high coating viscosity and low material density, appear to less well related. Increasing the drum size had differing effects dependent on the particle density; low density particles coated more quickly in small drums whereas high density material coated quicker in larger drums. This is thought to be a result of differences in particle mixing.

In Chapter 6, a more industrially relevant particle, sodium percarbonate, will be used to investigate the effect of various parameters, both operational and material related. It is hoped that more data pertaining to this low density material will help elucidate findings in the region which, so far, are not well modelled by the Co number.

6. Mechanistic understanding of contact spreading: Study of material characteristics and drum properties

Sodium percarbonate has been used to study material characteristics beyond those available through the testing of model materials. The effect of particle size, size distribution, solution viscosity, drum speed and size have all been investigated, with varying degrees of effect on the contact spreading; particle size distribution and liquid viscosity have the biggest effect on the rate of coating. Although contact spreading was observed in these systems, the extent of the coating was less than for the model alumina systems. This can be attributed to 1) the ingress of liquid and 2) the agglomeration under certain conditions. Higher viscosity solutions promote greater agglomeration, as do higher percentages of fines in a size distribution, and lower drum speeds. Small-scale studies compliment this work and look at the development of liquid bridges between two particles; the bridge development rate varies with the particle velocity and solution viscosity, corroborating results from the main work. The collision number is presented for the experiments in this chapter and shows that parameters other than those captured in the Co number are clearly important for mapping the contact spreading.

6. Mechanistic understanding of contact spreading: Study of material characteristics and drum properties

6.1 Introduction.....	160
6.2 Methods.....	161
6.3 Results and discussion.....	166
6.4 Conclusions.....	192

6.1 Introduction

In both Chapters 4 & 5, alumina particles have been used as a model system; they are spherical, white, non-reactive and have a narrow size distribution. However, although this allowed a basic understanding of some factors affecting the contact spreading of liquids between these particles (density, viscosity, drum size, drum speed), more complex systems are needed for further investigations, relevant to industrially realistic systems. Here, sodium percarbonate was chosen. The material has a wide size range, more irregular surface structure, increased porosity, and is potentially reactive with other materials including coating liquids. It comprises greater than 10 % by volume of most commercial powdered detergents (Zonfrilli et al., 2009), and is still compatible with the current image analysis technique due to its white colour.

The sodium percarbonate will allow an extension of the effect of material characteristics described in Chapter 4 to be completed. The density is even less than that of the Alumina 2 particles and therefore furthers the study of particle density. As discussed in Chapter 5, agglomeration was observed to be a factor in contact spreading. The sodium percarbonate, being extremely light and having a much larger percentage of small constituent particles than either the alumina particles, may be expected to agglomerate in the presence of a coating liquid. Unlike the model alumina materials, sodium percarbonate is relatively porous, and liquid ingress may also be a factor to consider.

The main objectives for this chapter are;

- Confirmation of findings from earlier chapters using a non-model particle.
- Investigation into drum agglomeration, and identification of how this is likely to affect liquid contact spreading.
- To gain an understanding of the effects of realistic particle properties on the contact spreading mechanism. This includes addressing the material porosity, the size distribution, and the particle density.
- Micro scale liquid bridge experiments to study the evolution of liquid bridges under dynamic conditions.

6.2 Methods

Here, instead of the two model alumina materials used in Chapters 4 and 5, sodium percarbonate is used as a more industrially applicable material. However, the experimental methodology and the data analysis technique will remain the same (Chapter 3, Section 3.4). A recap of the particle properties is presented in Table 6-1, and those of the liquid are presented in Table 6-2.

Table 6-1. Particle properties for sodium percarbonate.

Property	Sodium Percarbonate
Envelope density (g/cm ³)	1.62 ± 0.027
d ₁₀ (μm)	370
d ₅₀ (μm)	840
d ₉₀ (μm)	1314
Porosity (%)	24.2

As can be seen from Table 6-1, the size distribution of the sodium percarbonate is very large, with a very high number of fines (refer to Figure 3.3, Chapter 3, for further detail). The porosity is also very much increased in comparison to both of the alumina particles.

Table 6-2. Coating liquid properties for the 50 % PEG aqueous solutions and 50 % PEG in 10 % ethanol /water PEG solutions.

Property	Molecular weight (Da)			
	4,000	10,000	20,000	35,000
50 % PEG aqueous solutions				
Viscosity (mPa.s)	179.3 ± 0.947	810 ± 4.43	4,080 ± 69.9	20,200 ± 630
Surface tension (mN/m)	56.1 ± 0.47	56.14 ± 0.82	56.8 ± 0.81	56.0 ± 0.76
50 % PEG in 10 % ethanol / water solutions				
Viscosity (mPa.s)	102 ± 3.57	512 ± 5.80	2,920 ± 55.7	14,600 ± 528
Surface tension (mN/m)	55.14 ± 0.55	56.89 ± 0.89	57.74 ± 1.27	55.33 ± 0.99

Chapter 6

Mechanistic understanding of contact spreading: Study of material characteristics and drum parameters

The liquid data pertains to the normal 50 % water / PEG solutions used as standard in Chapters 4 & 5 and the 50 % PEG in 10 % ethanol / water solutions used exclusively in this chapter, which have slightly different viscosity values but very similar surface tensions. When the original 50 % water / PEG solutions were mixed with the sodium percarbonate, there was some evidence of the PEG precipitating out of solution. To combat this, 10 % ethanol was added to the PEG solution (Chapter 3, Section 3.3).

When calculating the liquid addition for the alumina experiments, only the surface area needed to be considered as the particles are extremely non-porous. The sodium percarbonate however, has a high porosity, irregular shape and large size distribution and finding the correct volume of liquid to add to the experiments to ensure they are comparable to the alumina experiments presented difficulties. Addition of the same mass (0.71 g) of liquid would have left little to no liquid on the particle surface due to liquid ingress. However, if the liquid addition was calculated by attempting to account for the sodium percarbonate porosity, shape irregularities and wide size distribution, the value for liquid addition was far too high (3.04 g), with trials showing excessive amounts of liquid left over. Excess liquid is undesirable as it could act as a 'spray' when moving particles into the drum, and the point of the experiments is to isolate the contact spreading mechanism by removing the liquid spray. The assumptions used to calculate the liquid mass needed were perhaps too broad, and therefore a more trial and error approach was adopted in order to find a mass of liquid which did not result in excess liquid being leftover. A number of trials were completed whereby different volumes of liquid were added to the particles and the resulting mixture was assessed for its available surface liquid content by visual inspection. A liquid mass of 1.4 grams was eventually decided upon and used in all experiments in Drum A when using the size fraction with the < 800 μm sized particles removed, showing a comparable surface wetness to the alumina experiments. The surface wetness was deemed comparable to that seen in the experiments using alumina particles purely by visual inspection of the particles and the liquid loading. The liquid masses added to when using different size fractions can be seen in Table 6-3.

Table 6-3. Size fractions of sodium percarbonate used in experiments with corresponding liquid volumes.

Size fraction (μm)	Liquid mass (g)
850-2,000	22.26
425-610	2.02
710-850	1.72
1,400-1,700	1.12

The decision to use the 10 % ethanol / water PEG solutions was taken as a result of the precipitation of the PEG out of solution when the original fully aqueous PEG solutions were used; more details of which can be found in Chapter 3, Section 3.3. This effect was seen more strongly when using the high molecular weight PEGs; the 4,000 MW showed no signs of precipitation in aqueous solution and was used successfully in a number of experiments. All the results presented herein indicate clearly which solution was used as the coating agent.

6.2.1 Tumbling drum experiments

Drum A (length 0.17 m, diameter 0.11 m) was used for most of the experiments completed in this chapter, with a 10 % drum fill level and run at 70 rpm (cascading regime). However, a larger drum (C) (length 0.408 m, diameter 0.263 m) was used for studying the effect of scale . Again, all experiments were completed *without the use of a spray component* in order to study contact spreading only. Before being placed in the drum, 10 % of the total particle volume was coated as evenly as possible with a liquid solution (either 50 % aqueous PEG or 50 % PEG in 10 % ethanol /water) outside the drum.

Table 6-4. Dimensions of drums used in this chapter.

Drum	Diameter (m)	Length (m)	Volume (m^3)
A	0.11	0.17	0.0016
C	0.265	0.408	0.0225

Chapter 6

Mechanistic understanding of contact spreading: Study of material characteristics and drum parameters

The remaining 90 % of the uncoated particles were added to the drum and tumbled to allow the cascading flow regime to develop. The coated particles were then added to the uncoated particles in the tumbling drum through the use of a delivery arm inserted into a hole in one of the drum ends, and a stopwatch was simultaneously started. After a certain tumbling time, the drum was stopped and the entire batch was removed for sampling and analysis. A fresh batch of particles was then added to the drum, and the procedure was repeated for a number of different tumbling times, ranging from zero seconds through to 600 seconds. After allowing each batch to dry, the particles were riffled using a chute splitter to obtain a representative sample of approximately 10 g. Sixteen images were then taken of each sample, and Labview software was used to determine the RGB value of each individual particle. As was described in Chapter 3, section 3.4.2, the coating variability is quantified by the coefficient of variation seen in the red value, and is calculated as the standard deviation seen in the red intensity value divided by the mean red intensity value. The coefficient of variation was calculated for each of the 16 images and averaged to give a representative value for each time point. The CoV can then be plotted as a function of tumbling time to give an indication of how the coating uniformity changes with time. A more detailed description of the methodology and imaging analysis can be found in Chapter 3, Section 3.4.

6.2.2 Liquid bridge growth experiments

Preliminary experiments (Sherburn & Green, 2018) were completed to investigate the behaviour of liquid bridges upon single particle-particle collisions in the presence of a coating liquid. The experimental set-up is shown in Figure 6-1.

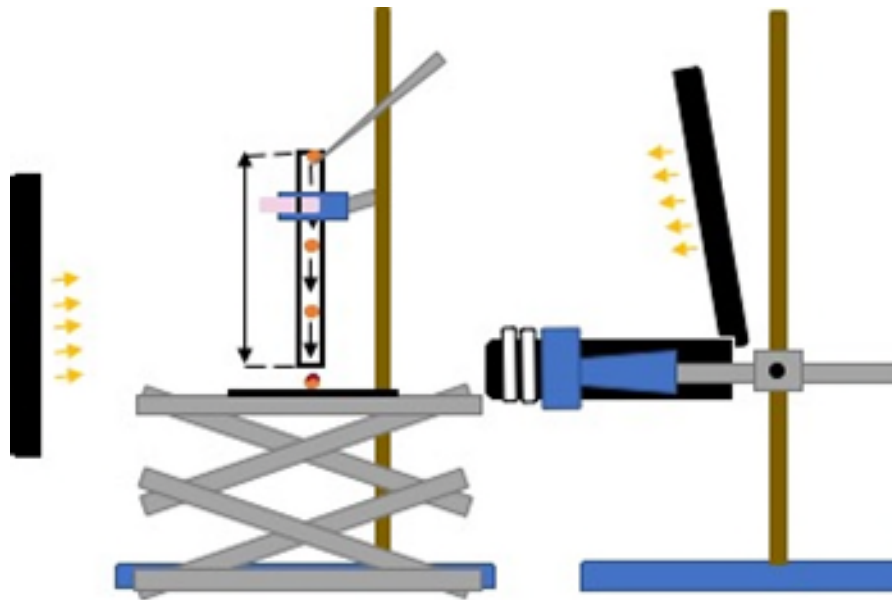


Figure 6-1. Experimental set-up of particle-particle collision experiments.

A high-speed camera (Mikrotron EoSens MC1363) was focussed on a single stationary particle, adhered to adhesive tape, and captured images at a rate of 110 frames per second. A micropipette (Thermo Scientific Finnpiette F2) was used to apply a liquid droplet (volume 0.30 mm^3 or 0.52 mm^3) to the stationary particle and a second particle was then dropped onto the stationary particle. The time between placing the drop on the first particle and releasing the second particle was minimised as far as possible (maximum 10 seconds) to ensure the droplet drying did not affect the results of the experiment. Glass tubing (internal diameter 2 mm) was positioned directly above the stationary particle, with a 200 mm gap from the bottom of the tubing to the top of the stationary particle, to guide the falling particle onto the stationary particle. The tube length was varied to change the collision velocity (0.71 m/s and 1.7 m/s). To provide adequate lighting, one light (Godox LED308C) was positioned in front of the particle and another behind it. Sodium percarbonate particles in the size fraction 1.7 – 2 mm were used to improve the image capture ability, and improve the chances of locating a droplet on the particle surface. ImageJ was used to process the images and measure the width of the liquid bridge.

6.3 Results and discussion

The aim of the work in this chapter is to understand the influence of using a realistic powder material. The results here again show the effect of liquid viscosity as well as the effect of the size distributions of the particles to be coated.

6.3.1 Effect of particle size distribution

The first set of experiments used the entire unsieved size range of the sodium percarbonate (i.e. the product was used as delivered from the supplier) and the 179 mPa.s solution and were completed in Drum A. Figure 6-2 shows images taken from one such experiment at various time points.

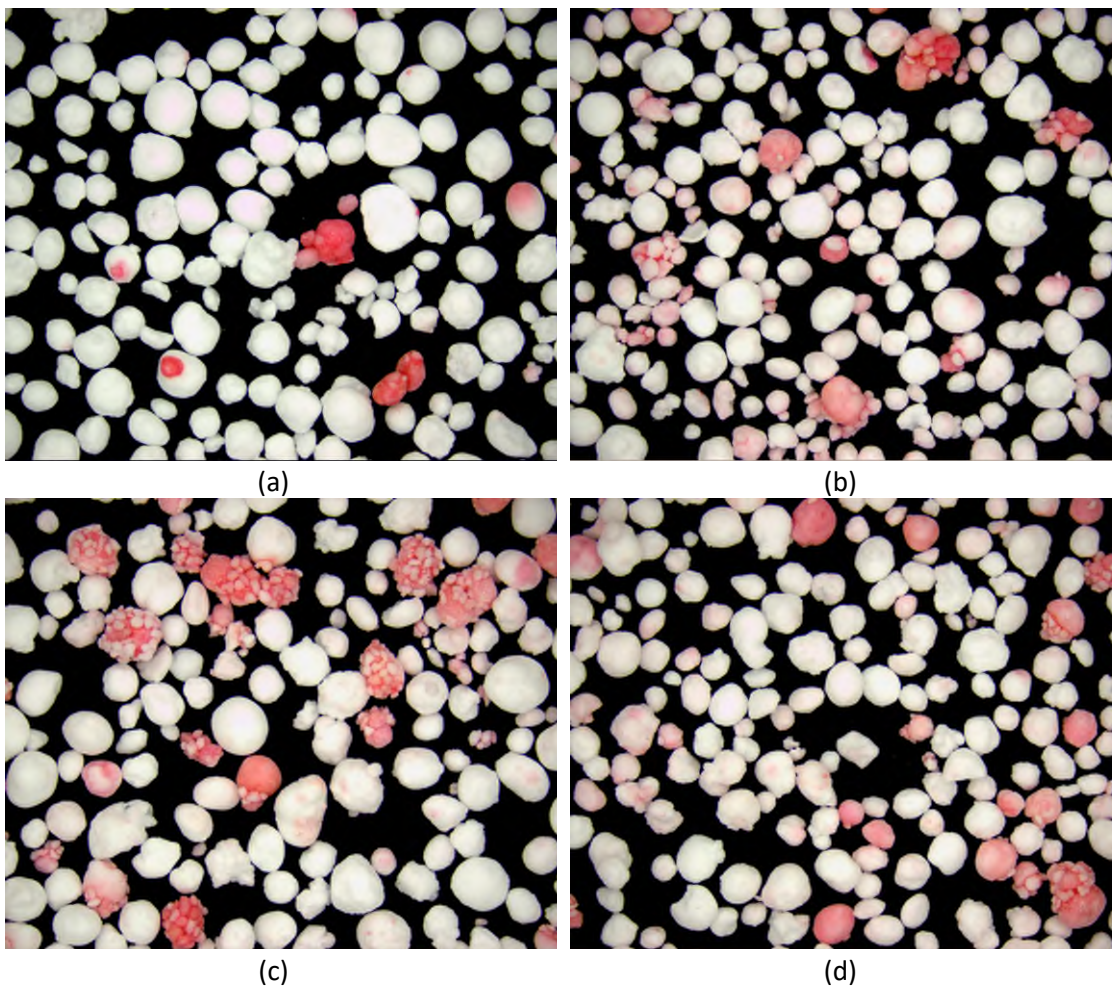


Figure 6-2. Sodium percarbonate particles coated with 179 mPa.s viscosity PEG solution and tumbled for a) 0 seconds, b) 30 seconds, c) 60 seconds and d) 300 seconds.

Because of the large extent of agglomeration, particularly between one large and several fine particles, it was difficult to obtain quantitative data. The Labview software was unable to separate the constituent particles from the agglomerates. However, regardless of the lack of quantitative data, there are still signs of contact spreading. Many of the particles at the zero second time point appear to be almost brilliantly white, a feature which is not present at any of the other time points even though the same brightness and contrast was used to image all of the particles. Figure 6-3 shows the CoV data that was acquired from this experiment; obviously due to severe agglomeration, there appears to be no decrease of the CoV with time. A relatively low initial CoV increases before plateauing around 7.5 %. The initial value could be low due to the fact that all the solution is trapped within a small percentage of the particles and it is difficult to extract data from these larger agglomerates because they are covered in fines. There is, therefore, clearly a large effect of the particle size distribution on the liquid distribution and CoV of the system.

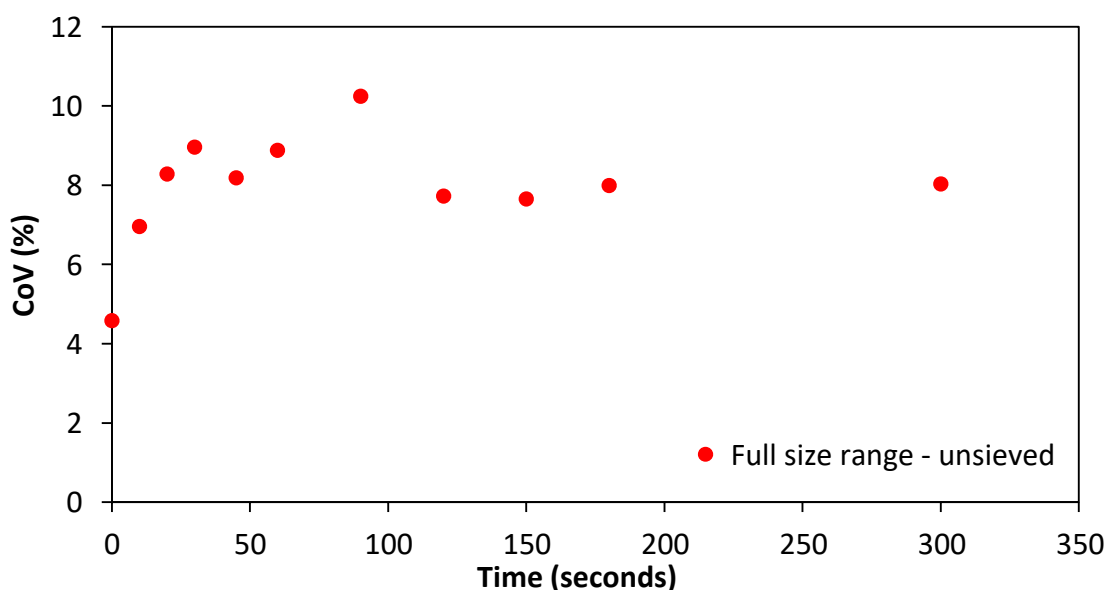


Figure 6-3. CoV as a function of tumbling time for unsieved sodium percarbonate coated with 179 mPa.s viscosity PEG solution in Drum A.

In an attempt to control the size distribution of the particles, the material from the supplier was sieved into size fractions before it was placed in the drum and each batch

of powder used at each time point was made up of the same size distribution of material. The size fractions are shown in Table 6-5.

Table 6-5. Sodium percarbonate size fractions.

Size fraction (µm)	% of material in size fraction
< 500	10
500 – 1,000	30
1,000 – 1,500	40
1,500 <	20

In Figure 6-4, an experiment using the size fractions presented in Table 6-5 is shown as the triangular data points ('Full size range – sieved'). A very similar pattern for the CoV is seen for the sieved data compared with the unsieved data. This could indicate that the size fractions of the material used at each of the time points for the unsieved experiments was not varying extensively, i.e. they had the same size distribution as the sieved material just by chance, or the CoV was being dominated by a particular size fraction, e.g. having 10 % fines dominated the system regardless of the size of the remaining 90 % of particles.

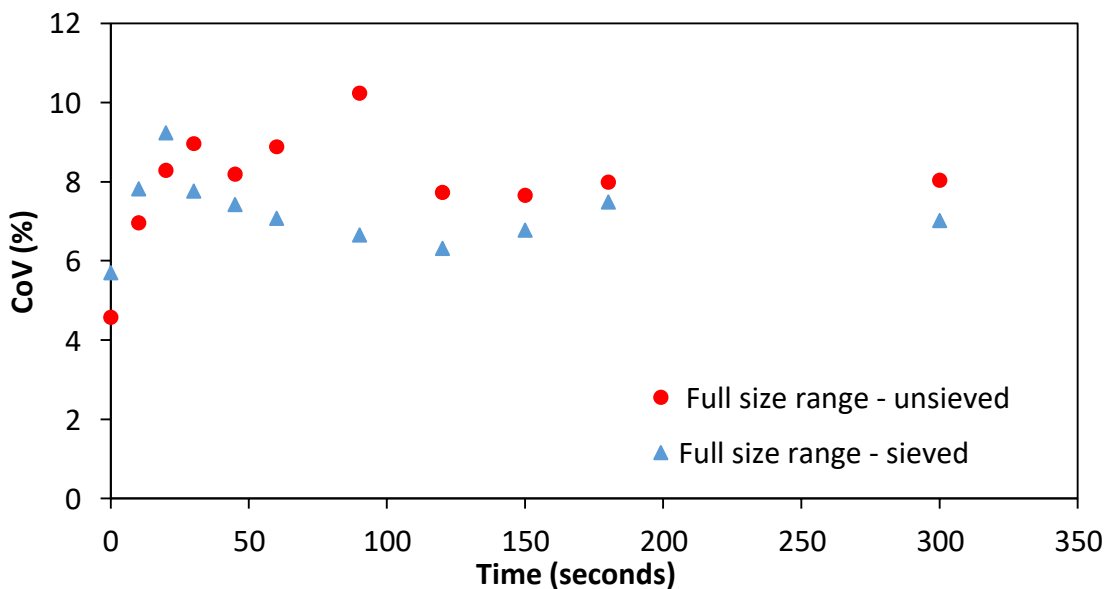


Figure 6-4. Unsieved sodium percarbonate compared to sieved sodium percarbonate (size fractions as per Table 6-4) in Drum A.

Other authors (e.g. Wang et al., 2015) have shown the tendency of smaller particles to typically grow by agglomeration in comparison to larger particles which tend to grow by layering (obviously, this is dependent on system conditions). As a result of this, experiments were conducted in which all the finer material (< 850 μm) had been removed, and each time point had the same size distribution, as seen in Table 6-6.

Table 6-6. Updated size fractions with fines < 850 μm removed.

Size fraction (μm)	% of material in size fraction
<850	0
850 - 1080	30
1080 - 1400	40
1400 <	30

As well as having a controlled size distribution, this also gave the material a size distribution more comparable to that of the alumina particles, making it easier to make direct comparisons between the two materials. Three experiments were then completed using the new size distribution and the 179 mPa.s viscosity 50 % PEG solution, as seen in Figure 6-5.

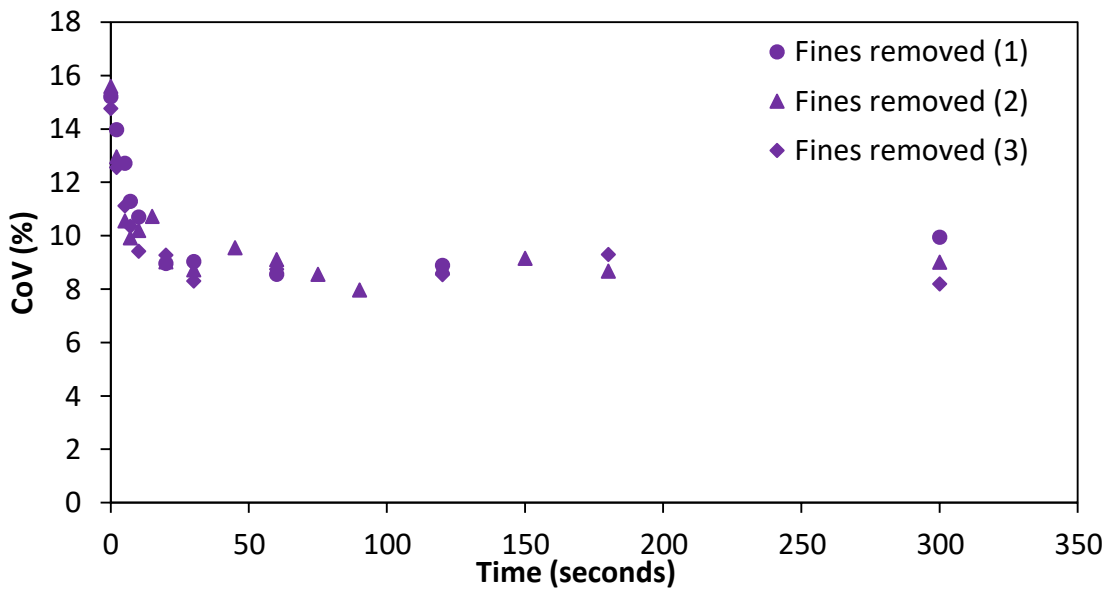


Figure 6-5. CoV as a function of tumbling time for sieved sodium percarbonate (>850 μm) coated with 179 mPa.s viscosity coating solution in Drum A. Brackets in legend refer to experiment repeat number.

The experiments are very repeatable, starting with a CoV around 15 % and finishing with a CoV around 9 %. After approximately 20 seconds there is no change in the CoV with time but clearly the liquid is not homogenously distributed. This could be a result of low liquid availability due to adsorption or drying on the particle surface. This will be investigated further in Section 6.3.4.

The difference between Figure 6-4 and Figure 6-5 can be explained as a result of a difference in agglomeration. Figure 6-6 shows the percentage of agglomerates as a function of the tumbling time for the full size range (both sieved and unsieved) experiments and the experiments with the fines (<800 μm) removed. Both of the experiments using the full size range show extensive agglomeration which persists even after 300 seconds of tumbling. When the fines are removed, agglomeration is not a concern when using the 179 mPa.s solution in Drum A. After 5 seconds, less than 2 percent of the entire sample is made from agglomerates compared with up to 15 % for the unsieved full size range samples.

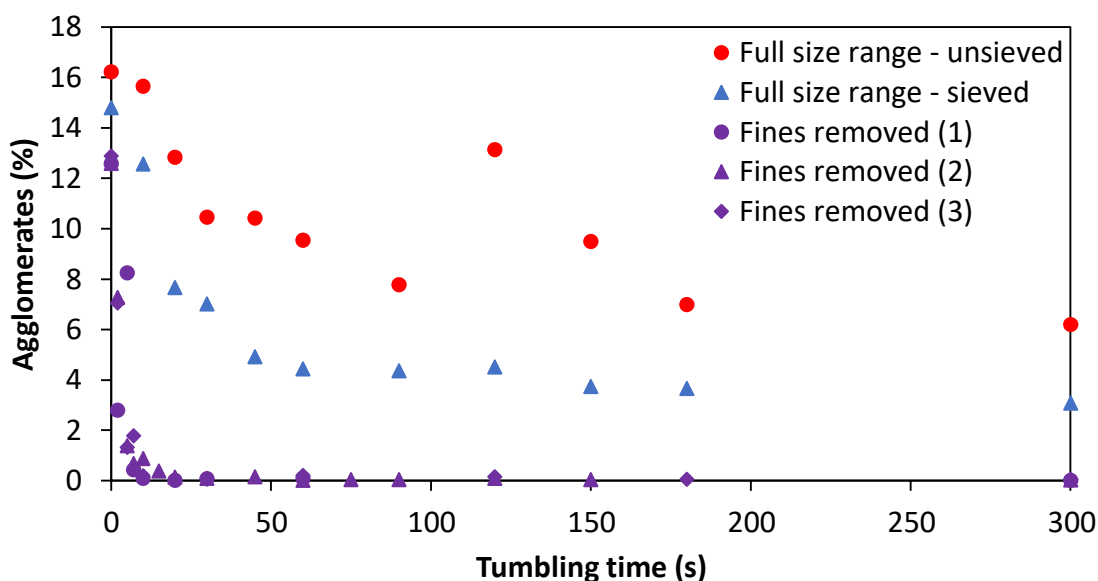


Figure 6-6. Percentage of agglomerates as a function of tumbling time for the full size range unsieved and sieved compared with experiments where the fines have been removed (179 mPa.s coating solution) in Drum A.

Figure 6-7 shows the sodium percarbonate with fines less than 850 μm removed compared with both the Alumina 1 and Alumina 2 model particles. All the experiments were conducted in Drum A with 179 mPa.s viscosity 50 % PEG solution.

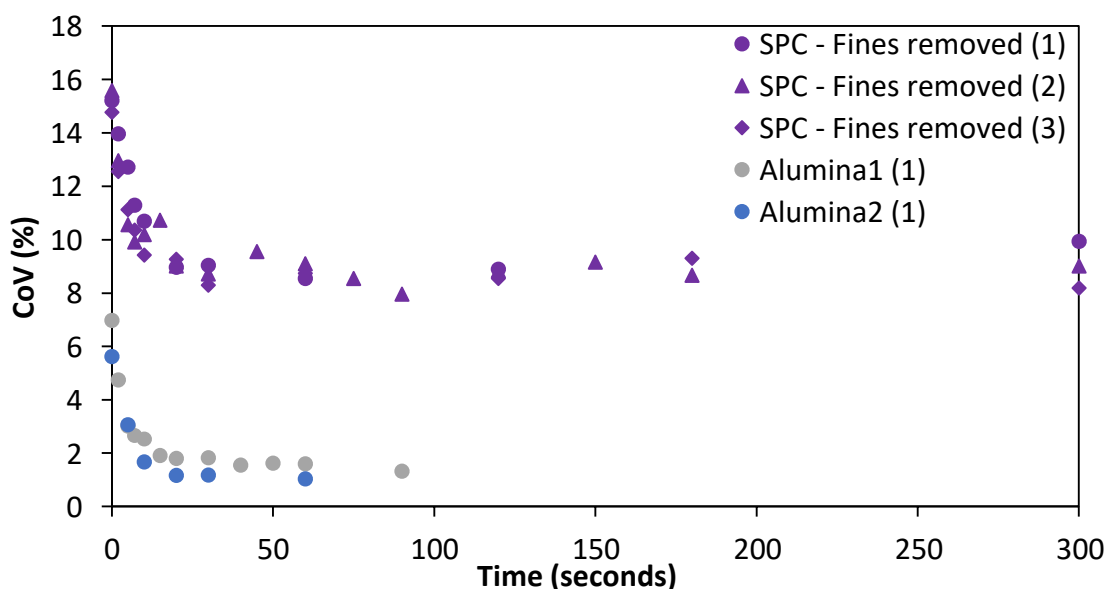


Figure 6-7. Comparison of the effect of particle material on the CoV as a function of time, all coated with 179 mPa.s viscosity PEG solution in Drum A. Legend shows particle material and experiment repeat number in brackets.

Chapter 6

Mechanistic understanding of contact spreading: Study of material characteristics and drum parameters

The trend is remarkably similar; however, the absolute values are drastically different. The sodium percarbonate systems start with a CoV of approximately 15 % and decrease down to 9 %, whereas the alumina systems start around 7 % and decrease to approximately 1 %, showing a much greater homogeneity by the end of the coating process. This lower asymptotic value could be due to two reasons; the particle density which influences the agglomeration, or the volume of liquid which is available to transfer. Although the liquid volume was determined to give a similar surface wetness (as explained in Section 6.2), it is very difficult to quantify the rate of liquid ingress into the particle structure, the evaporation of the solution, any possible reaction of the sodium percarbonate with the PEG solutions and to account for the sphericity (or lack thereof) of the particles.

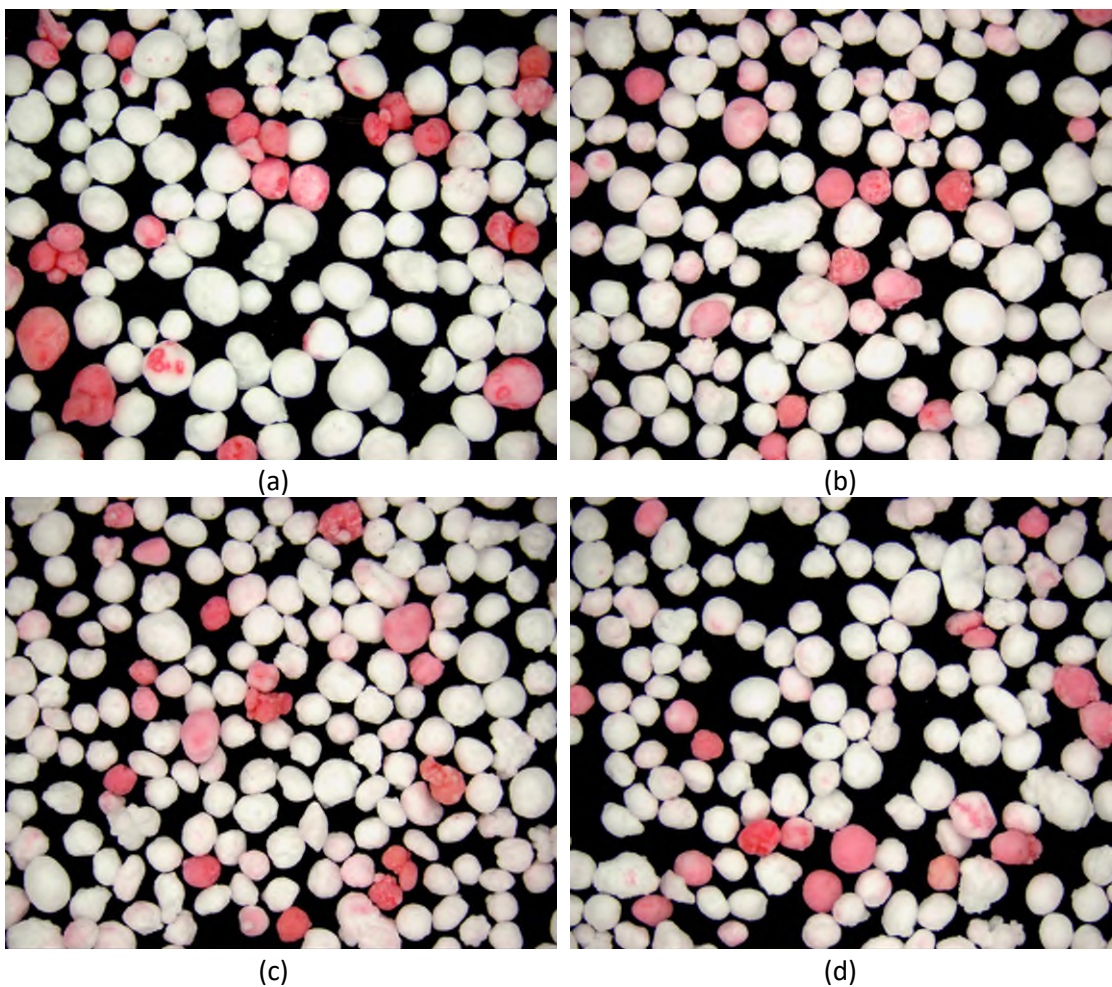


Figure 6-8. Sodium percarbonate particles greater than 850 μm coated with 179 mPa.s viscosity 50 % PEG solution and tumbled for a) 0 seconds, b) 30 seconds, c) 60 seconds and d) 300 seconds.

Figure 6-8 shows qualitative images of the contact spreading on the sieved sodium percarbonate particles with each time point having a controlled particle size distribution. There is a drastic difference between the images seen here and between the earlier images in Figure 6-2. The removal of the fine particles results in far less agglomeration which, therefore, allows more contact spreading to occur. There are obvious signs of small quantities of red material present on a number of particles even after 30 seconds. It is unlikely that these particles were part of the mass that is coated outside the drum; these appear much more intense in red colour. After seeing the drastic effect that the fines were having on the coating process, several experiments were completed to try and quantify the effect of particle size on the coating spreading.

6.3.2 Effect of particle size

Figure 6-9 shows the effect of the initial particle size on the contact spreading, as quantified by the CoV, with time. For each of the sizes, the repeats closely match; there is some variation in the 1400 - 1700 μm size range, but enough consistency to have confidence in the results.

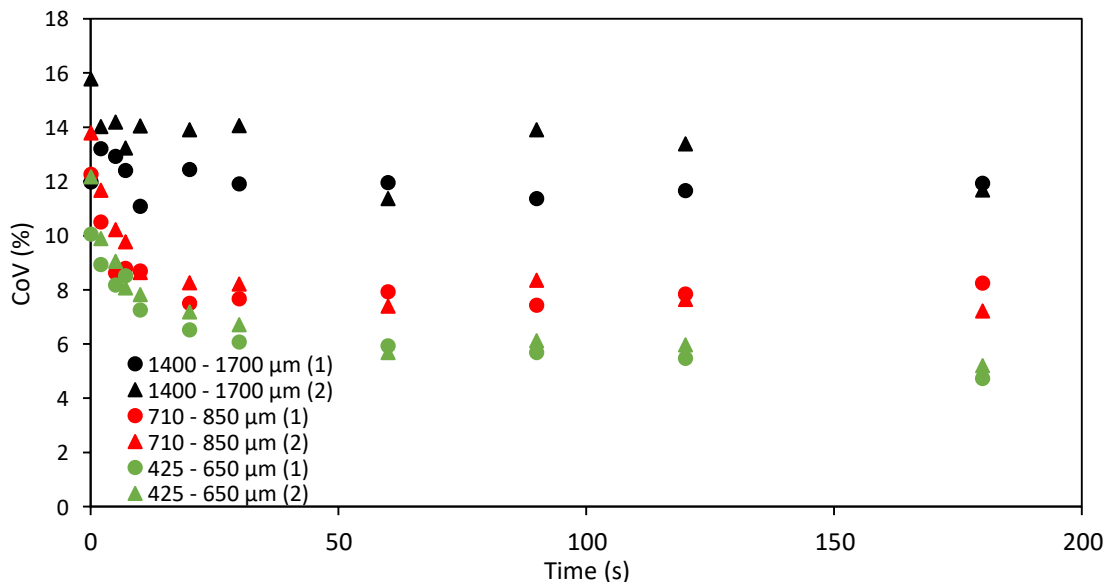


Figure 6-9. Effect of initial particle size on the CoV as a function of tumbling time using 179 mPa.s viscosity PEG solutions in Drum A. Legend shows particle size range and experiment repeat number in brackets.

Chapter 6

Mechanistic understanding of contact spreading: Study of material characteristics and drum parameters

Interestingly, the smaller particle size (425 - 610 μm) coats to the lowest asymptotic CoV in the quickest time, reaching an asymptotic value of approximately 5 % after 30 - 40 seconds. The 710 – 850 μm size asymptotes at approximately 7 %, but does show a very rapid initial decay, similar to the small particles. The large particle size shows virtually no contact spreading; there is a decrease in the CoV from around 14 % to 12 %, but due to the variation in this data these values are hard to accurately determine. This effect was unexpected. Previously, narrowing of the size distribution through removal of the fines resulted in a drastic improvement of the contact spreading. Here, although the size range is narrow, the smallest particles show the best contact spreading.

Figure 6-10 shows qualitative data for the effect of particle size. The magnification was adjusted for each of the particles to ensure a similar number of particles were being captured in each image. When considering the largest particle size, there appears to be no contact spreading; particles are either red from the initial application of the liquid, or are still perfectly white. This suggests there is no liquid available for transfer between the particles, or the uncoated particles are not colliding with the coated particles. Even though the material has the same composition no matter the size fraction, perhaps there is some difference in the internal and / or surface structure which aids the ingress / trapping of liquid, making it unavailable for liquid transfer. Both of the smaller particle size ranges do show contact spreading, with the 425-610 μm range reaching the lowest asymptotic value (approximately 5 %).

There is also a notable difference in the shape of the size fractions. From Figure 6-10 it appears that the larger particles are more spherical in structure, whereas the smaller particles have less spherical structures. This is not unexpected; assuming at least some small particles are the result of larger particles fracturing, it is almost impossible they would fracture and result in spherical chippings. It would, however, be interesting to isolate and assess the effect of this parameter on contact spreading in some future work.

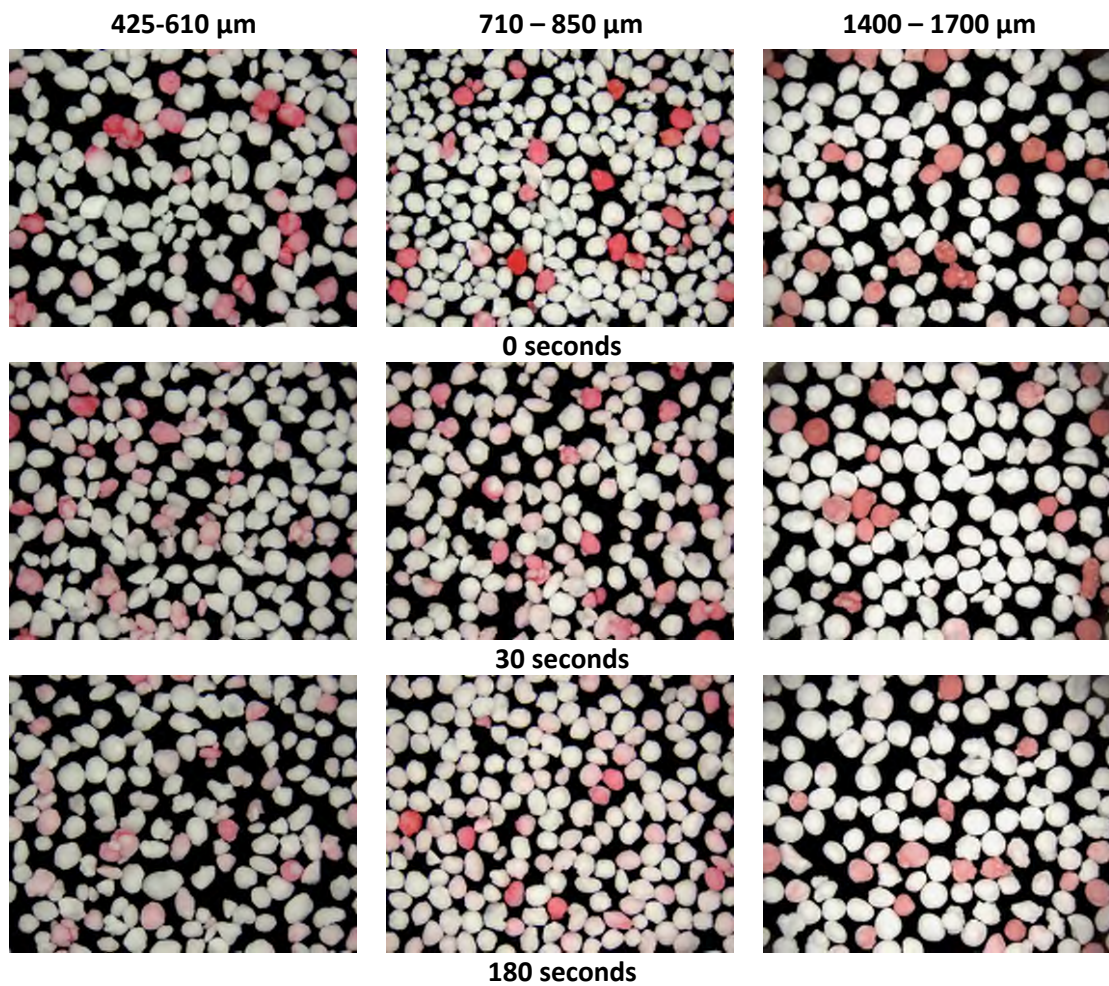


Figure 6-10. Comparison of images of different sodium percarbonate particle sizes coated with 179 mPa.s viscosity PEG solutions.

Figure 6-11 shows the percentage of agglomerates present at each time point for 3 different experiments using different particle sizes. Both of the smaller particle size fractions show much greater agglomeration than is seen with the larger particle size. This does make sense; removal of the fines in the earlier experiment reduced agglomeration. It also rules out agglomeration of the larger particle size fraction as the mechanism preventing contact spreading; this must be a result of the lack of liquid availability due to liquid absorption as opposed to the liquid being trapped in agglomerates.

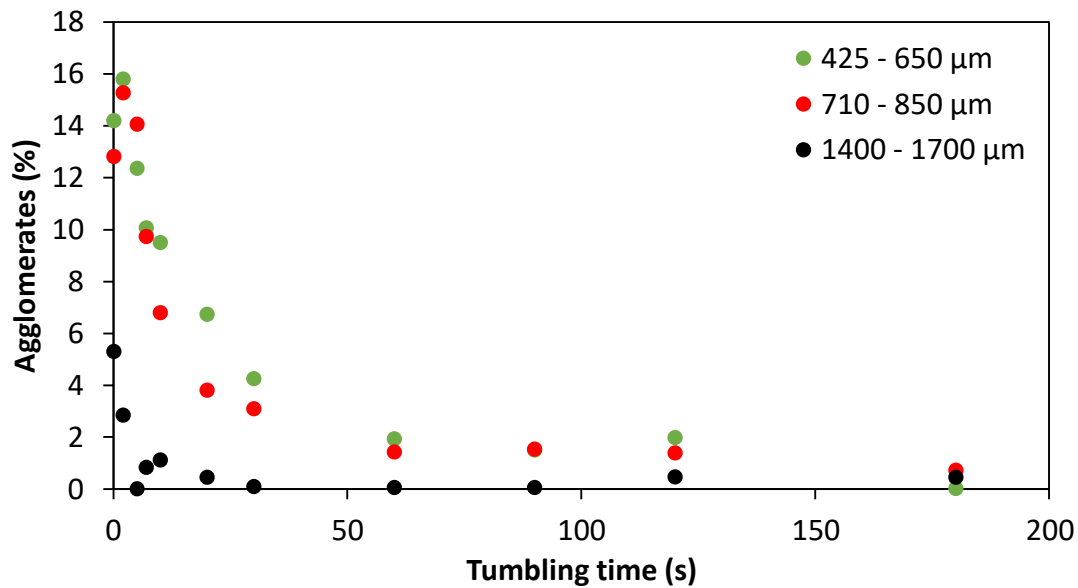


Figure 6-11. Percentage of agglomerates present at each time point for systems using various sized particles.

6.3.3 Effect of viscosity

The second parameter to be investigated using the sodium percarbonate is the effect of viscosity; the four 10 % ethanol / water solutions range from 102 mPa.s to 14,600 mPa.s, as discussed in Section 6.2. Figure 6-12 shows the coefficient of variation as a function of time for these four solutions in Drum A. Although starting out at different absolute values, both the 102 mPa.s and 512 mPa.s solutions show some decay of the CoV with time. On the other hand, the 2,920 mPa.s and 14,600 mPa.s solutions do not show much, if any, variation with time, starting around 12 % and ending at around 10 %. The volume of liquid added to each system was the same, and the particle sizes were controlled as much as possible, using the percentages detailed earlier in Table 6-6. It is therefore sensible to assume that any differences are a direct result of the particle-liquid interactions i.e. solution viscosity. One explanation for this could be the increased agglomeration seen with the increases in solution viscosity.

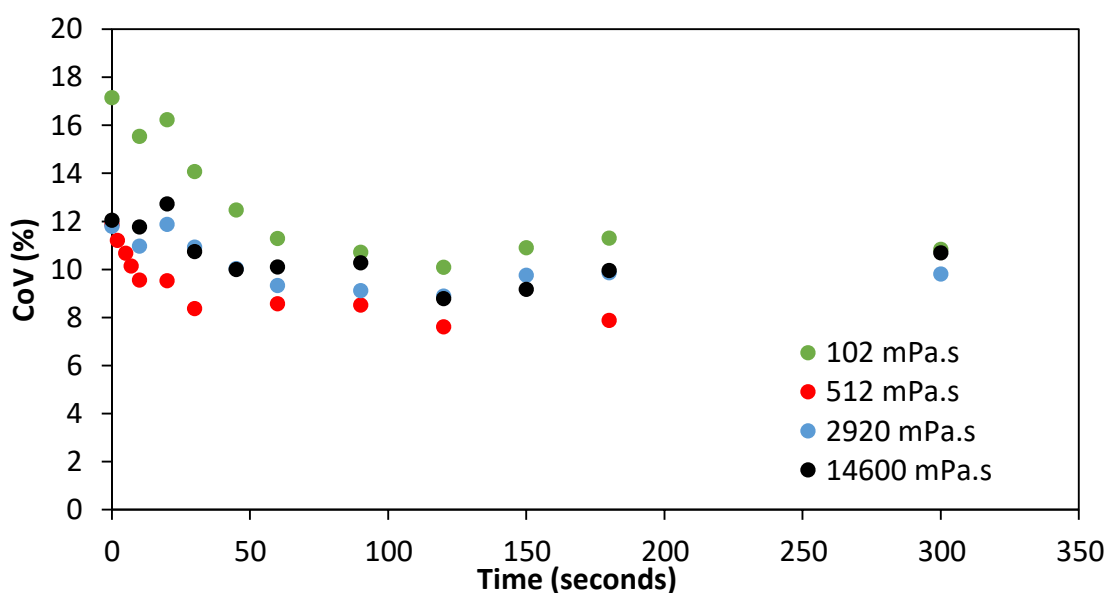


Figure 6-12. Effect of solution viscosity on liquid contact spreading for the 50 % PEG in 10 % ethanol / water solutions.

The extent of agglomeration is shown in Figure 6-13. Here, the most agglomeration is seen for the highest viscosity solution, which corresponds with the lack of contact spreading as seen in Figure 6-12.

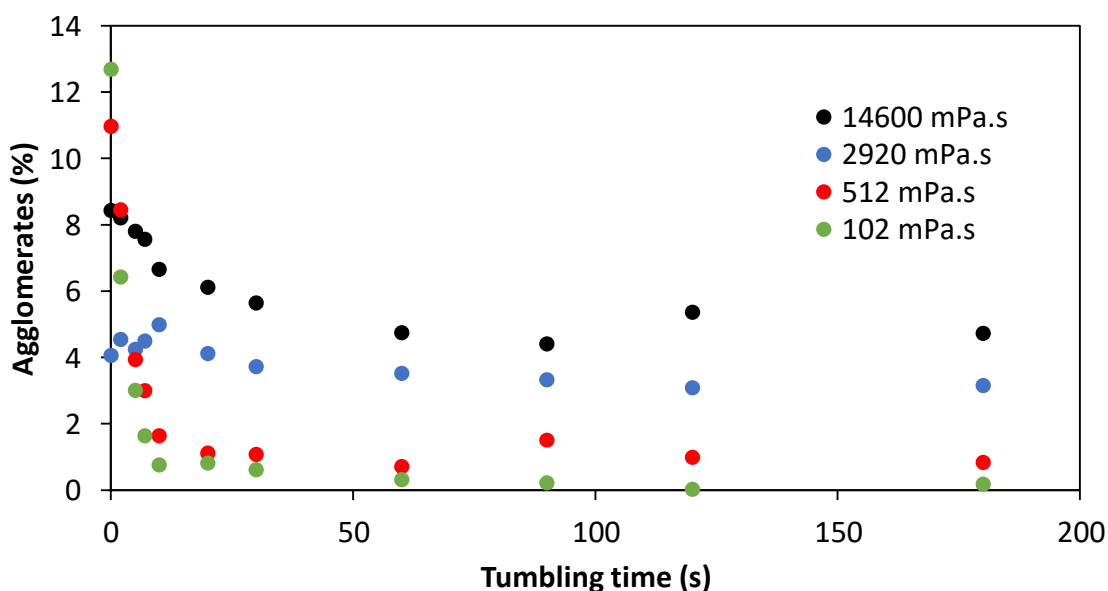


Figure 6-13. Agglomeration as a function of tumbling time for four different 10 % ethanol /water PEG solutions.

Chapter 6

Mechanistic understanding of contact spreading: Study of material characteristics and drum parameters

Slightly below this, but still showing very high levels of agglomeration, is the 2,920 mPa.s solution; again, this corresponds well with the CoV data. The 102 mPa.s and 512 mPa.s show very low levels of agglomeration, both being consistently under 2 % after 7 seconds. Again, this matches closely with the decay in CoV as seen on Figure 6-12. As a result of these experiments, all further experiments in this chapter have been restricted to the use of the 102 mPa.s and the 512 mPa.s viscosity coating solutions.

6.3.4 Liquid ingress and surface properties

As mentioned in Section 6.3.1, because of the porous nature of the sodium percarbonate, liquid ingress is thought to heavily influence the liquid available on the particle surface for contact spreading. Here, several particles have been dissected to investigate this and the effect of solution viscosity. The particles were submerged in solution for 1 hour and then removed and left to dry overnight. Larger particles were used to make the dissection easier, however it could be interesting to look at the differences in ingress rate between differently sized particles. Figure 6-14 shows six images of sodium percarbonate particles coated with 102 mPa.s viscosity solution which have been dissected. Interestingly, the particles all show some form of liquid ingress.

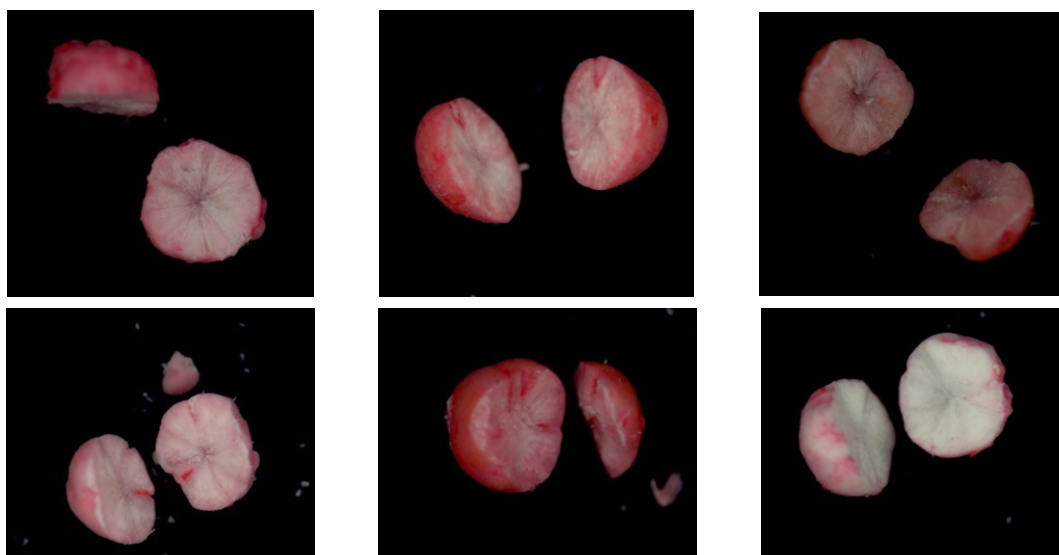


Figure 6-14. Dissected sodium percarbonate particles coated with 102 mPa.s viscosity PEG solution.

Although it is possible to coat particles and observe the ingress without putting them in the drum, it is not possible to observe the ingress as a result of liquid spreading in the tumbling drum; there is no way to identify the original 'uncoated' particles once they have been contacted by the solution. This makes drawing conclusions from the analysis conducted here rather difficult. However, there is one visible difference between the particles coated with the low viscosity coating solutions and the higher viscosity coating solutions.

The higher viscosity solutions (Figure 6-15 and Figure 6-16) show considerably less ingress than the low viscosity solution. As was previously stated, there is no way to know whether this is a direct result of the coating solution viscosity, or it is linked to which particles have been chosen for analysis, i.e. whether the particles are part of the initial group that are coated or are part of the initially uncoated mass in the drum.

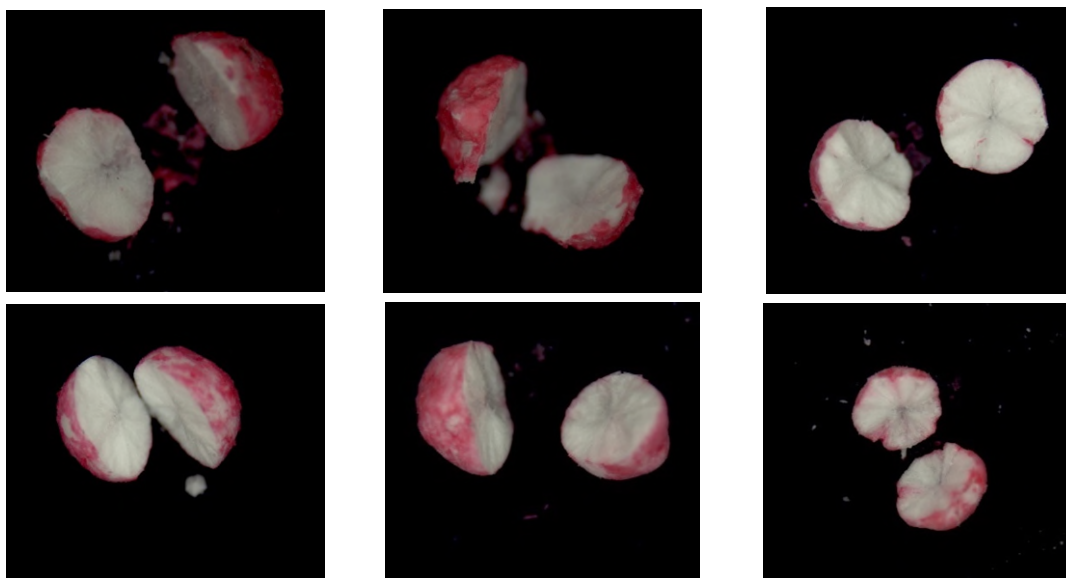


Figure 6-15. Dissected sodium percarbonate particles coated with 2,920 mPa.s viscosity PEG solution.

It is also difficult to quantify differences in ingress based on solution viscosity; this would require a more in-depth study which is out of scope of this work. However, here it has been shown that ingress is a significant contributor to the contact spreading, or lack thereof, seen with the experiments using the sodium percarbonate. If even a third of

Chapter 6

Mechanistic understanding of contact spreading: Study of material characteristics and drum parameters

the particles exhibit liquid ingress (as seen in Figure 6-16), this will drastically reduce the volume of liquid available for contact spreading.

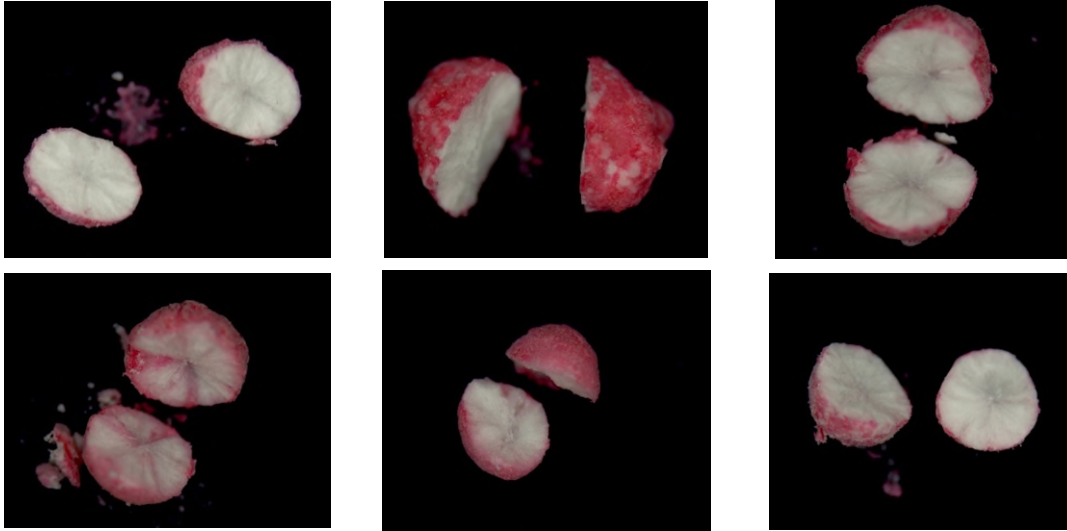


Figure 6-16. Dissected sodium percarbonate particles coated with 14,600 mPa.s viscosity PEG solution.

As well as the liquid ingress, the surface roughness of the particles has also been investigated using SEM, as seen in Figure 6-17.

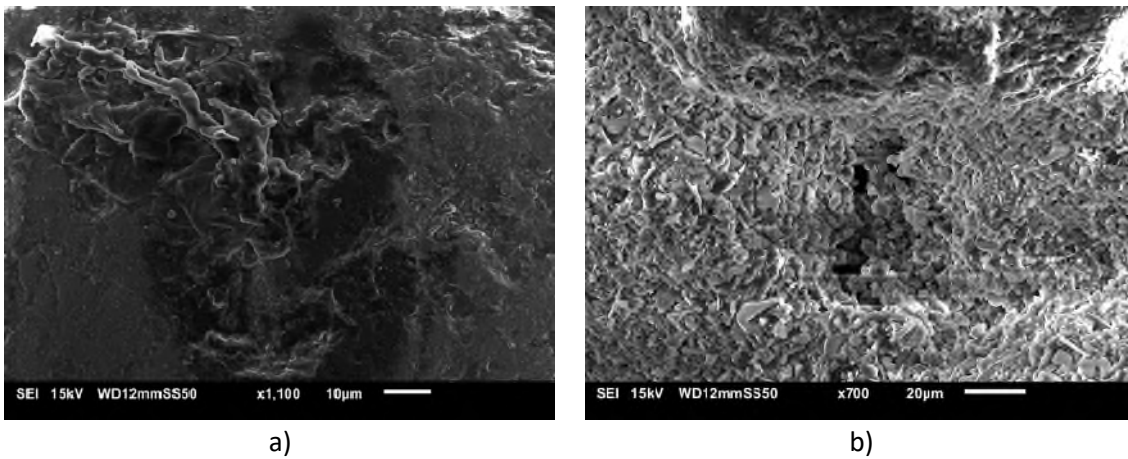


Figure 6-17. SEM images of surfaces of a) Alumina 1 and b) Sodium percarbonate.

Figure a) shows the surface of Alumina 1 at 1,100 magnification. The surface appears relatively smooth, especially when compared to the image seen in figure b). Figure b) shows the surface of a sodium percarbonate particle at only 700 magnification. Due to the irregular particle surface, magnifications higher than 700 produced unclear images. The higher degree of irregularity on the sodium percarbonate particle surface could also

be contributing to the contact spreading seen in the systems. More asperities result in liquid being trapped on the particle surface and being unable to contribute to possible liquid formation bridge formations, therefore reducing the amount of liquid available for transfer.

6.3.5 Effect of drum speed

The third parameter to be investigated was that of drum speed. For these experiments, only a 179 mPa.s viscosity aqueous PEG solution was used because the higher viscosity solutions, as seen in Section 6.3.3, showed very minor levels of spreading. All the sodium percarbonate was sieved to remove fines below 850 μm , and the material for each time point was weighed to include the fractions as seen in Table 6-6.

Figure 6-18 shows the effect of drum speed on the contact spreading as a function of tumbling time, for Drum A, tumbled at 30 rpm, 70 rpm and 90 rpm. These speeds corresponded to rolling, cascading and a more intense cascading regime. As 90 rpm represents the upper limit of the machine capability, it was not possible to analyse the effect of a higher regime (i.e. cataracting / centrifuging). Similarly, below 30 rpm would not generate any data as the powder showed no minimal movement below this speed. Because of the very quick initial decay seen with the CoV, it is difficult to note any effect of drum speed. There is very little difference seen between the 70 rpm and 90 rpm experiments; both still correspond to the same cascading regime and therefore it is logical to not expect to see too much difference. On the other hand, 30 rpm corresponds to a much slower rolling regime, yet it also shows a very rapid initial decay of the CoV with time, similar to that seen with the cascading regime. This either suggests that the collisions at the slowest drum speed already have enough energy to overcome the bridge forces that adding energy into the collisions by increasing the drum speed is superfluous, or that there is simply no liquid available for transfer, and the reduction in the CoV is not necessarily the spreading, but could be affected by the drying/adsorption and hence colour intensity reduction of the solution. The similarity between the data could also be a result of scatter. It appears that the experiments run at 70 and 90 rpm tend towards a more well-coated system more quickly than the experiments at 30 rpm,

however, due to the scatter this is hard to determine. The increased speed of the drum could promote faster, more aggressive mixing between the particles. This would increase the likelihood of particles colliding but decrease the likelihood of particles agglomerating, thereby promoting faster liquid spreading. The fact that there is not a large difference between the drum speeds suggests that the mixing is not a controlling mechanism for this system.

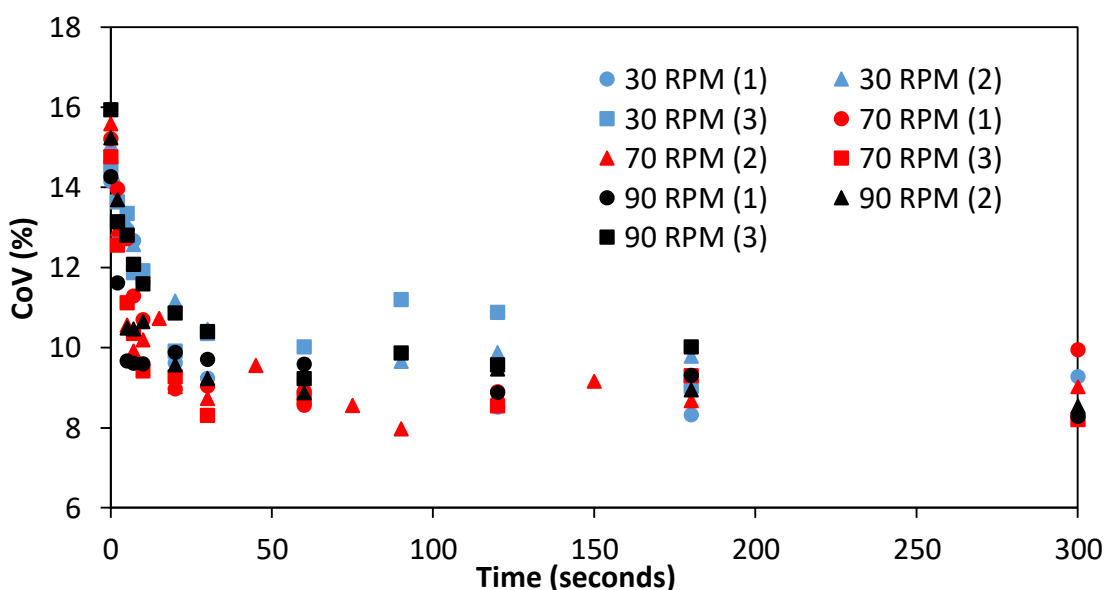


Figure 6-18. CoV as a function of tumbling time for a number of different drum speeds in Drum A. Coated using 179 mPa.s viscosity PEG solutions. Legend indicates tumbling speed with experiment repeat number shown in brackets.

Figure 6-19 shows the same data as a function of drum revolutions. Similar to Figure 6-18, there is no discernible difference between the different viscosity coating solutions. This suggests that the collision velocity is not impacting the spreading seen in this system.

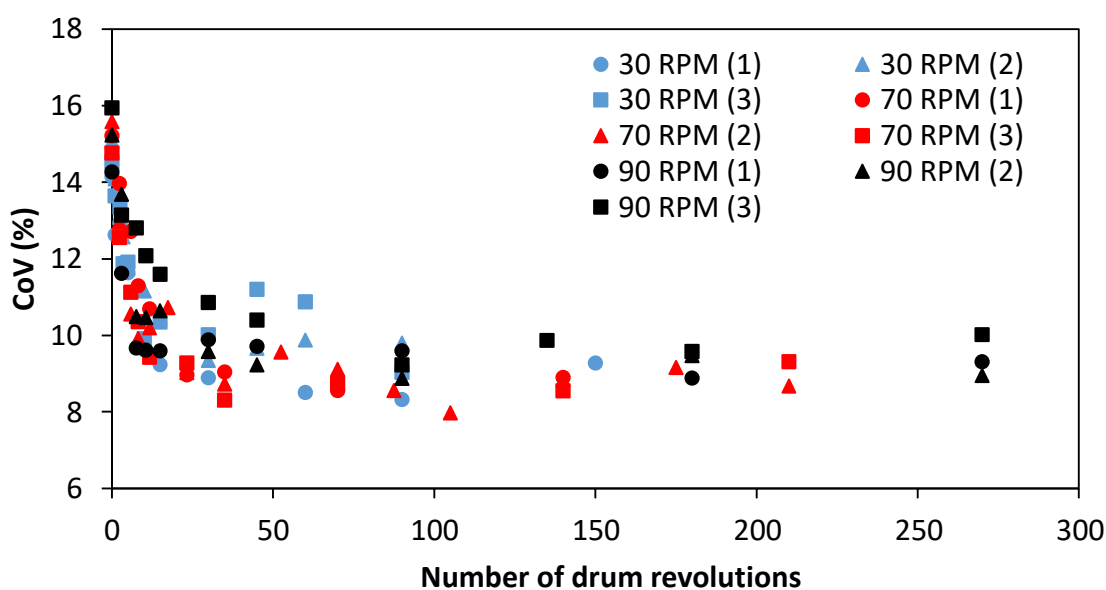


Figure 6-19. CoV as a function of number of drum revolutions for a number of different drum speeds in Drum A. Coated using 179 mPa.s viscosity PEG solutions. Legend indicates tumbling speed with experiment repeat number shown in brackets.

Figure 6-20 shows the agglomerates for the experiments seen in Figure 6-18 plotted as a log-normal graph as a function of tumbling time. As indicated previously, drum speed appears to have no impact on the contact spreading, nor any long-term impact on the particle agglomeration. At early time points, the agglomeration seen at 30 rpm is much higher than that seen when the drum is operated in the cascading regime (70 and 90 rpm). However, by 10 seconds there is no difference in the agglomeration in any of the experiments, all being far below 2 % of the total data point mass. This suggests that, as opposed to being only liquid viscosity which influences agglomeration formation, the volume of the liquid is also an important factor. At higher tumbling speeds, the high volumes of liquid found at the beginning of the process are more quickly dispersed compared with the slow-moving systems, meaning agglomerates have less change to develop.

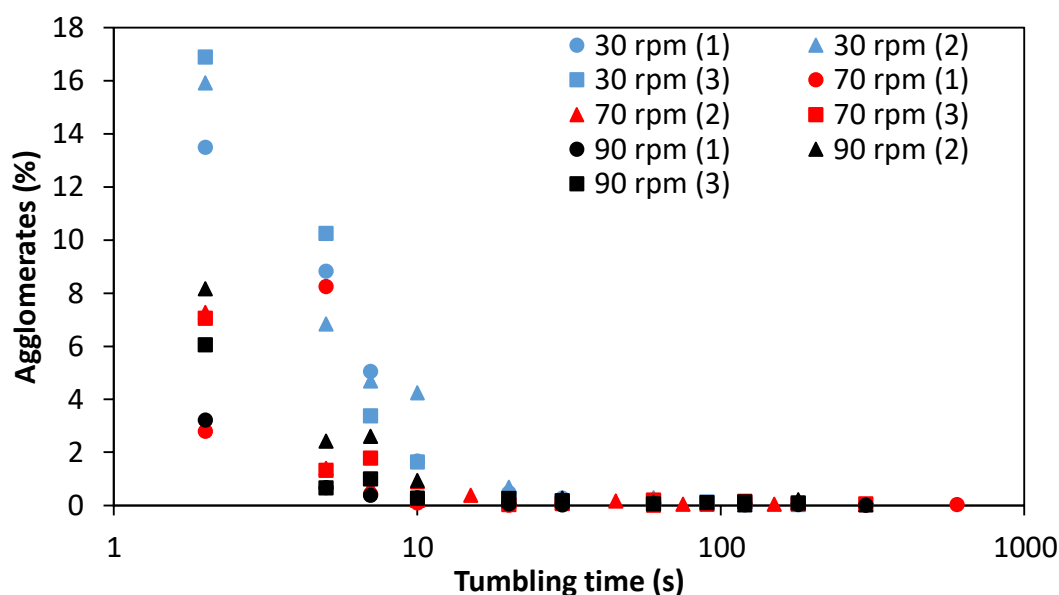


Figure 6-20. Log-normal plot of percentage of agglomerates as a function of tumbling time for 30, 70 and 90 rpm. Legend indicates tumbling speed with experiment repeat number shown in brackets.

6.3.6 Effect of drum size

When considering the effect of drum size, it is possible to control the variables in two ways. Firstly, the rotation rate of the drum could be held constant. However, this would lead to the development of different regimes with the drums. The Froude number would be considerably different and, therefore, the effect of drum size would not have been isolated. Instead, the second option is to maintain a fixed Froude number (0.3) and change the rpm to reflect this. The second option was used here. Figure 6-21 compares the effect of drum size using Drum A and Drum C using normalised data (dimensions detailed in Table 6-4), both coated with the 102 mPa.s viscosity coating solution. As can be seen, Drum C promotes quicker contact spreading. This is surprising; Chapter 5 showed that smaller drum sizes were favoured by the lighter Alumina 2 particles. It should have been expected therefore, that sodium percarbonate, which is even lighter still, should also favour the smaller drum sizes. However, it should also be recalled that the alumina particles are a model system; they are spherical and smooth. Sodium percarbonate, on the other hand, is irregular in shape compared to the model particles, absorbs the coating solution and the surface is not smooth. Even though the Froude number is maintained, the number does not capture the effects of these variables and

it is therefore possible that different flow regimes and/or mixing patterns are developed. Here, the larger drum perhaps promotes greater mixing; the increased friction between the drum wall and the particles and the particle-particle interactions themselves could be promoting a more chaotic mixing pattern which favours better contact spreading.

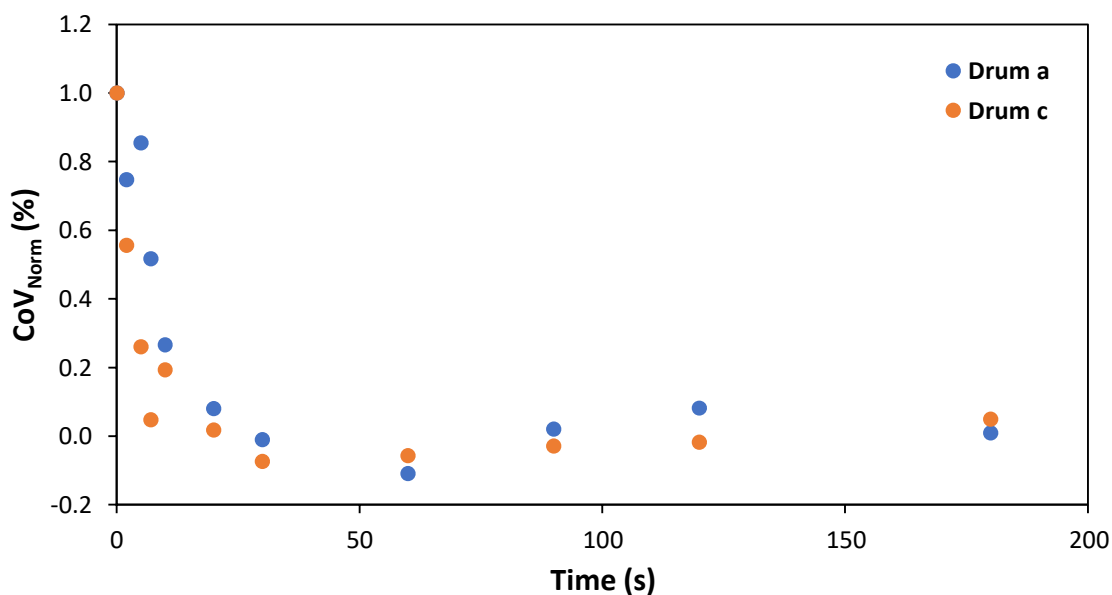


Figure 6-21. Normalised CoV as a function of time for sodium percarbonate tumbled in Drum A (70 rpm) and Drum C (45 rpm) and coated with 102 mPa.s viscosity PEG solution.

To prove this, a more detailed investigation into the mixing within the drums is required. This could be achieved by developing an entirely transparent drum with a camera/video set-up. This set-up was not available for this study, however, these types of experiment could form an important part of future work.

6.3.7 Liquid bridge strength: effect of collision velocity and droplet size

Here, experiments show the transfer of liquid between two particles at the micro scale. This understanding is important and allows a greater understanding of the factors affecting the contact spreading within the drum.

Preliminary work recently completed by Sherburn & Green (2018) shows the formation of liquid bridges between sodium percarbonate particles for 179 mPa.s, 810 mPa.s and

Chapter 6

Mechanistic understanding of contact spreading: Study of material characteristics and drum parameters

4,080 mPa.s viscosity 50 % PEG solutions (without ethanol). The work looked to investigate the development of liquid bridges between the porous, surface rough sodium percarbonate particles through high speed imaging and analysis. A Labview script was used to determine the bridge width after images of the bridge evolution had been captured. A known volume of liquid was placed on a stationary particle onto which a second particle was then dropped. The particles were not equal in size. The first particle was chosen from the largest size fraction of the sodium percarbonate to increase the chances of being able to successfully place a liquid drop on the particle, and the second particle size was constrained by the tube diameter which was used to guide the particle onto the first particle from the drop height. The height from which the second particle was dropped controlled the collision velocity, which was varied from 0.71 m/s to 1.7 m/s. The 20,200 mPa.s viscosity solution proved too viscous to be able to create a droplet small enough to sit on a sodium percarbonate particle, and hence this solution was not tested. The remaining 3 solutions were tested, however, and two separate control volumes were used (0.3 mm³ and 0.5 mm³). Clearly this is much larger than the volume of liquid which has been assumed to be involved in the creation of liquid bridges in the tumbling drum experiments, particularly in the calculation of the collision number (Co). The absolute values may be different. However, the drops formed here were the smallest possible which were repeatable with the available equipment. Regardless of this, the work is still useful in identifying trends associated with the effect of viscosity and the drop height on the bridge formation. Table 6-7 shows images of the liquid bridge development for various solution viscosities over various times. There are two bridge volumes present; 179 mPa.s and 810 mPa.s use 0.3 mm³ of liquid, whereas the 4,080 mPa.s solution uses 0.5 mm³. As explained previously, this was a result of not being able to create small droplets of the viscous solution. Before the experiments began, it was expected that a number of the particles would rebound upon impact. However, either due to the liquid bridge volume being too great or the impact collision velocity not being large enough, only the experiments using the 179 mPa.s saw particles rebound, and only 20 % of the particles tested using this low viscosity solution rebounded. Further experiments in this area should focus on reducing the liquid bridge volume and capturing the bridge formation.

Table 6-7. Liquid bridge development for 179 mPa.s, 810 mPa.s and 4,080 mPa.s solutions over various time points.

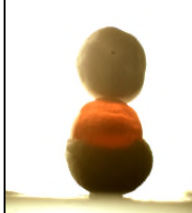
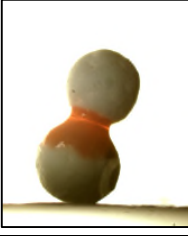
Time (s)	179 mPa.s	810 mPa.s	4,080 mPa.s
0			
0.45			
0.99			
8			

Figure 6-22 shows the effect of liquid bridge volume on bridge width (measured at the narrowest point of the bridge - known as the neck) as a function of time for the 179 mPa.s viscosity solution dropped with a collision speed of 0.71 m/s and 1.7 m/s. As would be expected, the larger volume of liquid ultimately results in a larger bridge neck width. However, both bridges appear to develop at a similar rate and reach a maximum bridge width after approximately 0.5 seconds. The collision velocity appears to impact the initial rate of bridge development, yet does not impact on the final bridge width. This is interesting as it suggests any changes to the system which impact on the particle velocity could impact on the rate of spreading. If a low particle velocity collision results in bridge formation, it will take longer for the bridge to become fully formed and reach

the maximum bridge strength, leaving it susceptible to further collisions which could more easily rupture the liquid bridge. If a bridge develops as a result of a high particle velocity collision, the bridge will reach maximum bridge width much quicker, reducing the chance that further collisions will separate the particles.

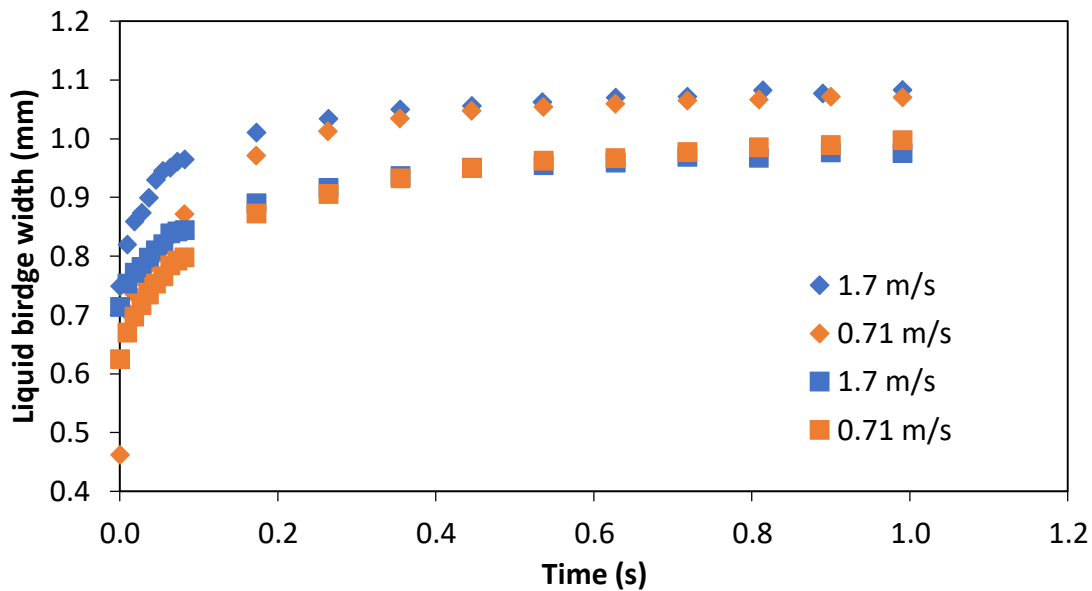


Figure 6-22. Effect of collision velocity for two different drop sizes of the 179 mPa.s solution. \blacklozenge are 0.52 mm³ and \blacksquare are 0.30 mm³ droplet volumes.

Figure 6-23 shows the effect of liquid viscosity on bridge width for the smaller drop volume. After 1 second of development, the 179 mPa.s bridge appears to have reached a stable maximum. However, this is less certain for the 810 mPa.s solution.

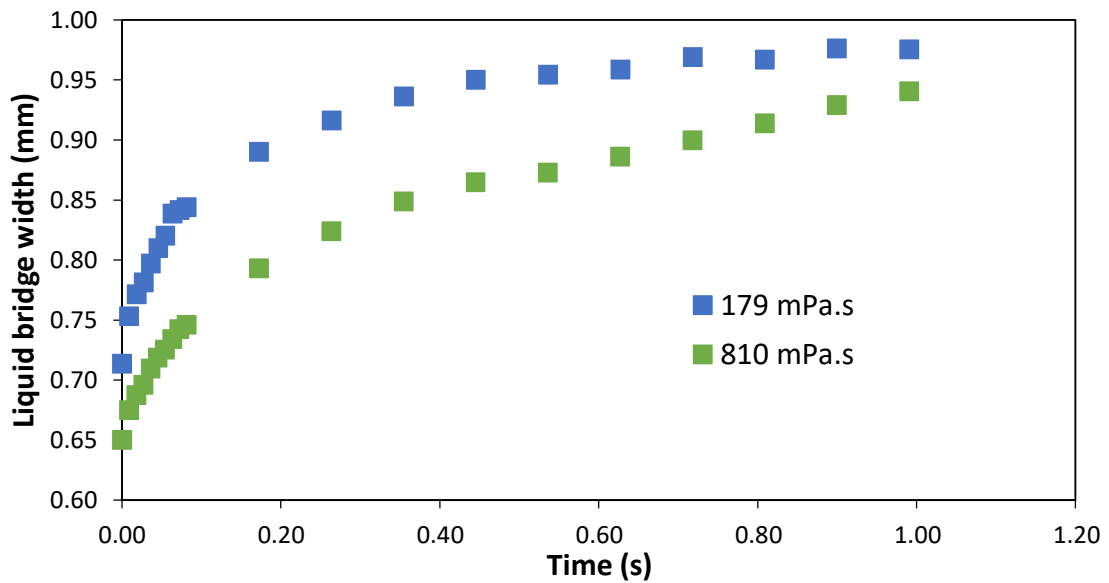


Figure 6-23. Effect of liquid viscosity on liquid bridge width as a function of time (0.3 mm³ drop volume and 1.7 m/s collision velocity).

For both solutions, there appears to be a rapid increase over the first 0.1 second, followed by a slower increase until the maximum is reached. This fits with the earlier mentioned theory (Chapter 2, Section 2.5) that liquid bridge formation occurs in two parts; the first is rapid and driven by surface tension, and the second is slower and driven by solution viscosity. Both solutions have similar surface tensions, so it follows that this initial period should be similar. However, the second stage is clearly slower for the more viscous material. This is further reinforced through Figure 6-24; the 4,080 mPa.s solution does not show a discernible difference between the two phases, indicating that at higher viscosities, the surface tension driven phase is negligible and the viscosity driven stage dominates. . Like the 810 mPa.s solution, it appears unlikely that the bridge has reached a stable shape after the 1 second period, unlike the 179 mPa.s solution. Further work in this area could be interesting. Although the experiments completed here have shown interesting results, there are several parameters which have not been considered; e.g. surface roughness or particle porosity. It would also prove interesting to investigate the bridge development using more realistic (i.e. smaller) bridge volumes.

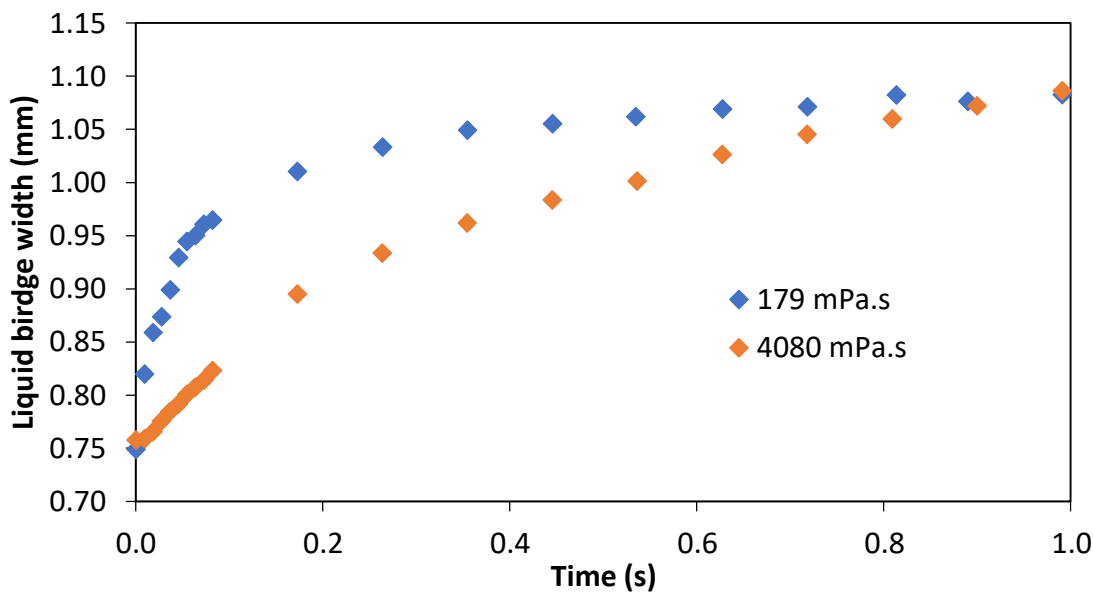


Figure 6-24. Effect of liquid viscosity on liquid bridge width as a function of time ($\sim 0.5 \text{ mm}^3$ drop volume and 1.7 m/s collision velocity).

6.3.8 Collision number

As discussed in Chapters 4 & 5, the collision number is potentially an important dimensionless number for capturing the impact of many parameters of these systems. Figure 6-25 shows all the Co values as a function of the coating completion time for the experiments completed using sodium percarbonate. Here, all the experiments have been completed in Drum A (with the exception of one completed in Drum C), and so this label is not present. The main parameters which have been varied are the particle size, the liquid viscosity, and the drum speed. The experiments which occupy the lower left area of the graph are those related to the lowest solution viscosities; the 4,000 MW PEG (aqueous solution and 10 % ethanol / water; $179 \text{ mPa}\cdot\text{s}$ and $102 \text{ mPa}\cdot\text{s}$ respectively). The top right is occupied with experiments completed using the higher solution viscosities, i.e. those made with the 20,000 and 35,000 MW PEGs in 10 % ethanol / water solutions. The majority of experiments were conducted at 70 rpm; those using either 30 rpm or 90 rpm show no variation from those conducted at 70 rpm. This agrees with the information seen to date; no discernible difference could be seen between the three tumbling speeds. With regard to particle size, the viscous force model used to compute the strength of the liquid bridge has only previously been used for single particle-particle

interactions, or in modelling systems where only 2 particle sizes are assumed. For the narrower size distributions used in this work, the span is not significantly large and hence this is not too great of an issue. However, for the size distributions which use 800 – 2,000 μm , there is considerable distribution represented by only one value (1,400 μm). In reality there is, of course, a distribution of Co numbers which account for variations in the particle velocity, size, liquid loading etc. However, to capture that here would be extremely difficult.

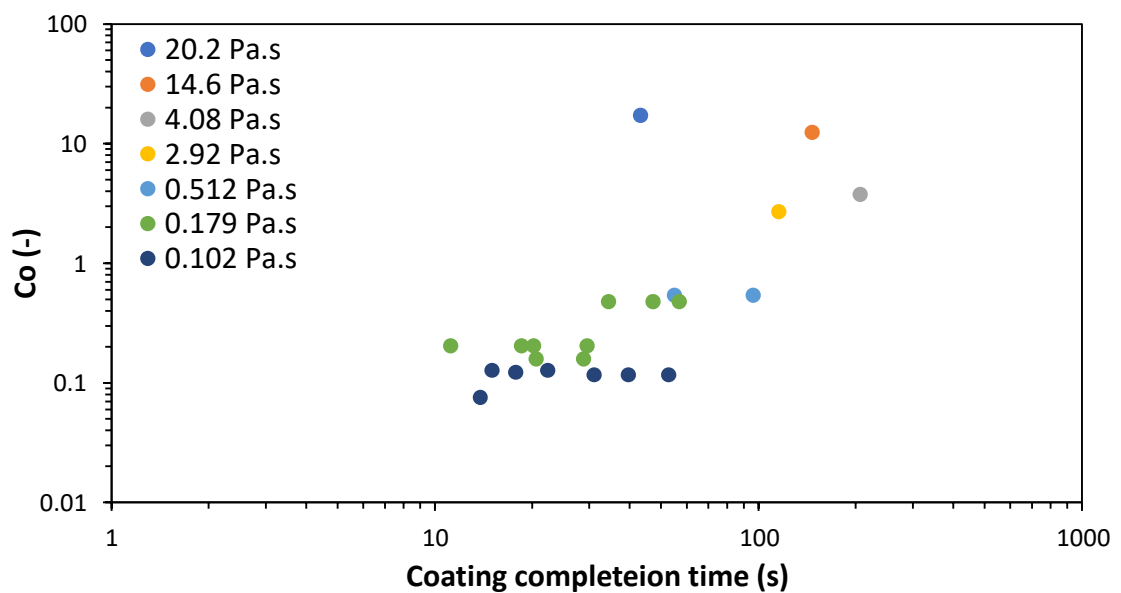


Figure 6-25. Co number as a function of tumbling time for all the experiments completed using sodium percarbonate.

Unlike Alumina 1 and Alumina 2, which are model particles, sodium percarbonate introduces a host of new factors to be considered. For example, the particles have been shown to be significantly rougher than the relatively smooth alumina particles, they have a porous internal structure leading to liquid adsorption which influences the volume of liquid available for transfer, they are irregular in shape and have a very wide size distribution (as discussed above). As has been shown, these parameters may influence the collision energy and the liquid bridge force, but they also influence the mixing and agglomeration seen within the drum. Some attempt must be made, therefore, at defining a parameter to capture the effects of these variables, focusing on the agglomeration and mixing. This will be presented in Chapter 7.

6.4 Conclusions

In this Chapter, a porous, light, polydisperse, irregular and granular particle has been used to study the effect of material properties and operational parameters on contact spreading.

Investigations covered the effect of particle size, whereby it was shown that smaller particles appear to promote contact spreading much more than larger particles. Studies showed this was not a result of agglomeration, and therefore it has been suggested that this is to do with a lack of liquid availability due to particle porosity.

It was seen that only the lowest viscosity solutions showed a decrease in the CoV with time. Both the highest viscosity solutions caused almost instantaneous agglomeration in their respective systems. The lower viscosity solutions showed minor agglomeration in the early stages of tumbling (<5 seconds), but agglomerates were quickly destroyed after this time. Even though there was a change in the CoV for the low viscosity solutions, they did not decrease to levels indicative of a homogenous coating; they too suffered from a lack of liquid availability. Liquid ingress appeared to show that the low viscosity solution penetrated the particles more than the higher viscosity solutions, however, limitations of these findings have also been noted.

Investigations into drum speed showed no effect on the rate of coating or time to reach coating completion; agglomeration studies showed very minor differences between the systems, with the agglomeration from the low speed system being greater than the high-speed systems for the first 10 seconds of tumbling. This is most likely a result of the high concentrations of solution. Even though the viscosity is low, the sheer volume of liquid forces particles to agglomerate until the particles are tumbled about the bed.

Drum size was investigated; the larger of the two drums investigated promoted faster liquid spreading, however, further work in this area is recommended.

Interesting results regarding the development of liquid bridges upon single particle-particle interactions have been detailed; larger droplet volumes lead to larger bridges, as would be expected. Collision velocity was shown to affect the rate at which the

bridges develop, supporting the understanding that liquid bridges develop in two stages driven first by surface tension and secondly by liquid viscosity.

Finally, the collision number has been calculated for all the experiments completed in this chapter. It appears that several parameters affecting the contact spreading are not being captured by the Co number alone, and some function which captures the mixing and agglomeration seen in these systems is desirable. This will be addressed in Chapter 7.

Chapter 6

Mechanistic understanding of contact spreading: Study of material characteristics and drum parameters

7. Regime map development: a discussion on mixing, segregation and a collision number

Data from all three experimental chapters, incorporating both the model alumina particles and the sodium percarbonate particles, have been analysed. The research completed here has been compared with experiments from previous published literature to enable trends to be drawn across a larger database. A basic regime map is proposed based on the collision number and a mixing function, and an introduction to mixing and segregation within tumbling drums is considered.

7. Regime map development: a discussion on mixing, segregation and a collision number	
7.1 Introduction.....	196
7.2 Need for a regime map.....	196
7.3 Co number.....	198
7.4 Mixing and segregation.....	200
7.5 Thoughts on a mixing function.....	203
7.6 Conclusion.....	205

7.1 Introduction

Spray coating is used in many industries, including pharmaceuticals, detergents and food processing. Often, the design of the coaters is based on scale-up experiments, and as of yet, no methodology exists which captures the impact of liquid contact spreading. It has been shown in previous chapters that the collision number (Co), the ratio of the bridge force owing to the liquid viscosity to the collision force, captures a lot of the experimental data from this thesis well. However, there are several points in which other factors are clearly also impacting on the results. For example, at high viscosities, regardless of other parameters, very high levels of agglomeration are seen. On the other hand, at low viscosities, mixing becomes more important. If two independent parameters can be determined which capture the effects of the most important variables on the contact spreading mechanism, a regime map can be developed with which to predict the outcome of processes which involve contact spreading.

7.2 Need for a regime map

Regime maps offer the ability to understand the effects of process variables on the process outcome i.e. if the liquid viscosity is high, agglomeration will occur, if particles are heavier, time to reach coating completion is shorter. This could offer the potential for users to mitigate processing issues based solely on an understanding of material characteristics and some simple calculations, as opposed to determining optimum conditions via trial and error and/or scale up rules.

As was previously mentioned, it is believed the Co number captures several of these material characteristics well, and will provide the basis for the primary axis on a regime map. However, although some agglomeration studies have been completed, no work has been done on the mixing and segregation in the research conducted here. It is believed that some function incorporating these effects will comprise the secondary axis. Here, such a function has been termed $f(\text{mix})$. A basic understanding of the shape of such a map has been detailed in Figure 7-1.

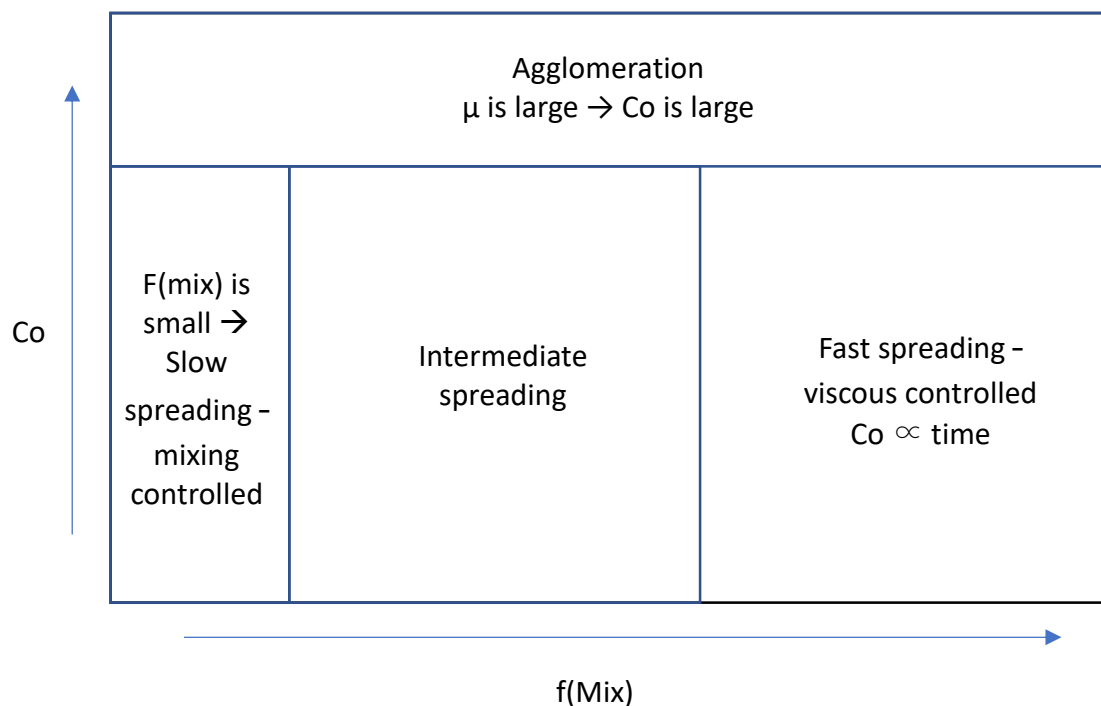


Figure 7-1. Basic regime map for understanding contact spreading.

As can be seen from Figure 7-1, at very high Co numbers, when the viscosity of the fluid is extremely high and when the density of the particles is low, the system is expected to see very high levels of agglomeration. Liquid bridges become the controlling mechanism, and without sufficient energy to rupture the bonds, bridges begin to solidify. In the fast spreading regime, the mixing is good and offers suitable opportunities for particle interactions and liquid spreading. Viscosity and particle collision energy become important and hence the time taken to reach coating completion is proportional to the Co number.

At the other end of the x-axis is slow spreading. Here, the results of the contact spreading are controlled by mixing in the drum. Poor mixing leads to agglomeration whilst improved mixing increases the spreading rate. There will no doubt be some intermediate region between these two extremes; however, the size of all the regions of the map are yet unknown. To try and discern an appropriate form of the mixing function, a further look at the Co number and an introductory examination of particle segregation and mixing issues in rotating drums will be given.

7.3 Collision number (Co)

In previous chapters, the Co number has been calculated for each system, and plotted against the time to reach coating completion. In the case of the high density material, this appeared to produce a linear relationship over the range of viscosities tested here (179 mPa.s to 20,200 mPa.s). With the introduction of the lower density model material (Alumina 2), variation from this relationship was seen when using the higher viscosity coating solutions; this is expected to be a result of the different mixing patterns developed within the drum. Sodium percarbonate, seen most recently in Chapter 6, again showed variation, particularly with high viscosity solutions. Figure 7-2 is a map of all the experiments completed, showing the Co number and the coating completion time.

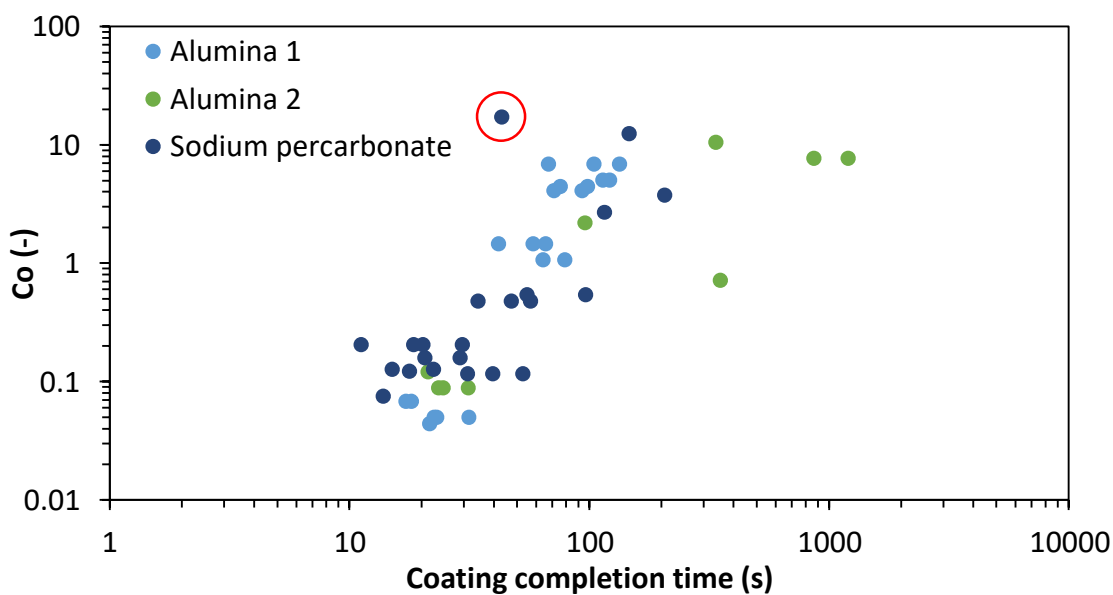


Figure 7-2. Log-log plot of the Co number and coating completion time for all experiments completed in this thesis.

From Figure 7-2 it is evident that the denser Alumina 1 material is the most well represented through a linear relationship; both the Alumina 2 and sodium percarbonate show some form of scatter. At the top right are experiments completed using high viscosity solutions with the lighter Alumina 2. Here, it is thought that agglomeration and poorer mixing resulted in less liquid being available to contact spread (top of the map in Figure 7-1). At the top of the data is a point corresponding to an experiment using 20,200

Regime map development: a discussion on mixing, segregation and a collision number

mPa.s solution and sodium percarbonate (identified on Figure 7-2 with a red circle); this system behaved differently from the high viscosity liquid with Alumina 2 particles. This could be for a number of reasons. The sodium percarbonate has a rough surface, it has a much wider size distribution, it is porous and even lighter still than the Alumina 2 particles. The system showed almost instantaneous agglomeration and no reduction in the coating variation as a function of time. This point, and others like it, represent the 'agglomeration' region earlier identified on Figure 7-1; high liquid viscosity and low particle density compound to give a very high Co number. In the lower left corner of the plot, the sodium percarbonate shows a range of completion times, ranging from 11 seconds to 52 seconds for similar Co numbers of 0.1 to 0.2. Again, repeatability of these experiments is the lowest of all three materials; the 'non-model' properties of the material mean the systems behave slightly differently every time. Numerous factors surrounding the interaction between the liquid and the particles are important; the volume of the liquid upon addition and its axial distribution in the drum, the volume of liquid available for transfer, the mixing provided by the drum etc. At this stage, factors other than those captured by the Co number are relevant. However, despite this, it is important to remember that the aim of this project is the development of a useable engineering tool; complete understanding and prediction of the way in which every possible variable affects the system is unachievable at this stage.

Earlier work completed by Yusof et al. (2018) has also been added to the data from this thesis in Figure 7-3. They studied the effect of solution viscosity and the effect of tumbling speed using Alumina 1. All these experiments show a remarkably good fit with the data from this thesis.

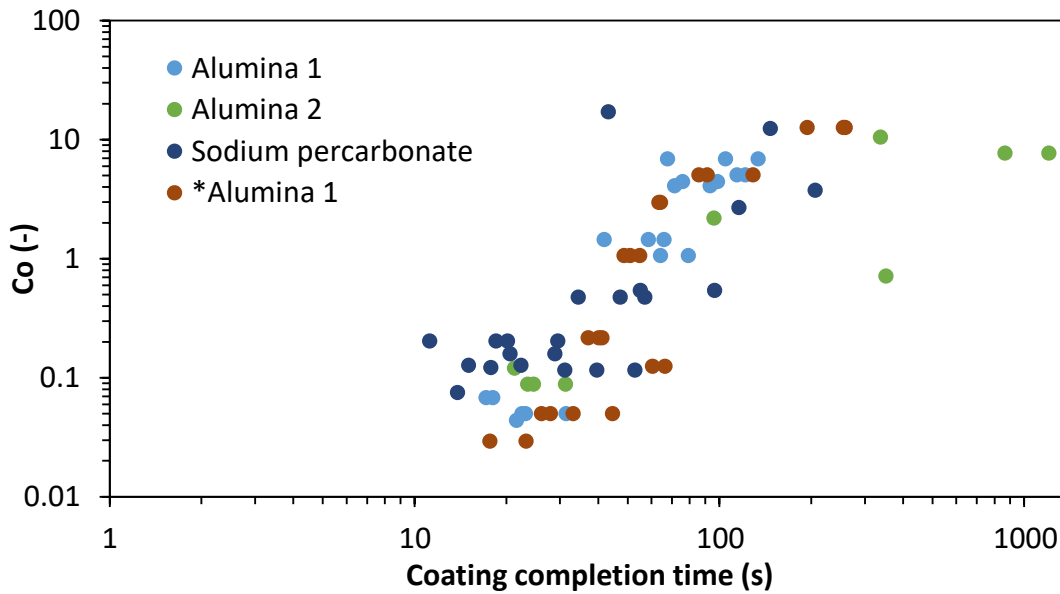


Figure 7-3. Log-log plot of the Co number and coating completion time for all experiments completed in this work, and experimental data from Yusof et al. (2018).

7.4 Mixing and segregation

Along with the Co number, which captures the collision energy and the force of the liquid bridge, a mixing function offers another method through which the impacts of various parameters can be assessed. Segregation (or demixing), occurs due to differences in particle properties, differences in interactions between liquids and particles, and interactions with the equipment surfaces. It has been the focus of much research (Ottino & Khakhar, 2000; Li & McCarthy, 2003), but is often restricted to binary particle mixtures (Cui et al., 2014), low viscosity or no liquid binder systems (Santomaso et al., 2004), or quasi 2D equipment which looks at only the radial segregation (ignoring axial mixing)(Khakhar et al., 1999).

Several reports which are relevant to this thesis cover the effect of liquid on segregation of granular media and the end wall effects, which are often cited as heavily influencing the particle mixing (Maneval et al., 2005; Pohlman et al., 2006; Arntz et al., 2013; Liu et al., 2018). Dury et al. (1998) studied the wall effects on the angle of repose and showed a drastic increase compared to the centre of a drum. Pohlman et al. (2006) quantified this effect and stated that if the drum length to diameter ratio is less than 1 then the two segments that are affected by the end walls will merge, producing a flow in which

Regime map development: a discussion on mixing, segregation and a collision number

the axial velocity is decreased; however, their system did not include a liquid. For all the systems used in this work, an L / D of ~ 1.5 was maintained. This results in a three-sectioned bed, two sections which are at the end and affected by the walls and one in the middle which is not. In this case, the flow in the centre can be thought of as similar to one in an infinitely long drum and independent of wall effects. The free surface of the flowing layer near the walls suffers from decreased velocity due to friction effects, but also an increased angle of repose; the material characteristics obviously play a large role in the extent of this friction. Sodium percarbonate has the roughest particle surface and, therefore, it could be expected that the greatest range of dynamic angles of repose would be seen with this material. These studies are out of scope for this work, however, should be considered for future work. Jarray et al. (2018) studied the effect of the cohesion forces on the flow characteristics. The capillary number for their systems was far below 1 and, hence, they did not consider the viscous forces. However, they noted similar observations to those seen in this work; increased cohesion results in “particles becoming more closely packed and acting as clusters” (agglomerates), rather than individual particles. They also explained that the cohesive forces increase the resistive force which is applied to the flowing layer from the free body, reducing the particle speed.

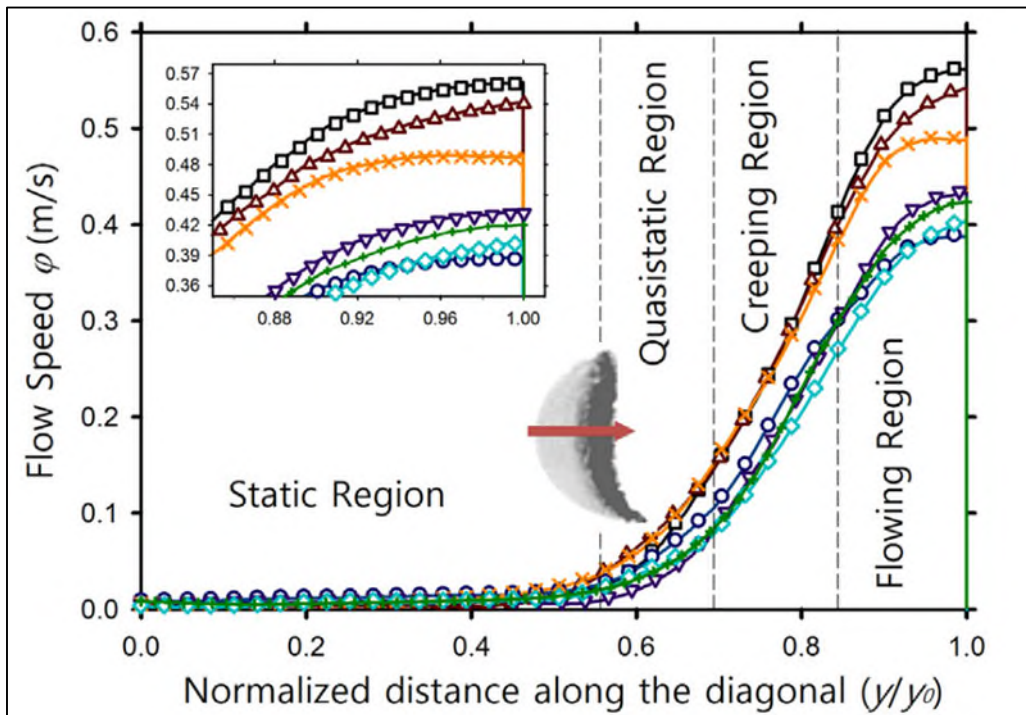


Figure 7-4. Flow speed as a function of the normalised direction in the radial direction through the powder bed (Jarray et al., 2018).

Figure 7-4 shows the flow speed at different points through a radial cross section of the powder bed, with the particle speed increasing from the stationary ‘Static region’ to the fastest moving ‘Flowing region’. The coloured lines correspond to changes in the cohesive force, with the top-most line (black) being a dry system, and the bottom-most (turquoise) having the greatest cohesive force. Here, only one separation velocity was considered; the effect of the liquid presence, and its viscosity, on the velocity was not accounted for. Because the work of Jarray et al. (2018) did not include the viscous component of the bridge force, there is no way to predict the change in flow speed as a result of changes to solution viscosity from the flow speed changes seen in Figure 7-4. These results are, however, reconcilable with the results from this thesis; increased viscosity (or increased cohesion) increases the number of agglomerates seen within a system, and these take longer to break up due to the increased bond strength but also perhaps due to the reduction in the particle speed, reducing collision energy. To quantify this, further studies using real-time particle imaging would be necessary.

7.5 Thoughts on a mixing function

In this thesis, mixing was not explicitly considered. An unbaffled system was used which was scaled with a constant Froude number to try and maintain a similar flow pattern. However, it is evident that particle properties and the addition of liquids can drastically alter the mixing regime within a drum, as can the presence of baffles. To quantify the level of mixing, some authors have used a segregation index, S (Chou et al. 2010; Liu et al. 2013), which shows the local concentration of particles in binary mixtures. A segregation index of 0.5 indicates complete segregation, whereas 0 represents perfect mixing. However, to define the segregation index at a specific time point depends on the final segregation value (amongst other parameters), which is not ideal for a predictive tool.

A second approach is to try and logically determine the parameters which are important for the mixing function. Firstly, a number which captures the distribution of the initial particle configuration could be important, i.e. initial segregation ($S_{initial}$). This could be further extended; considering the spatial arrangement of particles within the drum. If the drum was split along its axis into ten equal sections, one arrangement could see the 90 % uncoated particles occupying 9 neighboring sections with the 10 % coated particles occupying the remaining section. Another arrangement could be 90 % uncoated particles at the base of the drum with the coated 10 % situated on top. Both of these scenarios are likely to result in different coating times due to the difference in likelihood that particles will interact, however, they could have the same $S_{initial}$ value. The first arrangement is dependent on axial mixing, whereas the second is more controlled by radial mixing. Some understanding, therefore, of the difference in the initial radial and axial segregation could also be important. As well as this, the ratio of coated to uncoated particles will be important (P_C/P_U), again a higher value will increase the likelihood that coated particles will meet uncoated particles. In this thesis, the number of coated particles was fixed at 10 % and was not investigated. However, logically, an increase in the number of coated particles in a system which is otherwise fixed will result in a quicker coating time. Similarly, an increase in the volume of liquid (V_L) will also increase the rate of spreading. This was briefly investigated by Yates &

Chapter 7

Regime map development: a discussion on mixing, segregation and a collision number

Green (2017) who varied the liquid loading from 5 % to 25 % and showed an increase in the coating time with decreases in the liquid content when using the Alumina 1 particles. As well as the liquid viscosity being important in the collision number, it should also be factored into the mixing function. Much research has shown the effect of cohesion on the mixing patterns developed in drums. However, defining the actual dependence is out of scope of this research.

Further to the effects of the liquid distribution, there are considerations which relate to the drum and ultimately effect the flow regime i.e. fill level (f), drum speed (v), and drum size (V_D). A mixing function ($f(mix)$) can therefore be written as some function of the following parameters (and potentially other parameters as well);

$$f(mix) = f\left(S_{initial}, \frac{P_C}{P_U}, V_L, f, v, V_D, F_B\right) \quad \text{Equation 7-1}$$

These parameters (where F_B is the liquid bridge force and all other parameters are defined in the above text) can be separated into two groups; those which affect the liquid coating and those which affect the likelihood of particles meeting. This means the mixing function described above can be:

$$f(mix) = f(Initial\ distribution, k) \quad \text{Equation 7-2}$$

Where k is a mixing rate constant, and is influenced by a number of both operational parameters and material characteristics. The initial distribution is a function only of the ratio of coated particles to uncoated particles, and the liquid volume.

If this is related to the proposed regime map from Figure 7-1, it can be seen that the following is true. When either low volumes of liquid, or low numbers of coated particles are introduced, the spreading rate is controlled solely by mixing within the drum. The initial distribution is low and relies on the mixing to promote particle interactions and liquid redistribution. If, however, high liquid volumes or a large number of coated particles are introduced, mixing is less important to promote particle interactions. Instead, in this regime, the liquid distribution will be controlled by the Co number, in

which the ratio of the collision energy to the viscous liquid bridge strength is important. No matter what the mixing, an extraordinarily high liquid viscosity will result in particle agglomeration, and this is not dependent on the mixing, but rather on the collision energy. In the intermediate regime, there is dependence on both mixing and the Co number.

7.6 Conclusions

A regime map, based on the viscous collision number and a mixing function, has been proposed which aids the understanding of the liquid contact spreading mechanism. Further experiments are needed to determine the mixing function, however, here a preliminary approach has been detailed based on literature and observations made from experiments conducted in this thesis. Four regimes have been proposed relating to different values of Co and $f(\text{mix})$.

The following chapter will present the final conclusions, along with a short section detailing the recommended future work.

Chapter 7

Regime map development: a discussion on mixing, segregation and a collision number

8. Conclusions

8. Conclusions	
8.1 Conclusions	208
8.2 Future work	210

8.1 Conclusions

It has been shown that contact spreading is an important mechanism in many coating unit operations, additional to the spray mechanism which has, to date, received far more attention. Understanding this complex mechanism is, however, far from easy; numerous parameters affect myriad properties of the liquid bridges which are the main route via which contact spreading occurs. In this thesis, a colourimetric image analysis technique has been used to quantify the variation in coating as a function of the various systems which have been investigated. Three different particles - two different model alumina ceramic particles and industrially used sodium percarbonate - allowed the effect of various material characteristics to be investigated, including particle size, size distribution and particle density. These particles were coated with four different molecular weight PEG solutions, allowing the effect of solution viscosity to be investigated. Various drum configurations allowed experiments to be conducted over a range of process conditions.

The effect of particle density was shown to have a significant impact on contact spreading; lighter particles showed drastically increased coating completion times. This was postulated to be a result of the decreased collision energy; this in turn resulting in a higher percentage of collisions resulting in agglomeration as opposed to rebounding, breaking the liquid bridge and redistributing liquid around the particle bed. Once agglomerates form, longer tumbling times are required to rupture the liquid bridges and release the liquid from the bonds. As well as examining the particle density, Chapter 4 also investigated the effect of solution viscosity, varying from 179 mPa.s to over 20,000 mPa.s. Increases in viscosity were shown to produce similar effects; stronger liquid bridges proved harder to overcome than those formed from lower viscosity solutions. It was shown via a capillary number that for the liquids investigated here, the viscous component of the liquid bridge force was several orders of magnitude greater than the component arising from effects of surface tension. Accordingly, a ratio of the bridge strength owing to the viscous forces to the collision energy was proposed and termed the viscous collision number, Co_{vis} .

In Chapter 5, the effect of drum size on contact spreading has been considered using the two model alumina particles and three coating solutions. With the denser alumina particles, two trends were observed; the high viscosity solutions coated faster in larger drums, whereas lower viscosity solutions showed no change in coating behaviour with drum size. The lighter Alumina particles again showed no effect of drum size when using the low viscosity solution; high viscosity solutions coated faster in smaller drums. This was suspected to be a result of different mixing regimes being developed for the different density alumina particles. Here, the Co_{vis} number was not capable of predicting the coating particularly well; other parameters were clearly involved.

Chapter 6 saw the introduction of sodium percarbonate, a more industrially applicable powder. Here, several parameters were again investigated to see if the observations made when using the model system held true. The effect of viscosity was somewhat amplified; high viscosity solutions agglomerated almost instantaneously and agglomeration persisted throughout the process. Due to the reduction in particle density with sodium percarbonate, the collision number was higher than for comparable systems using the alumina particles. However, several other factors could also be enforcing this tendency to agglomerate, for example particle size. Early studies using a very wide size distribution saw intense agglomeration and almost no contact spreading. After removing particles $< 850 \mu\text{m}$ in diameter, this phenomenon was avoided and contact spreading was observed. Here was the first indication that particle size influenced contact spreading. Further investigation produced interesting results; larger particles showed significantly less contact spreading compared to small particle size classes. However, this did not appear to be a result of particle agglomeration, and particle porosity was proposed as the controlling feature. Ingress of the coating solutions was briefly explored, but conclusive results proved difficult to determine; liquid penetration into particles *appeared* to reduce with increasing solution viscosity. If this is to be believed, the higher levels of surface available liquid could also be contributing to the increased levels of particle agglomeration. As to why this difference is seen, it may be that the increased chain length of the higher viscosity solutions prevents them from entering the pores.

Chapter 8

Conclusions

After these effects were seen, studies investigating the effect of drum speed on the contact spreading were completed using the lower viscosity solution and with a controlled particle size distribution. No effect of this parameter was ultimately seen when investigating a drum speed of 30 to 90 rpm. Lower speeds did produce more agglomerates in the times before 10 seconds, but were comparable to the speeds corresponding to the cascading regime after this. Here again, the Co_{vis} was not capable of predicting the tumbling time over the entire range of experiments; in contrast to *model* particles, the interactions between the liquid and particle are influenced by differing surface roughness, variations in particle shape and size, and liquid pore penetration. A function which captures these variables, or the effect they produce on the contact spreading in the tumbling drum is needed to fully represent the system.

In Chapter 7, this function is explored. A regime map which captures the effect of various parameters has been proposed. The viscous collision number captures (i) the bridge strength, dependent on the particle size, separation velocity, separation distance and viscosity, and (ii) the collision energy, dependent on the particle size, particle density and shear rate. A mixing function was discussed and shown to be dependent on a vast number of parameters. However, a simplified mixing function was presented and captures a number of parameters which were otherwise overlooked.

The importance of contact spreading has been highlighted, and the impact of several parameters on this mechanism have been investigated. Elucidation of the factors affecting the mechanism will aid in the understanding of liquid distribution in spray coating processes.

8.2 Future Work

Throughout the completion of this work, several areas have been highlighted which would benefit from further development, allowing the findings here to be extended to other systems, or simply to confirm findings from the present study. These include;

- Identification of a more porous model material, similar in size and shape to the Alumina particles, allowing the effect of liquid ingress to be isolated and investigated. Preferably, such a material would have a consistent porosity

throughout the structure and not exhibit a shell and core type structure as identified in this study.

- Investigations into the timescales of bridge formation, particle interaction, and, if applicable, liquid ingress, in order to determine the rate limiting step in contact spreading.
- Simulations of the studies completed above using Discrete Element Method (DEM) to more accurately track several relevant parameters i.e. particle velocity and liquid transfer.
- And finally, baffled experiments could help to truly isolate the effect of drum size, ensuring a similar flow pattern is developed inside the bed regardless of the size.
- More precisely defining the mixing index to help complete the axis on the regime map.

More areas of investigation would, of course, lead to a greater understanding of this mechanism and the parameters which are most greatly affecting the contact spreading. However, some priority must be given and the suggestions above are based on the areas which potentially offer the greatest possibility for expansion of understanding.

9. References

- Abberger, T., Seo, A., Schæfer, T., (2002). The effect of droplet size and powder particle size on the mechanisms of nucleation and growth in fluid bed melt agglomeration. *International Journal of Pharmaceutics*, **249**(1–2), pp.185–197.
- Abe, E., Yamada, N., Hirose, H., Nakamura, H., (1998). Coating mass distributions of seed particles in a tumbling fluidized bed coater. *Powder Technology*, **97**(1), 85–90.
- Adams, M.J. & Edmondson, B., (1987). Forces between particles in continuous and discrete liquid media. In: B.J. Briscoe, M.J Adams, ed(s). *Tribology in Particulate Technology*. Bristol, England: A. Hilger. pp. 154-172.
- Adams, M.J. & Perchard, V., (1985). The cohesive forces between particles with interstitial fluid. *Institution of chemical engineers symposium series*, **91**, pp.147-160.
- Adetayo, A.A., Litster, J.D., Desai, M., (1993). The effect of process parameters on drum granulation of fertilizers with broad size distributors. *Chemical Engineering Science*, **48**(23), pp.3951–3961.
- Agrawal, A.M. & Pandey, P., (2015). Scale Up of Pan Coating Process Using Quality by Design Principles. *Journal of Pharmaceutical Sciences*, **104**(11), pp.3589–3611.
- Alexander, A.W., Muzzio, F.J., (2001). Batch size increase in dry blending and mixing. In: J. Swarbrick, ed. *Pharmaceutical Process Scale-Up*. New York, America: Marcel Decker, pp. 115–132.
- Alghunaim, A., Kirdponpattara, S., Newby, B.Z., (2016). Techniques for determining contact angle and wettability of powders. *Powder Technology*, **287**, pp.201–215.
- Allen, T., (2013). Sampling of Powders. In: T. Allen, ed. *Particle size measurement*. (3). Springer US, pp. 1–33.
- Arntz, M.M.H.D., Den Otter, W.K., Beftink, H.H., Boom, R.M., Briels, W.J., (2008). Granular mixing and segregation in a horizontal rotating drum: A simulation study on the impact of rotational speed and fill level. *AIChE Journal*, **54**(12), pp.3133–3146.
- Arntz, M.M.H.D., Den Otter, W. K., Beftink, H. H., Boom, R. M., Briels, W. J., (2013). The influence of end walls on the segregation pattern in a horizontal rotating drum. *Granular Matter*, **15**(1), pp.25–38.
- Bagnold, R.A., (1954). Experiments on a Gravity-Free Dispersion of Large Solid Spheres in a Newtonian Fluid under Shear. *Proceedings of the Royal Society A: Mathematical, Physical and Engineering Sciences*, **225**(1160), pp.49–63.
- Barnes, H.A., Hutton, J.F. & Walters, K.F.R.S., (1989). An Introduction to Rheology. *Journal of Non-Newtonian Fluid Mechanics*, **32**(3), pp.331-333.

Chapter 9
References

- Basu, A., De, A. & Dey, S., (2013). Techniques of Tablet Coating: concepts and Advancements: A Comprehensive Review. *Research and Reviews: Journal of Pharmacy and Pharmaceutical Sciences*, **2**(4), pp.1–6.
- De Bisschop, F.R.. & Rigole, W.J., (1982). A physical model for liquid capillary bridges between adsorptive solid spheres: The nodoid of plateau. *Journal of Colloid and Interface Science*, **88**(1), pp.117–128.
- Botterill, J.S.M., Teoman, Y. & Yüregir, K.R., (1982). The effect of operating temperature on the velocity of minimum fluidization, bed voidage and general behaviour. *Powder Technology*, **31**(1), pp.101–110.
- Buckton, G. & Newton, J.M., (1986). Assessment of the wettability of powders by use of compressed powder discs. *Powder Technology*, **46**(2–3), pp.201–208.
- Cassie, A.B.D. & Baxter, S., (1944). Wettability of porous surfaces. *Transactions of the Faraday Society*, **40**(5), pp.546–551.
- Chen, H., Tang, T. & Amirfazli, A., (2015). Fast Liquid Transfer between Surfaces: Breakup of Stretched Liquid Bridges. *Langmuir*, **31**(42), pp.11470–11476.
- Chen, W., Chang, S-y., Kiang, S., Marchut, A., Lyngberg, O., Wang, J., Rao, V., Desai, D., Stamato, H., Early, W., (2010). Modelling of Pan Coating Processes: Prediction of Tablet Content Uniformity and Determination of Critical Process Parameters. *Journal of Pharmaceutical Sciences*, **99**(7), pp.3213–3225.
- Cheng, X.X. & Turton, R., (2000a). The prediction of variability occurring in fluidized bed coating equipment. I. The measurement of particle circulation rates in a bottom-spray fluidized bed coater. *Pharmaceutical Development and Technology*, **5**(3), pp.311–322.
- Cheng, X.X. & Turton, R., (2000b). The prediction of variability occurring in fluidized bed coating equipment. II. The role of nonuniform particle coverage as particles pass through the spray zone. *Pharmaceutical Development and Technology*, **5**(3), pp.323–332.
- Chou, S.H., Liao, C.C., Hsiao, S.S., (2010). An experimental study on the effect of liquid content and viscosity on particle segregation in a rotating drum. *Powder Technology*, **201**(3), pp.266–272.
- Coletta, V. & Rubin, H., (1964). Wurster Coated Aspirin I: Film-Coating Techniques. *Journal of Pharmaceutical Sciences*, **53**(8), pp.953–955.
- Cui, Z., Zhao, Y., Chen, Y., Liu, X., Hua, Z., Zhou, C., Zheng, J., (2014). Transition of axial segregation patterns in a long rotating drum. *Particuology*, **13**(1), pp.128–133.
- Darabi, P, Li, T., Pougatch, K., Salcudean, M., Grecov, D., (2010). Modelling the evolution and rupture of stretching pendular liquid bridges. *Chemical Engineering Science*, **65**(15), pp.4472–4483.

- Denis, C., Hemati, M., Chulia, D., Lanne, J.-Y., Buisson, B., Daste, G., Elbaz, F., (2003). A model of surface renewal with application to the coating of pharmaceutical tablets in rotary drums. *Powder Technology*, **130**(1–3), pp.174–180.
- Dewettinck, K. & Huyghebaert, A., (1998). Top-Spray Fluidized Bed Coating: Effect of Process Variables on Coating Efficiency. *LWT - Food Science and Technology*, **31**(6), pp.568–575.
- Ding, Y.L. et al., (2001). Scaling relationships for rotating drums. *Chemical Engineering Science*, **56**(12), pp.3737–3750.
- Domike, R.D., Cooney, C.L., (2015). Particles and Blending. In: P.J. Cullen et al., eds. *Pharmaceutical Blending and Mixing*. Cichester: Wiley, pp. 81–101.
- Dury, C.M., Ristow, G.H., Moss, J.L., Nakagawa, M., (1998). Boundary effects on the angle of repose in rotating cylinders. *Physical Review E - Statistical Physics, Plasmas, Fluids, and Related Interdisciplinary Topics*, **57**(4), pp.4491–4497.
- Ennis, B.J., (2010). *Agglomeration Technology: Equipment Selection*. Chemical Engineering.
- Ennis, B.J., Li, J., Gabriel, I.T., Robert, P., (1990). The influence of viscosity on the strength of an axially strained pendular liquid bridge. *Chemical Engineering Science*, **45**(10), pp.3071–3088.
- Ennis, B.J., Tardos, G. & Pfeffer, R., (1991). A microlevel-based characterization of granulation phenomena. *Powder Technology*, **65**(1–3), pp.257–272.
- Epstein, N., Grace and J.R., (2010). *Spouted and Spout-Fluid Beds*. Cambridge: Cambridge University Press.
- Fisher, R.A., (1926). On the capillary forces in an ideal soil; correction of formulae given by WB Haines. *The Journal of Agricultural Science*, **16**(03), pp.492–505.
- Florence, A.T. and Attwood, D., (2015). *Physicochemical Principles of Pharmacy: In Manufacture, Formulation and Clinical Use*. London: Pharmaceutical Press.
- Freireich, B., Kumar, R., Ketterhagen, W., Su, K., Wassgren, C., Zeitler., (2015). Comparisons of intra-tablet coating variability using DEM simulations, asymptotic limit models, and experiments. *Chemical Engineering Science*, **131**, pp.197–212.
- Freireich, B., Ketterhagen, W.R. & Wassgren, C., (2011). Intra-tablet coating variability for several pharmaceutical tablet shapes. *Chemical Engineering Science*, **66**(12), pp.2535–2544.
- Freireich, B. & Li, J., (2013). A renewal theory approach to understanding interparticle coating variability. *Powder Technology*, **249**, pp.330–338.
- Freireich, B. & Wassgren, C., (2010). Intra-particle coating variability: Analysis and Monte-Carlo simulations. *Chemical Engineering Science*, **65**(3), pp.1117–1124.

Chapter 9

References

Grand view research., (2017). Laundry Detergent Market Worth \$205.2 Billion By 2025[online]. *Grand View Research*. 4th January 2018. Available at: <https://www.grandviewresearch.com/press-release/global-laundry-detergent-market>.

Henein, H., Brimacombe, J.K., Watkinson, A.P., (1983). Experimental study of transverse bed motion in rotary kilns. *Metallurgical Transactions B*, **14**(2), pp.191–205.

Hilton, J.E., Ying, D.Y. & Cleary, P.W., (2013). Modelling spray coating using a combined CFD-DEM and spherical harmonic formulation. *Chemical Engineering Science*, **99**, pp.141–160.

Hornbaker, D.J., Albert, R., Albert, I., Barabasi, A. L., Schiffer, P., (1997). What keeps sandcastles standing? *Nature*, **387**(6635), p.765.

Hotta, K., Takeda, K. & Inoya, K., (1974). The capillary binding force of a liquid bridge. *Powder Technology*, **10**(4–5), pp.231–242.

Iley, W.J., (1991). Effect of particle size and porosity on particle film coatings. *Powder Technology*, **65**(1–3), pp.441–445.

Iveson, S.M., Litster, J.D., Hapgood, K., Ennis, B.J., (2001) Nucleation, growth and breakage phenomena in agitated wet granulation processes: A review. *Powder Technology*, **117**(1–2), pp.3–39.

Jackson, L.S., Lee, K., (1991). Microencapsulation and the food industry. *Lebensmittel - Wissenschaft + Technologie*, **24**(4), pp.289–297.

Jain, N., Ottino, J.M., Lueptow, R.M., (2002). An experimental study of the flowing granular layer in a rotating tumbler. *Physics of Fluids*, **14**(2), pp.572–582.

Jarray, A., Magnanimo, V., Luding, S., (2018). Wet granular flow control through liquid induced cohesion. *Powder Technology*, [In Press].

Jiang, M., Zhao, Y., Liu, G., Zheng, J., (2011). Enhancing mixing of particles by baffles in a rotating drum mixer. *Particuology*, **9**(3), pp.270–278.

Kadam, K.L., (1990). *Granulation Technology for Bioproducts*, Taylor & Francis.

Kalbag, A., Wassgren, C., (2009). Inter-tablet coating variability: Tablet residence time variability. *Chemical Engineering Science*, **64**(11), pp.2705–2717.

Kan, H., Nakamura, H. & Watano, S., (2017). Effect of droplet size on particle-particle adhesion of colliding particles through droplet. *Powder Technology*, **321**, pp.318–325.

Karlsson, S., Rasmuson, A., Björn, I.N., Schantz, S., (2011). Characterization and mathematical modelling of single fluidised particle coating. *Powder Technology*, **207**(1–3), pp.245–256.

Ketterhagen, W.R., (2011). Modelling the motion and orientation of various pharmaceutical tablet shapes in a film coating pan using DEM. *International Journal of Pharmaceutics*, **409**(1–2), pp.137–149.

- Khakhar, D. V., McCarthy, J. J., Gilchrist, J. F., Ottino, J. M., (1999). Chaotic mixing of granular materials in two-dimensional tumbling mixers. *Chaos*, **9**(1), pp.195–205.
- Kiani, M., Rahimi, M.R., Hosseini, S.H., Ahmadi, G., (2017) Mixing and segregation of solid particles in a conical spouted bed: Effect of particle size and density. *Particuology*, **32**, pp.132–140.
- Kmieć, A., (1980). Hydrodynamics of Flows and Heat Transfer in Spouted Beds. *The Chemical Engineering Journal*, **19**(3), pp.189–200.
- Kucharski, J., Kmiec, A., (1983). Hydrodynamics, heat and mass transfer during coating of tablets in a spouted bed. *The Canadian Journal of Chemical Engineering*, **61**(3), pp.435–439.
- Kumar, R., Freireich, B., Wassgren, C., (2015). DEM–compartment–population balance model for particle coating in a horizontal rotating drum. *Chemical Engineering Science*, **125**, pp.144–157.
- Kumar, R., Wassgren, C., (2014). Inter-particle coating variability in a continuous coater. *Chemical Engineering Science*, **117**, pp.1–7.
- KuShaari, K., Pandey, P., Song, Y., Turton, R., (2006). Monte Carlo simulations to determine coating uniformity in a Wurster fluidized bed coating process. *Powder Technology*, **166**(2), pp.81–90.
- Li, H., (2005). *Impact of cohesion forces on particle mixing and segregation*. Ph.D. thesis, University of Pittsburgh.
- Li, L., (2015). *Particle motion, coating and drying in Wurster fluidized beds - An experimental and discrete element modelling study*. Ph.D. thesis, Chalmers University of Technology.
- Li, H., McCarthy, J.J., (2003). Controlling Cohesive Particle Mixing and Segregation. *Physical Review Letters*, **90**(18), p.4.
- Li, J., Wassgren, C. & Litster, J.D., (2013). Multi-scale modeling of a spray coating process in a paddle mixer/coater: the effect of particle size distribution on particle segregation and coating uniformity. *Chemical Engineering Science*, **95**, pp.203–210.
- Lian, G., Thornton, C., Adams, M.J., (1993). A Theoretical Study of the Liquid Bridge Forces between Two Rigid Spherical Bodies. *Journal of Colloid and Interface Science*, **161**(1), pp.138–147.
- Lievano, D., Velankar, S., McCarthy, J.J., (2017). The rupture force of liquid bridges in two and three particle systems. *Powder Technology*, **313**, pp.18–26.
- Lin, H., May, R.K., Evans, M.J., Zhong, S., Gladden, L.F., Shen, Y., Zeitler, J.A., May, R.K., Zhong, S., (2015). Impact of Processing Conditions on Inter-tablet Coating Thickness Variations Measured by Terahertz In-Line Sensing. *Journal of Pharmaceutical Sciences*, **104**(8), pp.2513–2522.

Chapter 9
References

- Litster, J.D., Hapgood, K.P., Michaels, J.N., Sims, A., Roberts, M., Kameneni, S.K., Hsu, T., (2001). Liquid distribution in wet granulation: Dimensionless spray flux. *Powder Technology*, **114**(1–3), pp.32–39.
- Liu, X., Ma, W., Hou, Q., Zhang, Q., Gong, B., Feng, Y., (2018). End-wall effects on the mixing process of granular assemblies in a short rotating drum. *Powder Technology*, **339**, pp.497-505.
- Liu, P.Y., Yang, R.Y., Yu, A.B., (2011). Dynamics of wet particles in rotating drums: Effect of liquid surface tension. *Physics of Fluids*, **23**(1).
- Liu, P.Y., Yang, R.Y., Yu, A.B., (2013). The effect of liquids on radial segregation of granular mixtures in rotating drums. *Granular Matter*, **15**(4), pp.427–436.
- Maneval, J.E., Hill, K.M., Smith, B.E., Caprihan, A., Fukushima, E., (2005). Effects of end wall friction in rotating cylinder granular flow experiments. *Granular Matter*, **7**(4), pp.199–202.
- Mani, R., Kadau, D., Herrmann, H.J., (2013). Liquid migration in sheared unsaturated granular media. *Granular Matter*, **15**(4), pp.447–454.
- Mann, U., (1983). Analysis of spouted-bed coating and granulation. 1. Batch operation, *Ind. Eng. Chem. Process Des. Dev.* **22**, pp.288-292
- Mann, U., Crosby, E.J., Rubinovitch, M., (1974). Number of cycles distribution in circulating systems. *Chemical Engineering Science*, **29**(3), pp.761–765.
- Mann, U., Rubinovitch, M., Crosby, E.J., (1979). Characterization and analysis of continuous recycle systems, *AIChE*, **25**, pp.873-882
- Matthewson, M.J., (1988). Adhesion of spheres by thin liquid films. *Philosophical Magazine A: Physics of Condensed Matter, Structure, Defects and Mechanical Properties*, **57**(2), pp.207–216.
- Mazzone, D.N., Tardos, G.I., Pfeffer, R., (1987). The behavior of liquid bridges between two relatively moving particles. *Powder Technology*, **51**(1), pp.71–83.
- Megias-Alguacil, D., Gauckler, L.J., (2011). Accuracy of the toroidal approximation for the calculus of concave and convex liquid bridges between particles. *Granular Matter*, **13**(4), pp.487–492.
- Megias-Alguacil, D., Gauckler, L.J., (2010). Analysis of the capillary forces between two small solid spheres binded by a convex liquid bridge. *Powder Technology*, **198**(2), pp.211–218.
- Mehrotra, V.P., Sastry, K.V.S., (1980). Pendular bond strength between unequal-sized spherical particles. *Powder Technology*, **25**(2), pp.203–214.
- Merkus, H.G., (2009). Particle Size Measurements: Fundamentals, Practice, Quality, Springer Netherlands.
- Micromeritics., (2018). AccuPyc II 1340 [online]. *Micromeritics*. 16th June 2018. Available from: <http://www.micromeritics.com/Product-Showcase/AccuPyc-II-1340.aspx>.

- Micromeritics., (2009). Micromeritics' GeoPyc 1360 Envelope Density Analyzer, an Important Analytical Tool for Pharmaceutical Roller Compaction Applications [online]. *Micromeritics*. 17th July 2018. Available from: <http://www.micromeritics.com/Pressroom/Press-Release-List/GeoPyc-1360-Press-Release.aspx>
- Mohan, B. Kloss, C., Khinast, J., Radl, S., (2014). Regimes of liquid transport through sheared beds of inertial smooth particles. *Powder Technology*, **264**, pp.377–395.
- Mueller, R. & Kleinebudde, P., (2007). Prediction of tablet velocity in pan coaters for scale-up. *Powder Technology*, **173**(1), pp.51–58.
- Mu, F. & Su, X., (2007). Analysis of liquid bridge between spherical particles. *China Particuology*, **5**(6), pp.420–424.
- Murase, K., Mochida, T., Sagawa, Y., Sugama, H., (2008). Estimation on the Strength of a Liquid Bridge Adhered to Three Spheres. *Advanced Powder Technology*, **19**(4), pp.349–367.
- Murase, K., Mochida, T., Sugama, H., (2004). Experimental and numerical studies on liquid bridge formed among three spheres. *Granular Matter*, **6**(2–3), pp.111–119.
- Nakagawa, M. Altobelli, S.A., Caprihan, A., Fukushima, E., Jeong, E.K. (1993). Non-invasive measurements of granular flows by magnetic resonance imaging. *Experiments in Fluids*, **16**(1), pp.54–60.
- Nase, S.T. et al., (2001). Discrete characterization tools for cohesive granular material. *Powder Technology*, **116**(2–3), pp.214–223.
- Naz, M.Y., Sulaiman, S.A., Ariwahjoedi, B., Shaari, K.Z.K. (2015). Effect of pre-coat solution temperature on fluidized bed urea coatings. *Surface Engineering*, **31**(7), pp.486–491.
- Newitt, D., Conway-Jones, J., (1958). A contribution to the theory and practice of granulation. *Trans. Inst. Chem. Eng.*, **36**, pp.422–452.
- de Oliveira, W.P., Freire, J.T., Coury, J.R., (1997). Analysis of particle coating by spouted bed process. *International Journal of Pharmaceutics*, **158**(1), pp.1–9.
- Orr, F.M., Scriven, L.E., Rivas, A.P., (1975). Pendular rings between solids: meniscus properties and capillary force. *Journal of Fluid Mechanics*, **67**(04), p.723.
- Ottino, J.M., Khakhar, D. V., (2000). Mixing and Segregation of Granular Materials. *Annual Review of Fluid Mechanics*, **32**, pp.55–91.
- Padday, J.F., (1978). *Wetting, spreading and adhesion*, London: Academic Press.
- Palmer, S., Ingram, A., Seville, J., (2010). The Wurster coater. In N. Epstein & J. R. Grace, eds. *Spouted and Spout-Fluid Beds*. Cambridge: Cambridge University Press, pp. 238–249.

Chapter 9

References

- Pandey, P., Song, Y., Kayihan, F., Turton, R., (2006). Simulation of particle movement in a pan coating device using discrete element modeling and its comparison with video-imaging experiments. *Powder Technology*, **161**(2), pp.79–88.
- Pandey, P., Katakdaunde, M., Turton, R., (2006). Modeling weight variability in a pan coating process using Monte Carlo simulations. *AAPS PharmSciTech*, **7**(4), p.83.
- Pandey, P., Turton, R., Joshi, N., Hammerman, E., Ergun, J., (2006). Scale-up of a pan-coating process. *AAPS PharmSciTech*, **7**(4), pp.E1–E8.
- Parker, D.J., Dijkstra, A.E., Martin, T.W., Seville, J.P.K., (1997). Positron emission particle tracking studies of spherical particle motion in rotating drums. *Chemical Engineering Science*, **52**(13), pp.2011–2022.
- Pasha, M., Hare, C., Ghadiri, M., Gunadi, A., Piccione, P.M., (2017). Inter-particle coating variability in a rotary batch seed coater. *Chemical Engineering Research and Design*, **120**, pp.92–101.
- Paul, E.L., Atiemo-Obeng, V.A., Kresta, S.M., (2004). *Handbook of Industrial Mixing: Science and practice*. New York, America: John Wiley & Sons.
- Pei, C. & Elliott, J.A., (2017). Asymptotic limits on tablet coating variability based on cap-to-band thickness distributions: A discrete element model (DEM) study. *Chemical Engineering Science*, **172**, pp.286–296.
- Pepin, X., Simons, S.J., Blanchon, S., Rossetti, D., Couarraze, G (2001). Hardness of moist agglomerates in relation to interparticle friction, granule liquid content and nature. *Powder Technology*, **117**(1–2), pp.123–138.
- Pepin, X., Rossetti, D., Iveson, S.M., Simons, S.J.R., (2000). Modeling the Evolution and Rupture of Pendular Liquid Bridges in the Presence of Large Wetting Hysteresis. *Journal of Colloid and Interface Science*, **232**(2), pp.289–297.
- Pepin, X., Blanchon, S., Couarraze, G., (2001). Power consumption profiles in high-shear wet granulation. II: Predicting the overwetting point from a spreading energy. *Journal of pharmaceutical sciences*, **90**(3), pp.332–9.
- Pirard, S.L., Lumay, G., Vandewalle, N., Pirard, J.P., (2009). Motion of carbon nanotubes in a rotating drum: The dynamic angle of repose and a bed behavior diagram. *Chemical Engineering Journal*, **146**(1), pp.143–147.
- Pitois, O., Moucheront, P., Chateau, X., (2000). Liquid Bridge between Two Moving Spheres: An Experimental Study of Viscosity Effects. *Journal of Colloid and Interface Science*, **231**(1), pp.26–31.
- Plateau, J.A.F., (1857). Experimental and theoretical researches on the figures of equilibrium of a liquid mass withdrawn from the action of gravity. *The London, Edinburgh and Dublin Philosophical Magazine and Journal of Science*, **14**(90).

- Pohlman, N.A., Ottino, J.M., Lueptow, R.M., (2006). End-wall effects in granular tumblers: From quasi-two-dimensional flow to three-dimensional flow. *Physical Review E - Statistical, Nonlinear, and Soft Matter Physics*, **74**(3), pp.1–13.
- Princen, H.M., (1968). Comments on “The Effect of Capillary Liquid on the Force of Adhesion between Spherical Solid Particles.” *Journal of Colloid and Interface Science*, **26**(2), pp.249–253.
- Qiao, M., Zhang, L., Ma, Y., Zhu, J., Chow, K., (2010). A novel electrostatic dry powder coating process for pharmaceutical dosage forms: immediate release coatings for tablets. *European journal of pharmaceutics and biopharmaceutics: official journal of Arbeitsgemeinschaft für Pharmazeutische Verfahrenstechnik e.V*, **76**(2), pp.304–10.
- Rawle, A., (2003). Basic Principles of Particle Size Analysis. *Surface Coatings International Part A Coatings Journal*, **44**(0), pp.1–8.
- R. Muliadi, A., E. Sojka, P., (2010). A review of pharmaceutical tablet spray coating. *Atomization and Sprays*, **20**, pp.611–638.
- Rege, B.D., Gawel, J., Kou, J.H., (2002). Identification of critical process variables for coating actives onto tablets via statistically designed experiments. *International Journal of Pharmaceutics*, **237**(1–2), pp.87–94.
- Rynhart, P.R., Mclachlan, R., Jones, J.R., Mckibbin, R., (2003). Solution of the Young-Laplace equation for three particles. *Research Letters in the Information and Mathematical Sciences*, **5**(4), pp.119–127.
- Sacher, S., G. Khinast, J., (2015). An Overview of Pharmaceutical Manufacturing for Solid Dosage Forms. *Methods in Pharmacology and Toxicology*, **32**, pp.311–383.
- Sahni, E., Chaudhuri, B., (2012). Experimental and modeling approaches in characterizing coating uniformity in a pan coater: A literature review. *Pharmaceutical Development and Technology*, **17**(2), pp.134–147.
- Sahni, E., Chaudhuri, B., (2011). Experiments and numerical modeling to estimate the coating variability in a pan coater. *International Journal of Pharmaceutics*, **418**(2), pp.286–296.
- Salcudean, M., Pougatch, K., Grecov, D., (2010). Numerical Studies of Stretching Liquid Bridges Between Two Solid. *ASME 2010 International Mechanical Engineering Congress and Exposition, November 10-18, 2010*. pp.1061-1069
- Saleh, K., Guigon, P., (2006). Coating and Encapsulation Processes in Powder Technology. In: A.D. Salman, M.J. Hounslow, J.P.K. Seville, eds. *Granulation*. Amsterdam: Elsevier, pp. 323–375.
- Saleh, K., Steinmetz, D., Hemati, M., (2003). Experimental study and modeling of fluidized bed coating and agglomeration. *Powder Technology*, **130**(1–3), pp.116–123.
- Sanfratello, L., Caprihan, A., Fukushima, E., (2007). Velocity depth profile of granular matter in a horizontal rotating drum. *Granular Matter*, **9**(1–2), pp.1–6.

Chapter 9
References

- Santomaso, A., Olivi, M., Canu, P., (2004). Mechanisms of mixing of granular materials in drum mixers under rolling regime. *Chemical Engineering Science*, **59**(16), pp.3269–3280.
- Sauer, D., Cerea, M., DiNunzio, J., McGinity, J., (2013). Dry powder coating of pharmaceuticals: A review. *International Journal of Pharmaceutics*, **457**(2), pp.488–502.
- Schmelzle, S., Asylbekov, E., Radel, B., Nirschl, H., (2018). Modelling of partially wet particles in DEM simulations of a solid mixing process. *Powder Technology*, **338**, pp.354–364.
- Schubert, H., Herrmann, W. & Rumpf, H., (1975). Deformation behaviour of agglomerates under tensile stress. *Powder Technology*, **11**(2), pp.121–131.
- Shariati, S., Ramadi, A., Salsani, A., (2015). Beneficiation of Low-Grade Phosphate Deposits by a Combination of Calcination and Shaking Tables: Southwest Iran. *Minerals*, **5**(3), pp.367–379.
- Shi, D., McCarthy, J.J., (2008). Numerical simulation of liquid transfer between particles. *Powder Technology*, **184**(1), pp.64–75.
- Shi, F.N., Napier-Munn, T.J., (1999). Estimation of shear rates inside a ball mill. *International Journal of Mineral Processing*, **57**(3), pp.167–183.
- Shuttleworth, R. & Bailey, G.L., (1948). Spreading of a liquid over a rough solid. *Disc. Faraday Soc.*, **3**(16), pp.16–22.
- Šibanc, R., Srčić, S., Dreu, R., (2013). Numerical simulation of two-phase flow in a Wurster coating chamber and comparison with experimental results. *Chemical Engineering Science*, **99**, pp.225–237.
- da Silva, C.A.M., Butzge, J.J., Nitz, M., Taranto, O.P., (2014). Monitoring and control of coating and granulation processes in fluidized beds – A review. *Advanced Powder Technology*, **25**(1), pp.195–210.
- Simons, S.J.R., (2007). Liquid Bridges in Granules. In: A.D. Salman, M.J. Hounslow, J.P.K. Seville ed(s). *Handbook of Powder Technology: Granulation*. Elsevier, pp. 1257–1316.
- Simons, S.J.R., Fairbrother, R.J., (2000). Direct observations of liquid binder-particle interactions: The role of wetting behaviour in agglomerate growth. *Powder Technology*, **110**(1–2), pp.44–58.
- Simons, S.J.R., Seville, J.P.K. & Adams, M.J., (1994). An analysis of the rupture energy of pendular liquid bridges. *Chemical Engineering Science*, **49**(14), pp.2331–2339.
- Song, Y., Turton, R., (2007). Study of the effect of liquid bridges on the dynamic behavior of two colliding tablets using DEM. *Powder Technology*, **178**(2), pp.99–108.
- Starov, V.M., Velarde, M.G., Radke, C.J., (2007). *Wetting and Spreading Dynamics*. Boca Raton: Taylor & Francis.

- Teunou, E., Poncelet, D., (2002). Batch and continuous fluid bed coating – review and state of the art. *Journal of Food Engineering*, **53**(4), pp.325–340.
- To, D. & Davé, R.N., (2015). Fluid bed film coating of fine ibuprofen particles. *Powder Technology*.
- Toschkoff, G., Khinast, J.G., (2013). Mathematical modeling of the coating process. *International journal of pharmaceutics*, **457**(2), pp.407–22.
- Turton, R., Cheng, X.X., (2005). The scale-up of spray coating processes for granular solids and tablets. *Powder Technology*, **150**, pp.78–85.
- United states pharmacopoeial commision, (2016). *Uniformity of Dosage Forms*. **41**(905).
- Walker, G.M., Holland, C.R., Ahmad, M.N., Fox, J.N., Kells, A.G., (2000). Drum granulation of NPK fertilizers. *Powder Technology*, **107**(3), pp.282–288.
- Wang, J., Hemenway, J., Chen, W., Desai, D., Early, W., Paruchuri, S., Chang, S-Y., Stamato, H., Varia, S., (2012). An evaluation of process parameters to improve coating efficiency of an active tablet film-coating process. *International Journal of Pharmaceutics*, **427**(2), pp.163–169.
- Wang, J., Shi, Q., Huang, Z., Gu, Y., Musango, L., Yang, Y., (2015). Experimental Investigation of Particle Size Effect on Agglomeration Behaviours in Gas–Solid Fluidized Beds. *Industrial & Engineering Chemistry Research*, **54**(48), pp.12177–12186.
- Washino, K., Miyazaki, K., Tsuji, T., Tanaka, T., (2016). A new contact liquid dispersion model for discrete particle simulation. *Chemical Engineering Research and Design*, **110**, pp.123–130.
- Washino, K., Chan, E.L., Matsumoto, T., Hashino, S., Tsuji, T., Tanaka, T., (2017). Normal viscous force of pendular liquid bridge between two relatively moving particles. *Journal of Colloid and Interface Science*, **494**, pp.255–265.
- Wesdyk, R. et al., (1993). Factors affecting differences in film thickness of beads coated in fluidized bed units. *International Journal of Pharmaceutics*, **93**(1), pp.101–109.
- Willett, C.D., Adams, M.J., Johnson, S.A., Seville, J.P.K., (2000). Capillary bridges between two spherical bodies. *Langmuir*, **16**(24), pp.9396–9405.
- Willett, C.D., Adams, M.J., Johnson, S.A., Seville, J.P.K., (2003). Effects of wetting hysteresis on pendular liquid bridges between rigid spheres. *Powder Technology*, **130**(1–3), pp.63–69.
- Wnukowski, P., Setterwall, F., (1989). The coating of particles in a fluidized bed (residence time distribution in a system of two coupled perfect mixers). *Chemical Engineering Science*, **44**(3), pp.493–505.
- Woodward, R.P., (2008). Surface Tension Measurements Using the Drop Shape Method. *First Ten Angstroms Inc Technical Information*, pp.1–6.

Chapter 9
References

Wurster, D.E., (1953). *US Patent No. US2648609A*, Method Of Applying Coatings To Edible Tablets Or The Like. Wisconsin, America: United States Patent Office.

Ye, C. & Chi, H., (2018). A review of recent progress in drug and protein encapsulation: Approaches, applications and challenges. *Materials Science and Engineering: C*, **83**, pp.233–246.

Yen, E.C. & Stirn, F.E., (1950). *US Patent No. US2512192A*, Silicone resin medicament coating. New York, America: United States Patent Office

Young, T., (1805). An Essay on the Cohesion of Fluids. *Philosophical Transactions of the Royal Society of London*, **95**, pp.65–87.

Yuan, Y. & Lee, T.R., (2013). Contact Angle and Wetting Properties. In: G. Bracco & B. Holst, eds. *Surface Science Techniques*. Berlin, Heidelberg: Springer Berlin Heidelberg, pp. 3–34.

Yusof, N., Green, J., Pitt, K., Arjmandi-Tash, O., Campbell, A.I., Ahmadian, H., Tantawy, H., Smith, R., (2018). A novel method for the analysis of particle coating behaviour via contact spreading in a tumbling drum: Effect of coating liquid viscosity, [Unpublished].

Zonfrilli, F., Germana, S., Guida, V., (2009). Thermal stability of dry detergent formulation containing sodium percarbonate. *The International Conference on Chemical and Process Engineering*, Pts 1-3, **17(1)**, pp.705–710.